Experimental Study of Expanding Hollow Cathode Discharges

Samuel Arthur Lazar Dixon

A thesis submitted for the degree of
Doctor of Philosophy of
The Australian National University

July 2014

Declaration

This thesis is an account of research undertaken between 16 January, 2011 and 4 July, 2014 at the Research School of Physics and Engineering, The Australian National University, Canberra, Australia.

Except where acknowledged in the customary manner, the material presented in this thesis is, to the best of my knowledge, original and has not been submitted in whole or in part for a degree in any university.

Samuel Arthur Lazar Dixon
4 July, 2014

Acknowledgements

Primarily I would like to thank Rod Boswell and Christine Charles for fostering such a wonderful educational environment in SP^3. The past three and a half years have shown me just how special and unique the group is. I very much appreciate all the time and effort that has gone into transforming me into a (hopefully) capable scientist.

The work presented in this thesis would have been impossible without the technical insight, experience, and expertise of Peter Alexander and Steve Holgate. It has been an absolute privilege to have such highly skilled professionals so willing to make themselves available to me throughout the course of my studies. I would also like to thank the electronics unit and school computer unit for their frequent assistance.

Sincere thanks are due to John Holland, Richard Gottscho, Wes Cox (both as a student and Lam employee) for their involvement in the work. Lam's generosity with both time and resources is very much appreciated. I would like to extend my gratitude to Timo Gans and Deborah O'Connell who helped facilitate the work performed with the ICCD camera. I would also like to thank Andor Technologies for the loan of said camera.

The friendship and guidance of my friends both within SP^3 and the wider research school have added great texture to my experience as a postgraduate student at the ANU. Thanks to Wes, Trev, James, Cameron, Shaun, Amelia, Yunchao, Craig, and everyone else. The administrative and support staff have been also been fantastic. Maxine and Uyen deserve special recognition for being so patient with my often late, and sometimes incorrect paperwork.

I want to thank my family for their enthusiasm and support over the course of my PhD. I would especially like to thank my Zaida, Len Dixon, for proofreading my thesis for grammar. Finally I would like to acknowledge the support of my lovely partner Elizabeth Dimo. Thank you for your generosity with time, effort, and patience in helping me through my studies.

Publications

The work presented in this thesis has resulted in the following publications in peer reviewed journals:

S. Dixon, C. Charles, R. W. Boswell, W. Cox, J. Holland, and R. Gottscho
Interactions Between Arrayed Hollow Cathodes
Journal of Physics D: Applied Physics 46, 145204 (2013).

S. Dixon, C. Charles, and R. W. Boswell
Spatial Evolution of EEPFs in a Millimetre Scale Radio Frequency Argon Plume
Journal of Physics D: Applied Physics 46, 365202 (2013).

S. Dixon, C. Charles, J. Dedrick, T. Gans, D. OConnell, and R. W. Boswell
Observations of a Mode Transition in a Hydrogen Hollow Cathode Discharge Using Phase Resolved Optical Emission Spectroscopy
Applied Physics Letters 105, 014104 (2014).

S. Dixon, J. Dedrick, C. Charles, T. Gans, D. OConnell, and R. W. Boswell
Phase Resolved Imaging of a Repetitive Extrusion of Hydrogen Plasma From a Hollow Cathode Source
Plasma Science, IEEE Transactions on 42, 2834 (2014).

Abstract

This thesis details work performed in the Distributed Array Shower Head (DASH) and Pocket Rocket systems over the past three years, and is targeted at use in surface processing applications. The DASH source produces plasma in an array of hollow cathodes. Pocket Rocket is a geometrically similar analogue to a single hollow cathode in the DASH source, used for its superior optical access. The work aims to investigate the physics that underpins the operation of such a plasma source.

To characterise the expansion plumes from the hollow cathodes, two dimensional maps of ion densities in argon are measured using a Langmuir probe. A peak density of 10^{18} m^{-3} is measured at the interface between hollow cathode and expansion chamber. Downstream of the plasma plume, densities are as low as 10^{14} m^{-3}. Plasma density in the plume has a $1/z^2$ dependence, as plasma freely diffuses into the expansion chamber. Further downstream, there is an abrupt change in behaviour as the plasma density becomes nearly constant with increasing distance from the hollow cathode.

A compensated Langmuir probe is used in conjunction with an emissive probe to make spatially resolved measurements of the plasma potential, floating potential, and electron energy probability function (EEPF). Inside the hollow cathode a Maxwellian distribution is observed with an electron temperature of 2 eV. The EEPFs measured in the plume show bi-Maxwellian behaviour, before becoming a single Maxwellian with temperatures as high as 11 eV far from the source.

To investigate its etching capabilities, the DASH source is also operated using SF_6 to produce atomic fluorine and to chemically etch unbiased silicon. Etch rates of up to 3.2 μm per minute are measured using a profilometer. Scanning Electron Microscopy of some processed wafers demonstrates the isotropic profile expected of the chemical etching process. It is shown that scaling of the DASH source to process a 300 mm wafer with uniformity of $\pm5\%$ uniformity of etch rate is possible.

To investigate the possible use of DASH in deposition processes, optical experi-

ments on hydrogen plasma with a pressure on the order of 1 Torr are performed in Pocket Rocket. Two operational modes are observed, named the diffuse and the bright modes after their respective appearances. Fulcher α spectroscopy yields gas temperatures of approximately 350 K for the diffuse mode and 500 K in the bright mode. Temperature is observed to be independent of pressure but strongly dependent on power.

Pocket Rocket is also investigated using an intensified CCD (ICCD) camera for spatially resolved, sub-rf cycle imaging of Balmer α emission. The diffuse mode is found to be operating as a typical γ capacitive discharge, while the bright mode displays evidence of some degree of inductive coupling. The bright mode has high enough gas temperatures to precipitate the formation of a supersonic shock as gas expands from the hollow cathode. The shock is stationary, but is only apparent once per rf cycle as a burst of energetic electrons passes through it.

Contents

Publications vii

Abstract ix

1 Introduction 1

1.1 Plasma . . . 1

1.1.1 Plasma Breakdown, Potential, and Sheath Formation . . . 3

1.1.2 Electron Energy Distributions and Temperature . . . 7

1.2 Capacitively Coupled Plasmas . . . 10

1.3 Hollow Cathode Plasmas . . . 11

1.4 Plasmas for Etching . . . 13

1.4.1 History of Plasma Etching . . . 14

1.4.2 Etching Mechanisms . . . 15

1.5 Scope of the Thesis . . . 18

2 Apparatus 19

2.1 The DASH Source . . . 19

2.1.1 The Pocket Rocket Source . . . 22

2.2 Vacuum System and Pressure Variation . . . 23

2.3 Probe and Wafer Mounting . . . 25

2.3.1 Movable Probe Port . . . 25

2.3.2 Wafer Mount . . . 27

2.4 Power Delivery and Matching Network . . . 28

2.5 Diagnostic probes . . . 32

2.5.1 Langmuir Probe . . . 32

2.5.2 Compensated Langmuir Probe . . . 37

2.5.3 Emissive Probe . . . 43

3 Plasma Plume Density Mapping **49**

3.1 Breakdown and Stable Operation 49

3.2 Single Hollow Cathode Operation 51

3.3 Multiple Hollow Cathode Operation 54

3.3.1 Measurements 55

3.3.2 Fitting and Reproducibility 59

3.4 Conclusion 62

4 Spatial Variation of the EEPF in a Hollow Cathode Plume **65**

4.1 Experimental Design 65

4.2 Variation in the EEPF Throughout Parameter Space 68

4.3 Relationship of T_e in the Source and V_p in the Plume 73

4.4 Spatially Resolved Langmuir Probe Measurements 78

4.4.1 Axial Measurements in the Expansion Chamber 78

4.4.2 Iterative Model of an EEPF 80

4.4.3 Lateral Measurements of EEPFs in the Plume 82

4.5 Conclusion 84

5 Etching Silicon Using SF_6 **85**

5.1 Experimental Design 85

5.2 Measured Etch Rates and Isotropy 86

5.3 Spatial Variation in Etch Rates 90

5.3.1 Axial Variation 90

5.3.2 Etch Uniformity 91

5.4 Scaling 93

5.5 Aluminium Fluoride Deposition 96

5.6 Conclusion 100

6 Gas Temperature Analysis Via Fulcher α Spectroscopy **103**

6.1 Experimental Design 104

6.2 Assumptions and the Corona Phase 106

6.3 Emission intensity 109

6.4 Rotational distributions and temperatures 110

6.5 Results . . . 113
6.5.1 Parameter Sweeps . . . 114
6.5.2 Mode Transition . . . 116
6.5.3 Static Gas . . . 118
6.6 Preliminary Absorption Spectroscopy . . . 119
6.7 Conclusion . . . 120

7 Phase Resolved OES of the Hydrogen Plasma 123
7.1 Experimental Design and Calibration . . . 124
7.2 Operational Modes . . . 130
7.2.1 Diffuse Mode . . . 130
7.2.2 Bright Mode . . . 137
7.3 Power Sweep . . . 143
7.3.1 Rear View . . . 143
7.3.2 Side View . . . 145
7.4 Pressure Sweep . . . 147
7.4.1 Rear View . . . 147
7.4.2 Side View . . . 149
7.5 Electrical Study of the Mode Transition . . . 152
7.6 Static Pressures . . . 154
7.7 Conclusion . . . 155

8 Conclusions 159
8.1 Summary of Results . . . 159
8.2 Future Work . . . 164

Bibliography 165

Introduction

This thesis details experiments performed in the Distributed Array Shower Head (DASH) plasma source, and its analogue Pocket Rocket. By virtue of its geometry, DASH seeks to exploit the characteristics of an arrayed hollow cathode device. The long term goal is to produce a uniform plasma with a high concentration of radical atomic species but lacking energetic ions. The thesis investigates the physics underpinning the operation of such a design, including comprehension of its benefits and drawbacks. Originally, the DASH source was envisioned purely as an etching source, but in later work is also investigated for possible applications in deposition processes.

1.1 Plasma

Plasma is often described as the fourth state of matter, and is thought to comprise some 99% of the visible universe [1]. It is a gas in which some or all of the constituent particles (be they atoms or molecules) are ionised [2]. Plasmas exhibit the properties of collective behaviour and quasineutrality. Collective behaviour occurs in a plasma because it is susceptible to influence by electric and magnetic fields. As such, regions of the plasma outside the range of collisional contact can affect one another. Quasineutrality refers to the fact that a plasma has no net charge, or in other words, that there are always an equal number of positive and negative charges present in the plasma. Quasineutrality also requires that the distribution of charged particles within the plasma suppresses the formation of electric fields within the plasma over a certain length scale, called the Debye length, λ_D. For a volume larger than a Debye sphere (with a radius of the Debye length), the densities of positively

and negatively charged particles will be equal [1]. The Debye length is defined as

$$\lambda_D = \left(\frac{\epsilon_0 T_e}{e n_0}\right)^{1/2} \tag{1.1}$$

where ϵ_0 is the permittivity of free space, T_e is the electron temperature, e is the fundamental electric charge, and n_0 is the density of charged species. The Debye length is important as it defines the space over which an applied potential can be shielded by the plasma, for example an earthed wall of a plasma reactor at 0 V. Considering some arbitrary potential, Ψ_0, applied to the plasma in one dimension, the reduction in potential at a distance x from the forced potential is defined by

$$\Psi(x) = \Psi_0 \exp(-|x|/\lambda_D) \tag{1.2}$$

This implies that over a single Debye length, the potential is reduced by $1/e$. In a typical laboratory plasma this becomes relevant where the plasma is in contact with the walls of the vessel within which it is contained. Due to the relative masses of ions and electrons, the plasma potential, V_p, must be higher than the potential of a grounded or floating wall. As a consequence of these unequal potentials, a sheath forms, a region in which the potential varies from that at the wall to V_p over some distance controlled by the Debye length [3].

Weakly ionised plasmas, such as those presented in this thesis, are dominated by collisions between particles in the gas phase. Broadly these can be grouped into two categories: elastic and inelastic collisions, such as excitation and ionisation. When the total energy of the incident particles is below the excitation and ionisation thresholds, elastic collisions are the only sort that can occur in a monoatomic plasma. For a chemically simple gas such as argon, these threshold energies are 12.14 and 15.76 eV respectively [4]. For a molecular plasma the situation becomes more complex due to the availability of excited vibrational and rotational states of the molecules. Above the excitation and ionisation energy thresholds, both elastic and inelastic collisions can occur. For a simple argon plasma the following reactions outline the basic processes present in the discharge

$$\mathrm{Ar} + \mathrm{e} \longrightarrow \mathrm{Ar} + \mathrm{e} \qquad \text{(Elastic collision)} \tag{1.3}$$

$$\mathrm{Ar} + \mathrm{e} \longrightarrow \mathrm{Ar}^{*} + \mathrm{e} \qquad \text{(Exciting collision)} \tag{1.4}$$

$$\mathrm{Ar} + \mathrm{e} \longrightarrow \mathrm{Ar}^{+} + 2\,\mathrm{e} \qquad \text{(Ionising collision)} \tag{1.5}$$

where the superscript * denotes an electronically excited state.

In reality, the number of reactions present are more complex, even in a plasma as simple as argon [5, 6]. Every collisional process within a plasma has an associated cross section (σ), mean free path (λ), and frequency (ν). The cross section gives an area of interaction for which a collision can occur. The mean free path describes the length scale over which the uncollided flux is reduced to $1/e$ of its original value [2]. The mean free path is defined by equation 1.6

$$\lambda = \frac{1}{n_g \sigma(\epsilon)} \tag{1.6}$$

where n_g is the neutral gas pressure, and the cross section, $\sigma(\epsilon)$, is a function of the energy of the incident electron [7]. Typically the processes described by these metrics consider an electron impact collision, although they are not limited to this. The collision frequency is defined by equation 1.7

$$\nu = n_g \sigma(\epsilon) v \tag{1.7}$$

where v is the velocity of the incident electrons.

1.1.1 Plasma Breakdown, Potential, and Sheath Formation

For a direct current (DC) discharge the breakdown voltage, V_b is described by the Paschen curve. The formula for breakdown voltage is defined in equation 1.8

$$V_b = \frac{Bpd}{\ln(Apd) - \ln(\ln(1 + 1/\gamma_{se}))} \tag{1.8}$$

where A and B are constants whose values vary depending on the gas used, p is the pressure in the discharge, d is the separation of the electrodes, and γ_{se} is the secondary electron emission coefficient of the cathode. It can be seen from equation 1.8 that there is a minimum value for the breakdown voltage dependent on an optimised pressure-distance product, pd.

In an rf system the breakdown voltage is lower than in a DC plasma due to the time varying nature of the fields present in the discharge. Provided an electron has not had an inelastic collision with either the wall or another particle when the time varying field reverses, it will have its direction reversed and continue to gain energy from the applied field. This process effectively increases the path length from the electron's frame of reference. As such, the strength of the applied field need not be as strong as the direct current case [8].

During the breakdown process the plasma will eventually come into contact with the walls of the chamber within which it is contained. For the plasma to be in a steady state, the flux of both positive and negative charges to the walls of the chamber must be equal. The ions in the plasma will always be significantly more massive than the electrons, hence electron velocity is much higher than ion velocity. This means that for the fluxes to balance, a potential that retards electron motion towards the walls must form. This is the sheath, whose width is determined by the Debye length. An example of a sheath is represented diagrammatically in figure 1.1.

The approach used in [2] is followed to understand the sheath mathematically. The voltage at the boundary of the presheath and sheath is arbitrarily set to 0. The speed of the ions at this point is defined as u_s, and invoking the law of quasineutrality, the densities of ions and electrons are equal. Considering a one dimensional system, and ignoring collisions between ions and the background neutral gas, the conservation of energy of the ions yields

$$\frac{1}{2}M_i u^2(x) = \frac{1}{2}M_i u_s^2 - e\Phi(x) \tag{1.9}$$

where M_i is the mass of the ions, $u(x)$ is speed, and $\Phi(x)$ is the potential at some position within the sheath x. If the sheath is collisionless and no ionisation can occur

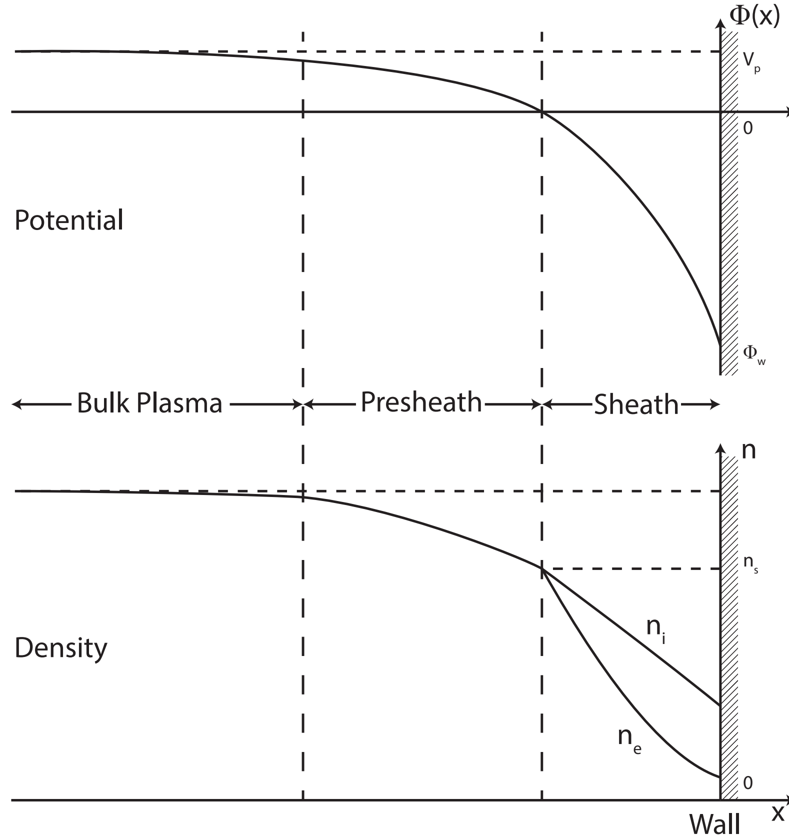

Figure 1.1: *Top*: Variation of plasma potential near a wall. The field in the presheath region accelerates ions from the bulk plasma to the Bohm velocity. *Bottom*: Variation in charged species density near the wall. Inside the sheath, electron density is reduced due to the sheath potential [2].

within it, then the continuity of flux at the presheath-sheath boundary is defined by

$$n_i(x)u(x) = n_{is}u_s \tag{1.10}$$

where $n_i(x)$ is the ion density at some position x, and n_{is} is the ion density at the sheath edge. Now assuming that the electron density is described by the Boltzmann relation, then

$$n_e(x) = n_{es}\exp(\Phi(x)/T_e) \tag{1.11}$$

where $n_e(x)$ and n_{es} are the electron density at x and at the sheath edge respectively, and T_e is the electron temperature. The electric field is the gradient of the potential, $\mathbf{E} = -\nabla\Phi$, coupling this with Poisson's equation yields

$$\nabla^2\Phi = -\frac{\rho}{\epsilon_0} = -\frac{e}{\epsilon_0}(n_i - n_e) \tag{1.12}$$

This can be expanded by replacing the ion and electron densities with their explicit values to read

$$\frac{d^2\Phi}{dx^2} = \frac{en_s}{\epsilon_0}\left[\exp\left(\frac{\Phi(x)}{T_e}\right) - \left(1 - \frac{\Phi}{\mathcal{E}_s}\right)^{-1/2}\right] \tag{1.13}$$

where $\mathcal{E}_s$ is the initial ion energy $\mathcal{E}_s = \frac{1}{2e}M_i u_s$. Equation 1.13 is the general form that governs the potential profile and charged particle densities in a collisionless sheath. Integrating equation 1.13 with respect to position, x, gives

$$\frac{1}{2}\left(\frac{d\Phi}{dx}\right)^2 = \frac{en_s}{\epsilon_0}\left[T_e \exp\left(\frac{\Phi}{T_e}\right) - T_e + 2\mathcal{E}_s\left(1 - \frac{\Phi}{\mathcal{E}_s}\right) - 2\mathcal{E}_s\right] \tag{1.14}$$

Due to the fact the the LHS of equation 1.14 is a square, for there to be a solution the RHS is necessarily positive. Interpreting this result physically means that the ion density in the sheath must always be greater than electron density, which is seen in figure 1.1. Physically this can be interpreted by as the electrons in the discharge moving much faster than ions, and the flux to the wall of both species must be equal. To ensure that the RHS is positive, a Taylor expansion can be performed with respect to Φ. Satisfying the resulting inequality for the RHS to be positive yields the following relation

$$u_s \geq u_B = \sqrt{\frac{eT_e}{M_i}} \tag{1.15}$$

This relation is known as the Bohm criterion and defines a minimum speed at which ions must enter the sheath to ensure an equal flux of ions and electrons to the walls of the chamber. The Bohm velocity, u_B, is also equivalent to the sound speed, c_s, of the incident ions [9]. Since the ions in the plasma will be only slightly above room temperature, an electric field between the bulk plasma and the edge of the sheath is required to accelerate the ions to the Bohm velocity. This region is called the presheath and is depicted in figure 1.1. The potential drop across the presheath region is defined by

$$\frac{1}{2}M_i u_B^2 = eV_p \tag{1.16}$$

Where V_p is the plasma potential defined relative to the $\Phi = 0$ at the presheath-sheath boundary. Substituting the expression for the Bohm velocity and using

the Boltzmann relation from equation 1.11, the relative densities between the bulk plasma density and the density at the sheath is found to be

$$n_s = n \exp\left(\frac{-V_p}{T_e}\right) \approx 0.61n \tag{1.17}$$

Now that the density and speed of the ions are defined, the flux of both electrons and ions to the wall can be calculated, and are respectively found to be

$$n_s u_B = \frac{1}{4} n_s \bar{v}_e \exp\left(\frac{V_w}{T_e}\right) \tag{1.18}$$

where V_w is the wall potential and $\bar{v}_e$ is the electron thermal velocity, since the electron flux is isotropic. The ion flux is directed due to the accelerating fields. Solving for the wall potential gives

$$V_w = -\frac{T_e}{2} \ln\left(\frac{M_i}{2\pi m_e}\right) \tag{1.19}$$

The width of the sheath can be calculated by integrating equation 1.14 again and yields what is known as the Child-Langmuir law.

$$s = \frac{\sqrt{2}}{3} \lambda_{Ds} \left(\frac{2e\Phi_s}{kT_e}\right)^{3/4} \tag{1.20}$$

where s is the sheath width, λ_{Ds} is the Debye length at the sheath edge, and Φ_s is the potential at the sheath edge relative to the wall.

1.1.2 Electron Energy Distributions and Temperature

Once a plasma has reached a steady state after breakdown, the electrons' energies will have a certain distribution that depends on the pressure, geometry, and power coupling mechanism of the discharge [10–13]. Typical laboratory plasmas are sometimes called non-equilibrium plasmas due to the fact that the ion and electron populations are not in thermal equilibrium [1].

For a population of particles in thermal equilibrium, the velocity distribution is a

Maxwellian. A one dimensional Maxwellian velocity distribution is given by

$$f(u) = n\left(\frac{m}{2\pi kT}\right)^{1/2} \exp\left(\frac{mu^2}{2kT}\right) \tag{1.21}$$

where u is velocity, n is the density of the particles, m is their mass, k is Boltzmann's constant, and T is a quantity defined as the temperature. It can be seen from equation 1.21 that the temperature of the particles controls the width of their distribution. In other words, for a higher temperature, a greater proportion of the particles have higher velocity. By summing over three dimensions and converting to energy, the following equation describing the distribution of energy of the particles can be derived

$$F(\epsilon) = n \times 2\sqrt{\frac{\epsilon}{\pi}}\left(\frac{1}{kT}\right)^{3/2} \exp\left(-\frac{\epsilon}{kT}\right) \tag{1.22}$$

where ϵ is energy. In equation 1.22 the temperature, T, is measured in Kelvin. However when discussing parameters such as electron temperature, it is often more convenient to use units of electron volts (eV). To convert from Kelvin to eV, equation 1.23 is used

$$k_B T = 1 \text{ eV} = 1.6 \times 10^{-19} \text{ J} \rightarrow 1 \text{ eV} = \frac{1.6 \times 10^{-19}}{1.38 \times 10^{-23}} = 11600 \text{ K} \tag{1.23}$$

where k_B is Boltzmann's constant.

Therefore, when discussing the temperature of a Maxwellian electron distribution 1 eV = 11600 K. Figure 1.2 shows how the distribution of electrons varies for four different temperatures ranging from 1 to 10 eV. As mentioned previously, the processes in a plasma are controlled by collisions, and the cross sections for these collisions have an energy dependence. Therefore the electron temperature of the plasma is important in determining plasma chemistry, as it will directly affect the likelihood of each type of collision occurring.

It is worth noting that it is rare for an electron distribution to be exactly Maxwellian in a laboratory plasma, especially at low pressure. In a capacitive discharge for example, the electron energy distribution is often found to have a hot tail [14]. Such a distribution is said to be bi-Maxwellian, as it can have two different temperatures ascribed to different energy ranges. There are many other

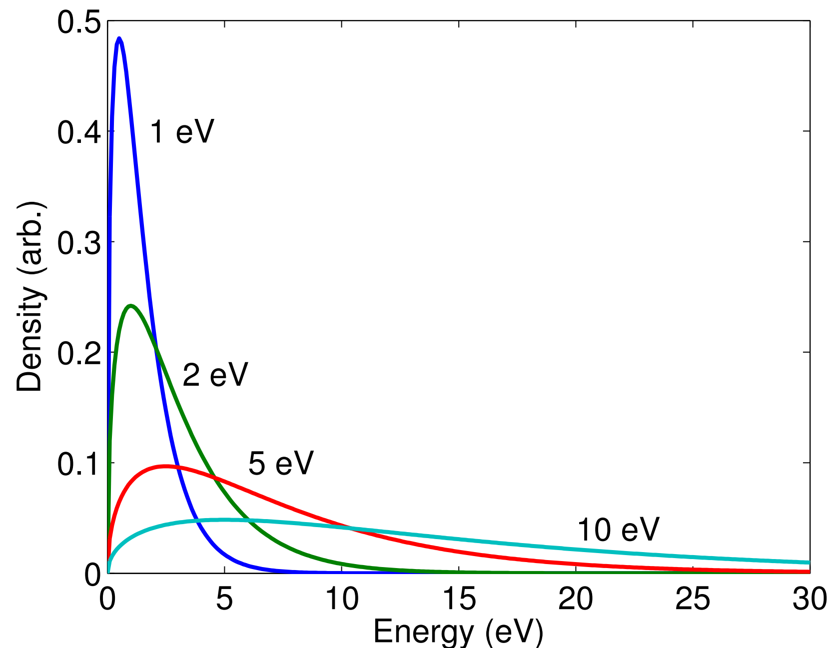

Figure 1.2: Maxwellian energy distributions for a population of particles with temperatures ranging from 1 to 10 eV.

distributions that can be measured in physical plasmas [15].

Electron energy distributions can be measured in a number of ways, but broadly these diagnostics fall into two categories: invasive and non-invasive. Invasive diagnostics rely on probes inserted into the plasma to make measurements [16]. Invasive techniques have the advantage of being able to easily make spatially resolved measurements. However, they introduce a perturbing surface into the plasma, and can sometimes significantly distort the parameters they are being used to measure [17]. Non-invasive diagnostics instead typically rely on optical techniques to make measurements. Measurements of the electron energy distribution are possible using spectroscopic techniques [18, 19]. Such techniques do not generate the same effect as an invasive probe, but they often lose spatial resolution. Both techniques have limitations based on the operating parameters of the plasma. Ultimately the nature of a particular experiment is critical to deciding which technique is best.

1.2 Capacitively Coupled Plasmas

There are three main coupling mechanisms for power deposition in a plasma. They are: capacitive coupling, inductive coupling, and wave driven coupling. Each of these three mechanisms respectively produce higher plasma densities. A capacitive plasma uses the high voltage that forms on the sheath of the driven electrode to deposit power to the bulk plasma [2]. An inductive plasma couples the evanescent fields that surround an electrode carrying an alternating current to the mobile electrons in a plasma to heat them [20]. Finally a wave coupled plasma launches electromagnetic waves through the plasma itself. Under some conditions, the electrons and waves can exchange energy, providing an additional source of heating [21, 22].

Capacitive coupling is unique amongst the three of these broad coupling mechanisms in that it is present to some extent in nearly any rf plasma. For example, an inductive discharge driven by a single loop antenna will have an element of capacitive coupling between the two ends of the antenna due to the voltage drop across the loop [23]. Furthermore, if a plasma discharge is ignited by a applying a voltage to an electrode or antenna, it forms in a capacitive mode, even if only briefly as they pass to more efficient modes of coupling.

In a typical capacitive plasma there are two modes by which power is transferred to the electrons. They are: ohmic (collisional) heating, and stochastic (collisionless) heating. Ohmic heating is the result of momentum transfer between electrons oscillating in the rf fields present in the plasma and the background neutral gas. Stochastic heating is the result of reflection of electrons from the large electric fields present in a moving high voltage sheath [24]. An analogy frequently used to describe the mechanism is the collision of a ball and a moving wall. The velocity of the reflected electron is described by

$$u_r = -u + 2u_s \tag{1.24}$$

where u_r is the reflected velocity of the electron parallel to the direction of motion of the sheath, u is the electron's initial velocity, and u_s is the velocity of the moving sheath. However detailed modelling of this interaction suggests other mechanisms

might be responsible for this effect [25].

A plasma operating in a capacitive mode can fall into one of two categories: α mode or γ mode. The α mode relies on the heating mechanisms described above and has a lower density than the γ mode. By contrast the γ mode relies on secondary electron emission from the walls of the discharge vessel to be sustained [26].

1.3 Hollow Cathode Plasmas

In a DC system the cathode is the negatively charged electrode. A hollow cathode is one whose geometry has been altered to have a hollow structure, thereby increasing its surface area. Hollow cathodes were first produced in 1916 where they were used as thermionic electron sources due to their long lifetimes [27]. A general diagram of a DC hollow cathode can be seen in figure 1.3.

In 1954, Little and Engel published evidence of the hollow cathode effect in a DC plasma [28]. They found that by reducing the spacing between two separate cathodes, they were eventually able to combine the negative glows present in front of both, and greatly increased the current density in the discharge. This effect was the result of a second scaling law, similar to the Paschen curve described in section 1.1.

Initially, plasma breakdown occurs between the cathode and anode according to

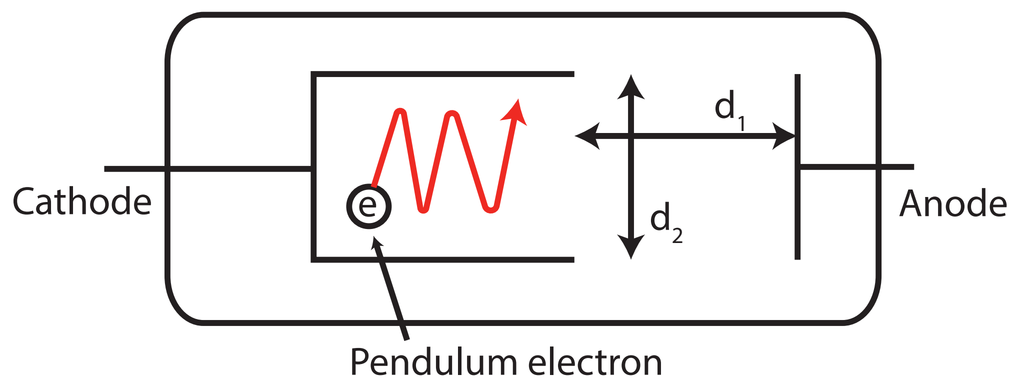

Figure 1.3: Schematic diagram of a simple hollow cathode discharge. The geometry of the cathode allows promotes the production of pendulum electrons, for which a typical path is shown. The length d_1 is used in the calculation of the pressure power product for Paschen breakdown, d_2 is used for activation of the hollow cathode effect.

the Paschen relation, with d_1 as shown in figure 1.3 providing the relevant length scale. When the pressure distance product of the interior of the hollow cathode lies between 0.1 and 10 Torr.cm using d_2 as a guide, and a precursor discharge is present, the hollow cathode effect can be activated [29]. If the current density in the DC discharge is high enough, the positive space charge that forms in front of the cathode moves into the hollow cavity. This in turn produces an electric field within the hollow cathode with a strong radial component. When secondary electrons are emitted from the cathode surface they are trapped in a potential well inside the hollow cathode [30]. These electrons, sometimes referred to as pendulum electrons, pass across the space between cathodes many times, participating in multiple ionisation events [31]. This trapping of electrons and the subsequent increase in ionisation frequency within the hollow cathode is what causes the discharge density to increase once the hollow cathode effect is activated.

Once the hollow cathode effect is active, the voltage drop between cathode and anode decreases, while the current continues to increase [32]. This is called negative differential resistance and is characteristic of the hollow cathode effect. Due to the nature of operation of a hollow cathode discharge, the electron energy distribution is strongly non-Maxwellian [33]. The pendulum electrons that sustain the hollow cathode mode form a hot tail and can have energies as high as the plasma operating voltage.

The first rf hollow cathode plasma device was developed by Horwitz in 1983 [34]. It was designed as a plasma processing tool for increasing the etch rate of SiO_2. At the time of publication, Horwitz achieved etch rates between 10 and 100 times greater than the current benchmark from dielectric etch processes.

The process by which a hollow cathode operates in an rf system differ in two significant ways from its DC analogue. Firstly the hollow cathode effect is initiated by a second avalanching breakdown within the hollow cathode. Recalling that in the DC case, the plasma moves into the hollow cathode as current increases. The second difference concerns the formation of a self bias on the hollow cathode [35].

In a typical rf system, the grounded area is much larger than the powered electrode, and in the presence of a blocking capacitor this leads to the formation of a self bias

on the powered electrode [36]. In some cases this self bias can be as large as V_{rf}, the amplitude of the rf signal, and can result in very large sheath voltages on the hollow cathode. Secondary electrons emitted from the surface of the hollow cathode can have energies of hundreds of eV. This results from the large sheath voltages present when the applied voltage is at its full negative excursion. Rather than the earthed surfaces, the plasma itself forms a virtual anode for the hollow cathode. Therefore the DC self bias on the hollow cathode performs the same role as the applied voltage in a DC hollow cathode discharge. The self bias rather than the applied voltage is what sustains the hollow cathode mode in an rf environment.

Since Horwitz's work, rf hollow cathode discharges have found applications in etching [37, 38], sputtering [39–41], and deposition [42–46] systems. In more recent years, atmospheric pressure hollow cathode plasmas have become a source of interest for possible uses in surface processing. To activate the hollow cathode effect at such high pressures, the diameter of the hollow cathode must be reduced. Often systems such as these have diameters of less than a millimetre, and have thus gained the name microplasmas [47]. Due to their small size, microplasmas are often operated in an array [48, 49]. They have found use in gas phase chemical modification [50], ultraviolet (UV) light sources [51], and maskless etching [52], as well as in other areas.

A hollow cathode discharge provides two potential benefits to the design of the DASH source. The first is that the plasma density increase drives up the density of chemically active species. The second is that by flowing gas through the hollow cathode, plasma generation can be done remotely, reducing ion damage to the surface.

1.4 Plasmas for Etching

Modification of surfaces via plasma techniques was adopted as the industry standard for transistor production in the 1970s, as the undercut left by wet chemical etching became intolerable. Creating a plasma from a molecular gas allows access to complex chemistry in the gas phase at a surface, such as a wafer. This can be used

either for removal of material from a surface (etching) or for addition of material to a surface (deposition) [53, 54]. As discussed earlier, the DASH source was primarily designed for use as an etching machine, although later chapters of the thesis investigate the production of hydrogen plasmas, which are typically used in deposition processes. Due to their widespread use, these techniques and their optimisation form the backbone of a large industry that recorded $78.47 billion in global sales for the first quarter of 2014 [55].

1.4.1 History of Plasma Etching

Plasma etching is an extension of the physical sputtering process first recorded by Grove in 1852 [56]. Yet it wasn't until the 1960s that sputtering with a plasma was used in a laboratory environment by Lepselter *et al.*, in the production of beam-lead switching transistors [57]. In 1969, Davidse used an argon plasma to develop an rf sputtering technique [58]. Almost simultaneously plasmas were beginning to be used for chemical etching, specifically using an oxygen plasma for photoresist stripping [59]. Meanwhile, the use of atomic fluorine for chemical etching was being investigated [60]. At the time, fluorine was desirable due to the fact it could etch silicon nitride, where previously no wet chemical etchant had been available. Furthermore, fluorine displayed good selectivity between Si and SiO_2, which could be enhanced through increasing the complexity of the plasma chemistry [61, 62]. By 1979 it had become possible to produce an integrated circuit using no wet chemical processes, reducing undercut in the process as well as eliminating the need for costly oil based solvents and their associated disposal problems [63].

The first generation of plasma etch devices were developed to use reactive ion etching [64, 65]. These devices were rf capacitively coupled, and exploited the physical assistance sputtering brought to the etching process, especially through the formation of a self bias on the smaller electrode brought on by asymmetry between the powered and grounded electrodes [66].

As dry processes were taken up by industry, efficiency of production and throughput became key concerns. At first this was dealt with by increasing the size of the reaction chamber, but this led to problems with uniformity in each batch. The so-

lution was to increase etch rates, which was achieved through several means. These included: magnetic enhancement [67], decoupling the plasma density and ion energy in the discharge [68], and plasma density enhancement through alternative coupling mechanisms such as inductively coupled [69], helicon [70], and electron cyclotron resonance plasmas [71].

Modern commercial etching reactors tend to use a mixture of these technologies to achieve optimal properties of the processing plasma [72]. Alongside improvements in the technologies generating the plasma, the size of the wafer being etched has steadily increased over time. The first etch machines mainly used wafers of 100 mm diameter. In the early 1990s wafer size increased to 200 mm [73], then again around 1999 to 300 mm [74]. Currently apparatus is in development for the use of 450 mm wafers [75]. The benefit of increasing the size of the wafer is that it increases throughput, however the challenge is to maintain an acceptable etch rate and uniformity while combating problems such as wafer loading [76].

The DASH source falls into a particular subcategory of etching devices that are designed to only flow active species and few charged particles onto a wafer surface [77–79]. These devices differ from ion enhanced etching tools by producing the plasma away from the wafer, rather than in the same chamber as the wafer as is conventionally the case. Because of the geometry of the source and non-local plasma production, many of the charged species do not reach the wafer surface, whereas radical neutrals can. As such, these reactors produce an isotropic etch, and are often used in photoresist stripping [80–82]. However it is also possible to use such a device for chemical etching of silicon with atomic fluorine [83]. By reducing the interaction between charged particles and the wafer, selectivity of the process between a film and substrate can be enhanced.

1.4.2 Etching Mechanisms

Broadly there are four distinct modes of etching that can exist within a plasma environment. The first of these is sputtering, where material is removed from the target by the energetic impact of charged particles. The second is pure chemical etching, where material is removed via energetically favourable chemical reactions

at the surface of the wafer. Third is reactive ion enhanced etching, where the plasma supplies both gas phase chemical etchants as well as energetic ions. The fourth is inhibitor etching, where a passivating component is introduced to the plasma to protect the wafer from chemical etching [84].

Sputtering is an anisotropic process, and as such can be used to assist in pattern transfer processes [85]. Pattern transfer is the name given to the transferring of an 'image' from a mask, usually made with photoresist, to a wafer. The anisotropy of the process is crucial to reducing the size of features (transistor gate length), and their spacing (called the half-pitch). The process works like a stencil, exposing parts of the wafer to the incident plasma/neutrals and allowing it to be etched. The sputtering yield is also sensitive to the angle of incidence of the bombarding ions [86]. Perpendicular ions (angle of incidence is 0°) will sputter the target, while grazing ions (angle of incidence is 90°) will not sputter at all. The angle of greatest sputter yield lies between 0 and 90°. Since sputtering is a physical process, it is largely material independent and only weakly depends on the surface binding energy of the target and the masses of the incident and target particles [2]. Due to its angular dependence and material independence, sputtering can lead to faceting of the photoresist, which can be a problem in etch processes.

Chemical etching occurs when the plasma supplies chemically active species that react with the wafer material to form volatile molecules that can be pumped out of the system. The chemical etching process is capable of very high selectivity, such as atomic fluorine discriminating between Si and SiO_2. The most basic example of chemical etching of silicon by fluorine is

$$\mathrm{Si(s)} + 4\,\mathrm{F} \longrightarrow \mathrm{SiF_4(g)} \tag{1.25}$$

However in reality the chemical process that leads to the silicon atom being removed is potentially more complicated [87]. A simplified schematic diagram of the chemical etching process of silicon by atomic fluorine can be seen in figure 1.4. Since the chemical etching process does not usually have a directional dependence, the process is isotropic, although it produces far less undercut than the wet chemical etch it replaced some 40 years ago [88].

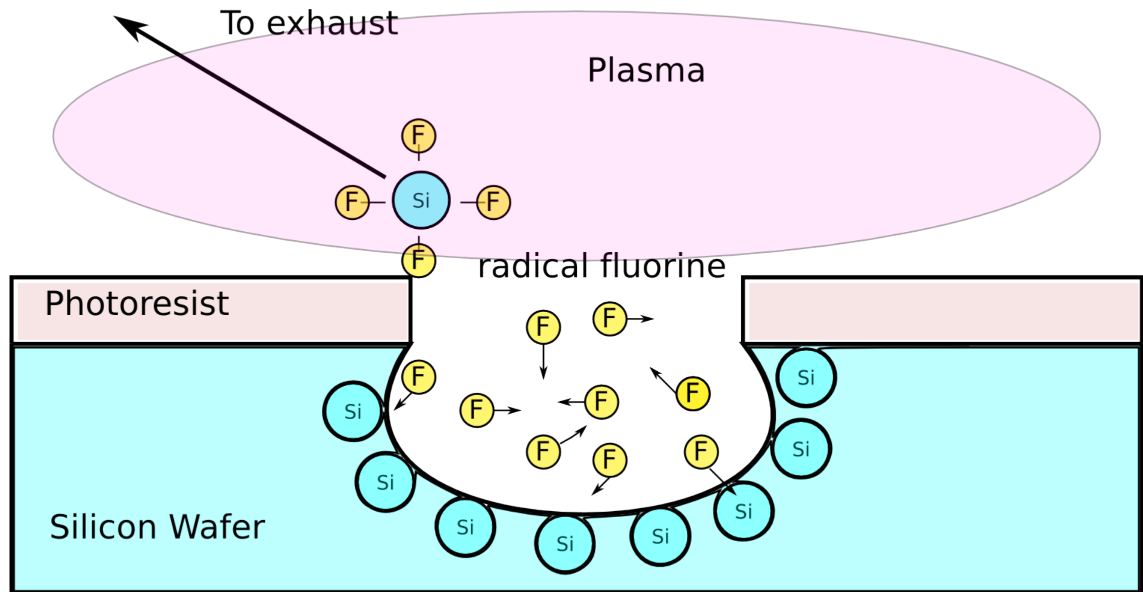

Figure 1.4: Schematic diagram outlining the chemical etching process. Due to its isotropy, there is some undercut beneath the photoresist.

When both physical and chemical processes occur in tandem in ion enhanced processes such as reactive ion etching (RIE), the resulting etch rate is higher than the sum of the two contributing processes [88]. To achieve this the discharge must supply both the chemically active etching agents (such as atomic fluorine), and energetic ions to bombard the surface. It has been suggested that the etching mechanism in this regime is chemical, but the reaction rate is determined by the energy of the bombarding ions [89]. Because of the presence of energetic ions this process can be anisotropic, but at the expense of selectivity. In modern etching devices, multiple frequency coupling is used to achieve independent control of the ion energy (through bias on the substrate) and the anisotropy at low frequencies, and plasma density and selectivity at high frequencies.

Inhibitor etching exploits both a more complex plasma chemistry and the lack of selectivity of bombarding ions to produce very high anisotropy etching. A good example of inhibitor etching is the Bosch process, developed in the 1990s at Robert Bosch GmbH [90]. The Bosch process comprises two phases: a standard etch phase with both chemical etching and ion bombardment, and a passivation phase. During the passivation phase, the wafer is coated as a chemically inert polymer is deposited. Then during the etch phase, the bombarding ions remove the polymer from a vertical

direction while simultaneously the exposed wafer is isotropically etched [91]. As the wafer is processed, the sidewalls become passivated during deposition, and the bombarding ions do not remove polymer from the sidewall as effectively as from the bottom of the trench. During the etching phase, only the bottom of the trench is exposed to the chemical etchants in the plasma. Over multiple cycles this process causes a 'scalloping' effect due to consecutive isotropic chemical etchings occurring at the bottom of the trench. The Bosch process can yield highly anisotropic etches, and is one method used for Deep Reactive Ion Etching (DRIE).

1.5 Scope of the Thesis

Before considering the results of the experiments, chapter 2 describes the DASH source and its auxiliary components, as well as the electrostatic probes used to diagnose the plasma. The structure of the results chapters is broken into three distinct stages. The first is a fundamental study of the basic operation of the DASH source, presented in chapters 3 and 4. To simplify the discharge, this is performed in argon rather than a chemically reactive gas to make analysis more straightforward. Invasive probe diagnostics are used to understand the plasma density, electron temperature, plasma potential and how these parameters vary spatially.

The second stage is a study of the discharge using SF_6 to dissociate atomic fluorine and delivering it to the surface of silicon wafers, and is presented in chapter 5. These experiments give an indication of achievable etch rates and uniformity. They also explore some challenges associated with chemistry within the source, attributed to the production and deposition of aluminium fluoride on the wafer surface.

In the third stage, the DASH source and its analogue, Pocket Rocket, are used to conduct optical studies of a hydrogen discharge such as would be used in a deposition process. These results are described in chapters 6 and 7. Finally, chapter 8 summarises the interpretation of the experiments, and briefly comments on the future directions that work on the DASH source might take. It is envisaged that the results presented in this thesis will enhance understanding of the physics of the operation of arrayed shower head sources, particularly for use in surface processing.

2

Apparatus

This chapter describes in detail the physical apparatus used in the experiments presented in this thesis. The majority of the work is done with one of two incarnations of the Distributed Array Shower Head (DASH) source. The DASH source excites capacitively coupled plasmas in an array and enhances ion density through the activation of the hollow cathode effect [29]. The source attaches to one arm of a six way cross expansion chamber with access for the pumping system, pressure gauges, and diagnostic probes. Some of the later experiments detailed in chapters 6 and 7 are performed in the similar Pocket Rocket source [92] owing to its superior optical access.

2.1 The DASH Source

The DASH source is designed to simultaneously produce multiple plasmas in an array, with the number of active plasmas varied as required. The source comprises five adjacent plates alternating between aluminium and alumina depending on the plate's position within the stack and desired function. Figure 2.1 shows an exploded view of the source with all five plates present. Each plate is 6 mm thick, with a diameter of 89 mm, except the powered electrode that has a diameter of 80 mm. The reduced size of the powered electrode allows it to sit within an alumina guard ring that also has an outer diameter of 89 mm, preventing contact between it and nearby earthed surfaces. The left and rightmost plates are earthed and have a mechanical connection to the expansion chamber to keep them in electrical contact with the common ground. The long rod is the radio frequency (rf) feed that passes through an o-ring to atmosphere outside the vacuum chamber. It is surrounded with a Macor

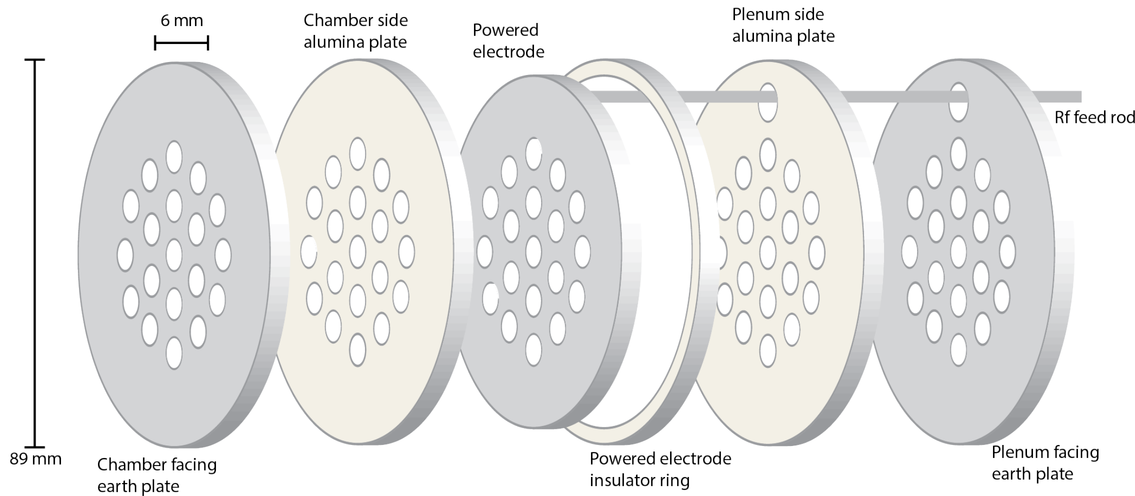

Figure 2.1: Exploded view of the Distributed Array Shower Head (DASH) source. From left to right the plates are: aluminium ground, alumina insulator, aluminium powered electrode, alumina insulator, aluminium ground. Each plate is 6 mm thick and has a diameter of 89 mm, excepting the powered electrode. The powered electrode has a diameter of 80 mm and is surrounded by an alumina guard ring.

housing to prevent it contacting with earthed surfaces.

The conductance between the plenum and the expansion chamber is limited by the number of active hollow cathodes and this causes a strong pressure gradient through the DASH source, described in more detail in section 2.2. As the gas flows from plenum to chamber, it passes through each active hollow cathode and an individual plasma is ignited in each one. The number of holes in operation at any given time is controlled via the use of alumina plugs inserted into the source. The plugs have a tab on one end to hold them in place against the gas flow. The use of these plugs can increase the power density of each plasma for a given total power by reducing the number of active hollow cathodes. It is found that optimal operation of each hollow cathode requires a minimum power density and flow. Due to the inherent limitations of the system such as: pumping capacity, output power of the rf generator, and heat strain, it is impossible to operate all the hollow cathodes simultaneously, making the plugs a necessary addition to the system.

The total configuration of the system can be seen in figure 2.2 (a). The DASH source attaches to the rightmost arm of the six way cross chamber as shown in the schematic. The zoom of the source shows the electrode stack within its housing as well as the rf feed rod passing through the plenum to atmosphere. The turbo

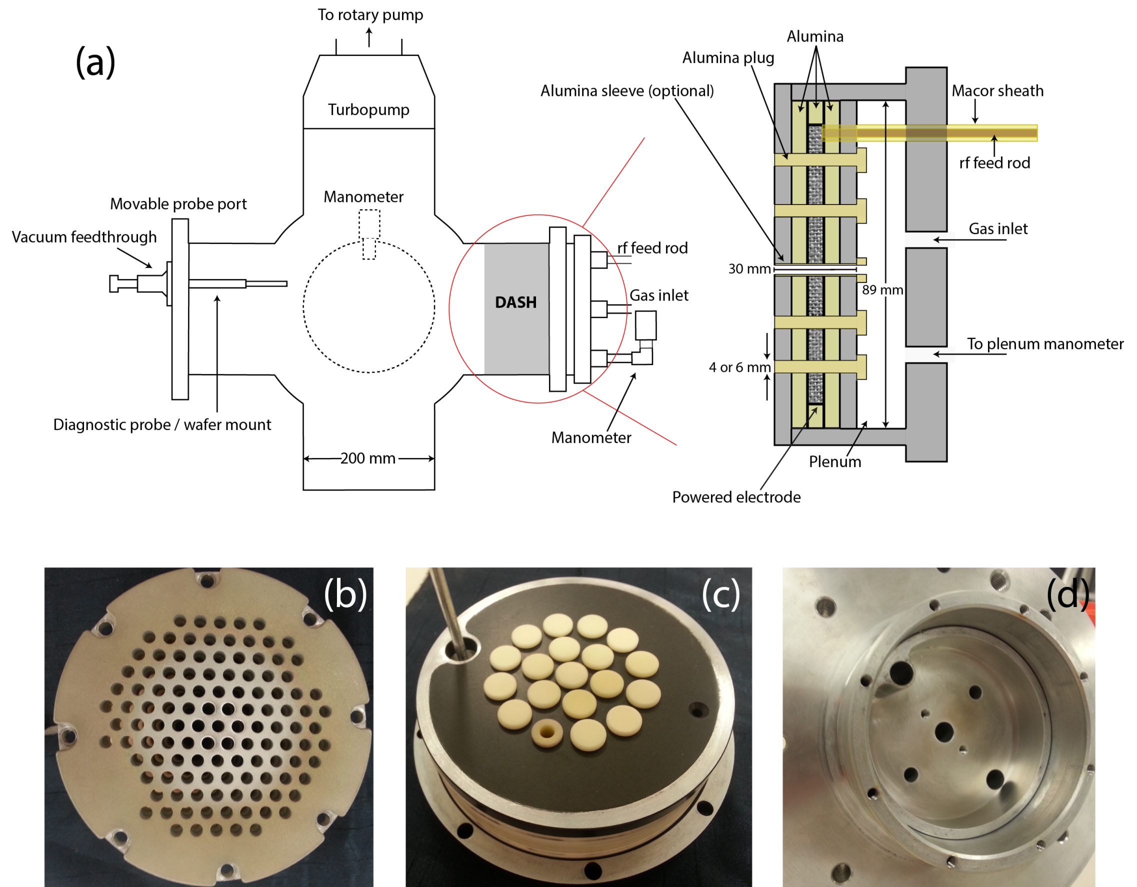

Figure 2.2: (a) A schematic diagram showing the assembled DASH source and its position within the six was cross chamber. Opposite the source is the movable probe port. Manometers are mounted on one arm of the chamber and to the plenum of the DASH source. Panel (b) shows a photograph of the front earth plate in the 4 mm source, and also shows the hole configuration. Panel (c) shows the 6 mm source rear earth plate on top of the full electrode stack. It also shows the alumina blocking plugs, an alumina sleeve, and the rf feed rod. Panel (d) shows the inside of the DASH housing and plenum. The three holes in the back of housing allow connection to the plenum for gas flow, rf power, and manometer.

molecular pump is attached to the topmost arm of the cross, and its exhaust is connected to the input of the primary pump. The arm opposite the DASH source is fitted with a movable probe port used with the various invasive diagnostic probes and wafer mounting system.

Two versions of the source were used during experiments, one with 117 hollow cathodes with an inner diameter of 4 mm and one with 19 hollow cathodes with an inner diameter of 6 mm. The two configurations can be seen in figure 2.2 (b) and (c) respectively. With the implementation of guarding sleeves into the system the

transition was made to the 6 mm source such that once the sleeves were inserted the inner diameter of the active holes remained at 4 mm. Panel (c) also shows a top down view of the alumina blocking plugs and one of the foremost holes has a guard sleeve inserted. The sleeves and plugs are represented diagrammatically in the zoom of the DASH source in figure 2.2 (a). The panel also shows the rf feed rod extruding from the electrode stack, although in this photograph the Macor shield is removed.

The electrode stack is housed within an aluminium body that mechanically attaches to the six way cross expansion chamber. Figure 2.2 (d) shows the cavity in the DASH housing that holds the electrode stack. The ridge in the cavity has a press fit with the plenum-facing earth plate, and the space below the ridge forms the plenum of the system when the DASH electrode stack is in place. Panel (d) also shows the access points for the rf rod, the gas flow and the plenum pressure gauge.

2.1.1 The Pocket Rocket Source

Chapters 6 and 7 require optical diagnostic techniques. The DASH source has poor optical access and as such the Pocket Rocket system is used as an analogue of single hollow cathode from the DASH. The Pocket Rocket hollow cathode design is very similar to that used in the DASH. It has superior optical access with a window looking through the plenum and into the hollow cathode. Plasma expands into a glass tube giving optical access to the plume as well. Baratron manometers are fitted to both the plenum and expansion chamber to monitor pressure on either side of the plasma creation region. A schematic of the source is shown in figure 2.3 and a detailed description of the Pocket Rocket source can also be found in [92]. The discharge is ignited in an alumina sleeve, similar those used in the DASH. The pipe has an inner diameter of 4.2 mm, and length of 20 mm. Surrounding the centre of the alumina is the powered electrode, which is a copper band 5 mm in width. At either end of the alumina pipe are the two earthed electrodes, which are 3 mm wide and made of aluminium. The configuration of the electrodes around the alumina are seen to closely mirror the configuration of a hollow cathode from the DASH source, although the dimensions of the components are slightly different.

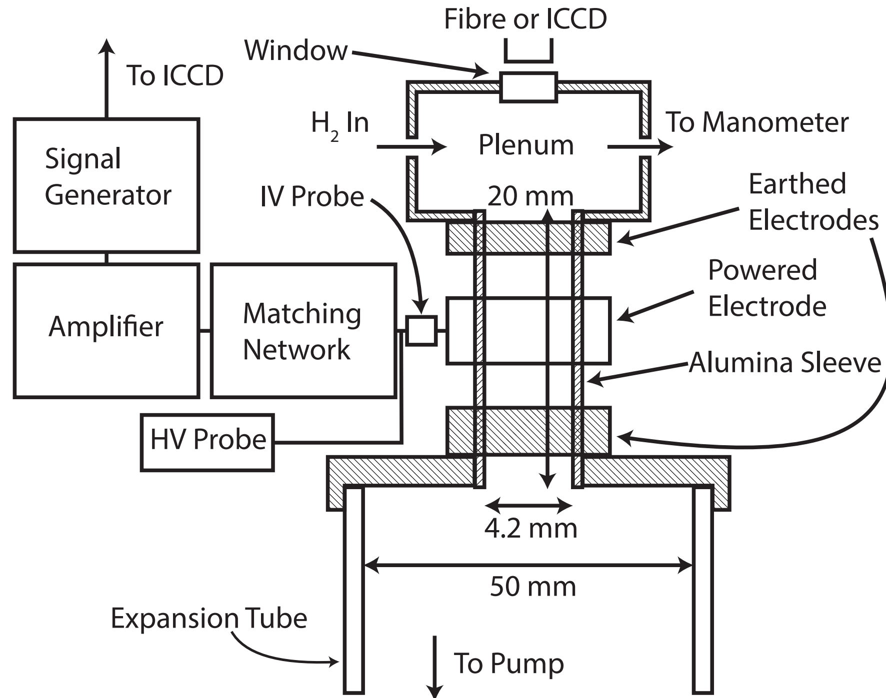

Figure 2.3: Sketch of the Pocket Rocket apparatus showing the configuration of the electrodes, power system, and the plume expanding into the attached glass tube [92].

It is worth noting for both sources that once ignited, plasma will diffuse from the active hollow cathode(s) into the plenum as well as into the expansion chamber. However due to the design of the DASH and Pocket Rocket systems, meaningful measurements of the plenum plasma are not possible with either invasive or optical techniques. Some confirmation of the presence of plasma in the plenum is provided through fluid modelling of the Pocket Rocket system performed by Greig *et al.*, which clearly shows the presence of plasma diffusing against the flow of gas [106].

2.2 Vacuum System and Pressure Variation

The system is pumped by a rotary pump and turbo molecular pump in series. The rotary pump is a Leybold Trivac and is capable of pumping the system down to a base pressure of approximately 1 mTorr with a pumping speed of 40 m^3/h. The turbo molecular pump is an Alcatel pump and cannot be activated until the rotary pump has reduced the pressure in the chamber below 75 mTorr. It has a pumping

speed of 400 L/s and reduces the base pressure in the system to 5×10^{-7} Torr.

As has already been mentioned, due to the poor conductance between the plenum and chamber, there is a strong pressure gradient present in the system while gas is flowing. This effect is modified by the number of operating holes, the more holes that are open to gas flow, the better the conductance and the less severe the pressure differential. To gain greater understanding of the operation of the system, it is necessary to measure the pressure profile present during operation. Measurements of the full axial pressure profile from plenum to chamber are made in three stages.

To measure the pressure in the plenum a Baratron manometer is used. It is assumed that pressure throughout the plenum is uniform. To measure the pressure inside an active hollow cathode a replica of one is used with three holes drilled and tapped in the side to allow for axial pressure measurements. A schematic diagram of the pressure test rig can be seen in figure 2.4 (a) and a photo can be seen in 2.4 (b).

The pressure test rig has a single hole of 4 mm inner diameter and 30 mm length drilled through to simulate a hollow cathode in the DASH source. The plenum has the same dimensions as the DASH plenum and the gas feed is in the same location. The pressure test rig is attached to a blank plate covering one arm of the six way cross such that the pumping is the same also. The three holes drilled into the side of the replica hollow cathode allow the Baratron manometer to be affixed to measure the pressure 10 mm from each end and in the middle, 15 mm from the end.

To make measurements of the pressure in the plume, a Pitot tube system is employed. A hollow stainless steel pipe is fed through the movable probe port with one of two manometers with maximum ranges of 50 mTorr or 10 Torr attached. This allows for two dimensional spatially resolved sweeps of the pressure to be made. The combined axial profile measurements can be seen in figure 2.5 (a). Panel (b) shows the pressure in the gas plume at 33 sccm as it expands into the six way cross chamber with the pumping active. It can be seen that pressure variation between the plenum and the downstream region of the expansion chamber varies by nearly three orders of magnitude.

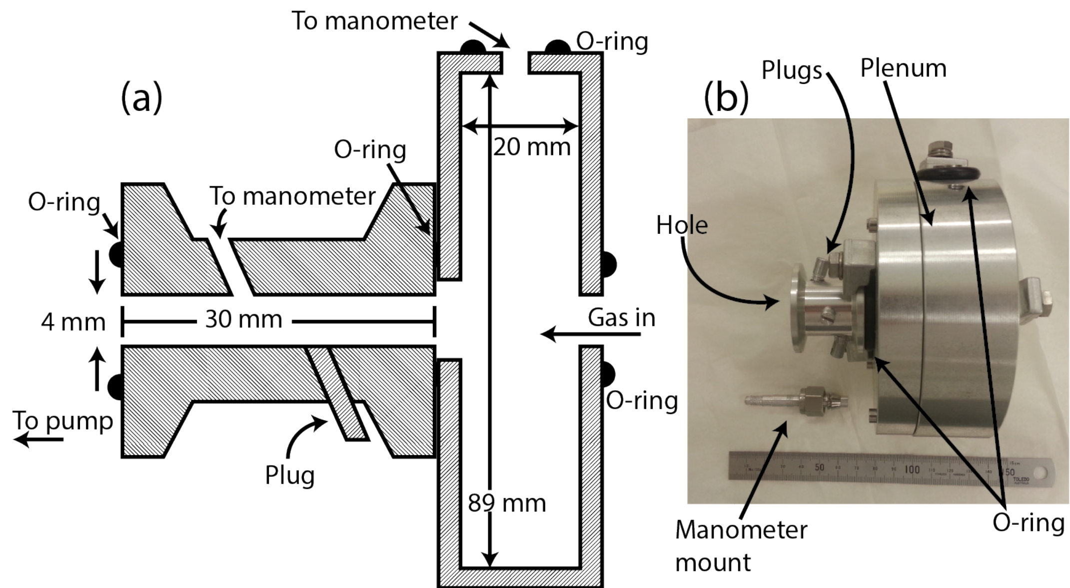

Figure 2.4: The pressure test setup used to determine gas pressure inside a single hollow cathode during operation. Panel (a) shows a schematic cross section of the system. Panel (b) shows a photo of the rig, along with the mount for a Baratron manometer attached to make the measurements.

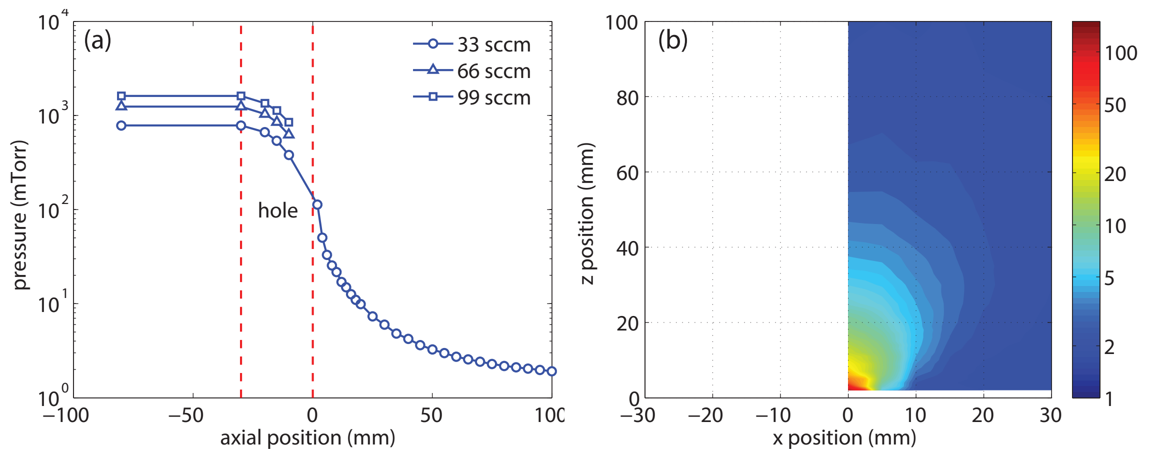

Figure 2.5: Panel (a) shows the axial variation of pressure measured on a log scale from plenum to chamber for a flow of 33 sccm using a combination of three methods. Panel (b) shows a two dimensional pressure map made using a Pitot tube mounted through the movable probe port.

2.3 Probe and Wafer Mounting

2.3.1 Movable Probe Port

Two dimensional sweeping of the diagnostic probes form a critical component of the experiments performed for this thesis. To be able to accurately and repeatably position the probe tip, defects in the probe shaft had to be accounted for. To this end

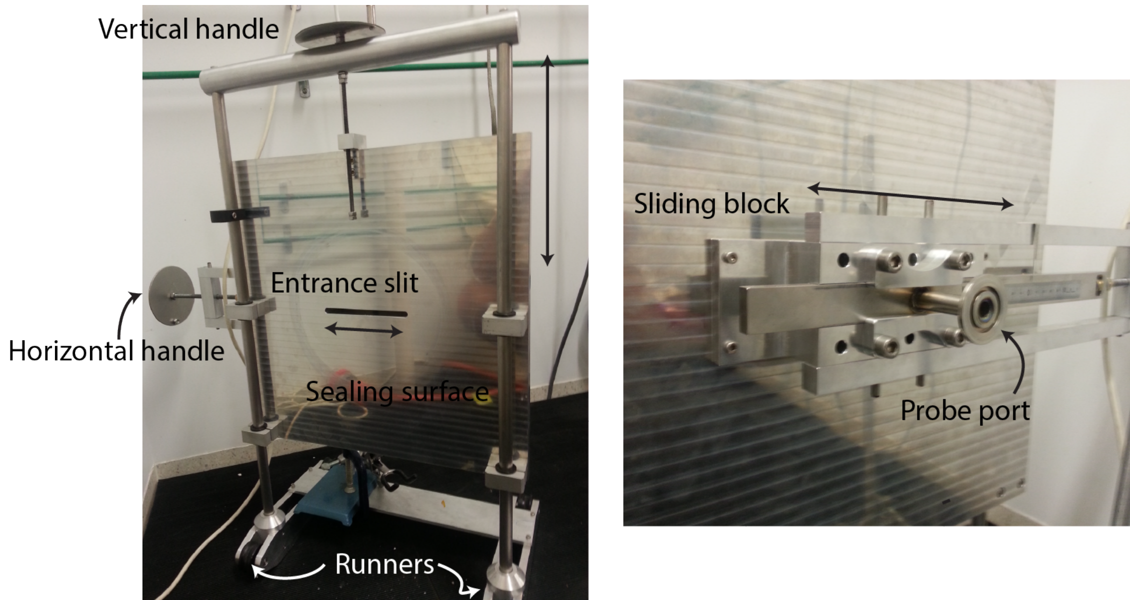

Figure 2.6: Photographs of the front (left) and rear (right) of the movable probe port. The front of the system seals to the six way cross chamber. The handle on top of the system translates the entire plate vertically while at atmosphere. The sliding block visible on the back of the system can be translated horizontally under vacuum by the handle on the side of the system. The 12 cm slit in in the middle of the plate visible from the front shows the extent to which the probe can move in the horizontal direction.

a probe port capable of three dimensional translation is designed and built in-house. Being able to move a diagnostic probe in a cartesian coordinate system eliminates the need for bent or dogleg probes [93]. The benefit of this is that bent probes reduce spatial accuracy through having more degrees of freedom. It also means that all parts of the chamber are accessible, whereas with a conventional access port this is not the case. Finally, the moving probe port allows the probe to have a straight shaft, reducing the profile and volume of the probe when approaching the source. Photographs of the movable probe port can be seen in figure 2.6.

The movable probe port seals with an o-ring mounted on the arm of the six way cross chamber facing the DASH source. The o-ring is proud, and seals against the smooth face of the movable probe port. This design allows the o-ring to seal wherever it sits on the main plate of the movable probe port. The main plate hangs between two support poles mounted to the base of the system. The plate can slide up and down these poles to change the vertical position of the probe. The height of the probe port is adjusted by means of a manually operated handle that can be

turned to push or pull a threaded piece of metal attached to the main plate up or down. Because of the nature of the seal, vertical adjustments of the movable probe port can only happen while the system is not under vacuum as the seal with the chamber moves.

Figure 2.6 also shows a slit in the centre of the main plate of the movable probe port. This slit is 12 cm long and marks the extent to which the probe port can translate in the horizontal direction while remaining under vacuum. The sliding block that contains the probe feedthrough seals against the outside face of the main plate. The slit is surrounded by a rectangular o-ring to which the flat face of the sliding block seals. By turning the horizontal translation handle the sliding block is slowly pushed along the o-ring, moving the probe horizontally without breaking vacuum.

2.3.2 Wafer Mount

The experiments presented in chapter 5 require the presence of a wafer or wafer coupon in the chamber, often facing the DASH source. Typically in an etching device, the wafer mount will be temperature controlled, and often have a bias applied or even be independently powered at a second frequency to control ion flux to the wafer [94]. However experiments in the DASH system focus on using the wafers as a metric for calculating the flux of active species to the wafer, rather than optimising a particular process. As such, the wafer mount is a simple mechanical clamp attached to a stainless steel pipe operated through the movable probe port. A photograph of the clamp can be seen in figure 2.7. There is a thread tapped into the holes in each arm, allowing wafer coupons of different sizes to be clamped easily.

By operating the wafer mount through the movable probe port, the distance between the coupon and the face of the DASH source could be varied. Additionally it also allowed for the coupon to be translated in any direction parallel to the source. This was an important feature as the number of holes operated was varied, moving the operational centre of the system.

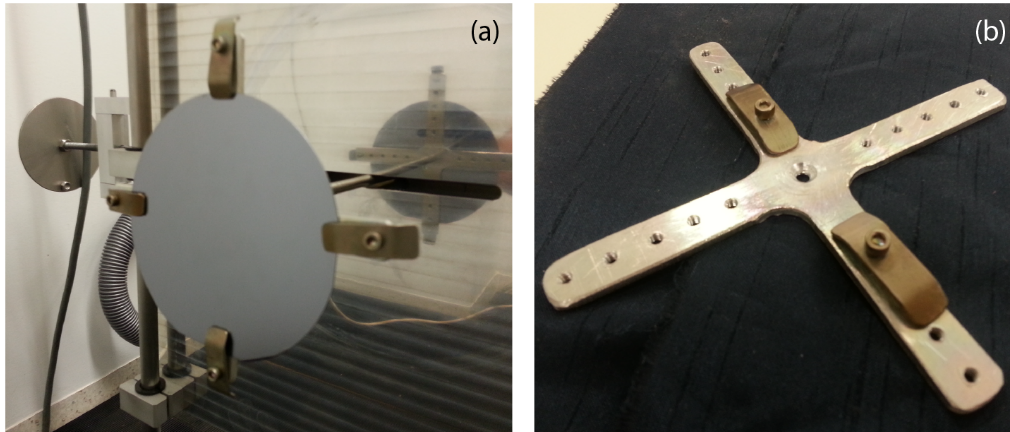

Figure 2.7: Photographs showing: (a) the wafer mounting system holding a 100 mm diameter wafer mounted through the movable probe port, and (b) the wafer mount alone.

2.4 Power Delivery and Matching Network

Power to the DASH source is delivered from an ENI ACG-5 rf generator, with a maximum output of 500 W and an impedance of 50 Ω. The generator is capable of delivering power in either continuous wave (CW) mode or in a pulsed mode. To measure the power applied to the system and determine the quality of the match between generator and load, a Daiwa CN-801 standing wave resonance (SWR) meter and a −50 dB directional coupler are placed in series between the generator and the matchbox. The SWR meter is used during CW operation and gives absolute measurements of both forward and reflected power in the system. When the system is pulsed, the directional coupler is a more appropriate tool as it provides a real time measurement of the forward and reflected power throughout the on cycle of the pulse. All the rf connections were made with RG-58 cable with industry standard 50 Ω impedance and capped with N-type connectors.

To ensure the SWR meter and directional coupler provide accurate measurements of the applied power, the system is calibrated using a 50 Ω load to ensure an ideal match with negligible reflected power. The SWR and dial readings are then compared to those of an independently calibrated Bird rf power meter. It is found that both the SWR meter and the Bird meter agree well and as such the SWR meter is used during the course of normal experimentation. The directional coupler is found to behave as expected showing no returned signal when plugged into the 50 Ω load.

A typical laboratory plasma has a complex impedance of the order of $|Z| = 1$ to 100 Ω [95]. Because the rf generator and cables are designed for operation at 50 Ω, there must be an intermediary piece of circuitry to make the plasma appear to have an impedance of 50 Ω also. If this is not the case, some portion of the power will be reflected and dissipated in the cables and generator. This means that the plasma is operating inefficiently, and large reflected powers can cause component failures due to excessive heating.

The matching network for the DASH system is an L-network consisting of two MEIVAC variable capacitors and can be seen schematically in figure 2.8. The load capacitor is a SCV-520M with a capacitance of 2000 pF and a rated voltage of 5 kV. The tune capacitor is an SCV-155M with a capacitance of 500 pF and rated to a voltage of 15 kV. A hand wound inductor connects the tune capacitor to the output of the matchbox. The precise value of each capacitor is controlled by a manually adjusted knob. Because the system is susceptible to heating, a fan is mounted in the casing to aid in cooling the current carrying components of the matching network. Stray rf fields can strongly interfere with electronic systems elsewhere in the laboratory. It is important, therefore, that the matching network be shielded. The network is housed in a solid copper box, which forms a protective Faraday cage around the components.

Figure 2.8 shows a schematic diagram of the matching network in which it can be seen that the larger capacitor (the load capacitor) is in parallel with the source. This is because the impedance match is between a high impedance source, the generator, and a low impedance load, the plasma [96]. The location of the tune capacitor adjacent to the plasma is important as it ensures that a self bias can develop on the powered electrode. This self bias results from an asymmetry between the surface area of powered and grounded electrode [97]. If the capacitor is not present, a strong DC current can flow in the system causing damage to the rf generator.

To understand how the L matching network works, first consider the circuit presented in figure 2.9 (a). Z_S is the source impedance $Z_S = 50$ Ω, Z_L is the impedance of the load capacitor, and Z_P is the plasma impedance, taken for this example to be $Z_P = 5 - iX$ Ω. This means the plasma has a resistance (real component of the

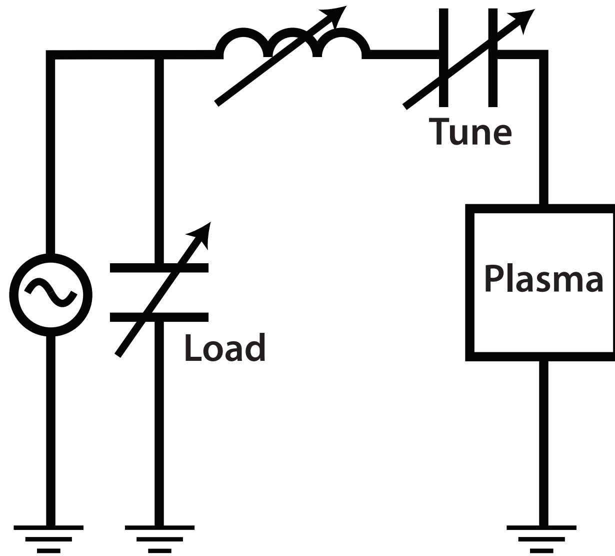

Figure 2.8: Diagram of the L-network circuit used to match the DASH source to the 50 Ω generator.

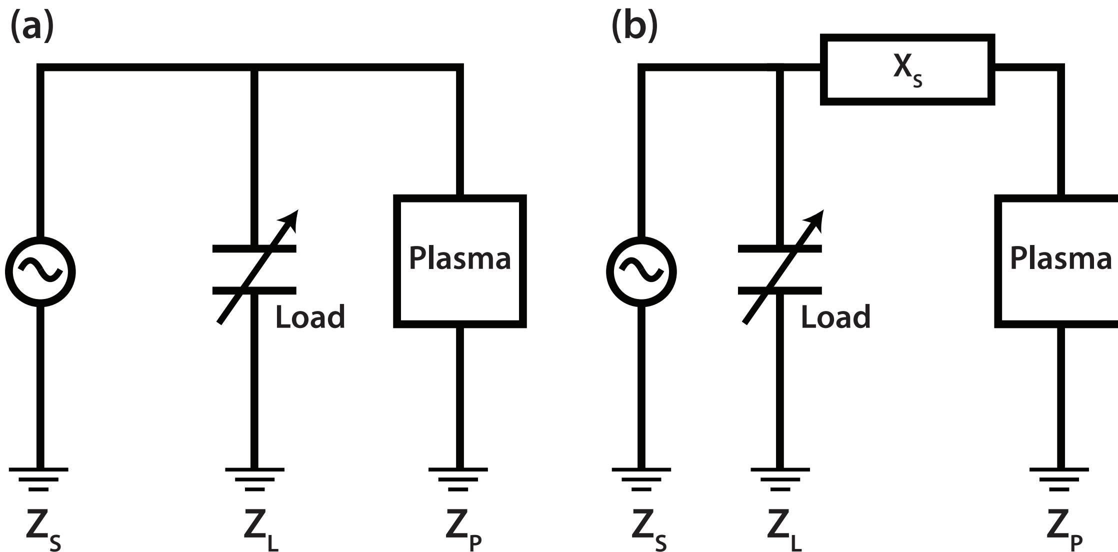

Figure 2.9: Example networks showing (a) a capacitor matching the real component of the plasma impedance, and (b), the complex component of the plasma impedance.

impedance) of 5 Ω, and a reactance of X Ω [96].

Using Z_L it is possible to match the real component of the plasma impedance, (5 Ω), to the 50 Ω generator. To calculate the capacitance required for this, the equation for describing impedance for a capacitor is used $Z_C = -i/\omega C$. To calculate

the total impedance of a set of parallel impedances, the following equation is used

$$Z_{total} = \frac{1}{Z_1} + \frac{1}{Z_2} + ... + \frac{1}{Z_n} \tag{2.1}$$

For this network there are two parallel impedances to consider so the system can be described by

$$Z_P = \frac{Z_S Z_L}{Z_S + Z_P} \tag{2.2}$$

Recalling the definition of the impedance of a capacitor, that the plasma impedance has been defined as $Z_P = 5 - iX$, and assuming a frequency of $f = 13.56$ MHz, the following equation can be derived

$$Z_p = 5 - iX = \frac{50(-i/\omega C_L)}{50 - i/\omega C_L} \tag{2.3}$$

Taking equation 2.3 and multiplying by the complex conjugate and equating the real part with the resistance of the plasma yields

$$\frac{50}{(50\omega C_L)^2 + 1} = 5 \ \rightarrow \ C_L = 704 \text{ pF} \tag{2.4}$$

The complex component of equation 2.3 can now be solved to calculate the reactance for the plasma yielding $X = 15\ \Omega$. So a capacitor of 704 pF will match the real part of the plasma impedance to the 50 Ω generator, but leaves the reactance of the plasma, $X = 15\ \Omega$, still unaccounted for. Now consider figure 2.9 (b). This circuit has an undefined reactance placed in series with the generator and the plasma. If the reactance is considered to be purely inductive, the necessary inductance can be easily calculated from the equation $X = 2\pi f L \rightarrow L = 0.18\ \mu$H [96].

Unfortunately during experimentation in a real plasma, the resistance and reactance of the plasma are liable to vary significantly. The changing resistance of the plasma can be matched by making the load capacitor variable as seen in figure 2.8. However, since a variable inductor is more difficult to modify, and a series capacitor is required for the development of a self bias, it is much more convenient to add a second capacitor, called the tune capacitor, after the inductor. This means a rough value for the inductor can be selected and then mostly ignored, with the tuning of

the series reactance done by the tune capacitor.

As an example, assume that instead of $L = 0.18$ μH, the inductor has been set at $L = 1$ μH. The series reactance is defined by $X_S = X_{inductor} - X_{tune}$, since inductors and capacitors have opposite reactances. The required capacitance for the tune capacitor can be calculated as $C_T = 167$ pF. It can be seen from these calculations that the matching network design for the DASH system is capable of efficiently depositing power into the plasma.

2.5 Diagnostic probes

Invasive probes are an effective and cost efficient method of making spatially resolved measurements of some of the fundamental plasma parameters, including: plasma potential (V_p), electron temperature (T_e), electron energy probability function (EEPF), and plasma density. The experiments presented in chapters 3 and 4 use three different probes: an uncompensated Langmuir probe, a radio frequency compensated Langmuir probe, and an emissive probe. All three probes are mounted through the movable probe port allowing for two dimensional translation while under vacuum.

The design, operation, and analysis of these probes is described in detail in this chapter, while the diagnostic tools used in chapters 5 to 7 are left until they are relevant. This is because the invasive probes described here are designed and constructed in-house. It is therefore appropriate that they are explained in detail, as this information is not available elsewhere, and serves to give confidence in the results they produce.

2.5.1 Langmuir Probe

An uncompensated Langmuir probe is one of the most simple electrostatic probes in terms of its design. At its most basic, it is simply a piece of conducting material, exposed to the plasma to draw ion and electron current [98]. This probe is used for making density measurements within the plasma. Because it is uncompensated it is unsuitable for measurements of the EEPF, T_e, or V_p, as these will be strongly perturbed by the rf fields present in the system. However a compensated probe

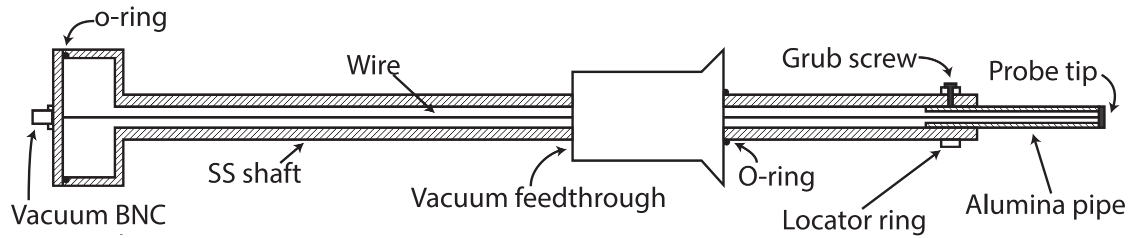

Figure 2.10: Schematic diagram of the uncompensated Langmuir probe used primarily in chapter 3. The probe has a straight shaft and is inserted through the movable probe port, allowing two dimensional translation under vacuum. Since it is an uncompensated probe, it can only be reliably used to measure ion density.

is a much more complex and fragile piece of apparatus than its uncompensated counterpart. Since large data sets are required for the density measurements made in chapter 3, the robustness of the probe is a critical consideration. The uncompensated probe has a much longer lifetime without requiring any maintenance due to the simplicity of its design and can still be reliably used to investigate n_i.

Probe Design

Figure 2.10 shows a schematic diagram for the uncompensated Langmuir probe built for this experiment. The outer housing of the probe shaft is stainless steel pipe 6 mm in diameter. To shield signal carrying wires inside the probe, the shaft exposed to the plasma is a grounded conducting material. If left to float the surface of the probe shaft can strongly perturb the plasma by becoming biased relative to the grounded walls of the chamber. The back of the probe must be capable of holding vacuum, as the interior of the probe is pumped down with the chamber. The back plate is fitted with a vacuum BNC connection to allow a bias voltage to be put on the probe tip and to extract the current collected by the probe tip. Further down the shaft the vacuum feedthrough is fitted to the steel shaft. The vacuum feedthrough connects to the movable probe port, creating a seal and allowing the probe to move axially without breaking vacuum.

It is important to have a section of insulating material between the probe tip and the grounded exterior of the probe shaft. If there is only a short distance between the tip and the steel shaft, when the tip is biased it can create strong electric fields in the region around the probe tip, and distort the measurement. A number of insulating

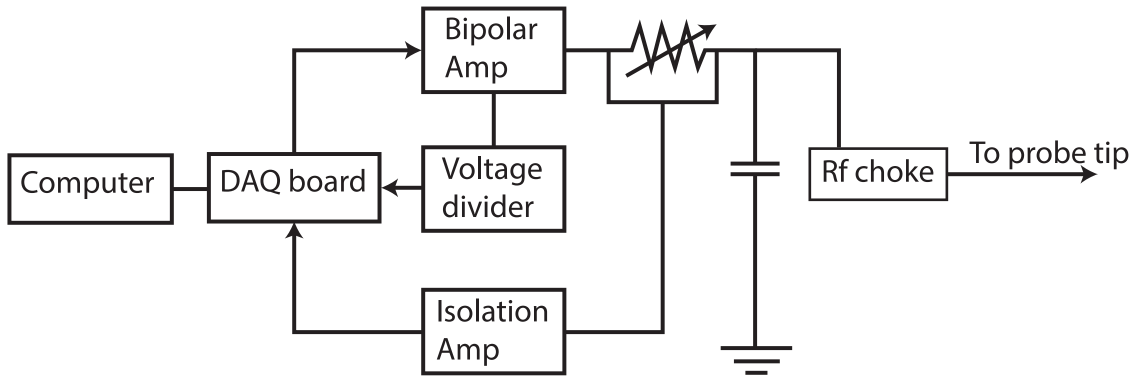

Figure 2.11: Diagram of the operational circuit used with the uncompensated Langmuir probe. The output and input signals are controlled from the computer via a DAQ board.

materials are suitable for use in this regard, but this probe uses a piece of alumina ceramic of 2 mm outer diameter. The alumina piece is attached telescopically to the stainless steel shaft via a locator ring and grub screw, it extends from the steel shaft such that 7 mm of alumina are exposed.

The probe tip is a nickel disc 2 mm in diameter and approximately 200 μm thick, press fit against the end of the alumina pipe. This means that the exposed surface of the probe tip will be limited to one side of the disc. This is done to ensure that if the plasma has any flowing component then the backside of the probe tip will not distort measurements of the plasma density. The back side of the nickel probe tip had a nickel tab spot welded to it and this is wrapped with a monofilament wire for a mechanical connection. The wire passes through the steel pipe to connect the vacuum BNC connection and on to the bias supply and return current to the measurements system.

Figure 2.11 shows a schematic diagram of the simple circuit used to bias the probe tip, extract the collected current, and convert it to a voltage signal for analysis.

A voltage ramp is sent from the Data Acquisition (DAQ) board to the Hewlett-Packard 6827A bipolar amplifier. The high voltage (HV) signal is branched and sent through a junction box to bias the probe tip, and at the same time returned via a voltage divider to the DAQ board. This allows the system to monitor the applied bias voltage in real time. The current collected from the probe tip flows through a simple rf choke and through a resistor where it is converted to a voltage signal. The

voltage signal is passed through an isolation amplifier to ensure no current flows to the DAQ board during measurement of the probe signal.

Theory of Density Measurement

When the bias on the probe tip is such that the probe collects no net current, the probe is said to be at the floating potential, V_f. An ungrounded surface within the plasma will naturally float at V_f to create an equal flux of ions and electrons. If the bias on the probe tip is more negative than V_f, the ion current drawn to the probe is stronger than the electron current. The majority of electrons from the bulk plasma are repelled by the field around the probe tip, and a net positive current is measured. Once the voltage on the probe tip is negative enough relative to the floating potential for all the electrons from the plasma to be excluded, the ion current plateaus. This part of the IV curve is called the ion saturation region (although true saturation does not occur as will be discussed) and can be used to calculate the ion density. Assuming quasineutrality within the plasma and only singly ionised ions, the plasma density can be equated to the ion density, that is $n = n_i = n_e$.

The ion saturation current is preferable for making density measurements because biasing the probe to achieve electron saturation requires a bias voltage higher than the plasma potential, V_p, which strongly perturbs the plasma. When making a measurement with an invasive diagnostic probe, it is always desirable to reduce the impact the probe has on the plasma to get accurate measurements of the unperturbed plasma.

To calculate the ion density from the ion saturation current the equation 2.5 can be used [2]

$$I_{sat} = 0.61 e n_i A_p u_B \tag{2.5}$$

where I_{sat} is the ion saturation current, e is the electronic charge, n_i is the ion density, A_p is the collecting area of the probe tip, and u_B is the Bohm velocity. The Bohm velocity is defined as the velocity with which ions must enter the sheath and is defined as $\sqrt{kT_e/M_i}$, where k is Boltzmann's constant, T_e is the electron temperature in eV, and M_i is the ion mass. At a first glance it might be expected that the collecting area for the probe could simply be defined by its size as a disc,

πr^2. However in reality the collecting area for the ion current to the probe tip is the boundary of the sheath that surrounds the probe tip. Any ion that passes the sheath edge will be accelerated to the probe tip and measured as current.

The sheath size is directly affected by the bias voltage applied, becoming larger as the bias voltage becomes more negative. It is for this reason that there is no true saturation of the ion current measured during an IV sweep of the Langmuir probe. As the sheath expands and the collection area increases, the ion current to the probe tip is also increased. When measuring the density with a Langmuir probe a bias voltage well below the floating potential is chosen and the size of the sheath must be considered. This effect can be compensated for using the theory for sheath size around a planar probe tip derived by Sheridan in [99]. The sheath area relative to the probe area is given by the equation 2.6

$$\frac{A_s}{A_p} = 1 + a\eta_p^b \tag{2.6}$$

where A_s is the area of the sheath, and the true collecting area, A_p is the area of the probe disc, η_p is the probe bias defined as $\eta_p = -eV_p/kT_e$, and a and b are constants. The constants a and b are defined by

$$a = 2.28\rho_p^{-0.749} \tag{2.7}$$

$$b = 0.806\rho_p^{-0.0692} \tag{2.8}$$

where $\rho_p = r_p/\lambda_D$, r_p is the probe radius and λ_D is the Debye length. It can be seen then, that the definitions of a and b in equations 2.7 and 2.8 respectively have a dependence on the plasma density n. This poses a problem to the overall goal of a more accurate density measurement as the set of equations has become self referential. To combat this, an iterative system is implemented starting with an assumed density defined by equation 2.5. This calculated density is used to define values for the constants a and b, which in turn defines a sheath size and thus a new collecting area. This new collecting area is returned to equation 2.5 and the process is repeated. Through each iteration the sheath size increases and consequently the calculated density of the plasma decreases. The iterative process is allowed to

continue until the change in the calculated density reaches some cutoff threshold. In the case of the calculations done in this system the density decreases until the ratio between old and new density was less then one part in 10^6. This normally requires between 15 and 20 iterations and may result in a calculated density of up to an order of magnitude lower than those found using equation 2.5 when measuring in low density regions.

2.5.2 Compensated Langmuir Probe

A Langmuir probe is compensated if a system has been implemented to filter noise from the signal generated by the rf fields present in the discharge. These fields can lead to significant distortion of the EEPF and measurements of the electron temperature of the system. As such, any measurements of electron energy distribution made via a Langmuir probe necessitate compensation. There are several ways to compensate the probe, including both trying to remove rf noise *in situ* during the measurements with passive electrical components [100], with external circuitry designed to bias the probe tip with an rf potential and draw only a DC current [101], or in post-processing.

Probe Design

The compensated Langmuir probe in this system uses passive component filtering. It has a series of inductors and capacitors near the probe tip that create an electrical notch filter to reject signals at the fundamental frequency and first harmonic of the plasma [100]. This can be achieved because at high frequencies the capacitance between the turns of an inductor creates a resonant circuit within the coil. This self resonance is exploited as the inductor will block the rf signal at the resonant frequency while allowing a DC signal (the current drawn to the Langmuir probe) to pass unhindered. These frequencies are chosen to match the fundamental frequency and first harmonic of the rf generator: 13.56 and 27.12 MHz respectively. Figure 2.12 (a) shows a schematic diagram of the rf compensation system used in this probe and panel (b) shows a macroscopic schematic of the entire probe.

Figure 2.12 (a) also shows a thin sheet of nickel plate wrapped around the narrowed

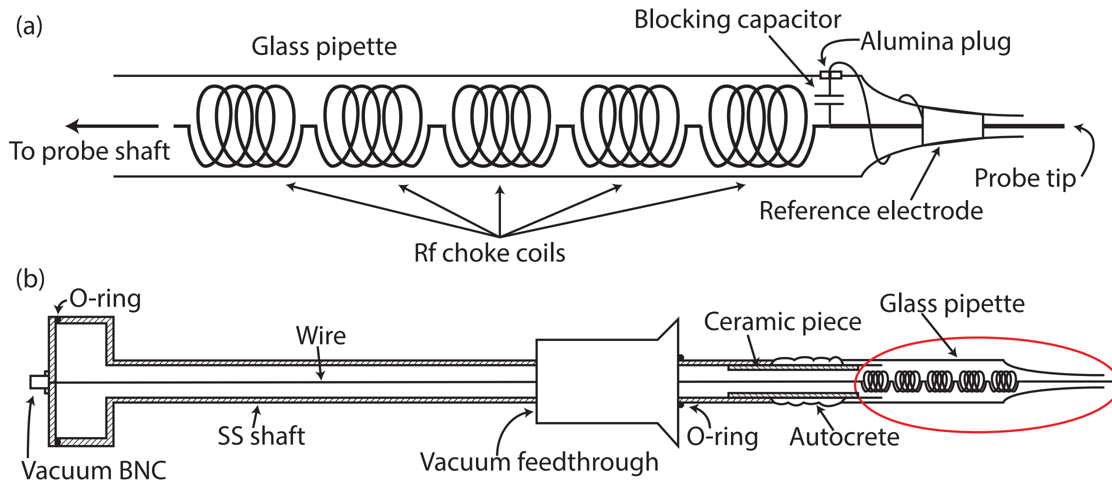

Figure 2.12: Schematic diagram showing the construction of the compensated Langmuir probe. Panel (a) shows a close up of the rf filtering system near the tip of the probe. Panel (b) shows a macroscopic view of the entire probe with the zoomed section highlighted.

section of the tip of the glass tube to act as a reference electrode. This plate is connected in series with a 4.7 pF capacitor to the inductor chain. The purpose of the reference electrode and capacitor is to cause the bias of the probe tip to vary with the plasma potential as it changes throughout the rf cycle. The conducting plate exposed to the plasma picks up the rf signal from the plasma but the blocking capacitor prevents DC current reaching the wire connected to the probe tip.

In the inductor chain there are three inductors with self resonance at the fundamental frequency of 13.56 MHz and two at the second harmonic of 27.12 MHz. To find the self resonance of an inductor the frequency response is measured with a Vector Network Analyser (VNA). The VNA can be set up to scan a frequency range, typically from 1 to 100 MHz and show the attenuation in signal over this range. For the entire compensated probe system signals at the fundamental frequency are reduced by approximately 95 dB and the second harmonic is reduced by 75 dB.

The rf compensation system is encased inside a glass tube contiguously attached to stainless steel pipe identical to that used in the uncompensated Langmuir probe. To attach the glass tube to the steel pipe, a short piece of alumina pipe 2 mm in diameter was bevelled on both ends to fit into the glass tube and steel pipe. Both connections are coated in a high temperature vacuum ready adhesive called Autocrete to hold it in place. The probe tip is a 3 mm length of nickel wire.

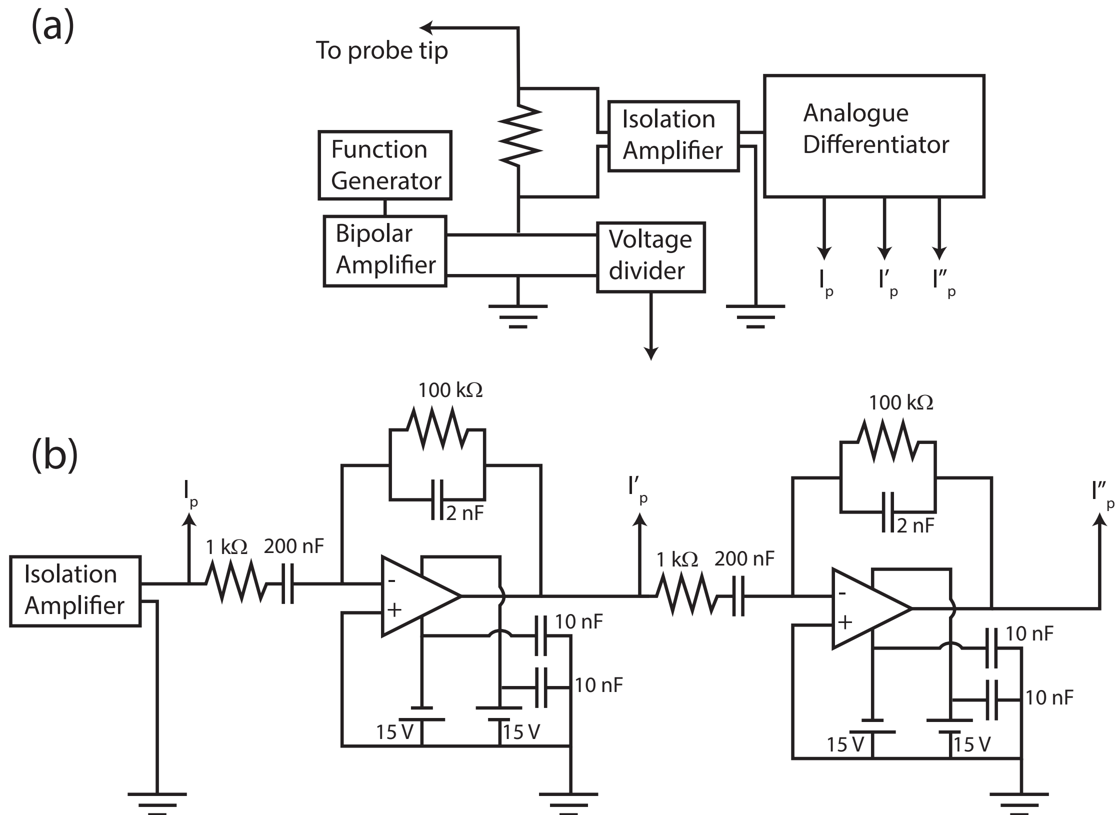

Figure 2.13: The measurement circuit associated with the compensated Langmuir probe. Panel (a) shows a broad view of each component of the measurement system. Panel (b) shows the analogue differentiator circuit in detail.

The measurement circuit for the compensated probe is more complex than for the uncompensated probe and it is drawn schematically in figure 2.13 (a). The probe bias is controlled from a 14-bit National Instruments PXI-5122 card. The bias signal passes through a Hewlett-Packard 6827A bipolar amplifier, with a gain of -20 (signal is amplified and inverted). This signal passes through a variable resistor junction box with a range of 1 Ω to 10 kΩ and to the probe tip. Collected current comes back to the junction box and is passed into an Otter isolation amplifier, and then to an analogue differentiator, whose circuit is shown in figure 2.13 (b). Similar to the uncompensated probe, the isolation amplifier removes the current signal from the Langmuir probe while retaining its associated voltage signal, which is defined by the selected resistance.

The analogue differentiator is used for the calculation of the EEPF as it outputs the double differential of the current relative to the probe voltage. Figure 2.13 (b) shows the cascaded active differentiator circuits. An active circuit such as this relies

on the relationship between changing voltage on a capacitor and current flowing through it. The current through a capacitor is defined by

$$I = C\frac{dV}{dt} \tag{2.9}$$

Since the input impedance of an operational amplifier (op-amp) is very high (assumed infinite), all the current in the system must flow through the feedback side resistors (100 kΩ in figure 2.13 (b)). By considering that the input voltage is the voltage measured across the capacitor and the output voltage from the op-amp is the voltage measured across the resistor in the feedback side, Ohm's law tells us that

$$V_{out} = -RC\frac{dV_{in}}{dt} \tag{2.10}$$

With a gain of $-RC$, and where for the differentiator shown in figure 2.13 (b), $R = 100$ kΩ, and $C = 200$ nF. However, the capacitance in a single differentiating element of the total circuit, $C = 200$ nF, is actually dependent on the frequency of the changing signal. Capacitive reactance is defined by

$$X_c = \frac{1}{2\pi fC} \tag{2.11}$$

Therefore, for a high frequency signal, the gain of the differentiator can become very large, causing the system to become unstable. To combat this, a second capacitor is placed in parallel to the feedback resistor and can be seen in figure 2.13 (b), with a capacitance of 2 nF. This capacitor suppresses the high frequency capability of the circuit by allowing a low resistance alternate path for the high frequency signal, increasing the overall stability of the circuit.

Theory of Electron Energy Probability Function Measurement

Figure 2.14 shows an idealised version of the collected current of a Langmuir probe whose bias has been swept from within the ion saturation region, where electrons are completely excluded, to the electron saturation region. If the EEPF has a Maxwellian distribution then the electron temperature (T_e) can be found from the gradient of the natural logarithm of the second derivative. In the event of a non-

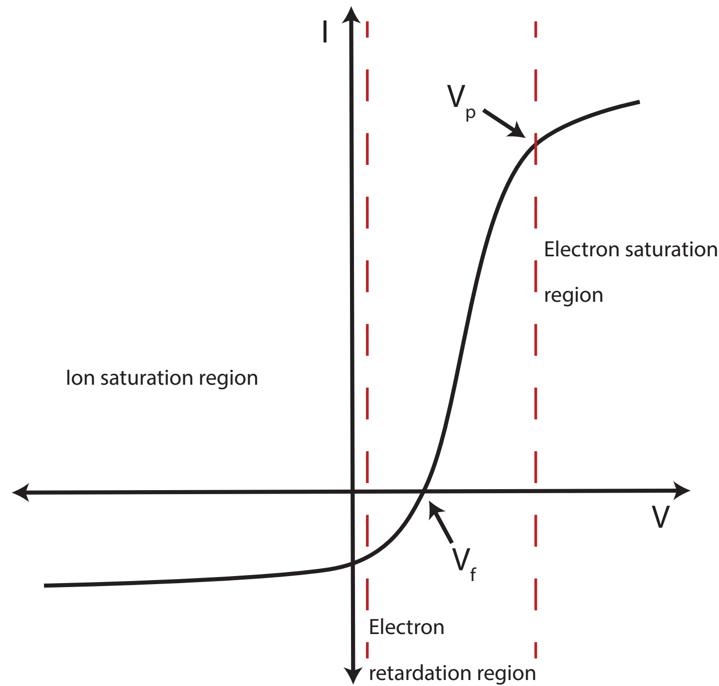

Figure 2.14: Idealised IV curve from a Langmuir probe. The trace has three regions: the ion saturation region, where only ion current is collected, the electron retardation region where both ion and electron current are collected, and the electron saturation region, where only electron current is collected.

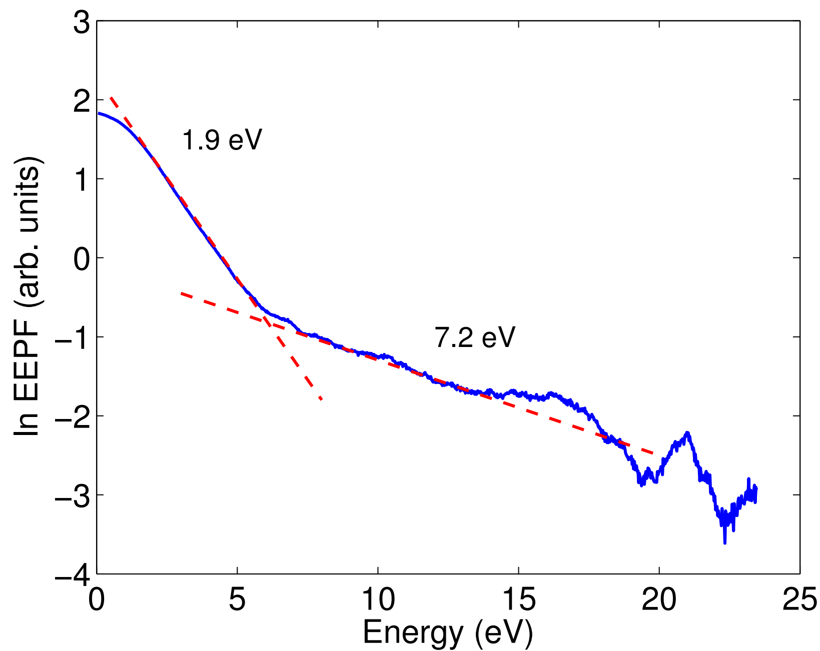

Figure 2.15: Example data taken from the compensated Langmuir probe described in this section. The natural logarithm of the second derivative of probe current with respect to bias voltage shows the EEPF to be a bi-Maxwellian with a hot tail.

Maxwellian distribution, the temperature of different sections of the distribution can be found via multiple line fittings. An example of a bi-Maxwellian distribution from the DASH system is shown in figure 2.15, showing how the two temperatures of the distribution are fitted and used to derive two values for T_e.

To extract the EEPF from the raw IV trace, and subsequently calculate values for the electron temperature, the Druyvesteyn method is employed [102, 103]. The electron energy distribution function (EEDF) is found to be proportional to the second derivative of the probe current with respect to bias voltage. This is illustrated in equation 2.12

$$F(\epsilon) = \frac{4}{A_p e^3}\sqrt{\frac{m_e \epsilon}{2}}\frac{d^2 I_e}{dV_b^2} \tag{2.12}$$

Where $F(\epsilon)$ is the electron energy distribution function (EEDF) and ϵ is a transformed variable representing $\epsilon = m_e v^2/2e$. A_p is the collecting area of the probe, m_e is the mass of an electron, V_p and V_b are the plasma and probe bias potentials respectively, and I_e is the electron current. The probability function associated with this distribution (the EEPF) is defined as

$$F_p(\epsilon) = \epsilon^{-1/2} F(\epsilon) \tag{2.13}$$

Therefore the EEPF is directly proportional to the second derivative of the collected current with respect to the bias voltage. The EEPF can be visualised directly simply by plotting $d^2 I_e/dV_b^2$ with respect to ϵ. However, if the EEPF is assumed to be Maxwellian it is found that [2]

$$\frac{d^2 I_e}{dV_b^2} \propto F_p(\epsilon) = \frac{2}{\sqrt{\pi}} n_e T_e^{-3/2} \exp\left(-\epsilon/T_e\right) \tag{2.14}$$

Taking the natural logarithm of both sides of equation 2.14

$$\ln\left(\frac{d^2 I_e}{dV_b^2}\right) \propto \frac{\epsilon}{T_e} + C \tag{2.15}$$

Where C is a constant. Equation 2.15 shows that plotting the natural logarithm of $d^2 I_e/dV_b^2$ will yield a straight line with a slope of $1/T_e$, provided the electrons have a Maxwellian energy distribution. As will be seen in the coming chapters, the

EEPFs measured in this work are Maxwellian or bi-Maxwellian (as shown in figure 2.15), and could be analysed using this method.

2.5.3 Emissive Probe

The primary use of the emissive probe used in chapter 4 is to make accurate and spatially resolved measurements of the plasma potential (V_p). The probe submits a thin filament to currents of up to 2.0 A, heating the filament and causing it to thermionically emit electrons. There are two common methods by which an emissive probe can be operated to measure the plasma potential, known as the inflection point method [104] and the floating potential method [105]. While the inflection point method is generally considered to be more reliable, the floating point method offers a more convenient and faster diagnostic. For this work, the relative efficiency of the floating point method is considered to be of more importance than the reduced error that the inflection point method offers. This is because the DASH source can only be operated for a limited time before suffering heat damage. The inflection point method requires several data acquisitions for every point in space, and such measurements are time intensive. By contrast the floating point method is fast, requiring only a single acquisition at each point. This feature makes it the best candidate for use in the DASH system because an entire spatial sweep can be collected in approximately five minutes, without having to turn off the plasma to let the DASH source cool.

Probe Design

The body of the emissive probe is similar in design to the uncompensated Langmuir probe and can be seen in figure 2.16. However, the alumina pipe has two adjacent holes bored through it rather than a single hole. The filament is a pre-made section of thoriated tungsten wire wound into a coil, and then wound a second time into another coil. The purpose of this winding pattern is to increase the length of the wire in the double coil and thus the number of electrons emitted by the filament. The shape of the winding also provides a useful method for attaching the filament to the current carrying wires inside the probes. Two stubs of copper wire protrude

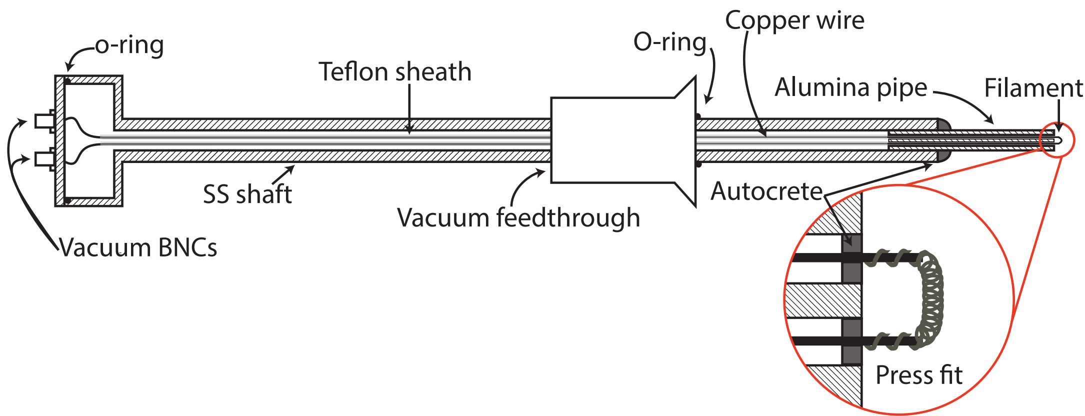

Figure 2.16: Schematic diagram of the emissive probe used. The zoom shows the tip of the probe in more detail, specifically the press fit of the thoriated tungsten filament over the wire stubs.

approximately 2 mm from the end of the ceramic pipe, which is capped in autocrete. The stubs are sanded to reduce their diameter and expose the conducting surface from beneath the enamel coating the rest of the wire. The filament is then press fit over the wire stubs to provide both a strong mechanical and electrical connection, without the need for any adhesive. It is important that the filament is fitted carefully as it is very fragile because of its small diameter relative to its length. Once attached to both stubs, the filament forms a rounded tip approximately 1 mm long. The copper stubs will cool the sections of filament they are in contact with, so only the section of filament not touching the wire stubs will heat enough to emit light, increasing the spatial resolution of the probe.

The operational circuit for the emissive probe can be seen in figure 2.17. The heating current is supplied from an Iso-Tech IPS 3303-D power supply unit (PSU), connected to a Ferguson TS 240/500 isolation transformer. This transformer ensures that the heating current is isolated from the measurement current drawn by the probe tip by floating the PSU, preventing distortion of the signal and damage to the measurement system. The computer is connected to the PSU via USB and controls the ramp of the current to the filament, over at least 30 seconds to minimise thermal shocks to the filament and reduce the chance of a failure. The current supplied is measured internally in the PSU and the computer monitors this value via the USB connection.

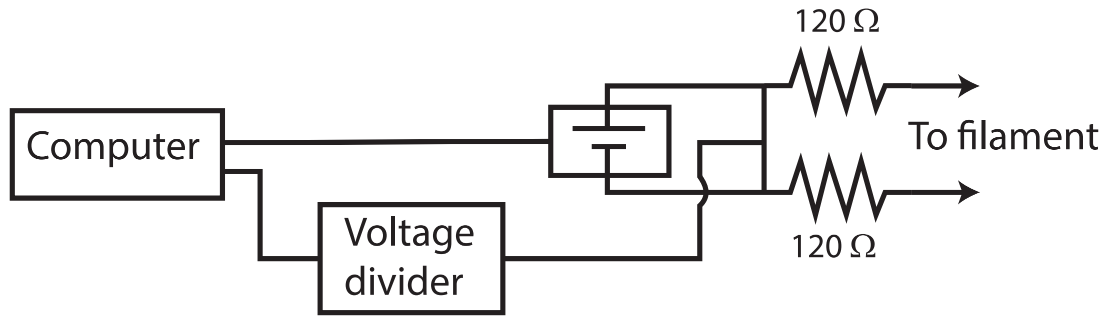

Figure 2.17: The measurement circuit used to operate the emissive probe. The power supply is floating and is controlled via a USB connection to the computer.

Theory of Measurement

The floating potential method for measuring the plasma potential of a plasma works by neutralising the sheath that forms on the emissive probe tip. The heating current applied to the filament is increased slowly over time, increasing the filament temperature. As temperature rises, a greater number of thermionic electrons are emitted from the probe tip. Eventually the emitted electron density is high enough to completely neutralise the sheath that naturally forms on the floating filament. When the sheath is suppressed by the neutralising current the filament floats to the potential of the surrounding plasma, which can be read from the probe as a floating voltage.

A set of example data from a current-voltage sweep of the emissive probe can be seen in figure 2.18. At low currents when the filament is not hot enough to emit, the floating potential is simply the floating potential of the plasma. As the filament begins to emit, the sheath is partly neutralised and the floating potential of the filament begins to rise. Once the sheath is completely neutralised there is an inflection point in the floating potential of the filament, and the voltage measured at this point is taken to be the plasma potential.

As has already been mentioned, the efficiency with which this diagnostic can be performed is its main advantage. However the strong emission from the filament is also a drawback. This emission can affect the emissive probe itself and perturb the surrounding plasma. Strong emission from the filament necessitates high temperatures. Because the filament is so thin, it is mechanically very weak and can break

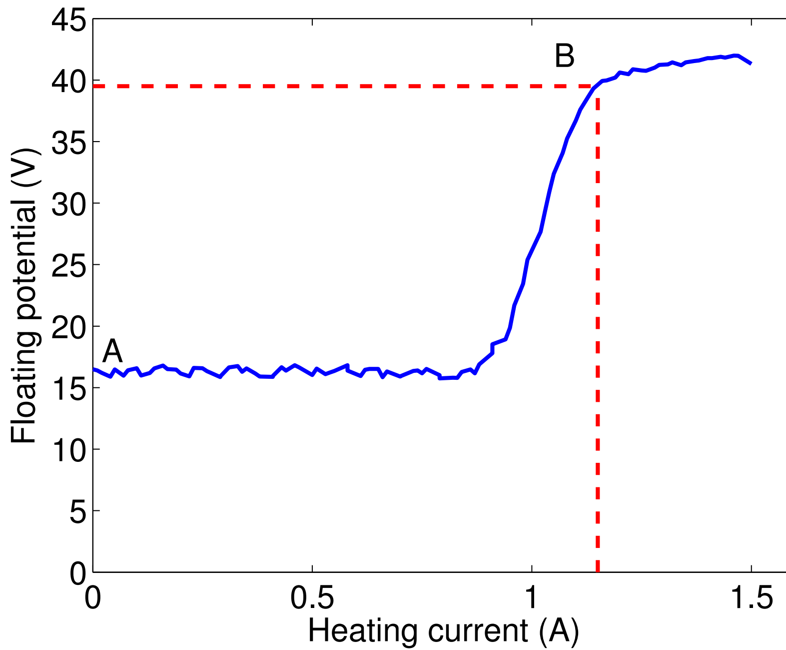

Figure 2.18: An example of raw data acquired using this emissive probe. The floating potential can be seen at point A, and the plasma potential at point B, for an emitting current of approximately 1.2 A and a measured $V_p = 39$ V.

easily. Sustained use at the high heating currents necessary in the floating potential method guarantee regular filament failures. When this occurs the filament must be replaced, requiring the dismantling of the probe system. The frequency of these failures can be reduced through careful operation. The most important parameter to control when concerned about the condition of the filament is the rate at which heating current is varied over time. Changing the heating current too fast causes a thermal shock to the filament, which will often result in a break. The thoriated tungsten filaments used in this system can withstand up to around 2.5 A for a period of a few minutes at a time.

To isolate the plasma potential 'knee' in the raw EP data, analysis of the second derivative of the raw signal was used. The second derivative was found by using a series of Saviztky-Golay smoothing functions and numerical differentiation. Although necessary for the analysis, one of the drawbacks of smoothing data for differentiation is that there is blurring of the signal in critical areas. For this reason the error in the plasma potential measurements made using this system is expected to be ± 2 V.

3

Plasma Plume Density Mapping

Due to the novel design of the Distributed Array Shower Head (DASH) system, a logical first step in understanding its operation is a fundamental study of its break down and steady state parameters. To aid this characterisation, argon plasma is used for its chemical simplicity. These experiments are performed in the 4 mm DASH configuration, with no sleeve covering the electrodes in the active regions. The bulk of this chapter deals with mapping the ion density in the expansion chamber for single and multiple hole operation. This data yields information on how a single hollow cathode produces plasma, how it diffuses into the expansion chamber, and how multiple hollow cathodes interact with one another during operation. This final consideration is crucial to realising the eventual goal of scalability of the system.

3.1 Breakdown and Stable Operation

Breakdown voltages in the DASH system are measured with a high voltage (HV) probe placed between the matching network and the powered electrode. This configuration enables measurement of the electrode voltage at breakdown after the input voltage has been amplified by the matching network. Figure 3.1 compares the breakdown voltages for a single hole in the DASH system with the similar Pocket Rocket system [92], and some typical parallel plate rf discharges.

There is very good agreement between the DASH and Pocket Rocket systems in terms of both the shape and voltages of the Paschen curves. The Pocket Rocket calculations are performed using $d = 4$ mm as this value represents both the diameter of the hollow cathode as well as the spacing between the powered and grounded electrodes. However, as mentioned in chapter 2, the DASH system has a hollow

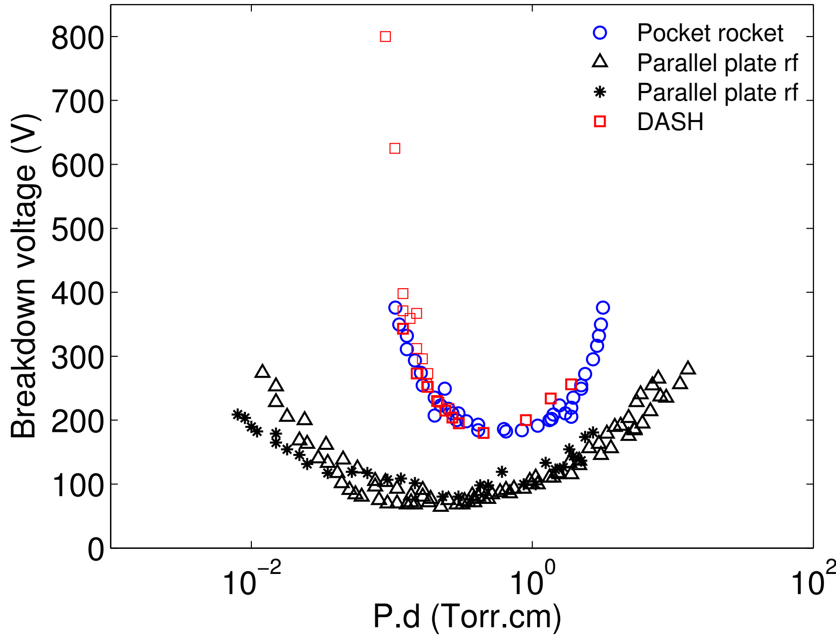

Figure 3.1: Paschen breakdown curves for the DASH and Pocket Rocket systems compared with parallel plate rf plasmas in argon.

cathode diameter of 4 mm and an electrode spacing of 6 mm. The data presented in figure 3.1 uses $d = 6$ mm to achieve the agreement with the Pocket Rocket data. If $d = 4$ mm is used as the characteristic length for breakdown in DASH, the data fails to agree with the Pocket Rocket breakdown voltages.

This implies that when breakdown occurs, the discharge forms in the areas between the powered and grounded electrodes. Simulation and in-hole ion saturation current measurements of the Pocket Rocket system show that during steady state operation the density peaks in the centre of the hollow cathode [92, 106]. It is reasonable then to suggest that the discharge ignites between the electrodes, as in a normal capacitive discharge, before moving the density peak into the hollow cathode.

When two or more hollow cathodes in the DASH source are operated simultaneously, it is observed that a minimum power and flow rate per hole is necessary to ensure stable operation. In this case, stable operation is defined by approximately equal emission intensity from all active hollow cathodes in the DASH source. It is further required that all the active hollow cathodes remain consistently ignited. By contrast when operating unstably, individual hollow cathodes within the array are observed to vary greatly in emission intensity, as well as flickering on and off during

operation. The stable operating characteristics in argon are found to be a minimum flow of 10 sccm and power of 2 W for every active hollow cathode in the array. If the flow per hollow cathode is reduced to 5 sccm, the necessary power increases to 20 W. In SF_6, 14 sccm and 5 W are required per hollow cathode, with power increasing to 20 W if flow is decreased to 10 sccm. Below these flow thresholds of 5 and 10 sccm for argon and SF_6 respectively, no plasma is achievable. The increased thresholds for SF_6 operation are due to its more complex chemistry providing an energy sink via processes such as dissociation.

3.2 Single Hollow Cathode Operation

The movable probe port introduced in chapter 2 allows for spatially accurate two dimensional sweeps with a diagnostic probe. The uncompensated Langmuir probe described in chapter 2 is used to make measurements of the ion saturation current. By adopting the method for the calculation of the sheath dimensions around a probe developed by Sheridan [99], and covered in detail in chapter 2, measurements are made of the ion density in the plume of plasma expanding from the hollow cathode source.

The simplest configuration for the system is single hole operation. Figure 3.2 shows a two dimensional sweep of ion density (n_i), operating a single hole at 33 sccm of argon and 33 W of applied power as measured between the generator and the matching network. These parameters are chosen to be well above the flow and power thresholds for stable operation to ensure reproducibility of the data.

Figure 3.2 contains 352 data points, interpolated over the spatial range to produce the contour plot. Measurements are made every 2 mm along the x axis. The first measurement on the z axis is at $z = 1$ mm, then every 2 mm from $z = 2$ to $z = 20$ mm and finally every 5 mm out to $z = 50$ mm. This measurement spacing is used for all subsequent density plots of this type. Displaying error bars on the plot is impracticable as the density range spans four orders of magnitude. The expected error for these measurements is $\pm 20\%$ [107].

At the interface between the hole and chamber, $z = 0$ mm, the density is slightly

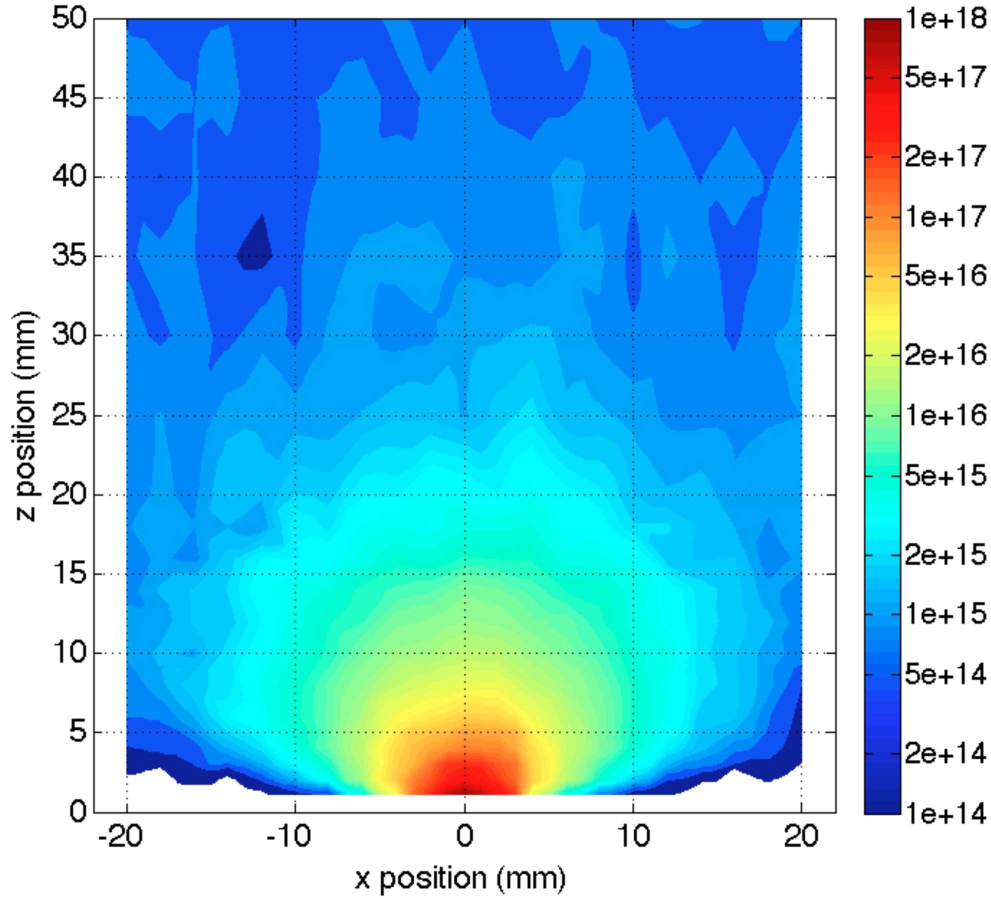

Figure 3.2: Map of the ion density (n_i) of a single plume measured with a Langmuir probe (displayed in m^{-3}). The colour map is presented in a log scale. The single hollow cathode is operated at 33 sccm of argon and 33 W.

above 10^{18} m^{-3}. Using the measurements of ion saturation current performed in the Pocket Rocket system by Charles *et al.* [92], a peak plasma density inside the hollow cathode of $n = 10^{19}$ m^{-3} can be inferred. Between $z = 0$ and $z = 50$ mm the density drops four orders of magnitude to 10^{14} m^{-3}. The plume extends out to around $z = 35$ mm with a density of 10^{15} m^{-3} before the ion density stops decreasing with distance from the source.

Figure 3.3 shows ion density data extracted from figure 3.2 along z for $x = 0$ mm (circles). The data has been normalised to the density at $z = 0$ mm to allow for easy comparison with the $1/z^2$ fit also shown in the plot. Between $z = 0$ and $z = 30$ mm, the ion density decreases in excellent agreement with $1/z^2$. Beyond $z = 30$ mm, the density diverges from $1/z^2$ and becomes nearly constant.

The agreement with the $1/z^2$ line close to the interface to the chamber sug-

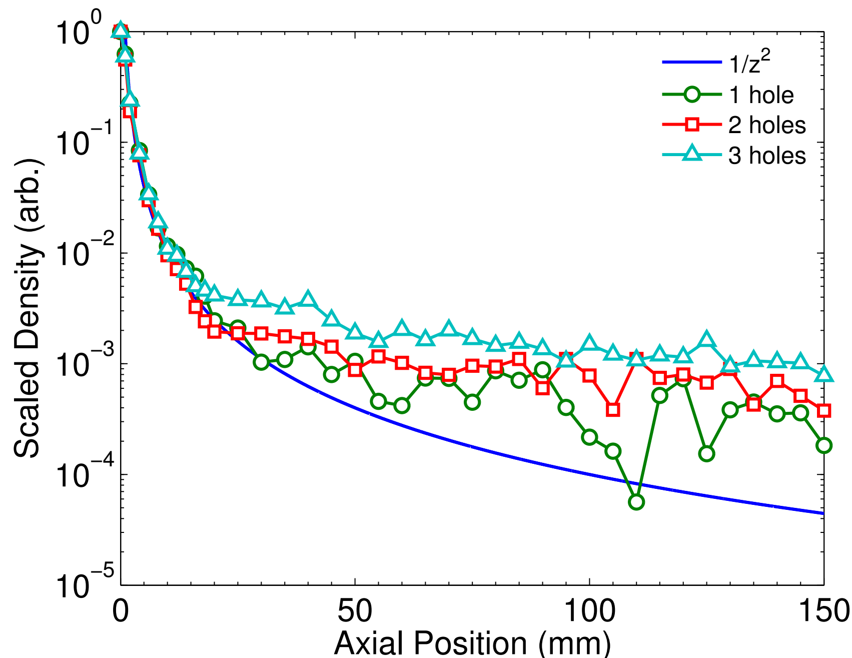

Figure 3.3: Normalised log-linear plot showing axial measurements of the ion density in line with an active hollow cathode for one, two, and three active hollow cathode arrangements. The data is normalised to the value at $z = 0$ mm for each set for easy comparison with each other and with the $1/z^2$ line. A flow of argon at 33 sccm and power of 33 W per hollow cathode is used for each configuration.

gests that the ions are behaving as though expanding from a point source at $z = 0$ mm [108]. This implies that limited or no ionisation is occurring in the plume and diffusion of plasma from the hollow cathode is the dominant process in this region. Beyond $z = 30$ mm the deviation from the $1/z^2$ line suggests that ionisation occurring in the main part of the chamber becomes dominant. The plasma in the chamber may be considered composed of two parts: plume and ambient. The plume is a spatially small, high density, and high pressure region near the interface between the hole and chamber. The plasma in the plume is created within the hollow cathode at around 600 mTorr, and is expanding into the chamber without any significant additional ionisation occurring near the interface. By contrast, the ambient plasma is relatively low density and is created via electron impact ionisation within the expansion chamber.

The suggestion that no significant ionisation occurs within the plume is justified by considering the mean free path for an ionising event for an electron in the plume.

The equation for a mean free path discussed in chapter 1 reads

$$\lambda_{iz} = \frac{1}{n_g \sigma_{iz}} \tag{3.1}$$

The pressure in the plume varies greatly with location. Using figure 2.5 as a guide, the pressure at interface to the chamber the pressure is expected to be 160 mTorr, while at the tip of the plume ($z = 35$ mm) it is around 10 mTorr. Because of the change in pressure, the mean free path for any collision varies throughout the plume. A pressure of 160 mTorr yields a neutral gas density of $n_g = 5.1 \times 10^{21}$ m^{-3} and using a cross section for electron ionisation in argon of $\sigma = 3 \times 10^{-20}$ m^2 [2], $\lambda_{iz} = 6.5$ mm. But at $z = 6.5$ mm the pressure has already dropped significantly and the mean free path will now be $\lambda_{iz} = 32$ mm, which is greater than the longest dimension of the plume. Due to the significant pressure gradient between the inside of the hollow cathode and the chamber, further ionisation in the plume is unlikely.

Repeating the same calculation for the pressure measured with the chamber manometer, 2 mTorr, produces a mean free path of 50 cm. Since this is shorter than the chamber, ionising collisions are possible. When considered in conjunction with the ion density measurements showing a deviation from $1/z^2$ behaviour far downstream of the source, this calculation suggests the existence of a second component of the plasma in the chamber, created outside the source. This plasma would have a much more uniform density distribution and be dominant away from the hole, once the plasma from the plume has diffused to such an extent as to have negligible density. Applying this explanation to the data presented for a single hole in figure 3.3 it can be seen that the ambient plasma density is approximately $10^{-3} \times n_{i,z=0}$. For values of z greater than $z = 30$ mm the density of ions diffusing from the hole drops below this ambient level and there appears to be a switch in dominant processes.

3.3 Multiple Hollow Cathode Operation

Having acquired a basic understanding of the behaviour and shape of the plasma as it expands from a single hollow cathode, a study is undertaken to measure the

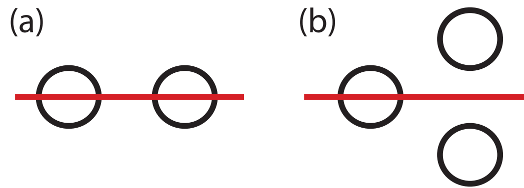

Figure 3.4: Schematic diagram showing the configurations for (a) two and (b) three active hollow cathodes. The red lines show the plane in which Langmuir probe measurements are performed.

effects of operating hollow cathodes in tandem. The aim of this is to observe how two or more hollow cathodes interact with one another and to determine whether the plasma they produce in the chamber can be considered as a simple superposition of multiple single hollow cathodes.

3.3.1 Measurements

Two more complex configurations of active hollow cathodes are investigated. They are: two hollow cathodes, both in the (x, z) plane and three hollow cathodes arranged in an equilateral triangle, one in the (x, z) plane and the other two above and below it respectively. The hollow cathode configurations are displayed schematically in figure 3.4. Each hollow cathode is supplied with 33 sccm of argon and 33 W, so for two active hollow cathodes 66 sccm and 66 W are applied, and 99 of each for 3 hollow cathodes.

It was found that regardless of the number of active holes, a peak density at the interface to the chamber was around 10^{18} m^{-3}. This implies that the internal operation of each hollow cathode is isolated from its active neighbours. However, the dependence of the ambient plasma density on expansion chamber pressure is supported by the data presented in figure 3.3 for values of $z > 25$ mm. All three configurations show the same $1/z^2$ dependence in the plume, but once the ambient plasma becomes dominant away from the interface, the density in the chamber is proportional to the number of holes open. Since the effect of increasing the number of operating holes in the DASH source is an increase in chamber pressure, it can be deduced that pressure in the chamber is the controlling influence of ambient plasma density.

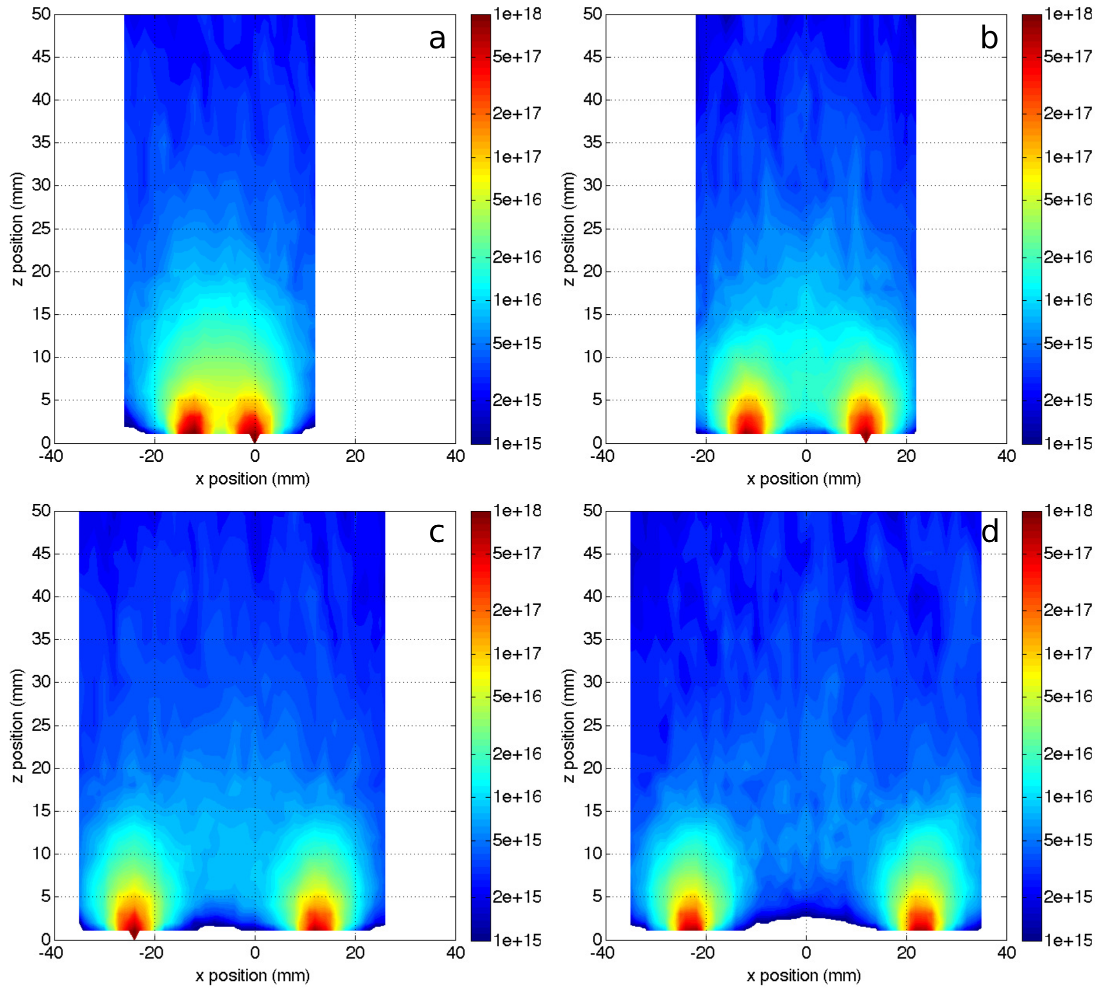

Figure 3.5: 2D ion density plots with a log scale colour map showing the downstream plasma density variation as the separation between two operational holes is changed. Panel (a) shows two active holes separated by 11 mm, (b) with 22 mm separation, (c) with 33 mm separation, and (d) with 44 mm separation. All four sets of data were taken with 33 sccm of argon and 33 W per hollow cathode.

Figure 3.5 shows a series of two dimensional ion density sweeps for two operational hollow cathodes with varying separation. The separation between the centre of the two active hollow cathodes was 11, 22, 33, and 44 mm in panels (a), (b), (c), and (d), respectively. In figure 3.5 (a) and (b), the plumes are so close to one another that their significant overlap obscures their individual shapes. However, in (c) and (d), it is possible to see that each plume retains the shape observed in single hollow cathode operation as seen in figure 3.2.

Further inspection of figure 3.5 suggests the densities in the chamber are more complex than a simple superposition of the data taken for a single hole. Panels

(b), (c), and (d) show an elevated density measured between the two active hollow cathodes' plumes. For example, in figure 3.5 (b) at the point $(x, z) = (0, 15)$ mm, there is a measured ion density of 1.5×10^{16} m^{-3}. By comparison, doubling the density measured at a point the same distance, $(x, z) = (11, 15)$ mm from the single hollow cathode gives 6×10^{15} m^{-3}. The measured ion density is more than twice the expected value for a simple superposition of two of the plumes presented in figure 3.2. This will be discussed in more detail in section 3.3.2.

Flow and pressure are not independently controllable, so to isolate the effect of the chamber pressure on the ambient plasma density three two dimensional ion density sweeps are made using 16.5, 33, and 50 sccm and 33 W per hollow cathode. The corresponding pressures measured for the chamber are 1.5, 4, and 7 mTorr, respectively. Two active hollow cathodes are used, separated by 11 mm, such as in figure 3.5 (a). The results of these sweeps can be seen in figure 3.6 panels (a) through (c). It is immediately obvious that the downstream plasma density is strongly dependent on the flow rate, whereas the shape and density of the plumes vary only weakly. For the 16.5 sccm per hollow cathode case shown in panel (a), the downstream density drops below 10^{15} m^{-3}, while for 50 sccm per hole the density at $z = 50$ mm is approximately 4×10^{15} m^{-3}.

To quantify the assertion that the ambient plasma density is dependent on the total flow rate in the DASH system, a generalised measurement of density far from the source is necessary. The densities along the x axis for $z = 45$ mm were averaged for each of the three flows shown in panels (a) through (c). Figure 3.6 (d) shows there was a steady increase in density measured far from the hole from approximately 1 to 4×10^{15} m^{-3} as the flow was increased from 16.5 to 50 sccm per hollow cathode. For $z = 45$ mm the expected density from a $1/z^2$ decay is calculated as the density at $z = 0$ (n_{peak}), divided by $r^2 = 45^2$. Since there are two active hollow cathodes, the density at $z = 45$ mm can be approximated as $2 \times n_{peak}/z^2$. These predicted densities are displayed as squares in figure 3.6 (d). Importantly, the difference between the circles (measured) and the squares (calculated) increases with pressure in the chamber, rising from 7×10^{14} to 1.3×10^{15} m^{-3}. This implies that as the flow through the active holes increases, the increase in the density measured far from the

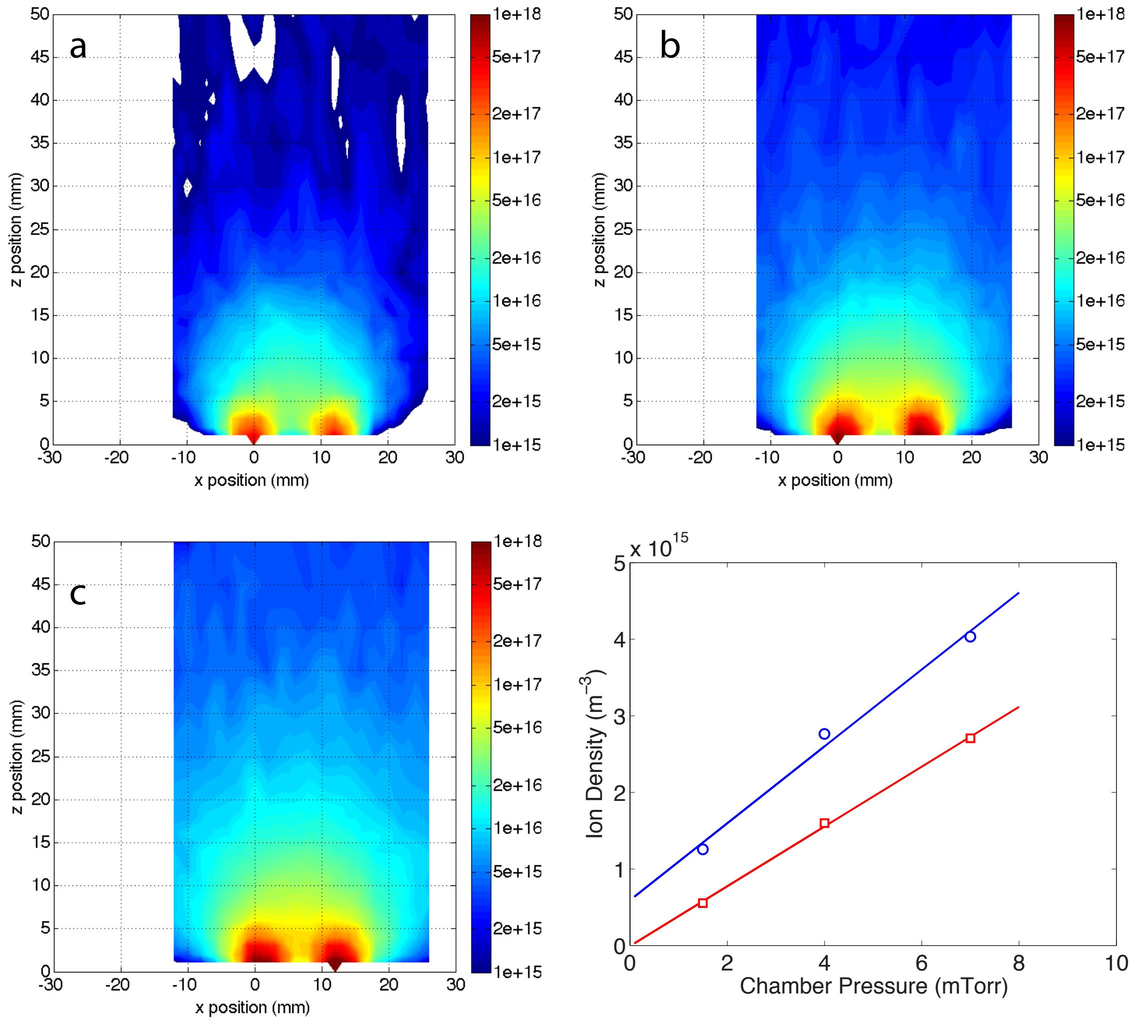

Figure 3.6: Two dimensional ion density sweeps for two active hollow cathodes separated by 11 mm with varying flow rate and a constant power of 33 W per hole. Panel (a) has 16.5 sccm per hole, (b) 33 sccm per hole, (c) 50 sccm per hole. (d) Averaged ion densities measured across the x axis for z = 45 mm (circles) for the data presented in (a)-(c). The expected densities for a $1/z^2$ decay for each flow are shown (squares). The linear fits serve to highlight the different rates of increase of density with respect to chamber pressure.

source cannot just be attributed to increased density in the holes. Therefore, the density of plasma being created downstream in the chamber must be a function of the downstream pressure.

It is likely there are three processes contributing to the overall distribution of ions throughout the combined plumes. They are: plasma drift via convection along neutral gas flows, the ambipolar diffusion of plasma from the holes, and the production of new plasma in the chamber. A quantitative determination of their relative impor-

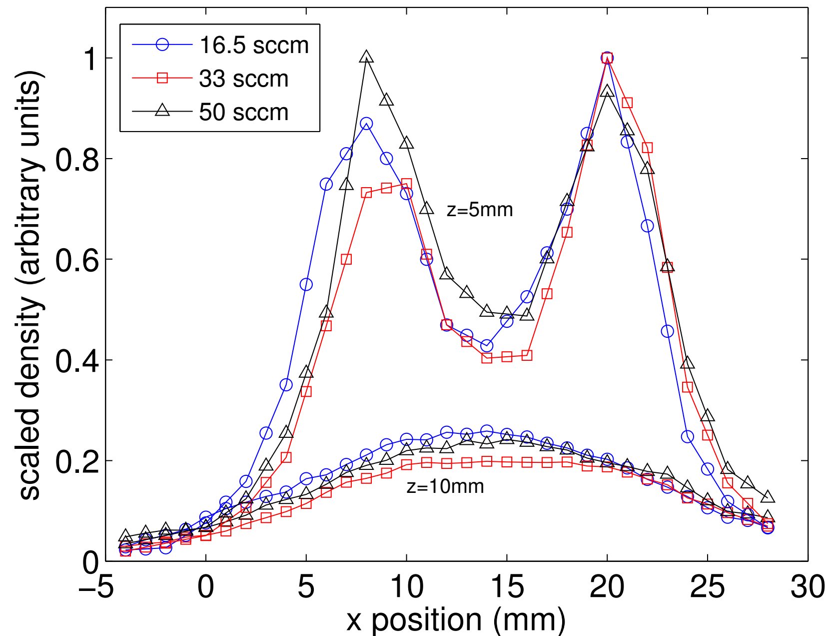

Figure 3.7: Density profiles along the x axis of the diffusion chamber for $z = 5$ and 10 mm. The data is scaled to the maximum of each flow at $z = 5$ mm. The legend shows the flow per hole for each of the two operating holes in the configuration.

tance is a complex task. In the work done by van Hest *et al.* background pressure rather than flow was found to control the geometry of the plume and strong coupling between the ions and neutral gas flow was observed [109]. Figure 3.7 shows density data extracted from figure 3.6 (a) through (c) along the x axis for $z = 5$ mm (twin peaks) and $z =$ 10mm (single peak), scaled to the maximum value at $z = 5$ mm. In this case, and contrary to the results of van Hest *et al.* there is no difference in the radial profiles of the ion density. Although this is inconclusive without verification via a 2D fluid model of the system, it indicates a stronger reliance on ambipolar diffusion and weaker coupling between gas flow and ions in the plume than seen in [109].

3.3.2 Fitting and Reproducibility

Earlier in the chapter it was suggested that the plasma in the expansion chamber is a product of both diffusion from the hollow cathodes and the presence of an ambient plasma. To support this, reproductions of the expansion chamber plasma density in two and three active hollow cathode configurations are attempted using the data

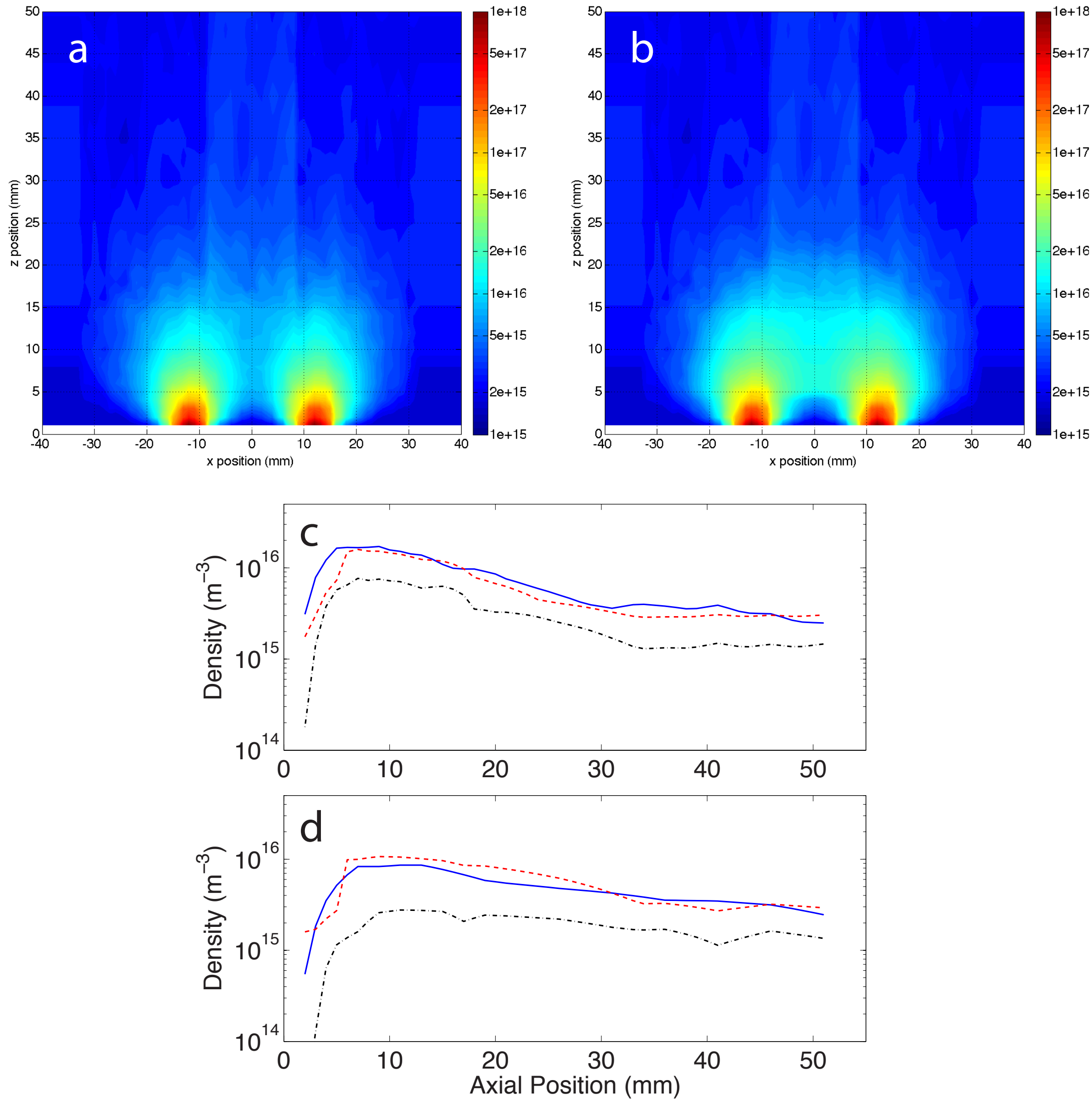

Figure 3.8: (a) Simple superposition of two single active hollow cathodes. (b) The same data as panel (a) but including a pressure dependent ambient plasma term. Panels (c) and (d) show Log-linear plots comparing measured data (blue solid line) and simulated data including an ambient term (red dashed line) and simple superposition (black dash-dotted line). Axial densities for $x = 0$ mm are presented. Panel (c) represents two holes separated by 22 mm and is the data used for the empirical fittings of the constants in the model. Panel (d) represents two holes separated by 33 mm using the same constants derived from (c) as a validation of the result.

measured for a single operational hollow cathode. The single plume measured in figure 3.2 is used as a building block to create a superposition of two single holes. Figure 3.8 (a) shows the result when adding the data from two of the single holes from figure 3.2 positioned at $x = -11, 11$ mm. Comparison with the measurements in figure 3.5 (b) show that this approach is too simplistic to account for the behaviour

observed experimentally.

To account for the ambient plasma in the chamber, it is assumed the density is proportional to the local pressure, and that pressure is proportional to distance from active hollow cathodes. The distance of each point in the simulated chamber from both active hollow cathodes is calculated and the enhancement to the density is weighted by the cumulative distance from both hollow cathodes d, where $d = \sqrt{x_1^2 + z_1^2} + \sqrt{x_2^2 + z_2^2}$, and (x_n, z_n) represents the distance from hollow cathode n. The simulated density at a specific point in the chamber given by equation 3.2

$$n_i(x,z) = \begin{cases} n_{superposition} + (1.4 \times 10^{16} - \frac{n_{peak}}{160} \cdot d) + \frac{n_{peak}}{700} & \text{if } \frac{n_{peak}}{160} \cdot d \leq 1.4 \times 10^{16} \\ n_{superposition} + \frac{n_{peak}}{700} & \text{if } \frac{n_{peak}}{160} \cdot d > 1.4 \times 10^{16} \end{cases} \tag{3.2}$$

The values of the constants in equation 3.2 are derived empirically. The term $n_{superposition}$ is the superposition of the single measured plume's densities, and n_{peak} is the maximum density recorded at the interface of a hole during operation. The second term, enclosed by parentheses, is a linear term that enhances the density based on the value of $d(x, z)$. Once this term becomes negative it is removed from the calculation as can be seen in the second part of equation 3.2. This says that as d becomes large, the pressure at that point is simply the ambient chamber pressure. The third term accounts for the slight increase in ambient density far from the holes caused when increasing the number of active holes from one to two as seen in figure 3.3.

Figure 3.8 (b) displays the same data as panel (a), but with this additional term to account for the ambient plasma present in the expansion chamber. This addition provides a much better fit to the measured data, and supports the suggestion that the measured density maps for multiple hollow cathodes are the combination of diffusing plasma and ambient plasma. Panel (c) compares the actual measured densities along z for $x = 0$ mm for this configuration with those acquired from panels (a) and (b). This serves to highlight the importance of the ambient plasma term in the fitting process. As a further check of the validity of this result, the same algorithm is applied to a second geometry, shown in figure 3.5 (c). The results are displayed in figure 3.8 (d), and there is also excellent agreement for this second

configuration. This provides further evidence for the presence of an ambient plasma term making a significant contribution to the chamber plasma density.

A limitation of this method is its restriction to two dimensions, as it can only account for active holes if they lie on a single axis. To increase the variety of the configurations that are possible as inputs, it is modified to represent a three dimensional system. The change is made by assuming azimuthal symmetry of a single plume. The two dimensional plume shown in figure 3.2 is rotated about the z-axis to produce a three dimensional plume. This plume is used in the same way as its two dimensional parent, and the method for calculating the ambient plasma term at each point is extended from two to three dimensions where $d = \sum_{n=1}^{N_{holes}} \sqrt{x_n^2 + y_n^2 + z_n^2}$, with new empirical constants selected. To test this three dimensional model of the chamber plasma, a 'slice' can be extracted to correspond to the two dimensional data taken for a three active hole configuration. Figure 3.9 compares the two, panel (a) shows the measured data and (b) the simulated data. The excellent agreement between the measured and simulated data confirms that the process is applicable for three dimensional geometries as expected. As such it is now possible to construct a three dimensional representation of the plasma density in the expansion chamber for an arbitrary arrangement of active hollow cathodes. Figure 3.9 (c) shows a cutaway of the three dimensional density profile for this system in the three hollow cathode configuration. The three dimensional representation is courtesy of Rhys Hawkins, and is created using the data set from with figure 3.9 (b) is taken.

3.4 Conclusion

This chapter provides an introduction to the basic operating mechanics of the DASH system. During breakdown the plasma ignites between the powered and grounded electrodes, before moving into the hollow cathode region. For stable operation a minimum power and flow are necessary, and these values are dependent on the fuel gas used. The expected density inside the hollow cathode is of the order of 10^{19} m^{-3}, and the density measured at the interface between source and expansion chamber

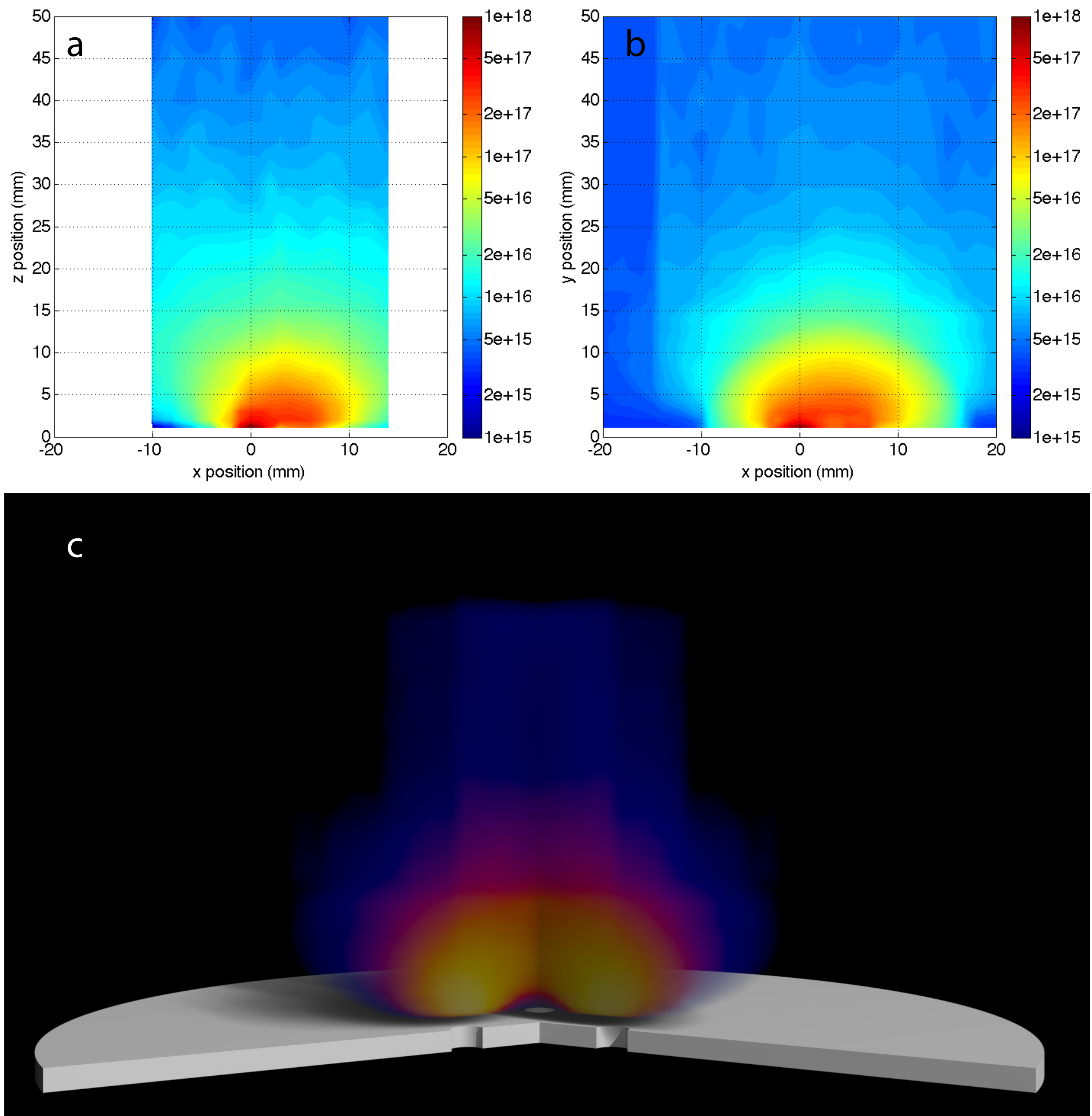

Figure 3.9: Comparison between: (a) measured data and (b) simulated data for a triangular, three active hollow cathode configuration. The measured data is taken using 33 sccm of argon and 33 W per hole. Panel (c) shows a cutaway of a three dimensional representation of this data.

is approximately 10^{18} m^{-3}. A background density level present far from the active hollow cathodes is measured to be 10^{14} m^{-3}.

It has been seen that the plasma in the expansion chamber consists of two parts. The plumes from the active hollow cathodes appear to be dominated by the diffusion of plasma from the DASH source. The ambient plasma created in the chamber is dependent on local pressure and is observed to dominate away from the interface between hollow cathode and chamber. Tests in two and three dimensions for verifi-

cation of this interpretation are produced and support this explanation of measured chamber ion density profiles.

Measured density distributions in the expansion chamber are reproduced by using the density map of a single hole as a building block. Superpositions of this single hollow cathode density map combined with an empirical ambient term to account for background plasma creation accurately reproduce measured data for both two and three dimensional configurations of active hollow cathodes. This means that fully three dimensional maps of the ion density can be calculated with confidence for an arbitrary number and configuration of active hollow cathodes. The process could be improved in future work by including a more rigorous term to describe the density of the ambient plasma in the expansion chamber.

4

Spatial Variation of the EEPF in a Hollow Cathode Plume

While investigating the basic operational parameters and mapping the plasma density in the expansion chamber provides useful insight into the DASH system's general behaviour, it doesn't probe the basic operating mechanisms of the hollow cathode itself. To understand more about the processes sustaining the discharge within an individual hollow cathode, the plasma potential, electron temperature, and the electron energy probability function (EEPF) can be investigated. Inelastic collisions between electrons and other particles are of crucial importance to understanding plasmas. This is due to the fact that collision cross sections are energy dependent (as discussed in chapter 1). For the sake of simplicity of chemistry, as well as analysis of the compensated Langmuir probe data, the experiments presented in this chapter are also performed in argon.

4.1 Experimental Design

To study the properties of the plasma produced in a single hole, the work presented in this chapter is performed with all but one hole blocked with alumina plugs. In contrast to chapter 3, the second iteration of the DASH source is used (see figure 2.2). In this configuration, the hollow cathode is 6 mm in diameter, but has an alumina sleeve that reduces its inner diameter to 4 mm. This configuration brings the DASH closer in design to the Pocket Rocket system that is its analogue.

Two probes are used in the acquisition of data: an emissive probe [110] and a compensated Langmuir probe [100], both of which are described in detail in chapter

2. Measurements of the EEPF and plasma potential in the plume of the DASH source are made along the x (horizontal) and z (perpendicular) axes, with the shaft of the probe aligned with the z axis, perpendicular to the face of the source. The point $z = 0$ mm is defined as the interface between the hole and chamber, and as in the previous chapter increasing z represents a position further from the hollow cathode. The Langmuir probe is operated with a 3 mm long tungsten tip with a 250 μm diameter. The tip is mostly oriented perpendicular to the shaft of the probe to increase spatial resolution along the z axis. The probe is connected via an isolation amplifier to an analogue differentiator to directly measure the first and second derivatives of the raw IV curves. The dynamic range is approximately three orders of magnitude, beyond which noise is significant. When measuring within the hollow cathode or at the orifice ($z \leq 1$ mm), the increase in noise changes the dynamic range to two orders of magnitude. It should be noted that the vertical axes on graphs displaying EEPFs is a natural logarithm. Each measured curve is averaged 50 times.

The Langmuir probe tip is swept from -80 to 80 V. Because the dimensions of the plume are similar to the probe, it is important to verify that the sweep is not disturbing the plasma during data acquisition. To monitor this a second (uncompensated) Langmuir probe is inserted into the expansion chamber as a witness probe. It is introduced through an auxiliary port allowing for translation in the x direction. Any significant perturbation to the plasma from the measurement probe will manifest in a change to the floating potential of the witness probe.

The measurement probe tip is positioned inside the plume at $(x, z) = (0, 2)$ mm with the witness probe approximately 7 mm away at $(x, z) = (6, 6)$ mm. Figure 4.1 shows the floating potential of the witness probe as the measurement probe is swept across the entire bias range several times. The vertical dashed line shows the plasma potential as measured with the emissive probe at $(x, z) = (0, 2)$ mm prior to the Langmuir probe test. While the measurement probe bias is below V_p, there is no significant distortion of the witness probe floating potential. However as the bias voltage on the measurement probe increases beyond V_p, the floating potential of the witness probe steadily increases, suggesting the measurement probe is affecting the

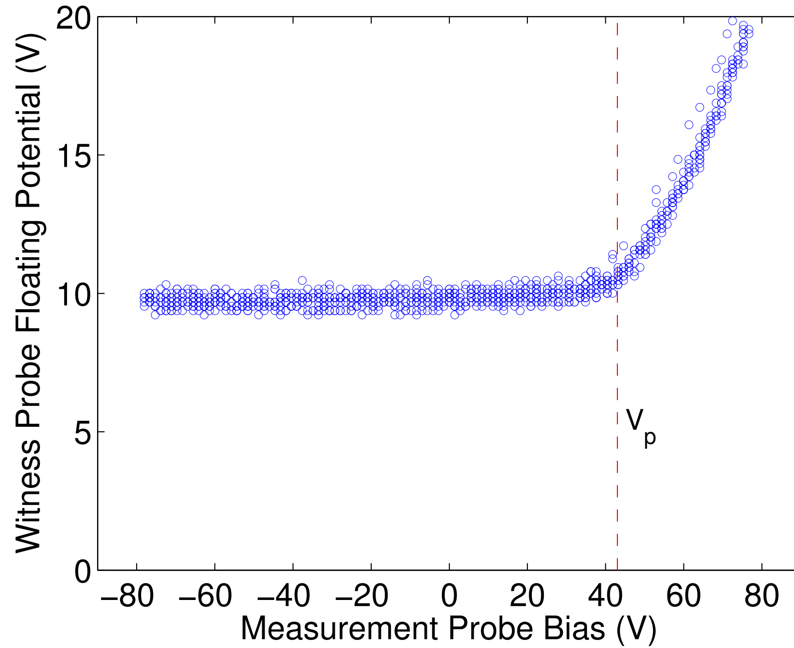

Figure 4.1: Floating potential measured by the witness Langmuir probe positioned at $(x, z) = (6, 6)$ mm as a function of bias voltage applied to the measurement Langmuir probe at $(0, 2)$ mm. The circles show individual measurements of the floating potential at points in the bias sweep over several ramps. The dashed vertical line denotes the plasma potential (43 V) previously measured with the emissive probe at $(x, z) = (0, 2)$ mm.

plasma plume. It is therefore reasonable to conclude that the EEPF data collected below V_p via the compensated Langmuir probe is unperturbed by the measurement itself. The region of the IV sweep above V_p is more prone to error and discounted from further consideration.

When the bias voltage on the measurement probe exceeds V_p, a strong electron current is drawn to the probe tip, producing a very dense and bright region of plasma. It is this process that is believed to be responsible for the increase in floating potential measured on the witness probe. This local increase in ionisation also has a significant effect on the current collected by the measurement probe above V_p, resulting in an obfuscation of the turning point in the EEPF. However, a measurement of the plasma potential via the EEPF can be obtained by observing the sharp change in the gradient of the second derivative of the IV curve when the parasitic region is present. For this reason the EEPFs presented further in the chapter lack a turning point, and the first few volts of the EEPF are to be neglected. Since this limitation occurs

outside the region of interest it is not considered further. The methodology described above is confirmed by comparing the compensated Langmuir probe measurements of V_p with those obtained with the emissive probe. The values of V_p are found to agree to within a few volts in all cases.

4.2 Variation in the EEPF Throughout Parameter Space

Chapter 3 and its corresponding publication show that both flow and power affect the spatial variation of ion density in the plasma plume [111]. In light of this, it is expected that the evolution of the energies of the electron population as a function of position will also be dependent on these parameters. Characterisation of the relationships between parameters is used to provide insight into the operation of a single hollow cathode in the DASH source.

Furthermore, making useful measurements of spatial variation requires that the other variable parameters in the system (in this case power and flow) remain constant to isolate the effects of changing the position of the probe tip. Because of this, it is necessary to select a power and flow at which all spatial data would be taken. To ensure that the selected point in parameter space gives consistent and repeatable results, measurements of the EEPF are made at a range of powers and flows to characterise the behaviour of the electron population in parameter space.

For a fixed flow rate of 25 sccm (and fixed pressure profile), varying power produces no significant difference in the shape of the EEPFs observed other than a change in density. Figure 4.2 shows EEPFs measured directly in front of the active hollow cathode at $(x, z) = (0, 6)$ mm for a flow of 25 sccm as the pre matching network applied power is swept from 30 to 80 W. All of the EEPFs manifest as a bi-Maxwellian distribution with a cooler low energy population and a hotter tail. The energy at which the temperature of the electron population changes will be referred to as the 'break' energy. For the low energy population below the break energy, the temperatures measured are all between 1.9 and 2.2 eV. For the hot tails, the electron temperatures were measured to be between 6.7 eV and 7.7 eV. It should

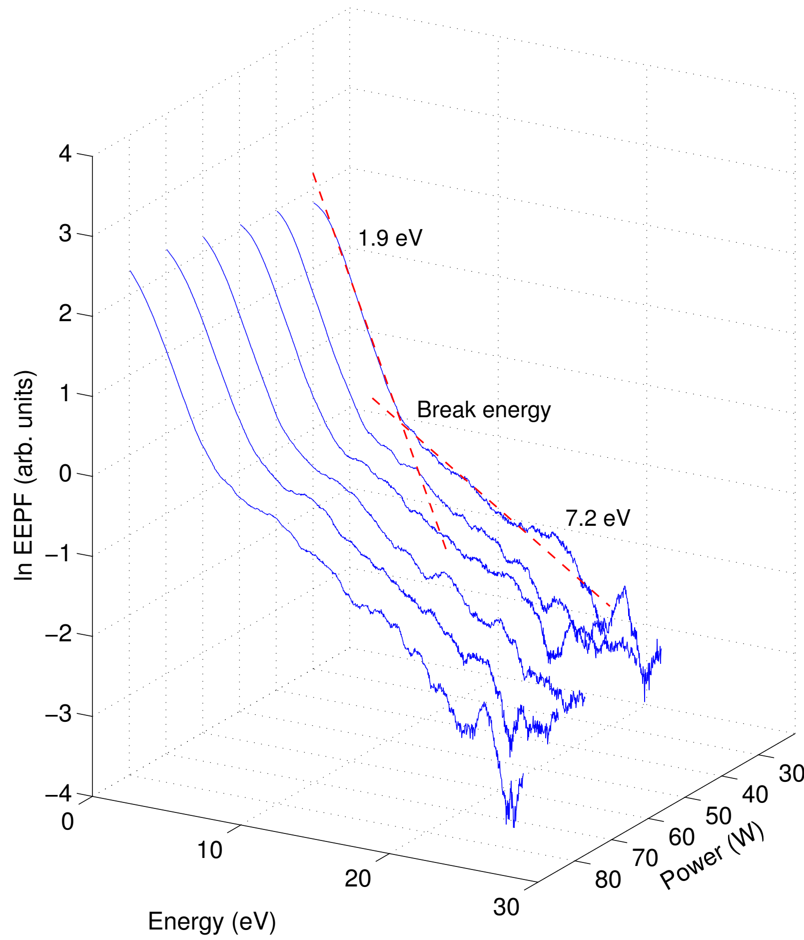

Figure 4.2: Compensated Langmuir probe measurements of EEPFs for varying power at a constant flow of 25 sccm at $(x, z) = (0, 6)$ mm. The dashed red lines show the two electron temperatures at 30 W: 1.9 eV at low energies and a hot tail of 7.2 eV. The point at which the temperature changes is referred to as the 'break' energy.

be noted that the dotted red lines are only a tool to guide the eye on the three dimensional plot. This agreement between the temperatures of each population is expected considering that electron temperature should not be affected by power as can be seen in the simple power balance equation [2]

$$P = en_0 u_B A_{\text{eff}} E_T \tag{4.1}$$

where P is the deposited power, n_0 is density, u_B the Bohm velocity, A_{eff} the effective

loss area of the plasma and E_T is the total energy lost per ion-electron pair exiting the plasma. Additionally, there is a proportionality between the applied power and density, as would also be expected from equation 4.1.

In contrast to the effect of varying the rf power, a change in flow (and consequently operating pressure) has a significant effect on the EEPFs obtained. Figure 4.3 (a) shows how the two temperatures of the bi-Maxwellian distribution change with flow increasing from 20 to 85 sccm, for 50 W of applied power. At 20 sccm of flow, the pressure in the plenum is 1.4 Torr and the chamber is 1.0 mTorr. Pressure increases linearly with flow up to 85 sccm, where the plenum is 3.1 Torr, and 5.9 mTorr in the chamber. The compensated Langmuir probe is again positioned at $(x, z) = (0, 6)$ mm. There are two noticeable trends in the evolution of the EEPFs with increasing flow. The first is the varying position of the break energy for the two temperatures. As the flow increases, the break energy decreases as shown by the dashed red lines in figure 4.3 (a), from 7.2 to 2.3 eV. The second trend is the variation in the temperatures of both populations of the EEPF. The temperature of the low energy portions of the EEPFs are all measured to be between 2.0 and 2.6 eV, increasing with increasing flow. However the hot part of the distribution has a strong dependence on the flow, displaying an inverse dependence. Figure 4.3 (b) shows the behaviour of the temperature of both the low energy and tail electrons explicitly. At 20 sccm, the tail is measured at 9.0 eV, with a low energy population temperature of 2.0 eV, by 85 sccm, the tail has fallen to 2.1 eV, where it is indistinguishable from the ambient plasma.

The position of the break energy is linked to the relative electron temperatures of the two electron populations. It can be explained by treating the observed EEPF as the sum of two distinct Maxwellian populations. It is seen that the temperature of the tail population decreases with increasing flow, while the low energy population remains stable. As the temperature of the second population of electrons decreases, there are more electrons at lower energies and fewer at higher energies, as can be qualitatively seen in figure 4.3 (a). The break energy will occur when there is a switch in the dominant population. The closer the temperatures of the two populations are, the lower this energy will be, explaining the inverse proportionality between

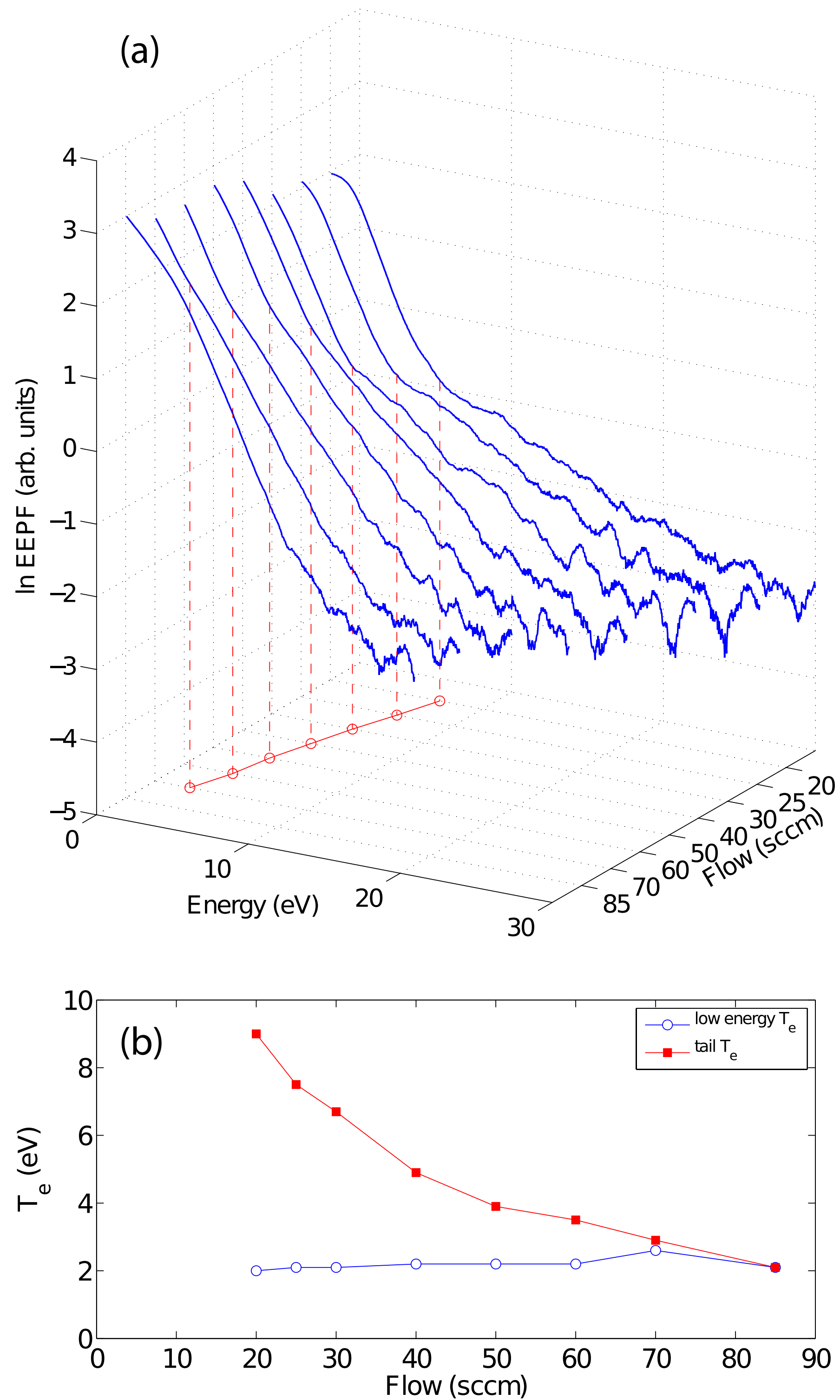

Figure 4.3: (a) Compensated Langmuir probe measurements of EEPFs at $(x, z) = (0, 6)$ mm for a power of 50 W and a flow from 20 to 85 sccm. The dashed red lines show the position at which the break energy occurs for each flow. (b) Variation in electron temperature as a function of flow for electrons below (open circles) and above (closed squares) the break energy.

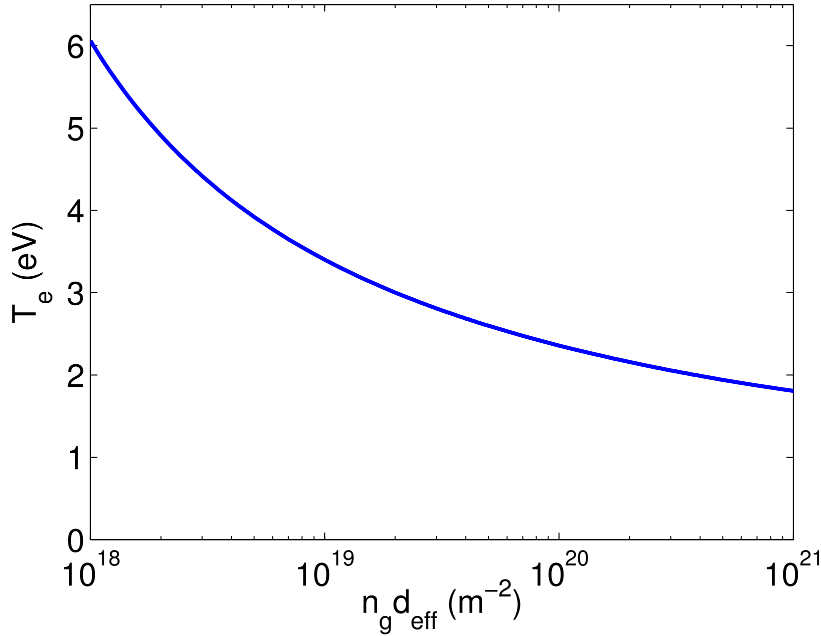

Figure 4.4: Electron temperature calculated for an arbitrary system using a simple particle balance with an inverse effective loss area of 0.5 m^{-2}.

flow and break energy. It is thought that the change in temperature of the tail is related to the pressure in the expansion chamber. Considering the two sections of the measured EEPFs, there is the 2 eV portion, produced in the source, and a hot tail, produced in the chamber. As such, a lower pressure in the chamber (caused by a reduction of flow in the system), produces a higher T_e, whereas the source is less sensitive to changes in flow due to its much higher pressure.

This sensitivity is highlighted in figure 4.4. The figure shows the results of a simple particle balance for an arbitrarily shaped system, calculated with an effective loss area of 0.5 m^2. It can be seen that for lower neutral gas densities, the electron temperature is much more sensitive to pressure. At higher pressures, the electron temperature is approximately $T_e = 2$ eV. This can explain why the electron temperature measured in the chamber is so dependent on the flow rate (and hence the expansion chamber pressure), whereas the electron temperature from the plasma produced in the hollow cathode is only weakly dependent on pressure.

4.3 Relationship of T$_e$ in the Source and V_p in the Plume

Given the results of the sweeps in parameter space, a flow of 25 sccm and a power of 50 W are used for the standard operating parameters for spatial measurements. These parameters give a plenum pressure of 1.6 Torr and a chamber pressure of 1.3 mTorr. The flow and power are selected to give strong signal to noise ratio and clear bi-Maxwellian behaviour in the plume. Based on previous experiments and the pressure profiles presented in chapter 2, the expected pressure in the plasma creation region is 1.1 Torr. The geometry of the system defines two distinct areas of operation, the source and the chamber. To fully understand the behaviour of electrons measured in the chamber, investigation of the electrons produced inside the hollow cathode is required. The electron temperature inside the active hollow cathode is measured with the Langmuir probe tip aligned parallel with the axis of the probe. This orientation is to allow for penetration of the hole with just the tip. Although this reduces the spatial precision of measurements made, it also reduces the impact of the probe on the flow of gas through the source by leaving the shaft outside the hole. It is worth noting that during these measurements there is no visible change to the plasma beyond what is expected as the bias voltage exceeds the plasma potential, and is therefore considered to remain undisturbed by the measurement.

The concept of a defined axial position for measurements made within the source is misleading since the extended probe tip is only one order of magnitude smaller in size than the hollow cathode itself. Because of this, the following 'positions' for the probe tip are measured: inserted completely, half the tip inside the source, and just the end of the tip inside the source. A single Maxwellian distribution is measured in all three cases, with temperatures of 2.0, 2.1, and 2.6 eV respectively. The disparity between the first two measurements and the third is expected to arise from the majority of the electrons being collected from the chamber rather than within the hole. This is because in the third position, most of the probe tip lies outside the hollow cathode, in the expansion chamber.

In chapter 3 it is seen that breakdown occurs inside the hole, between the powered electrode and ground plates, with pressures of the order of 1 Torr. Given the density of the plasma and geometry of the source, it is possible that Coulomb collisions between electrons are abundant enough to thermalise the electron population to a single temperature. The mean free path for Coulomb collisions inside the hole is calculated to be approximately 2 mm (the radius of the hole) for a density of 10^{19} m^{-3}. This is an order of magnitude higher than that measured outside the hole, but it is expected that there is a large density increase inside the source. Experiments performed in the 'Pocket Rocket' system showed ion saturation current measurements inside the source indicating an order of magnitude increase in density [92]. Assuming that the source successfully operates using the hollow cathode effect, it is probable that any population of hot secondary electrons driving the discharge is outside the dynamic range of the probe as the population will be very low in density relative to the 2 eV electrons [33, 112]. Irrespective of this, the 2 eV electrons dominate the measurement in this region, and will be treated as a Maxwellian in further analysis.

To validate the measurement, the following particle balance can be considered:

$$\frac{K_i(T_e)}{u_B(T_e)} = \frac{1}{n_g d_{\text{eff}}} \tag{4.2}$$

where K_i is the ionisation rate, u_B the Bohm velocity, n_g the neutral gas density, and d_{eff} the effective plasma size. The loss area is defined as a cylinder, open at both ends, with the dimensions of the hollow cathode as described chapter 2. Depending on the gas temperature used in the calculation, the calculated value for T_e is between 2.0 eV for a gas temperature of 300 K and 2.5 eV for a temperature of 1000 K [113]. This compares well with the measured values of the electron temperature inside the DASH source.

To complement these electron temperature measurements, emissive probe measurements of the plasma potential are made at a range of axial positions and flows. As described in chapter 2, emissive probe measurements have an error of ±2 V. Figure 4.5 shows that for all flows, there is a decrease in plasma potential from the exit of the hollow cathode to $z = 50$ mm downstream. There is also an inverse pro-

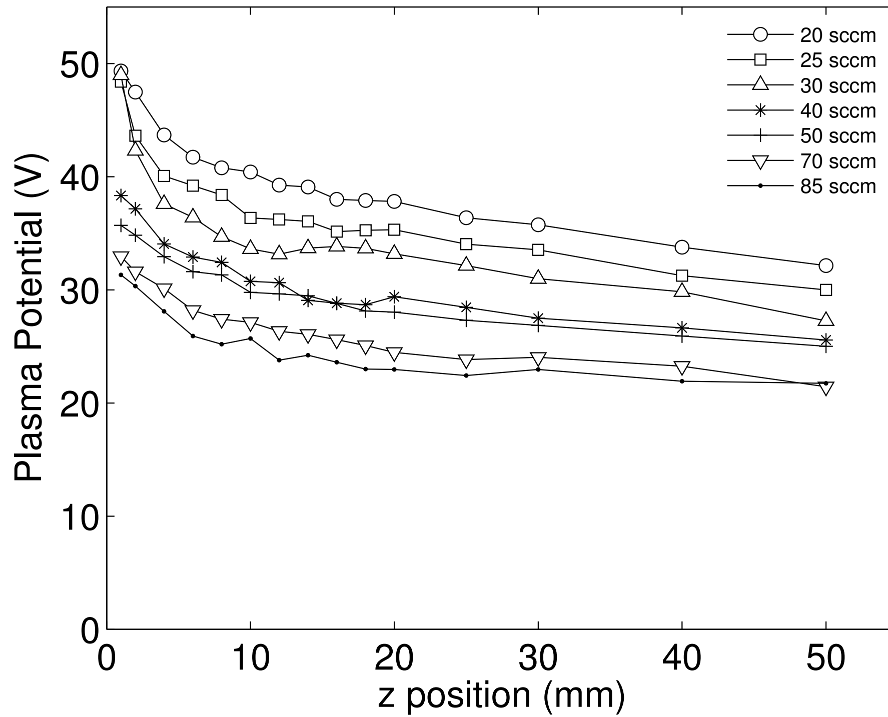

Figure 4.5: Emissive probe measurements of the plasma potential along the z axis at a range of flows of argon.

portionality between the flow (and pressure) of the system and the plasma potential in the plume. At the standard operating parameters for the spatial measurements of 25 sccm and 50 W, the plasma potential is measured to vary from 48 V at $z = 1$ mm down to 30 V at $z = 50$ mm.

The decrease in plasma potential within an expanding plasma has been well characterised in previous experiments, many dealing with plasma thrusters [114–117], and is often associated with the formation of a double layer. As the plasma expands, the density drops and if the electron temperature remains constant, the Boltzmann equation requires a reduction in the electric potential. The simplified Boltzmann equation on axis can be expressed as

$$n(z) = n_0 \exp(e\Delta V_p / kT_e) \tag{4.3}$$

assuming a Maxwellian electron energy distribution with temperature T_e, n_0 defines the source density, and $n(z)$ the density at a point on the z axis. Chapter 3 showed that the density of the plasma in the plume close to the exit of the DASH source

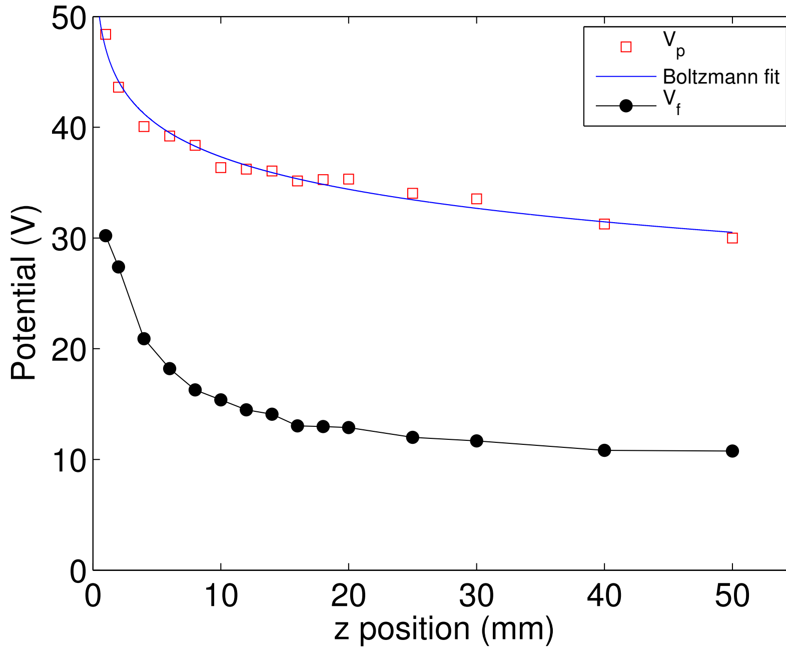

Figure 4.6: Emissive probe measurements of plasma potential (open squares) and floating potential (closed circles) for 25 sccm of argon and 50 W. A simplified Boltzmann equation (equation 4.3) is fitted to the plasma potential assuming a density decay of $n = n_0/z^2$, where n_0 is the density at the interface of hole and chamber.

decreases as a function n_0/z^2. Figure 4.6 shows a fit to the V_p measurements made with the emissive probe for 25 sccm and 50 W. Assuming a $1/z^2$ reduction in density, the value for T_e is deduced from the fit and calculated to be 2.1 eV. This agreement between Langmuir probe measurements, the particle balance, and the plasma potential gradient provides confidence in the methodologies used and the treatment of the source electrons as approximately Maxwellian.

In chapter 3 it is observed that the majority of the plasma near the exit of the source is created in the hole and diffuses into the vacuum chamber. As a result, the assumption of a single electron temperature in the Boltzmann equation is considered valid in spite of the bi-Maxwellian distributions measured in the chamber. This is because the relative density of electrons at 2 eV to electrons at the tail temperature will be very high. This assumption breaks down farther from the hole as plasma diffusing from the source becomes less dominant. However, the very good agreement between the value of T_e calculated from the plasma potential variation and the value measured with the Langmuir probe suggests the potential gradient that is measured

in the plume is the direct result of the free diffusion of plasma from the source.

The emissive probe is also used to measure the floating potential of the plasma. Figure 4.6 shows that variation in the floating potential follows the variation in the plasma potential. The data displayed in this instance is the floating potential for the 25 sccm case, although the same trend is observed at all flows. The floating potential varies from 30 V at $z = 1$ mm to 11 V at $z = 50$ mm and maintains a difference of approximately 18 V with the plasma potential throughout. This indicates that there should be fairly consistent electron temperatures throughout the plume, which is confirmed by subsequent Langmuir probe measurements, and highlighted in figure 4.7. Both the plasma and floating potentials drop over the course of the plume, which implies the presence of an electric field in this region that will act as a source of acceleration for ions and a retarding potential for electrons diffusing from the source.

In a simple treatment of a Maxwellian argon plasma, the floating and plasma potentials are separated by approximately $5.2\,T_e$ due to the ratio of masses between charged species [2]. The constant difference of 18 V measured between the two potentials implies a temperature of 3.5 eV, which falls between the electron temperatures of the two measured populations. In their work in [118], Goydak *et al.* considered the mean electron energy rather than temperature as they measured strongly non-Maxwellian populations of electrons. The same definition of mean energy is used here

$$\overline{u} = \frac{1}{n}\int_0^{30} u\,F(u)\,du \tag{4.4}$$

where n is the plasma density, u is the energy, $F(u)$ is the EEPF. The upper limit of the integral is set to 30 V, the cutoff at which the noise in the EEPF becomes too strong to distinguish a signal. Performing this calculation on the EEPF measured for 25 sccm and 50 W of power yields a mean electron energy of $\overline{u} = 4.2$ eV, much closer to the 3.8 eV expected from a simple treatment of the difference between the floating and plasma potentials.

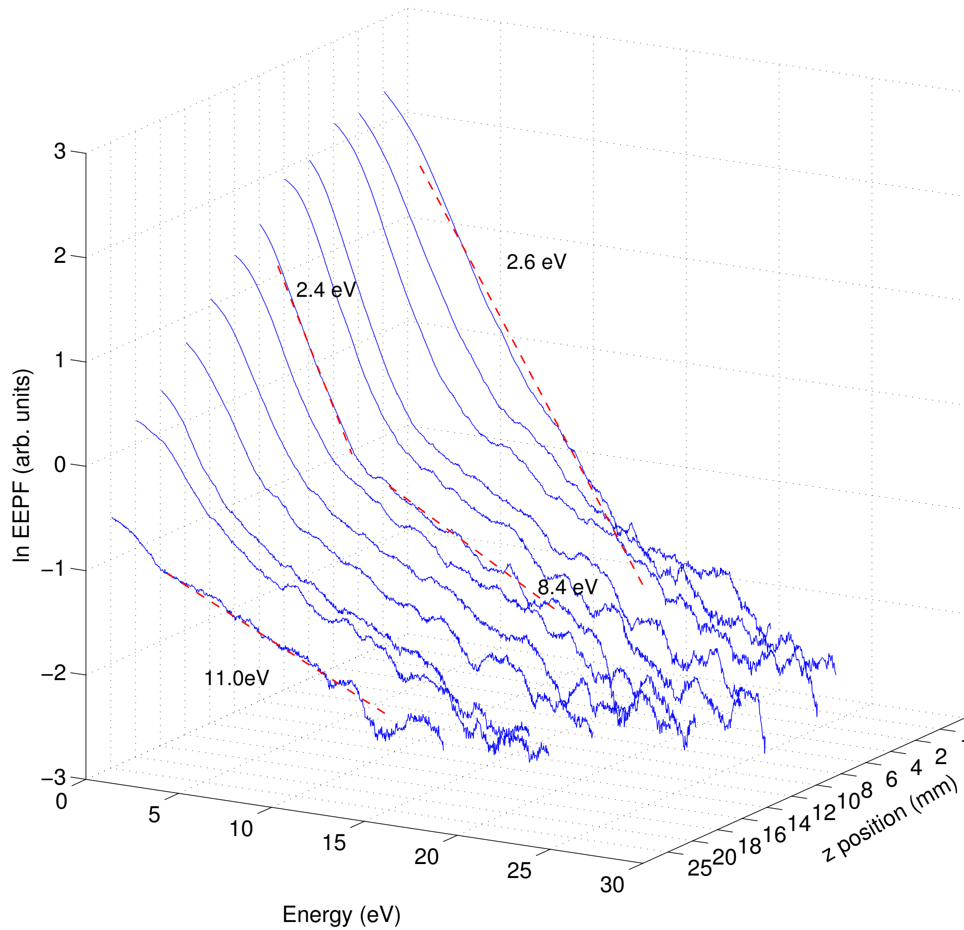

Figure 4.7: Measurements of the EEPF at a range of z axial positions for $x = 0$ mm at 25 sccm and 50 W. The z position axis is not drawn to scale. The dashed red lines show some of the electron temperatures measured at various z positions for both single and bi-Maxwellian distributions.

4.4 Spatially Resolved Langmuir Probe Measurements

4.4.1 Axial Measurements in the Expansion Chamber

The EEPFs collected in these experiments show significant differences from those collected in similar work done in less geometrically constricted systems, such as the expansion from a 15 cm diameter helicon source [100]. Typically for these sorts of experiments, the electrons below the break energy are hotter than those above it.

This occurs because the higher energy population of electrons is unrestricted by the potential barrier at the interface between source and expansion chamber. As such the higher energy electrons spend a portion of their lifetimes in the plume of the plasma, away from the heating region. By contrast the lower energy electrons are unable to overcome the potential barrier and are trapped in the source where they are constantly heated, increasing their temperature.

A different but self consistent trend in spatial evolution of the EEPF shape is observed in the DASH source for all flow and power regimes tested. Figure 4.7 shows an example of this at the standard operating parameters of 25 sccm of argon and 50 W of power. When the plasma diffuses into the chamber it initially has a Maxwellian structure, but by $z = 2$ mm it has developed into a bi-Maxwellian. The electrons exhibit the same characteristic behaviour seen in the parameter space sweeps with a low energy section at the same temperature as the plasma produced within the hole, and a hotter tail. As the plasma exits the source a single temperature of 2.6 eV is measured at $z = 1$ mm. From $z = 2$ mm, the low energy portion of the EEPF was measured to be between 2.0 eV and rises gradually to 3.0 eV by $z = 20$ mm. The temperature of the tail is measured to rise monotonically from 7.3 eV at $z = 2$ mm to 11.0 eV at $z = 25$ mm.

Two theories are presented as possible explanations for the evolution of these EEPFs in the plume. The first is based on data from chapter 3, and assumes significant ionisation occurs downstream in the expansion chamber. The local pressure in the expansion chamber decreases from around 160 to 1 mTorr with increasing distance from the source. If the hot tail is the result of ionisation in the chamber creating an ambient plasma, then the increase in temperature with position is likely a function of the pressure gradient in the chamber away from the source. To get an approximate idea of the expected electron temperature for plasma produced in this region, a second particle balance is considered using equation 4.2. The loss area and plasma volume terms reflect those of the six-way cross expansion chamber. For simplicity's sake, it is assumed that there is a uniform pressure in the expansion chamber, rather than trying to account for the spatial variations that occur. A chamber pressure of 1.3 mTorr and a gas temperature of 1000 K give an expected

value of $T_e = 9.1$ eV. This value lies in the middle of the range of temperatures measured for the tail in figure 4.7, which range from 7.3 to 11.0 eV. However it must be noted that at such low pressures the calculation is very sensitive to to both pressure and gas temperature. The temperature assumption of 1000 K is taken from work performed by Greig *et al.* in the Pocket Rocket system in argon [120].

The second possibility considered is that the axial evolution in shape of the EEPFs is caused by the redistribution of electrons driven by inelastic collisions within the plume. The crucial difference between these two explanations is the assumption of the size of the power deposition region. For the the ambient plasma case, the assumption made is that there is some heating mechanism in the chamber, possibly stray rf, sustaining a second plasma fuelled by neutral gas in the chamber. For the inelastic collision explanation, the assumption is that an insignificant amount of power is deposited in the chamber and no heating of electrons can occur. In this case no new energy can be added to the system, and can only be lost (via excitation) or redistributed (via excitation and ionisation). Because of its relative simplicity, the second explanation is investigated via a simple numerical simulation.

4.4.2 Iterative Model of an EEPF

An iterative model of the EEPF is used to investigate whether inelastic collisions within the plume could be responsible for the non-Maxwellian shape at a qualitative level. It is assumed for convenience that once particles have entered the chamber, they are excluded from reentering the source. Combining this with the assumption that the earth plates are completely effective in shielding the chamber from power deposition, there is no heating of expansion chamber electrons. Finally, the plume is assumed to be in a steady state temporally and flowing away from hole. This allows for a pseudo-spatial variation in one dimension by changing pressure from one iteration to the next rather than time. For each iteration the model recalculates the mean free paths for ionisation and excitation collisions based on pressure measurements presented in chapter 2.

The model starts with a Maxwellian distribution of electrons at 2.5 eV, which corresponds to measurements at $z = 1$ mm for 25 sccm and 50 W (figure 4.7). The

electrons are divided into bins of 0.01 eV and each bin has the number of ionising and exciting collisions undergone by its population determined by

$$N = \frac{dz \times \sigma(E)p(z)}{kT_g} \tag{4.5}$$

where N is the number of pre-existing electrons that undergo a collision (either ionising or exciting), dz is the spatial step over which the pressure is calculated, σ is the cross sectional area for that type of collision at a specific energy, p is the pressure at the specified axial position, and T_g is the temperature of the gas. Newly created electrons from ionisation events are arranged in a normal distribution around 5 eV and impacting electrons have their energies reduced by a corresponding amount. This is not a rigorous treatment of the newly created electrons [119], but is designed to promote the formation of the two temperature distribution measured in the chamber.

It is found that although these interactions do cause production of cooler, low energy electrons, the quantity in which this occurs is orders of magnitude too low to explain the measurements made in the plume. To enhance the production of low energy electrons, the reaction rates are artificially increased. While this is successful in producing a more significant population density of low energy electrons in the EEPF, the resulting depletion above the ionisation energy threshold ($E_i = 15.76$ eV) is significant. Due to the absence of an experimentally observed depletion above the ionisation threshold, it is determined that inelastic collisions do not dominate the formation of the EEPFs. Consequently, these results combined with the density measurements reported in chapter 3 suggest that the bi-Maxwellian shape observed is caused by power deposition in the expansion chamber sustaining an ambient, low density, high temperature plasma, rather than being caused by a redistribution of particles diffusing from the source.

Furthermore, for the same reasons discussed, the formation of the hot tail measured in the expansion chamber cannot be produced by inelastic collisions between very hot pendulum electrons from within the hollow cathode. The density of very hot electrons necessary to do this would imply that they should be visible on the Langmuir probe traces performed near the interface between the hollow cathode and

the expansion chamber. It should be noted however that this does not preclude this process from occurring at all, only that it cannot be the dominant process driving the bi-Mawellian nature of the measured EEPFs.

4.4.3 Lateral Measurements of EEPFs in the Plume

The Langmuir probe is translated laterally between $(x, z) = (0, 1)$ and $(8, 1)$ mm, with the corresponding EEPFs shown in figure 4.8. Centered over the hollow cathode at $x = 0$ mm, the EEPF appears to have only a single temperature at 2.5 eV, as is observed in the axial sweep, $x = 1$ mm also has a single temperature of 2.5 eV. By $x = 2$ mm, at the edge of the hole (diameter 4 mm), the EEPF has developed into the bi-Maxwellian profile characteristic of the plume. At this position, the low energy part of the plume drops to 2.1 eV, while the newly appeared hot tail is measured at 7.7 eV. For increasing x positions, the low energy part of the EEPF stays slightly above 2 eV, while the tail increases in temperature. By $x = 8$ mm, the low energy part of the EEPF has gone, leaving only a very weak signal dominated by the ambient chamber plasma, with a single temperature of 10.6 eV. Because of the proximity to the wall at $z = 1$ mm, beyond $x = 8$ mm, the density of the plasma is too low to collect an accurate EEPF measurement.

At this point it is useful to revisit figure 3.2 showing the density map of a single active hollow cathode taken with a Langmuir probe with 33 sccm of argon flow and 33 W. It is seen that in front of the hollow cathode at $(x, z) = (0, 1)$ mm, the ion density is peaked and decreases sharply with increasing x position. Between $x = 0$ and $x = 2$ mm (from the centre to edge of the hole), the density approximately ranges between 10^{18} and 10^{17} m^{-3}. By $x = 8$ mm, the limit of reading for the EEPFs, the density has dropped to its background level of approximately 10^{14} m^{-3}. Referring back to figure 4.7, it is seen that at $z = 25$ mm, there is only a single Maxwellian measured at the chamber temperature of 11.0 eV. By this point, the 2 eV electrons from the source have diffused to the point that they are no longer measurable in the EEPF. The ion density data in figure 3.2 shows that the points $(x, z) = (8, 1)$ and $(0, 25)$ mm have comparable densities.

The coincidence between the points at which density reaches its minimum value

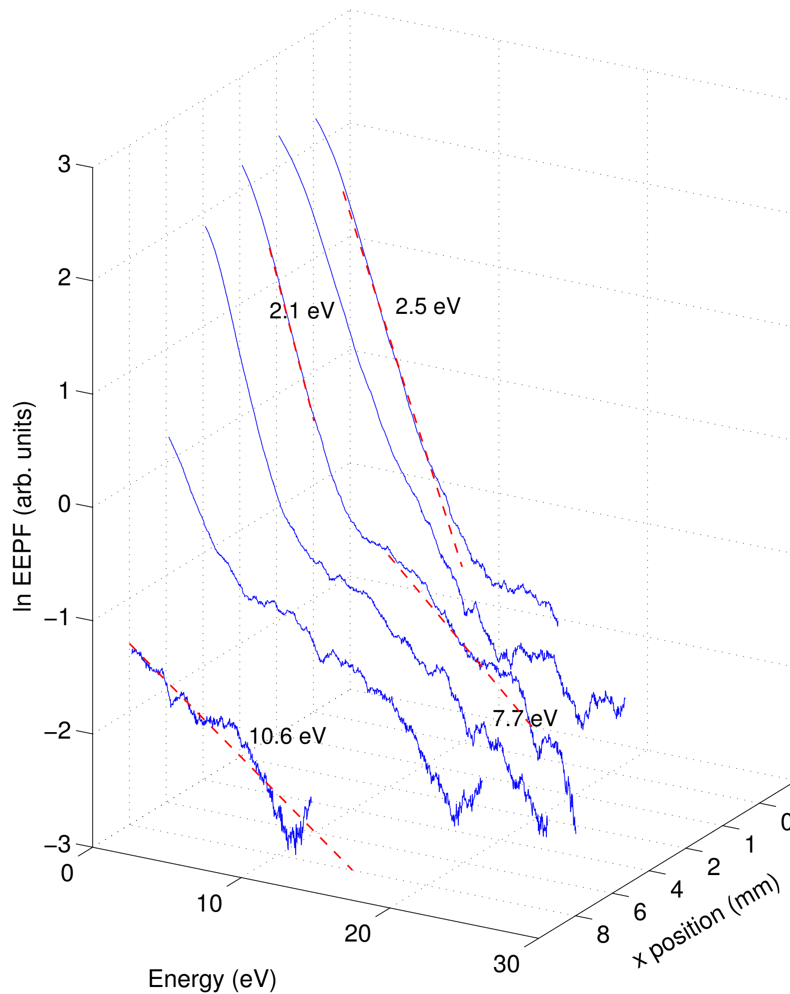

Figure 4.8: EEPF measurements at increasing x axial positions for $z = 2$ mm, 25 sccm of flow, and 50 W of power. The dashed red lines show electron temperatures for a range of x positions with both single and bi-Maxwellian distributions.

and the EEPF no longer contains electrons that have diffused from the source suggests the two phenomena are linked. Within a millimetre of the hole the plasma density is still high enough and in sufficient proximity to the source to retain the single Maxwellian. As the plasma diffuses, the density of the 2 eV plasma decreases and the ambient plasma becomes more visible in the EEPF. Further from the source, once the ambient plasma becomes the dominant component of the density; for example at $(x, z) = (0, 25)$ or $(8, 1)$ mm. As a result the 2 eV plasma is no longer visible in the EEPF because it is completely obscured by the ambient plasma. The

agreement between the evolution of ion density and EEPFs in both the axial and lateral directions supports the explanation that the EEPFs' hot tail is caused by the presence of a ambient plasma sustained in the expansion chamber.

4.5 Conclusion

Spatially resolved measurements of the EEPF in the plume of a single hollow cathode are made using a compensated Langmuir probe. Through this, the manner in which the EEPF changes with respect to both axial and lateral position is observed. It is found that plasma diffuses from the hollow cathode at a temperature of approximately 2 eV. This is confirmed by both direct measurement with the Langmuir probe, as well as by solving a particle balance equation for a single operational hollow cathode in the DASH source. Once in the chamber, the measured EEPF becomes a bi-Maxwellian distribution with 2 eV at low energies and a hot tail when varied in either the axial or lateral direction. Far from the hole the 2 eV electrons are no longer visible and only the hot tail remains. A simple numerical model based on the assumption that no power deposition occurs in the chamber rules out inelastic collisions in the expansion chamber causing the bi-Maxwellian profile. It is deduced that the hot tail in the EEPF is a result of an ambient plasma sustained in the chamber at a much lower density and higher electron temperature than the plasma created in the DASH source. This conclusion is in agreement with those derived from the two dimensional density maps presented in chapter 3.

5

Etching Silicon Using SF_6

One of the design goals of the DASH source is to produce reactive atomic species away from the target wafer for an isotropic chemical etch process. This chapter presents results exploring the production of atomic fluorine by DASH through observing etch rates, spatial uniformity and the isotropy of the resulting etches. These tests are performed using physical measurements of etch rates on a silicon wafer, Scanning Electron Microscope (SEM) imaging, and X-ray spectroscopy. A key concern of the design is its arbitrary scalability through the shower head configuration. This is addressed by extrapolating measured etch profiles into larger and more complex arrangements.

5.1 Experimental Design

To measure how effectively the DASH can perform the task of delivering atomic fluorine from a remote plasma source to a target, etch rates are measured on a series of wafers and wafer coupons of blank silicon. Each blank piece of silicon is masked by a second smaller piece, held mechanically against the surface of the target wafer using the wafer mount described in chapter 2. The silicon mask obscures part of the target wafer from the incident atomic fluorine and prevents any etching. This configuration produces a 'step' in the silicon at the boundary between etched and unetched regions of the wafer. Coupons are approximately 20 cm^2 in size and typically the mask covers between 40 and 50% of the coupon. Etch rates are measured by comparing the depth of this step with the time exposed. The depth of the step is measured with an α-step profilometer. Etch profiles across a wafer are achieved by making several profilometer measurements at different positions on an etched wafer. The

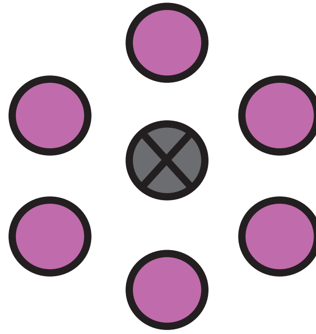

Figure 5.1: Illustration of the arrangement of the ring shaped arrangement of six active hollow cathodes used in the etching experiments. The central hollow cathode is blocked with an alumina plug and the surrounding hollow cathodes are active.

etch rates, profiles and SEM images presented in this chapter are performed using the 4 mm diameter DASH source, with exposed electrodes. However further testing using the 6 mm source with alumina and quartz inserts is also reported.

For SEM imaging and X-ray spectroscopy the silicon samples are prepared with a photoresist pattern. The positive photoresist is spun onto a wafer at a thickness of 1 μm. To pattern the resist conventional photolithographic techniques are employed. The mask has a series of circular holes of varying diameters arranged in gridded patterns.

For these experiments six hollow cathodes are operated simultaneously in a ring configuration, illustrated in figure 5.1. The width of the ring is varied in tests of etch profile uniformity and the diameter ranges from 12 to 70 mm. The SF_6 molecule can remove energy from the plasma via dissociation as well as ionisation. As a result, the production and sustainment of a dense discharge requires more power than when operating in argon, as mentioned in chapter 3. The applied power used in the etch measurements is often higher than in the argon characterisation of the source. This is to ensure that as much atomic fluorine is dissociated as possible. The maximum applied power is 500 W, the limit of the rf generator.

5.2 Measured Etch Rates and Isotropy

Figure 5.2 shows the variation in etch rate with power at an axial position of z = 3 cm. The total flow in the system is 85 sccm, meaning each active hollow cathode

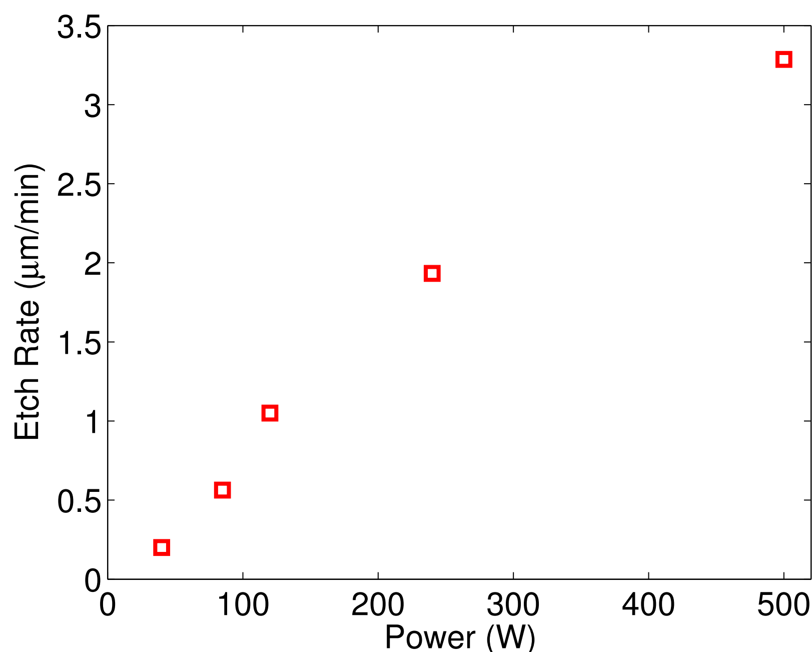

Figure 5.2: Variation of etch rate with applied power for a fixed flow of 85 sccm of SF_6. The wafer is positioned 3 cm in front of the DASH source that is using six active hollow cathodes.

is supplied with a flow of slightly over 14 sccm. This flow ensures stable operation of the hollow cathodes, as discussed in chapter 3. Figure 5.2 shows an approximately linear increase in the measured etch rate with increasing rf power. A maximum etch rate of 3.2 μm/min is observed at 500 W of applied power.

The etch rate is observed to vary only weakly with flow rate for a constant applied power. This can be explained by supposing that the level of dissociation of SF_6 molecules at the wafer surface is low. If this is the case, then varying the flow will only weakly affect fluorine atom density. This weak dependence would be associated with changes in the cross section for dissociation arising from variations in the electron temperature. In a system where dissociation were close to 100%, the limiting factor for fluorine atom production is the abundance of the parent SF_6 molecule, and strong variation could reasonably be expected.

To assess the suggestion that the fraction of SF_6 dissociated is low, the undirected flux of fluorine atoms necessary for achieving the maximum measured etch rate can be estimated. Assuming the simplest etching chemistry, $\mathrm{Si} + 4\,\mathrm{F} \longrightarrow \mathrm{SiF_4}$, covered in chapter 1, with a reaction rate between a fluorine atom and silicon atom of 20% [87],

an etch rate of 3.2 μm per minute can be used to calculate the flux of atomic fluorine arriving at the surface of the silicon wafer.

Taking the bond length for mono-crystalline silicon as 0.543 nm, the number of silicon atoms in a volume defined by a standard coupon size of 20 cm^2 that is 3.2 μm deep can be calculated to be $N_{Si} = 3.2 \times 10^{20}$. Due to the assumed reaction rate 6.4×10^{21} fluorine atoms must be incident on the surface over the course of a minute to achieve this etch rate. The effects of ion bombardment are ignored, as well as the more complex mechanisms by which chemical etching occurs. For the purposes of this calculation it is assumed that once four fluorine atoms arrive at the surface, one atom of silicon will be removed.

The flux of fluorine atoms to the surface of the wafer is defined by

$$\Gamma = \frac{1}{4} n \overline{v} \tag{5.1}$$

where n is the density of the incident particle (in this case fluorine) and $\overline{v}$ is the mean thermal velocity. Assuming the temperature of the atomic fluorine to be 700 K, the mean thermal velocity is defined by

$$\overline{v} = \sqrt{\frac{8 k_B T}{\pi m}} \tag{5.2}$$

where $m = 3 \times 10^{-26}$ kg is the mass of a fluorine atom, k_B is Boltzmann's constant, and $T = 700$ K. A temperature of 700 K is chosen in reference to the gas temperature measurements performed in argon and nitrogen by Greig *et al.* [120]. Solving for equations 5.1 and 5.2 yields a required density of fluorine atoms at the surface of the wafer to etch at 3.2 μm per minute. This density is calculated to be 2.8×10^{19} m^{-3}. Each molecule of SF_6 produces four fluorine atoms in this estimation ($SF_6 \longrightarrow SF_2 + 4\,F$), so the required density of SF_6 molecules is 7.1×10^{18} m^{-3}. Using the pressure measurements made in argon and described in chapter 2 as a guide, a pressure at the wafer surface of 50 mTorr is conservatively estimated. If the gas has not been ignited into a plasma, then this gives an SF_6 density of 1.6×10^{21} m^{-3}. As such, the fraction of the fuel gas estimated to still be dissociated by the time it reaches the wafer surface is approximately 0.4%.

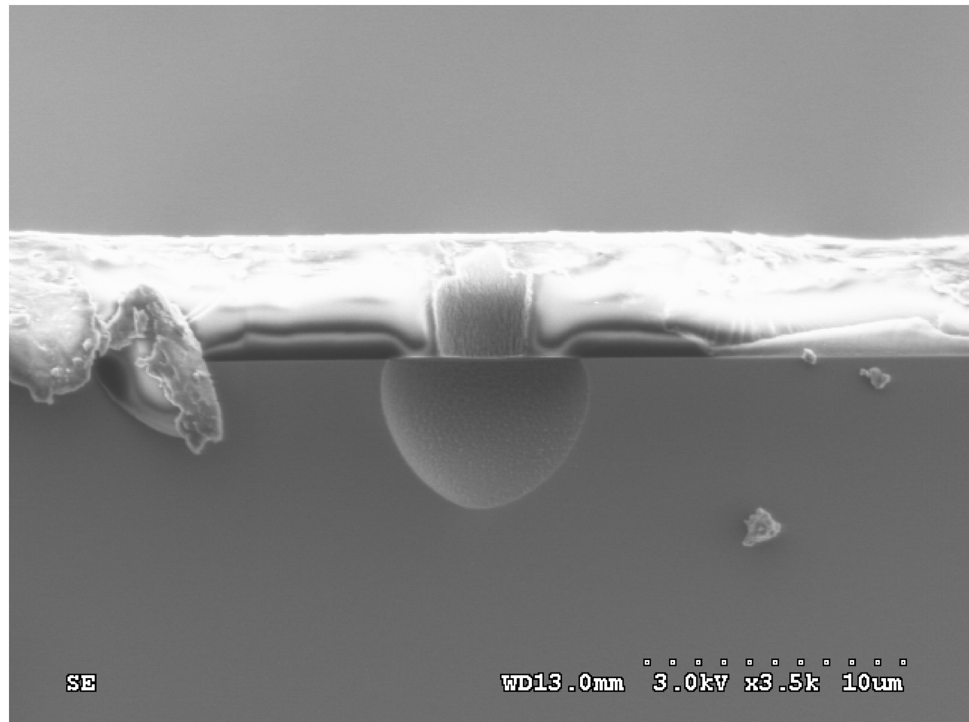

Figure 5.3: SEM image of an etch profile created in the DASH source. The wafer is masked with photoresist and exposes a circular region of silicon. The image clearly shows the isotropic nature of the etch.

This calculation supports the suggestion that a relatively low proportion of SF_6 is dissociated by the time it reaches the silicon wafer. As previously mentioned, this can explain why variations in applied power can have a strong impact on the measured etch rate, while variations in flow do not. To summarise, as power is increased the plasma density increases, and the collision frequency between electrons and neutral molecules will rise accordingly, increasing the density of atomic fluorine. By contrast, a change in flow will not alter the density of the dissociating electrons. As such, the collision frequency between electrons and neutrals will not change, and the density of atomic fluorine remains constant.

The isotropy of the etch process is observed by using a wafer masked with photoresist, cleaved, and placed in a SEM for imaging. Figure 5.3 shows an edge-on view of a sample prepared in the DASH system at a flow of 85 sccm and 150 W of power, exposed to the plasma for five minutes. The isotropic nature of the etch is clearly visible in the rounded side walls and the slight undercut of the photoresist. It is also worth noting that the photoresist is largely undamaged, further indicating

that few energetic ions are bombarding the wafer and high selectivity is maintained.

5.3 Spatial Variation in Etch Rates

Spatial variation of the etch rate in both the z and x directions are important for optimising the etching process in the DASH system. The closer the wafer is placed to the source, the higher the etch rate will be. However the closer the wafer is to the active hollow cathodes, the worse the effect of 'printing' will be. Printing is the transfer of the pattern of active hollow cathodes onto the wafer due to strong non-uniformity in the etch rate close to the source. To optimise the etching process, the distance between source and wafer, and the arrangement of hollow cathodes must maximise uniformity while maintaining the highest possible etch rate.

5.3.1 Axial Variation

The six active hollow cathodes are again configured in a compact ring, and the DASH source is supplied with a flow of 170 sccm of SF_6 and 250 W of power. By moving the wafer along the z axis with $x = 0$ mm, the distribution of atomic fluorine as it diffuses from the active holes is inferred [121]. Figure 5.4 shows the variation in etch rate at different axial positions in blue circles. The ambient etch rate is measured by placing small silicon coupons at a number of axial positions, but facing away from the source so that they are not affected by the expansion plume of plasma. The etch rates for these coupons can be seen as red squares in figure 5.4.

The peak etch rate observed when the wafer is 3 cm from the hole is just below 2 μm per minute, dropping to 0.25 μm per minute by $z = 25$ cm. Variation in the ambient etch rate is far less significant, and varies from 0.5 μm per minute down to 0.25 μm per minute. It can be seen in figure 5.4 that between $z = 0$ and $z = 10$ cm, the etch rate drops with a $1/z^2$ dependence, behaviour similar to that of the plasma density as measured in chapter 3. Beyond $z = 10$ cm the rate at which etching decreases slows, again in agreement with measurements of ion density performed in argon. This diffusive profile indicates that no significant quantity of fluorine is being produced in the plumes, which agrees with the inference from the

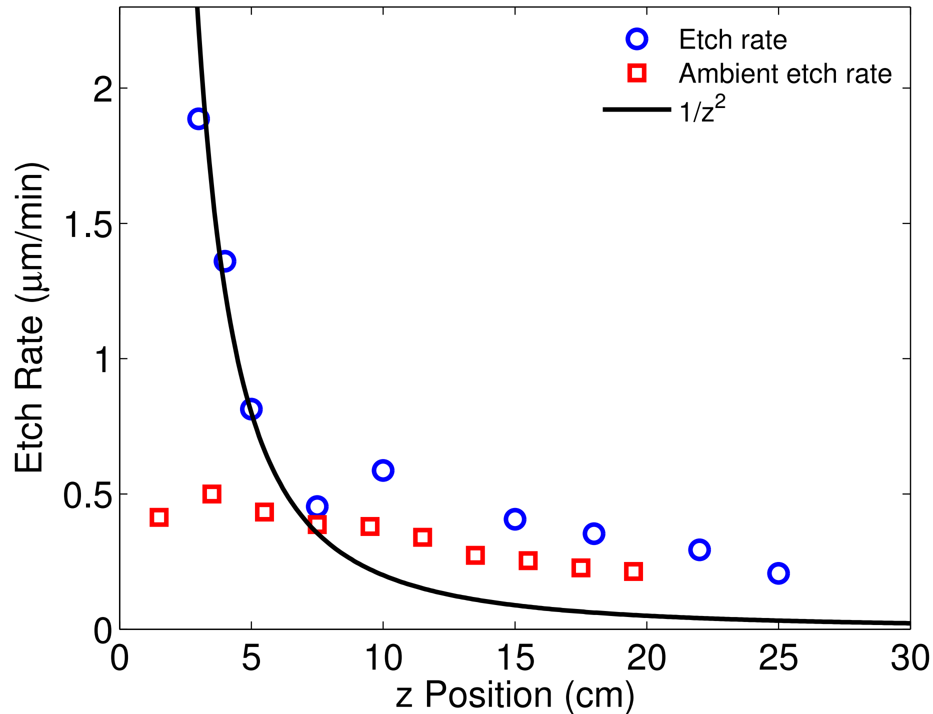

Figure 5.4: Axial variation of both total and ambient etch rate using 170 sccm of SF_6 and a power of 250 W in a six hole ring arrangement. Between $z = 0$ and $z = 10$ cm, the axial etch rate displays a $1/z^2$ trend.

measurements in argon that no ionisation occurs within the plumes. The point at which the decrease in etch rate diverges from a $1/z^2$ relationship coincides with the point at which the ambient etch rate crosses the $1/z^2$ line. The crossing of the $1/z^2$ line indicates a switch in the dominant production mechanism for atomic fluorine at that point. Just as with the density in the measurements made in argon, the downstream fluorine concentrations can be considered composed of two parts. They are fluorine diffusing from the hollow cathodes and fluorine created in the ambient plasma in the expansion chamber.

5.3.2 Etch Uniformity

Variation in etch rate in the x direction describes the uniformity of the etch rate across a wafer. Figure 5.5 shows etch rate profiles measured across three 150 mm wafers positioned at $z = 3$ cm as the ring of six active hollow cathodes is expanded. The wafers are too big to fit whole onto the profilometer, so they are cut and

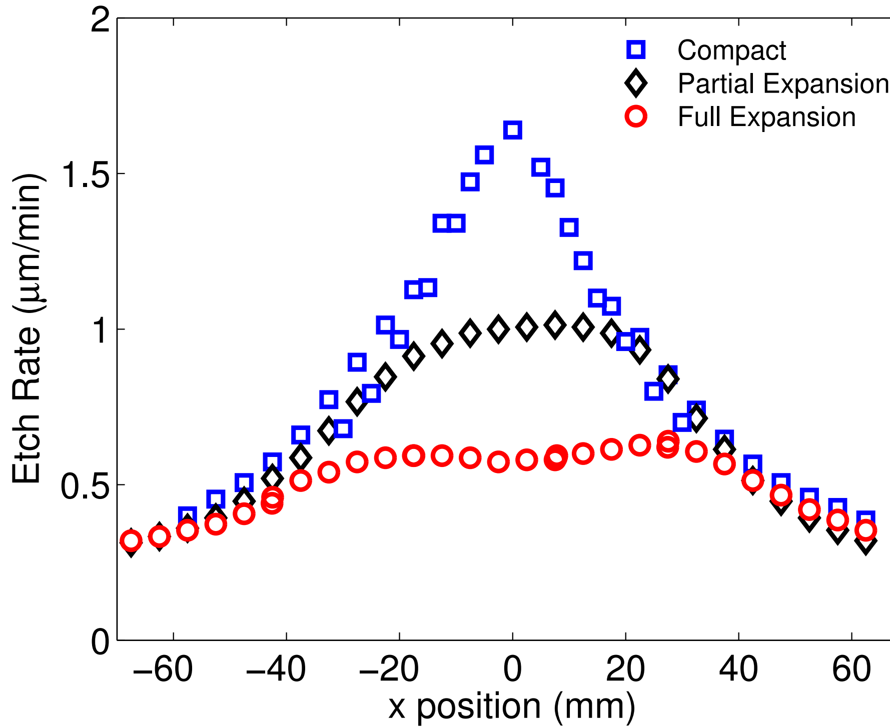

Figure 5.5: Etch rate profiles measured across three 150 mm wafers at $z = 3$ cm for the configurations of six active hollow cathodes. The sources is operated for 15 minutes with a flow of 170 sccm, and 250 W of power.

measured in sections, which is why some of the data points for each configuration are slightly offset from one another. The compact configuration of active hollow cathodes is the one described in figure 5.1. Partial expansion displaces the active hollow cathodes away from the centre by one hole. Full expansion separates the active hollow cathodes as much as the DASH source allows. The diameters of the three configurations are 12, 40, and 70 mm respectively.

For the compact configuration, the peak etch rate is measured at 1.7 μm per minute, and this occurs in the centre. For the partial expansion the peak etch rate is 1.0 μm per minute, also peaked in the centre. Finally for the full expansion the active hollow cathodes have become sufficiently separated that the peak in etch rate, 0.6 μm per minute occurs around $x = \pm 20$ mm. The minimum etch rate in every configuration is 0.3 μm per minute and found at the edges of the wafer. Furthermore this etch rate is found to be consistent across all three configurations.

To understand why the etch rate at the edges of the wafer is independent of active hollow cathode configuration, the geometry of the DASH is considered. The

diameter of the active part of the source is 89 mm (shown in chapter 2), and the largest distance between two hollow cathodes is 70 mm. The etch rate profiles for the three configuration start to merge at approximately $x = \pm 40$ mm, outside the plumes of the active hollow cathodes in any configuration. Therefore the agreement in etch rate at the extremities of the wafers can be attributed to the etching from the ambient plasma. Indeed the etch rate in these regions agrees well with the ambient etch rate displayed in figure 5.4.

Given that the ambient etch rate is so significant in the uniformity of the etch rate across the 150 mm wafer, it must be factored into consideration when comparing the uniformities. At a first glance the fully expanded geometry seems to offer the greatest uniformity, but this can be explained by recognising that it perturbs the ambient etch rate the least due to the distance between active hollow cathodes. The most important conclusion to be drawn from this data is that the spacing of the active hollow cathodes is critical to upscaling the design to an industrial sized wafer and plasma source.

5.4 Scaling

Part of the aim in designing the DASH source is to allow for arbitrary scaling of the design. To understand how the system might perform in a modern industrial system processing 300 mm wafers, the data presented in the previous section is used to validate a simulation. The etch profile for each active hollow cathode is placed in a linear superposition in much the same way as the empirical model presented in chapter 3. The etch profile from each active hollow cathode is treated as the sum of two gaussians. One gaussian represents the diffusion of fluorine from the active hollow cathode, and the second represents the slight increase in fluorine density expected on the edge of the plume. Finally a uniform background etch rate to account for the ambient plasma is added. The values describing the gaussians are fitted to the compact arrangement and the fit can be seen in figure 5.6 (a).

The model produces a two dimensional etch rate profile for an entire 300 mm wafer. To validate the model, the same method is applied to the two other configurations,

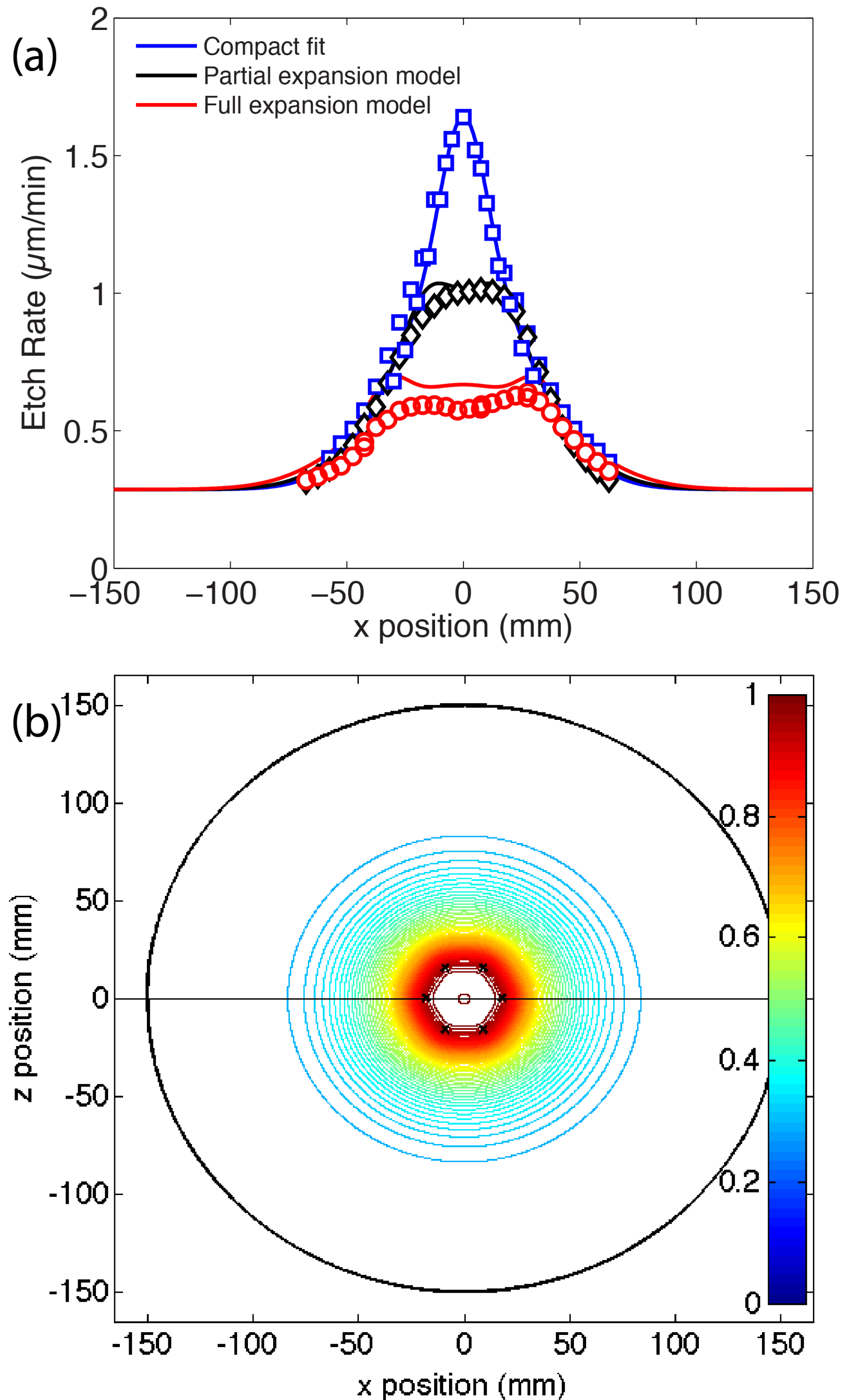

Figure 5.6: (a) Fit developed to match the measured the etch profile measured in the compact configuration. The partial and fully expanded etch rates are compared with their simulated counterparts (corresponding to the horizontal black line in (b). Panel (b) shows the two dimensional projection of the etch rate simulated for the partially expanded configuration onto a 300 mm wafer.

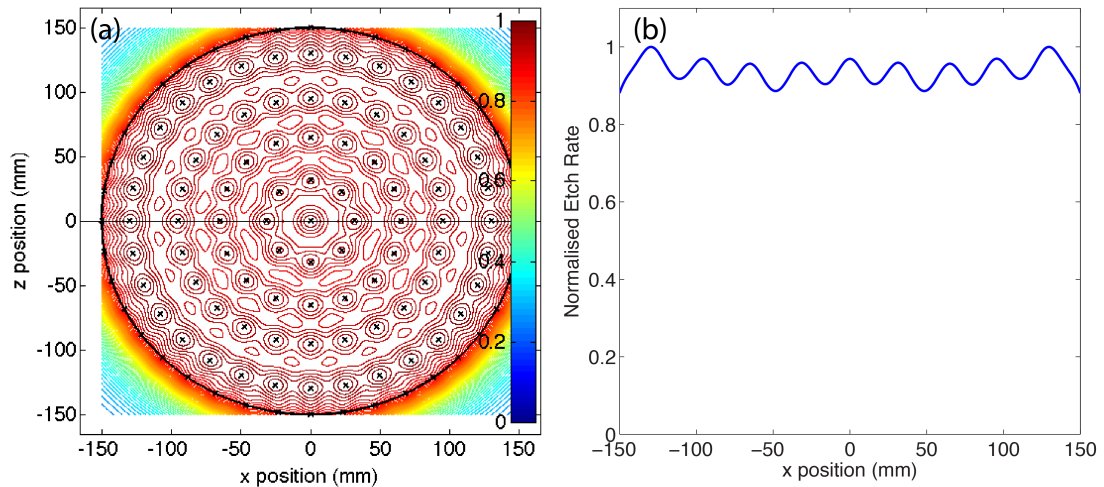

Figure 5.7: (a) Scaled model of array of concentric circles for hypothetical wafer of 300 mm diameter using 121 active holes (b) Predicted normalised etch rate for the 121 active hole array taken across the central line, shown in panel (a).

partially and fully expanded, and compared with the measured results. It can be seen that the simulation successfully reproduces the measured etch profiles. Figure 5.6 (b) shows the normalised results for the partially expanded configuration in two dimensions as projected onto a 300 mm wafer, outlined as a black circle. The positions of the active hollow cathodes are highlighted as black crosses. The values of etch rate along the horizontal black line across correspond to the measured data for the partially expanded configuration in panel (a). This validation of the model means that simulations of much larger arrays of active hollow cathodes' etch profiles over an entire wafer can be predicted with confidence.

Figure 5.7 (a) shows a simulated etch profile for a theoretical plasma source based on the DASH prototype for a 300 mm wafer. The configuration uses 121 active hollow cathodes. This would require approximately 3.5 L/s of SF_6 and an applied power of 5 kW, both of which are possible in an industrial setting. Additionally a more powerful vacuum system would be required to keep the expansion chamber pressure low. Figure 5.7 (b) shows the etch rate profile for the data presented in panel (a). The uniformity is predicted to be $\pm 5\%$. It is expected that by increasing the density of active holes the uniformity could be further increased, but this result is encouraging as a proof of concept for the design.

5.5 Aluminium Fluoride Deposition

After etching, it is sometimes observed that the DASH source has deposited a layer of aluminium fluoride onto the surface of the wafer. The presence of aluminium fluoride is a serious problem in the design of the DASH source with specific reference to chemical etching. The compound is inert and can completely block the etching process as well as contaminating the wafer it is deposited on. Figure 5.8 shows a photograph of a coupon after a five minute exposure to a 150 W and 85 sccm plasma. The film is clearly seen to be cracked and peeling back from the photoresist mask present on the wafer's surface. X-ray spectroscopy in the SEM is used to identify the dominant nuclei of both the peeling film and the surface beneath. The spectrum corresponding to point A in figure 5.8 shows strong peaks for aluminium, fluorine, and carbon. By contrast the spectrum for B shows only carbon, with trace amounts of other species. The carbon signal in both spectra can be attributed to the photoresist as it is an organic molecule. Since the aluminium fluoride film is thin, electrons can penetrate through and release X-rays from the photoresist beneath it. However the lack of any significant fluorine or aluminium signal in the spectrum of the photoresist confirms that the film is composed of aluminium and fluorine.

The thickness of the aluminium fluoride film deposited on the wafer is proportional to the time of exposure to the plasma. It does not bind well to the silicon or photoresist surfaces on which it is deposited, so direct measurements of the thickness are impossible. As an indirect measure, the strength of the aluminium and fluorine signals from the X-ray spectra of the films can be investigated instead. Three methods of valuing the strength of the spectral signal are used and all agree well. They are: k-ratio, peak area, and percentage of the atomic weight of the sample.

Figure 5.9 shows the peak heights for (a) aluminium and (b) fluorine of five coupons exposed for one, two, five, ten, and twenty minutes of a plasma with 150 W of power and 85 sccm of SF_6. The film of each sample is probed in three different locations on the coupon. It appears that aluminium fluoride deposition occurs but is quite slow during the first five minutes. Between five and twenty minutes of exposure the gradient of the slope of both aluminium and fluorine signal strength increases.

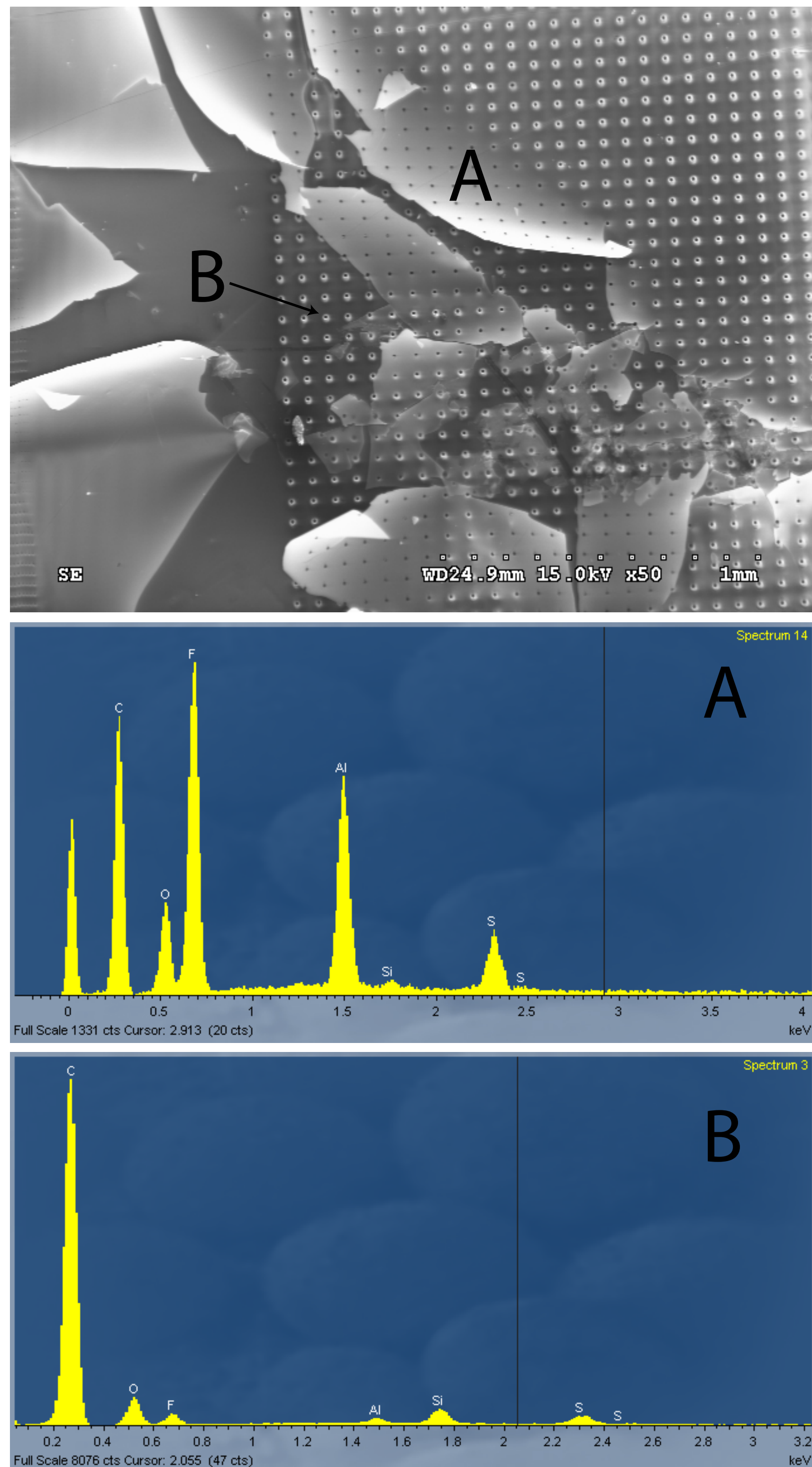

Figure 5.8: SEM image of aluminium fluoride film peeling from the photoresist mask of a silicon coupon. Point A and its corresponding X-ray spectrum shows strong peaks for aluminium, fluorine, and carbon in the deposited film. Point B shows only carbon emission in the photoresist spectrum.

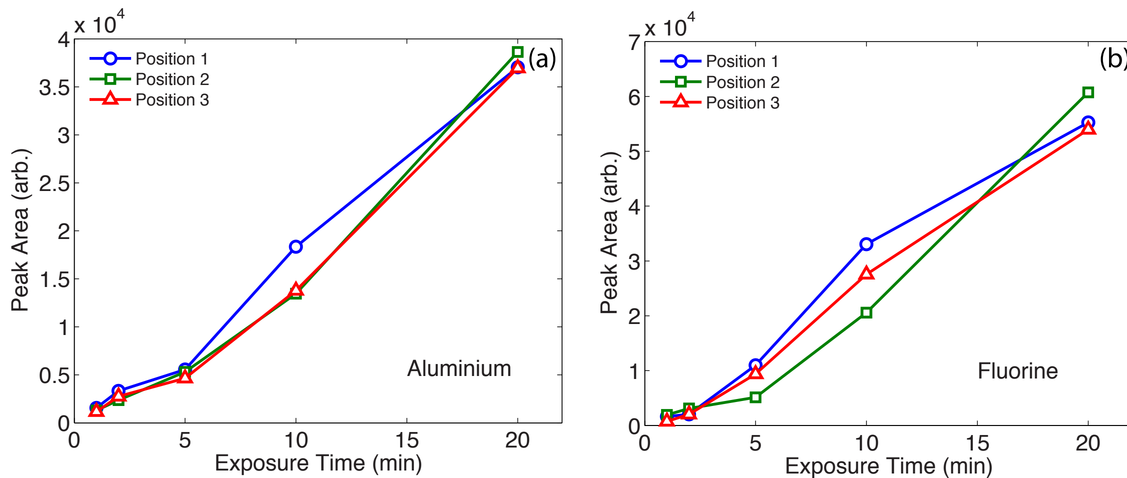

Figure 5.9: Evolution over time of the area of the aluminium and fluorine lines in the X-ray spectra acquired at three different locations on the film for each sample.

There are two sources of aluminium inside a hollow cathode from which the aluminium fluoride film could be developing. These are the pure aluminium powered and earthed electrodes, and the alumina insulators. To isolate which of the two is responsible for the production of the aluminium fluoride, the 4 mm source is substituted for the 6 mm source and individually tested with sleeves of both alumina and quartz. It is found that the use of an alumina sleeve greatly exacerbates the production of the aluminium fluoride film, while wafers etched with a quartz sleeve show no evidence of aluminium fluoride production or deposition. It is therefore suggested that the aluminium fluoride production is the result of the exposure of alumina to both the reactive fluorine atoms and the energetic ions bombarding the wall materials inside the hollow cathode.

After the plasma is extinguished, it is sometimes observed that the quartz sleeves glow orange due to the energy they absorb during longer exposures. A photograph taken looking at the hollow cathodes end on immediately after operation can be seen in figure 5.10. In the photo, three hollow cathodes are active due to the limited number of quartz sleeves available. Prior to taking the photo the plasma is run for five minutes with a power of 250 W and a flow of 60 sccm of SF_6. Using a blackbody radiation chart it is estimated from the colour of the sleeves that they are at a temperature of approximately 1200 K. If it is assumed that the sleeves' temperature is in a steady state after five minutes, and that all the energy deposited

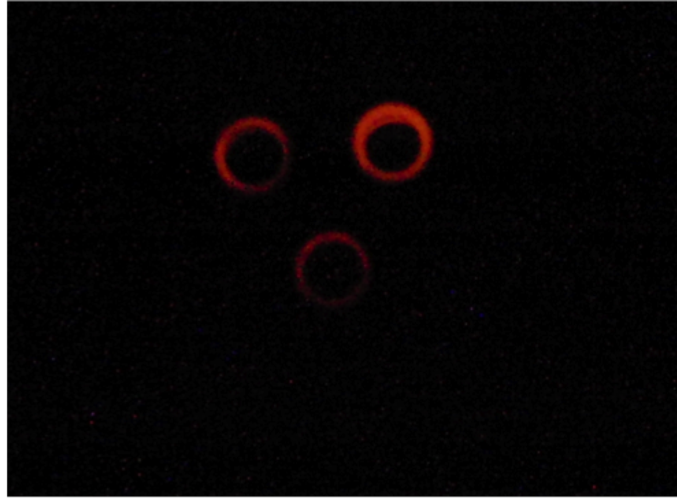

Figure 5.10: Photograph taken immediately after shutting off power to the plasma. The plasma is operated with three active hollow cathodes at 250 W and 60 sccm of SF_6 for five minutes.

in the sleeve is from ion bombardment, then an approximate ion flux to the interior surface of the sleeves can be estimated. A simple power balance representing the quartz sleeves is defined by

$$n_i u_i A e V_{rms} - \sigma T_s^4 \epsilon A - \frac{C_{SF_6} n_g (T_s - T_g)}{t_r} = 0 \tag{5.3}$$

The first term of equation 5.3 represents the energy gained by the sleeve due to ion flux from the plasma. Here n_i is the density of ions at the sheath edge, u_i is their speed after falling through the sheath, A is the loss area of the sleeves, and $V_{rms} = 350$ eV is the energy per ion taken from a typical measurement where $V_{rf} = 500$ V, with a DC offset of nearly 250 V. The second term of the LHS is the energy dissipated from the sleeves due to radiation, calculated via the Stefan-Boltzmann law and assuming the sleeves are perfect black bodies. The energy lost due to radiation is estimated to be approximately 43 W per hollow cathode. In this calculation $\sigma = 5.67\times10^{-8}$ is the Stefan-Boltzmann in SI units, T_s is the temperature of the sleeves, and $\epsilon = 1$ is the emissivity. The final term considers energy lost from the sleeves via convective heating of the neutral gas flowing through the hollow cathodes. Work performed by Greig *et al.* suggests that in a similar discharge, argon can be as hot as 1100K. Approximately half this heating is from the walls of the discharge [106, 120]. To estimate energy imparted from the sleeves to the

neutral gas the specific heat constant of SF_6 is taken to be $C_{SF_6} = 89$ J/(mol.K), the temperature of the gas is taken to be $T_g = 700K$, and the residence time $t_r = 100$ μs. The residence time is based on fluid modelling of gas flow in the Pocket Rocket system [106]. This yields an energy loss of approximately 7 W per hollow cathode from convection. Therefore the total energy lost from the sleeves via radiation and convective heating of the gas is estimated to be 152 W, and assuming these are the only energy loss mechanisms present gives a power deposition efficiency of around 60 % for the discharge.

Solving this energy balance for ion flux to the sleeve gives a value of $\Gamma = 2.5 \times 10^{21}$ $m^{-2}s^{-1}$, and an ion density at the sheath edge of $n_i = 8 \times 10^{16}$ m^{-3} assuming an average ion mass of 70 amu (SF_2). In turn this can be used to calculate a current of approximately 15 mA/cm^2 to the walls inside the hollow cathodes.

Despite its prevention of the formation of aluminium fluoride, the quartz sleeve is vulnerable to etching by the atomic fluorine inside the hollow cathode. This etching is enhanced next to the powered electrode, where ion bombardment during the negative part of the rf cycle is significant. After sustained use the quartz sleeve was cut in half by prolonged exposure to the discharge inside the hollow cathode. Based on the 1 mm sleeve wall thickness and the total time of operation before failure, it is estimated that the etch rate of the quartz in this region is approximately 10 to 15 μm per minute. As such, neither alumina nor quartz is a suitable dielectric sleeve to be used in the production of atomic fluorine in the DASH system. An ideal material suitable for further testing in this configuration is yet to be found, although boron nitride is a strong candidate.

5.6 Conclusion

The DASH source is found to be capable of producing reasonable chemical etch rates, as high as 3.2 μm per minute. It is expected that faster etch rates are possible with higher applied powers, however due to a lack of cooling apparatus for the electrodes, such high powers are unsustainable for more than a few minutes at a time. Pulsing the plasma provides another alternative to cooling the electrodes worth investigating

in future work. Variations in applied power are found to strongly affect the measured etch rate, while variations in flow are not. This is attributed to a relatively low degree of dissociation of SF_6 in the plasma.

By associating the measured etch rate with atomic fluorine density, it is found that the fluorine expanding from the hollow cathode follows a similar axial trend as the density maps performed in argon in chapter 3. The fluorine freely diffuses with a $1/z^2$ dependency before plateauing around $z = 10$ cm. This implies that operation in SF_6 produces an ambient plasma in the expansion chamber. The etch diverges from the $1/z^2$ trend at the point where the ambient etch rate in the chamber becomes higher than the expected etch rate from the diffusing fluorine, indicating a switch in dominant process.

By observing etch rate uniformity for different configurations of active hollow cathodes, a linear fitting algorithm is developed to accurately reproduce the measured etch profiles. The linear nature of the fitting allows for simulation of plasmas that the DASH source is incapable of producing, using more active hollow cathodes, power, and flow than are currently available. It is found that in a configuration using 121 active hollow cathodes that a 300 mm wafer could be etched with a uniformity of $\pm 5\%$.

Finally the alumina exposed to the SF_6 plasma is found to produce aluminium fluoride that is deposited on the wafer and blocks etching. This can be prevented with the insertion of a sleeve made of an aluminium free material, such as quartz. However, such a material must be naturally resistant to a harsh etching environment, which quartz is not. The quartz sleeves inserted failed after being completely etched through at the point of contact with the powered electrode. An etch rate of up to 15 μm per minute is estimated for the quartz, presumably enhanced by the very high energy bombarding ions, as well as very high densities of atomic fluorine inside the hollow cathode. A material such as boron nitride proves an interesting option for further development.

Gas Temperature Analysis Via Fulcher α Spectroscopy

The following two chapters discuss results from experiments in the Pocket Rocket source using hydrogen. As mentioned in chapter 1, the possibility of using a DASH styled plasma source for deposition is of interest. This necessitates study of the discharge in hydrogen, and at higher pressures than in chapters 3 to 5. These higher pressures require optical based diagnostics, and these techniques are the focus of the remaining results chapters.

Because hydrogen is diatomic, the emission spectrum from a hydrogen plasma contains not only lines from electronic excitation, but also bands from vibrational, and rotational excitations. The state of a molecule is described by a set of quantum numbers: n, v, J corresponding to the electronic, vibrational and rotational states. The rotational temperature of a state, T_{rot}, is a representation of the relative population densities of individual rotational states in a vibrational band and in certain circumstances can be equated to the gas temperature (sometimes called the translational temperature).

Hydrogen, and in particular the Fulcher α system, is well suited to molecular optical emission spectroscopy (OES) based analysis. This is because the branches of the the diatomic bands have emission lines that are in the visible spectrum, easy to resolve, and do not suffer strong interference from neighbouring lines. The Fulcher α system is the product of transition from the $d^3\Pi_u^-$ state to the $a^3\Sigma_g^+$ state, shown in figure 6.1. The Q branches ($\Delta N = 0$) of this transition are the most commonly measured due to their straightforward analysis. This work focusses on the Q branch of the $v' = 2$ to $v'' = 2$ transition in the Fulcher α series. The methodology of the

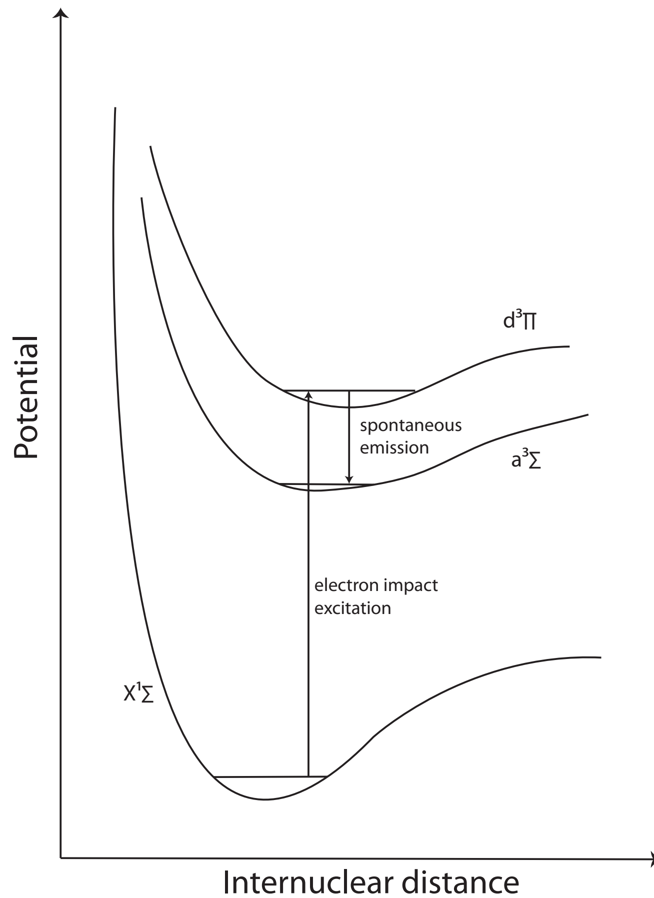

Figure 6.1: Potential diagram showing the excitation of the $d^3\Pi_u^-$ state from the $X^1\Sigma_g^+$ ground state via electron impact excitation. The excited level then decays in the Fulcher α system to the $a^3\Sigma_g^+$ state.

analysis of the raw data presented in this chapter loosely follows the work by de Graaf [122].

6.1 Experimental Design

For the optical techniques necessary to the experiments of the next two chapters, the Pocket Rocket source is used as an analogue to a single hollow cathode from the DASH source. The design of Pocket Rocket was introduced in chapter 2 and outlined the physical similarities between the two reactors. Like the DASH source, Pocket Rocket has an alumina sleeve with a central powered electrode adjacent to its outer wall, as well as earthed electrodes at either end. The difference between the two sources is the excellent optical access provided by Pocket Rocket. A window

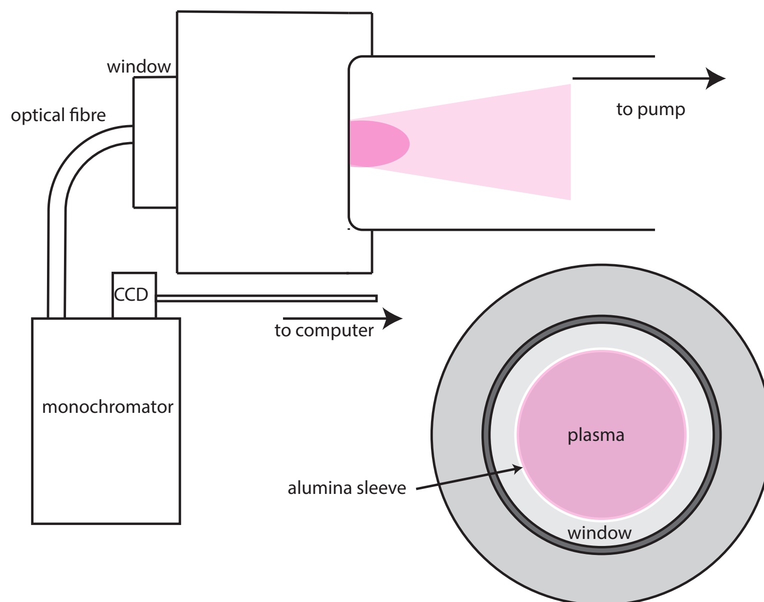

Figure 6.2: Sketch of the apparatus for the acquisition of the Fulcher bands showing a top down and end on view.

in the plenum allows optical access to the interior of the alumina sleeve from the rear. Additionally, the discharge expands into a glass tube, granting optical access to the plasma plume. These design features make the Pocket Rocket source an ideal system in which to perform the optical experiments required to understand the DASH source operation in hydrogen.

Pocket Rocket typically accepts powers of up to around 40 W before sustaining damage to the rf feed. In this experiment Baratron manometers are fitted to both the plenum and expansion chamber to monitor pressure on either side of the plasma creation region. Typically a pressure gradient of around a factor of about 2.5 is observed between plenum and expansion region. Local pressure measurements are made using a Pitot tube along the central axis of the expansion tube up to the orifice. No noticeable gradient in pressure is measured in this region, in contrast to Pitot tube measurements made on the DASH source that has a more vigorous pumping system.

Figure 6.2 shows the experimental set up for the acquisition of Fulcher emission. An optical fibre is mounted to the plenum window observing the plasma inside the hollow cathode. The fibre conveys the light to a SPEX500 monochromator equipped with a Garry3000 CCD array. The data acquired by this setup is averaged

both spatially and temporally, to provide a mean temperature for the entire plasma (including plasma that has diffused agasint gas flow into the plenum). Since the plasma is most dense within the hollow cathode, it emits light most strongly from the region adjacent to the driven electrode. Therefore the measured temperature is most likely the temperature in the centre of the hollow cathode.

The Garry3000 CCD array is calibrated for wavelength using a series of spectral lines identified in [123] as a reference and checking that the measured wavelengths match the reported values. The orientation of the CCD is checked by scanning the monochromator over the full width of the CCD's spectral range, 35 nm, and ensuring that the intensity of individual lines remained unchanged. During acquisition, data is averaged 30 times with individual exposures lasting $250, 500, 1000$ or 2000 ms depending on the intensity of the light being emitted. Owing to the nature of the measurement, the differing exposure times do not need to be compensated for when comparing data. This is a result of the fact that the temperature is extracted from the relative line strengths within a single scan. An example spectrum acquired using this technique can be seen in figure 6.3.

6.2 Assumptions and the Corona Phase

The total angular momentum of a molecule, $\vec{J}$ is defined by the quantum number J. Generally $\vec{J} = \vec{K} + \vec{S}$, where $\vec{K}$ is the total angular momentum excluding spin. The vector $\vec{K}$ can be defined by $\vec{K} = \vec{N} + \vec{\Lambda}$ where $\vec{N}$ is the angular momentum of the nuclear rotation and $\vec{\Lambda}$ is the component of the orbital angular momentum aligned with the internuclear axis. For a light molecule such as hydrogen, there is no coupling between the electron spin momentum and the internuclear axis. This is called a Hund's case (b), and is one of a set of coupling cases characterised by Hund [124]. The result of this uncoupled state is that the quantum number J can be replaced by K in the following calculations.

Equating the rotational temperature and translational temperature of an excited state is acceptable only if the rotational relaxation time and other processes involved in the redistribution of states is much shorter than the radiative lifetime. For the

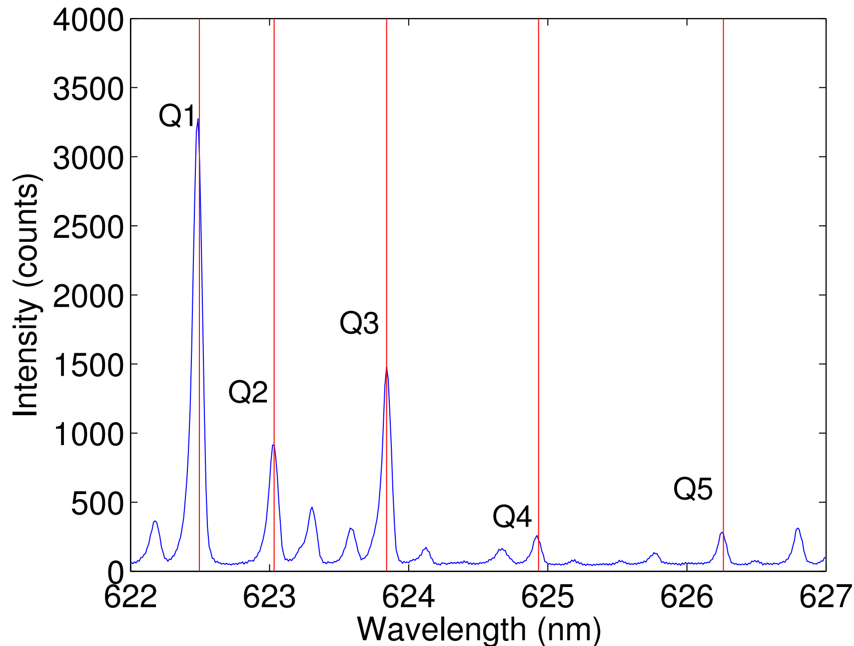

Figure 6.3: Example spectrum showing the first five lines of the Q branch of the $v' = 2$ to $v'' = 2$ transition of the Fulcher α system measured in Pocket Rocket.

Fulcher α system this is not a good assumption as the radiative lifetime of the $v = 2$ band of the $d^3\Pi_u^-$ state is measured to be 40 ns [125]. But by making further assumptions about the methods of population and destruction of excited states, the rotational temperature of the ground state may be inferred, and this can then be equated to the translational temperature. A typical set of assumptions used to estimate the ground state temperature are as follows [126]:

1. The rotational population of the $X^1\Sigma_g^+$ ground state obeys a Boltzmann distribution and is in equilibrium with the translational temperature.

2. The radiative lifetime of the excited states (40 ns) is much shorter than the relaxation time of the rotational levels, and is independent of quantum number.

3. Excitation from the ground state occurs without changing the rotational quantum number ($\Delta J = 0$). This means other allowed transitions such as $\Delta J = \pm 2, \pm 4$ are excluded from consideration. The implication of this is that rate coefficients of excitation are independent of rotational quantum number. Upon excitation the distribution of densities in the rotational ground state

will be preserved as the molecules move into excited states. This assumption will be discarded in later analysis.

4. These rate coefficients are suitable for use with the adiabatic approximation [127].

5. The population of the excited state is dominated by electron impact excitation from the ground state, and destruction is dominated by spontaneous emission to the $a^3\Sigma_g^+$ state. This is equivalent to the plasma being in corona equilibrium phase.

To justify the assumption that the plasma is in the corona equilibrium phase (assumption 1), the plasma density must be considered [128]. Van der Mullen describes a criterion for a hydrogen like molecule for which there is defined a principal quantum number of a state, p, given by [129]

$$p = Z\sqrt{\frac{R_y}{|E_{pi}|}} \tag{6.1}$$

where Z is the atomic number of the nucleus, R_y is the Rydberg constant, and E_{pi} is the ionisation energy from the level p. Considering the $d^3\Pi_u^-$ state, $Z = 1$, $R_y = 13.61$ eV, and $E_{pi} = 1.6$ eV, resulting in a value of $p = 2.9$. Van der Mullen then approximates a critical level, p_c, below which the corona equilibrium phase assumption is valid, whereas above it, the plasma suffers collisional de-excitation, also known as quenching [129]. The critical level is given by

$$n_e p_c = 9 \times 10^{23} \text{ m}^{-3} \tag{6.2}$$

In chapter 3 using argon and the same operating parameters, peak plasma densities of 10^{18} m^{-3} are measured using a Langmuir probe [111]. Considering the mass ratio between argon and hydrogen (molecular or atomic), the conservation of flux to the walls of the plasma implies a lower density in a hydrogen plasma for equal power and pressure. To ensure the validity of the calculation, the value of p_c is computed with $n_e = 10^{18}$ m^{-3}, yielding a result of $p_c = 4.59$. Since $p < p_c$ the assumption that the plasma is in the corona equilibrium is justified.

6.3 Emission intensity

The emission intensity for a molecular line can be expressed in a general form by [124]

$$I_{n'',v'',J''}^{n',v',J'} = \frac{64\pi\nu^3}{3h}\frac{1}{2J'+1}N_{n',v',J'}A_{n'',v'',J''}^{n',v',J'} \tag{6.3}$$

with units of photons $m^{-3}s^{-1}$. $N_{n',v',J'}$ represents the number density of the excited ro-vibrational state and $A_{n'',v'',J''}^{n',v',J'}$ represents the spontaneous emission (or Einstein) coefficient of the transition, controlled by the transition dipole moment, R. Finally ν represents the frequency of the transition. The Born-Oppenheimer approximation allows the dipole moment to be separated into three factors, expressed as [130]

$$R = \bar{R_e}^2 q_{v',v''} S_{J',J''} \tag{6.4}$$

where $\bar{R}_e^2$ is the electronic transition dipole moment, $q_{v',v''}$ is the Franck-Condon factor for the vibrational transition, and $S_{N',N''}$ is the rotational line strength, also known as the Hönl-London factor. The Franck-Condon approximation assumes that the variation in the electronic transition dipole is slow with respect to internuclear distance compared with vibrational eigenfunctions of the wave function. There has been some work performed to show that using the Franck-Condon approximation can lead to overestimation of the vibrational temperature, yet supports its use for calculations of rotational temperature in diagonal transitions [131].

Since all the transitions in a single set of rotational lines have the same vibrational transition, both the electronic transition dipole moment and the Franck-Condon factor can be assumed to be constant. The Hönl-London factors for a pure Hund's case (b) are given by [124]

$$\begin{aligned} S_{J,J+1} &= \frac{J}{2} && \text{(P-Branch)} \\ S_{J,J} &= \frac{2J+1}{2} && \text{(Q-Branch)} \\ S_{J,J-1} &= \frac{J+1}{2} && \text{(R-Branch)} \end{aligned} \tag{6.5}$$

Following this, the emission intensity of a line can now be written by combining equations 6.3, 6.4, and 6.5 as

$$I^{n',v',J'}_{n'',v'',J''} = \frac{64\pi\nu^3}{3h}\frac{1}{2J'+1}N_{n',v',J'}\bar{R_e}^2 q_{v',v''}S_{J',J''} \tag{6.6}$$

For the purposes of analysis of the spectral data obtained only the relative intensities of emission peaks are important. Additionally since the work performed measured emission from the Q-branch, there is no dependence on J. As such, all the terms that don't change in equation 6.6 can be absorbed into a single constant, giving

$$I^{n',v',J'}_{n'',v'',J''} = C\nu^3 N_{n',v',J'} \tag{6.7}$$

where C is a constant.

6.4 Rotational distributions and temperatures

The rotational distribution function for a vibrational band in thermal equilibrium can be described by the Boltzmann equation

$$f_J = \frac{g_I(2J+1)}{Q_r}\exp(-F(J)hc/k_B T_{rot}) \tag{6.8}$$

where g_I is the degeneracy due to nuclear spin, Q_r is the partition function, and $F(J)$ is the energy of the rotational state. The rotational levels are also degenerate by a factor $(2J+1)$, giving a total degeneracy of $g_I(2J+1)$. The term g_I is described by $(2I+1)$, either 3 or 1 depending on the rotational level. In the ground state, all even rotational levels are *para*-hydrogen ($I = 0$), giving $g_I = 1$. For odd levels, they are *ortho*-hydrogen, with $I = 1$, giving $g_I = 3$. Earlier it was discussed that for a pure Hund's case (b), the rotational number J could be equated to K, the quantum number describing the sum of the angular momentum of nuclear rotation and the angular momentum along the internuclear axis. As such, equation 6.8 can be rewritten as

$$f_K = \frac{g_I(2K+1)}{Q_r}\exp(-F(K)hc/k_B T_{rot}) \tag{6.9}$$

where Q_r, the partition function, is

$$Q_r = \sum_K g_I(2K+1)\exp(-F(K)hc/k_B T_{rot}) \tag{6.10}$$

The assumptions made regarding population of the $d^3\Pi_u^-$ state (specifically that $\Delta K = 0$) imply that the density of rotational states in a vibrational band is an undisturbed reproduction of the distribution in the $X^1\Sigma_g^+$ ground state. However, this is valid only at higher temperatures. Below 1000 K, the error this assumption introduces are significant [122]. If it is accepted that the distribution of densities in the excited state is not a replica of the ground state, then some method must be employed to infer the ground state density distribution from the excited state. This is achieved by considering the following equation describing the population of the $d^3\Pi_u^-$ state from the $X^1\Sigma_g^+$ state

$$f'_{rot}(K') = \sum_K^0 R_{K^0K'} f^0_{rot}(K^0) \tag{6.11}$$

where K^0 represents a rotational level in the ground state. $R_{K^0K'}$ is a coefficient describing the proportion of molecules from the ground rotational state K^0 that have transferred to the excited state K'. In his work, de Graaf has calculated these coefficients and they are displayed in table 6.1

Generally the transition where $\Delta K = 0$ is the most populous, in concordance with the assumption 3. However it can be seen from table 6.1 that molecules whose rotational state does change are more likely to be excited to a higher rather than a lower rotational state. The result of this is an overpopulation of higher rotational

	$K'=1$	$K'=2$	$K'=3$	$K'=4$	$K'=5$	$K'=6$
$K^0=0$	0.760	0.122	0.101	0.014	$< 10^{-4}$	$< 10^{-4}$
$K^0=1$	0.416	0.423	0.079	0.005	0.007	$< 10^{-4}$
$K^0=2$	0.130	0.407	0.345	0.066	0.044	0.006
$K^0=3$	0.033	0.147	0.402	0.309	0.061	0.040
$K^0=4$	0.010	0.036	0.163	0.401	0.290	0.058
$K^0=5$	0.001	0.013	0.038	0.219	0.400	0.277

Table 6.1: Coefficients of change to differing rotational states [122].

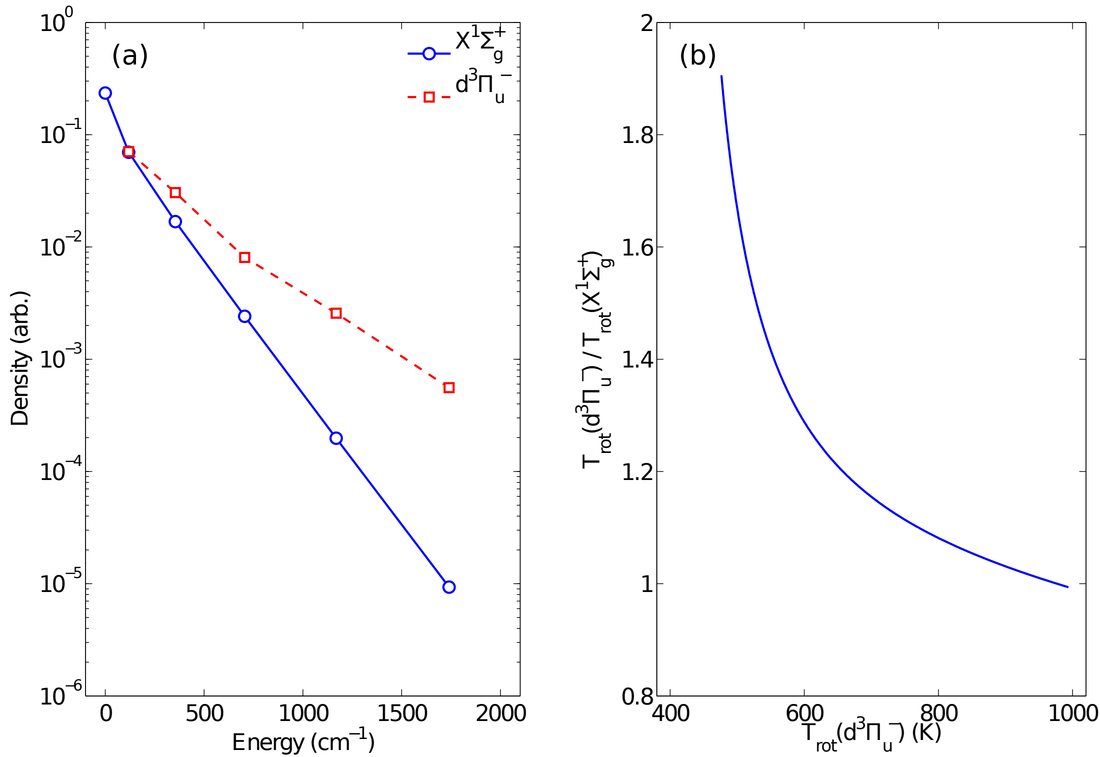

Figure 6.4: (a) The Boltzmann plot of the ground state and the $d^3\Pi_u^-$ state for a temperature of 272K. At this temperature the effect of overpopulation of the higher rotational levels is clearly visible. (b) Shows the ratio of the temperature as measured from a linear fit to the excited state relative to the ground state as a function of the measured temperature of the excited state.

states relative to the rotational distribution of the ground electronic state. If it is assumed that the excited state distribution of rotational state densities is a replica of the ground state, this can lead to overestimations of the rotational temperature of the ground state of 50% or greater. This overpopulation manifests itself in a hollowing of the Boltzmann distribution, an example of this is shown in figure 6.4 (a), where a ground state distribution for a temperature of 272 K has been converted to the excited state using the constants in table 6.1.

To compensate for this overestimation, de Graaf proposes two possible solutions [122]. The first and more complex is to use these constants to predict the relative line strengths of the emission, and search iteratively for the temperature that most closely predicts the observed spectrum. The second, and simpler method is to use a linear Boltzmann fit on the observed intensities and calculate a rotational

temperature, then modify the calculated temperature to reflect the overestimation of temperature of the ground state. To facilitate this process, a simulation of the excitation of a range of distributions with varying ground state temperatures to the $d^3\Pi_u^-$ state using the values from table 6.1 is performed. The variation of observed temperature in the excited state as a ratio to ground state for a measured temperature in the excited state can be seen in figure 6.4 (b). This plot enables the temperature in the $X^1\Sigma_g^+$ state to be directly inferred from a measurement of the temperature in the excited state. The general process for the calculation of the rotational temperature of the $X^1\Sigma_g^+$ state from the emission from the transition from the $d^3\Pi_u^-$ state to the $a^3\Sigma_g^+$ state can be summarised as follows:

1. Obtain the emission intensities from the Q branch of the $v' = 2 \rightarrow v'' = 2$ transition of the Fulcher α spectrum via the monochromator and CCD array.

2. Using equations 6.7 and 6.9, derive the relative density of each state. By plotting them against the energy of the ground state levels an overestimated value for the rotational temperature of the ground state can be derived.

3. Use an interpolation of the data presented in figure 6.4 (b) to calculate the actual ground state temperature from the measured temperature from the $d^3\Pi_u^-$ state emission.

Figure 6.5 shows an example of actual data acquired from Pocket Rocket, from which it can be observed that the Q1 and Q5 lines are above the linear fit, while the Q3 line lies below. This occurs in all the data sets acquired and is a direct result of these transitions between the $X^1\Sigma_g^+$ state and the $d^3\Pi_u^-$ state where $\Delta K \neq 0$.

6.5 Results

The measurements of gas temperature made in this experiment are intended to accompany the high speed phase resolved optical emission spectroscopy (PROES) measurements made on the same system. Furthermore, they form an essential input to future experiments in the DASH system using Lyman α absorption spectroscopy. To this end, the same set of positions in the available parameter space are examined

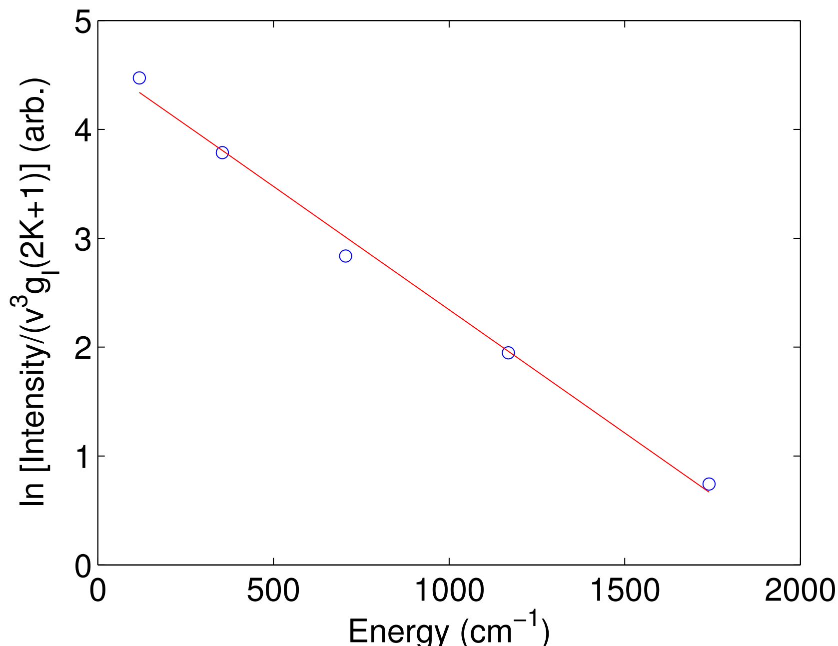

Figure 6.5: Example temperature calculation for a measurement made in the Pocket Rocket apparatus. Because of the hollowing of the excited state due to overpopulation of the higher rotational levels, the Q1 and Q5 points lie above the line of best fit, while Q3 lies below it.

with both techniques. Measurements are made at a range of pressures and powers to investigate the effects of variation in operating parameters on the gas temperature. The plasma produced in Pocket Rocket is observed to change operational modes, with no observable hysteresis, for a given pressure/power product of approximately 11 Torr.W. The two modes are named: the diffuse mode (below 11 Torr.W), and the bright mode (above 11 Torr.W) after their respective appearances. The temperature near the mode change is observed with more resolution in terms of operational parameters.

6.5.1 Parameter Sweeps

By virtue of its size, the Pocket Rocket system is unable to sustain a plasma with a power density above 40 W for more than a few seconds in CW mode without risking serious damage to the rf feed system. In hydrogen, the discharge is more difficult to ignite and sustain than in a heavier gas such as argon because of the relative ion masses and their effect on the Bohm velocity. As such the available operational

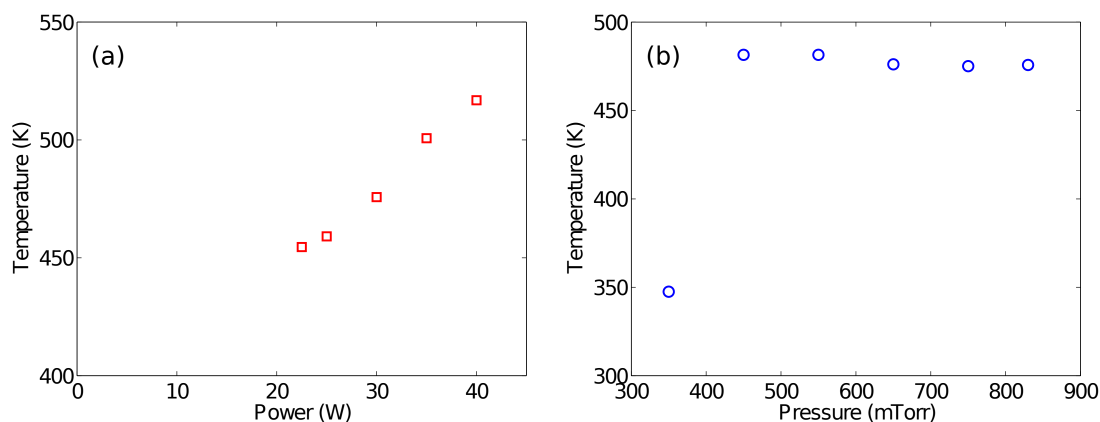

Figure 6.6: (a) Variation of ground state rotational temperature with power from 20 to 40 W. (b) Variation of temperature with the pressure value as measured in the expansion chamber for an applied power of 25 W.

window for power is 20 to 40 W. The mass flow controller allowing hydrogen to pass through the system has a range of 0 to 500 sccm. This gives an operational pressure range of 350 to 830 mTorr in the expansion chamber. Pressure in the plenum was consistently around 2.5 times the pressure of the expansion chamber. Based on the pressure data presented in chapter 2, it is expected the pressure in the plasma creation region is approximately halfway between the two values. The variation of the rotational temperature of the ground state with power for a pressure of 830 mTorr can be seen in figure 6.6 (a). The power sweep is performed at the maximum available pressure. The variation of temperature with pressure for a fixed power of 25 W can be seen in figure 6.6 (b). This power is selected as it is high enough to ensure repeatable results without unnecessary heating of the Pocket Rocket source, avoiding the risk of damage.

Figure 6.6 (a) demonstrates the gas temperature has a linear proportionality to applied power. At 22.5 W, just above the point of ignition, the gas temperature is measured to be 455 K, climbing to 519 K at the maximum applied power of 40 W. The increase of temperature with power makes intuitive sense. Higher power will result in an increase in plasma density, which in turn will cause a greater number of charge exchange collisions between ionised species and neutral hydrogen, heating the gas.

Figure 6.6 (b) shows the two modes of operation of the source. At 350 mTorr, the

plasma is in its low brightness mode (referred to as the diffuse mode, based on its appearance in the expansion chamber). At this pressure and a power of 25 W, the parameters fall below the mode transition threshold of 11 Torr.W. The emission in the diffuse mode is much weaker and also appears to result in a temperature around 100 K lower than in the bright mode. Once in the bright mode, the temperature of the gas is seen to stay constant with all five measurements reading between 475 and 481 K. The profile of the pressure sweep indicates that the electron density rather than the electron temperature controls the gas temperature, since the temperature changes strongly with power and is constant with pressure. It is reasonable to expect based on the work presented in chapter 4 that large changes in pressure in the DASH system would result in a significant change in the electron temperature. Since the temperature remains stable in the bright mode for different flows, it appears the role of the electron temperature in the neutral gas heating process can be discounted. In turn this suggests that chemical processes involving electrons are not contributing heavily to the heating of the gas, since these reactions are strongly dependent on electron temperature.

6.5.2 Mode Transition

To investigate the mode transition in more detail, the power and pressure are varied in smaller increments around the threshold value of 11 Torr.W, referenced to the expansion tube pressure. The power sweep is performed at the minimum pressure of 350 mTorr, as this caused the transition to occur between 30 and 32.5 W, which lies in the middle of the available applied power range. The pressure sweep is performed with a power of 25 W as this is the standard used in the earlier experiments. The power sweep covering the mode transition can be seen in figure 6.7 (a), and the pressure sweep can be seen in figure 6.7 (b).

Figure 6.7 (a) shows a continuation of the trend observed in the broad power sweep in that the temperature increases with power. However, by encapsulating the mode transition the linearity of the relationship is lost. Based on the conclusion that electron density is dominating the gas temperature, the data in panel (a) indicates that while density increases in both modes with applied power, the change from

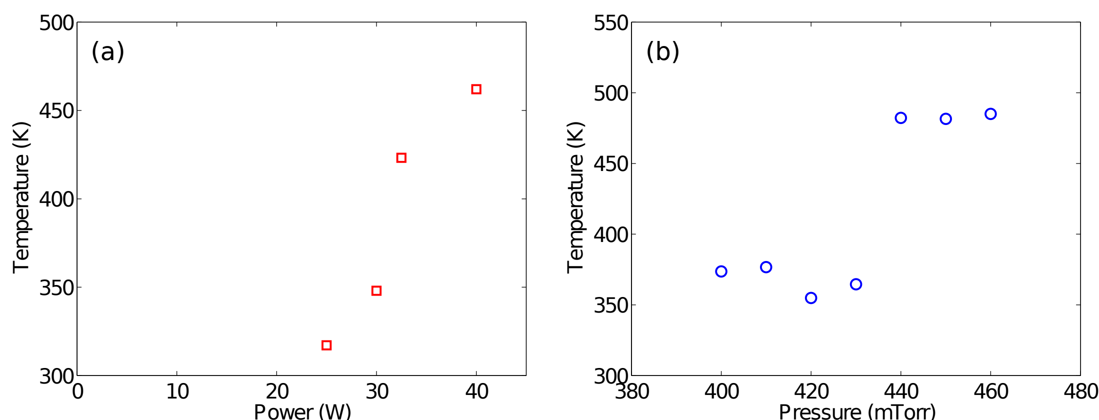

Figure 6.7: (a) The transition between the diffuse mode and the bright mode of operation for a chamber pressure of 350 mTorr and varying power. (b) The same transition but with a varying pressure in the expansion chamber and a constant power of 25 W.

diffuse mode to bright mode is also facilitating the production of significant increase in ionising collisions.

Figure 6.7 (b) also continues the trend observed in the broad pressure sweep of constant temperature with varying pressure. Again it can be seen that the temperature varies weakly in both the diffuse and the bright mode, which is not apparent from the broad sweep, as there is only a single data point in the diffuse mode regime. Because there appears to be a discontinuity in the temperature measured with changing pressure, it can inform further deductions about the mechanics of the mode change.

It is impossible to obtain a data point with a temperature that lies between the bright and diffuse modes with varying pressure, making it a reasonable supposition that the entire sustainment mechanism of the plasma is changing. If the two sustainment mechanisms can operate simultaneously, it would be expected that the transition between the two modes would produce points in parameter space to have a smooth transition from diffuse to bright mode as one mechanism became dominant over the other. Since this is not the case, it can be inferred that either only one mechanism is occurring at any given time in the plasma, or the sustainment mechanism of the bright mode is being turned on abruptly and completely masking the effect of the diffuse mode. It is important to note that these deductions can only be made by considering the pressure sweep as the gas temperature remains steady

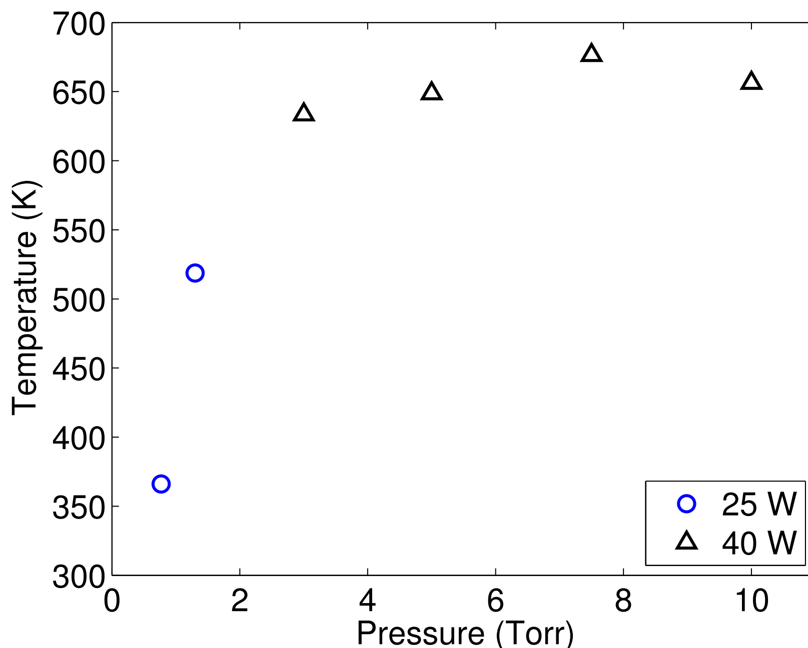

Figure 6.8: Gas temperatures measured for varying pressures between 770 mTorr and 10 Torr with no pumping on the system.

in each mode with varying pressure.

6.5.3 Static Gas

To further increase the pressure in the discharge, the pump could be closed off from the expansion chamber. This meant that although the pressure could be made to go higher than 830 mTorr in the expansion chamber, the gas is static in the system rather than flowing. A result of the lack of flow is that there is no pressure gradient present in the source (that is, the plenum and chamber pressures are the same). With this configuration, gas temperature measurements with pressures of up to 10 Torr are possible. Beyond 10 Torr, the emission of the plasma becomes so dim that the signal to noise ratio made it impossible for meaningful data to be extracted. It should be noted that at this pressure the validity of the Fulcher α method becomes uncertain. Figure 6.8 shows the data acquired for a range of pressure with no flow.

At 770 mTorr and 25 W, the plasma is in the diffuse mode. This is uncharacteristic of the results seen in the sweeps with a flowing gas, but can be understood by considering the lack of pressure gradient throughout the source. At 25 W the pressure at which the mode transition occurs is 450 mTorr, with a corresponding

plenum pressure of 1.3 Torr, giving an estimated pressure in the plasma creation region of approximately 780 mTorr. It is likely then that the critical factor controlling the operational mode of the plasma is the pressure inside the hollow cathode. This is further supported by the fact that at 1.3 Torr throughout the system, the bright mode is activated and the temperature can be seen to jump from 366 to 519 K.

At pressures above 2 Torr in the expansion chamber, the brightness of the plasma decreases and to get usable signal from 3 Torr upwards the power of the system is increased from 25 to 40 W. It is again seen that the temperature remains relatively constant for all four pressures measured with no flow. It is worth noting that all the data points are at higher temperatures than would be expected from the flowing gas set up. This can be explained by the fact that there is no mixing with room temperature gas from the plenum, and no losses of hot neutrals to the pumping system.

It is possible that the decrease in brightness is a result of quenching of the excited $d^3\Pi_u^-$ state by collisions, in which case the corona equilibrium has broken down and these results will have large errors. If it is due to some other mechanism, such as the plasma no longer being optically thin, then the temperature measured will be the temperature nearest the back of the plasma creation region, in the spot closest to the optical fibre. Even so, the data presented in figure 6.8 can still at least provide useful qualitative information, and the values measured are in good agreement with expectations, given the previous measurements and the fact that with no pumping higher temperatures would be expected.

6.6 Preliminary Absorption Spectroscopy

One of the future directions planned for the work presented in this thesis is absolute atomic hydrogen density analysis in the expansion plume of a hollow cathode in the DASH system. To achieve this a Lyman α lamp and CsI photodiode detector are attached to the DASH expansion chamber facing each other. They are positioned such that their mutual line of sight is approximately at $z = 2$ mm in front of the orifice of the hollow cathode.

The analysis technique to calculate atomic hydrogen densities is based on the experiments of Laimer *et al.* presented in [132]. The analysis uses the Doppler broadened line shapes for the lamp emission and absorption by atomic hydrogen to calculate a theoretical transmission for the lamp signal. Comparing the measured transmission with the plasma off and on allows determination of the absolute atomic hydrogen density across the line of sight of the detector.

The Fulcher α measurements are critical to this analysis as the high pressure in the system means that the atomic and molecular hydrogen are in thermal equilibrium. As such, the results from this chapter are used to calculate the theoretical Doppler broadened line shape of the atomic hydrogen absorbing the light from the Lyman α lamp.

Currently, if the active hollow cathode is placed in line of sight of the detector, the signal from the lamp is dominated by the Lyman α emission from the discharge itself. A possible solution to this is to pulse the discharge and measure absorption in the afterglow of each pulse. This data could be extrapolated to determine absolute atomic hydrogen density with the plasma on. To achieve this the acquisition timing software of the detector needs to be addressed as it samples every 100 ms without capacity for variation or triggering.

To validate the technique in the DASH system measurements of atomic hydrogen density diffusing from a hollow cathode that is not in line of sight of the detector is performed. The active hollow cathode is 35 mm away from the central hollow cathode of the DASH source. With a path length of 35 cm between the lamp and the detector, the average atomic hydrogen density is measured to be approximately 2×10^{17} m^{-3}. The atomic hydrogen density is also observed to increase with applied power, but no change is observed in varying pressure.

6.7 Conclusion

Spectroscopy of the Q branch of the $v' = 2 \rightarrow v'' = 2$ Fulcher α transition is undertaken on a hydrogen plasma produced by the Pocket Rocket source. The parameter space swept over the course of the experiment is designed to complement a

set of PROES measurements taken with an intensified CCD camera presented in the next chapter. It is found that the temperature of the plasma increases linearly with power, but is constant for varying pressure (excluding the mode change), indicating plasma density is the dominant factor in the determination of the gas temperature. A mode transition of the plasma is observed to reliably occur either side of a pressure power product of 11 Torr.W, referenced to the expansion tube pressure. This mode transition is observed to heat the gas to significantly higher temperatures. It is also deduced from close scrutiny of the temperature profile of the transition as pressure is varied, that the mode transition must be caused by either a complete switch in sustainment mechanism of the plasma, or the activation of an effect boosting plasma densities high enough that the diffuse mode is completely masked. Measurements of higher pressures are made by blocking the pumping system to the chamber. This removes the pressure gradient through the source and confirms that the pressure inside the hollow cathode of Pocket Rocket is critical to the determination of whether the plasma operates in the diffuse or bright mode.

7

Phase Resolved OES of the Hydrogen Plasma

To continue the optical diagnosis of the hydrogen plasma in Pocket Rocket, Phase Resolved Optical Emission Spectroscopy (PROES) using an intensified CCD camera is performed. An intensified charge coupled device (ICCD) camera is composed of two main parts: the CCD array, and the image intensifier. The CCD converts photons to electrons in a pixelated array, and these are sequentially read as current to compose a picture. The image intensifier greatly increases the sensitivity of the device to incident light, as well as providing a very fast gating mechanism (shutter speeds can be in the hundreds of picoseconds). Because of their very rapid gating, ICCDs can be used to make time resolved measurements observing phenomena that occur over short timescales. In the case of a radio frequency plasma, it allows an experimenter to resolve the fluctuations in emission that occur within a single rf period. By observing the intensity and position of emission of certain spectral lines within a plasma, both spatial and temporal resolution of an optical signal is possible [133].

The spectral line of interest in the following experiments performed is the Balmer α line. The Balmer α line represents the transition from $n = 3$ to $n = 2$ in atomic hydrogen. Because the energy required to excite hydrogen to the $n = 3$ state from the ground state is 12.1 eV and the energy to ionise the atom completely is 13.6 eV, it is reasonable to suppose that regions of excitation and emission are also regions in which ionisation are occurring. The intensity of the emission when caused by electron impact excitation is controlled by the proportionality shown in equation

7.1

$$I \propto f(\epsilon) n_e n_H \tag{7.1}$$

where $f(\epsilon)$ is the electron energy distribution function. The sheath mechanics of an rf hydrogen plasma are quite complex when compared with those of a rare gas plasma. There are three species of positive ions present in the plasma: H^+, H_2^+, and H_3^+. All three have more than one production channel and each play different roles within the plasma [134]. Hydrogen plasma is unusual because of the high relative mobility of ions to electrons due to their relative masses. Furthermore, the motion of electrons within the plasma is damped because of the hydrogen molecules' capacity for excitation to higher vibrational and rotational states.

Czarnetzki *et al.* have performed work using an ICCD camera coupled with analysis of the Stark splitting of the Rydberg states of hydrogen to analyse the fields and ion energy distribution functions in a capacitively coupled planar discharge [135]. They found four distinct phases within the rf cycle, including a sheath reversal phase, which has been seen to generate strong ionisation and emission in a pressure and power regime similar to that in which the Pocket Rocket source is operated [125]. The field reversal effect occurs when the potential on the driven electrode is positive, and forms a capacitor-like positive field that accelerates electrons towards the wall [136]. The grounded electrode does not experience a field reversal and behaves more like a simple capacitive sheath, tracking with the plasma potential.

7.1 Experimental Design and Calibration

The Pocket Rocket source is viewed from two positions with the ICCD camera: from the rear, looking into the hollow cathode, and from the side looking at the plume expanding into the chamber. The camera unit used is an Andor iStar DH-320T, borrowed from Andor Technologies. The camera has a CCD chip of 1024 pixels in the horizontal direction by 256 pixels in the vertical direction. An intensified CCD device has an image intensifier placed in front of the CCD. The intensifier has three components: a photocathode, a micro channel plate (MCP) and a phosphor screen. When incident light hits the photocathode it is converted into electrons. The MCP

is a honeycombed grid of glass that sits behind the photocathode. Each cell of the grid is less than 10 μm across. The MCP has a voltage of between 500 and 1000 V applied to it and the electrons cascade through the cells producing more electrons via secondary ionisation. The cascading electrons hit the phosphor screen, converting the electrons back to light which falls onto the CCD, producing the image. By setting the voltage on the MCP appropriately, the electrons from the photocathode can be blocked from hitting the phosphor screen. This mechanism is what allows such fast gating of the system, as well as providing image intensification when light is allowed to pass through. The gain of the MCP is variable and can be controlled via the software attached to the camera.

To enable rf phase resolved measurements of the plasma it is necessary for the triggering of the camera to be locked to the voltage driving the plasma. This is achieved with an Agilent 81150A dual channel phase locked signal generator. The hollow cathode is driven from one channel with a sinusoidal waveform at 12.5 MHz. This operational frequency is selected to be an integer multiple of the trigger frequency of the camera. This is essential to the proper synchronisation between the two signals, while still being within the tuneable range of the matching network designed for 13.56 MHz operation. The second channel from the signal generator is a 10 ns square pulse, repeating at 312.5 kHz, phase locked to the first channel. This signal controls the voltage present on the MCP, gating the incident light passing on to the CCD. The 12.5 MHz signal is passed through an ENI A150 rf power amplifier. The amplifier has a maximum output power of up to 300 W, although to prevent damage to the source, the system is never operated above 40 W.

During operation the camera is controlled by several parameters. The number of accumulations refers to the number of times the entire data acquisition process is performed. The exposure time controls the length of a single accumulation, and is the period for which the CCD is active. The trigger signal from the second channel of the signal generator samples 312 500 times per second, each at the same point within an rf cycle (because of the phase locking). This means that for an exposure time of 1 second, and for a single accumulation, the CCD is exposed to light from the plasma 312 500 times before the CCD is read off and refreshed. For more accumulations,

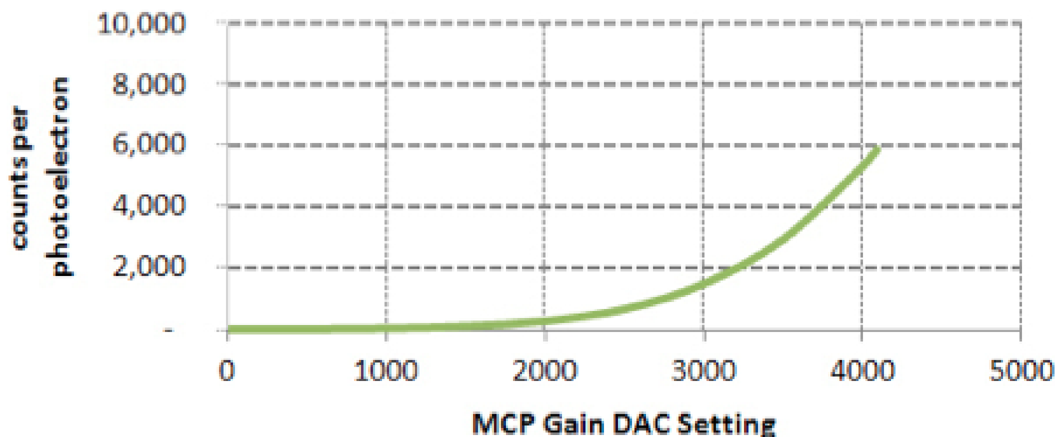

Figure 7.1: Plot taken from the Andor iStar ICCD manual showing the increase in photons delivered to the CCD by the MCP after varying the arbitrary gain factor in the control software [137].

the number of total counts increases proportionally. The number of individual rf cycles sampled during one step is given by the exposure time multiplied by the trigger frequency multiplied by the number of accumulations. The kinetic length of an acquisition describes the number of time steps for an individual data run. A kinetic length of ten frames with the previous parameters means that ten single accumulations of an exposure of one second will occur. The gain of the MCP can be varied on an arbitrary scale between 0 and 4095, with a strongly nonlinear variation. A plot showing how the gain affects the counts per photoelectron can be seen in figure 7.1.

The spacing of the individual kinetic steps within an rf cycle is controlled by the step width. The span of time covered by the data run will be given by the kinetic length multiplied by the step width. The gate width controls how long the MCP passes light to the CCD each time it is activated. The gate width refers to the

	Exposure	Accumulations	Kinetic Length	Gain
Rear view	0.3 s	16	50	2000
Side view	0.5 s	16	40	4000

	Step Width	Gate Width	Delay
Rear view	2 ns	4 ns	80 ns
Side view	2 ns	4 ns	80 ns

Table 7.1: Typical operational parameters of the Andor iStar ICCD camera during data acquisition.

electrical gate width, and is the time between the start and end signal for each command to acquire light. The optical gate width is not well defined, but is shorter than electrical gate width. The delay setting introduces a lead time between the trigger from the signal generator and the response from the camera. Typical camera settings for the acquisition of data in the following experiments are displayed in table 7.1.

The configuration of the experimental set up can be seen in figure 7.2, showing the positioning of camera and lens relative to the Pocket Rocket source and its expansion chamber. Figure 7.2 also displays photographs of the system in both configurations.

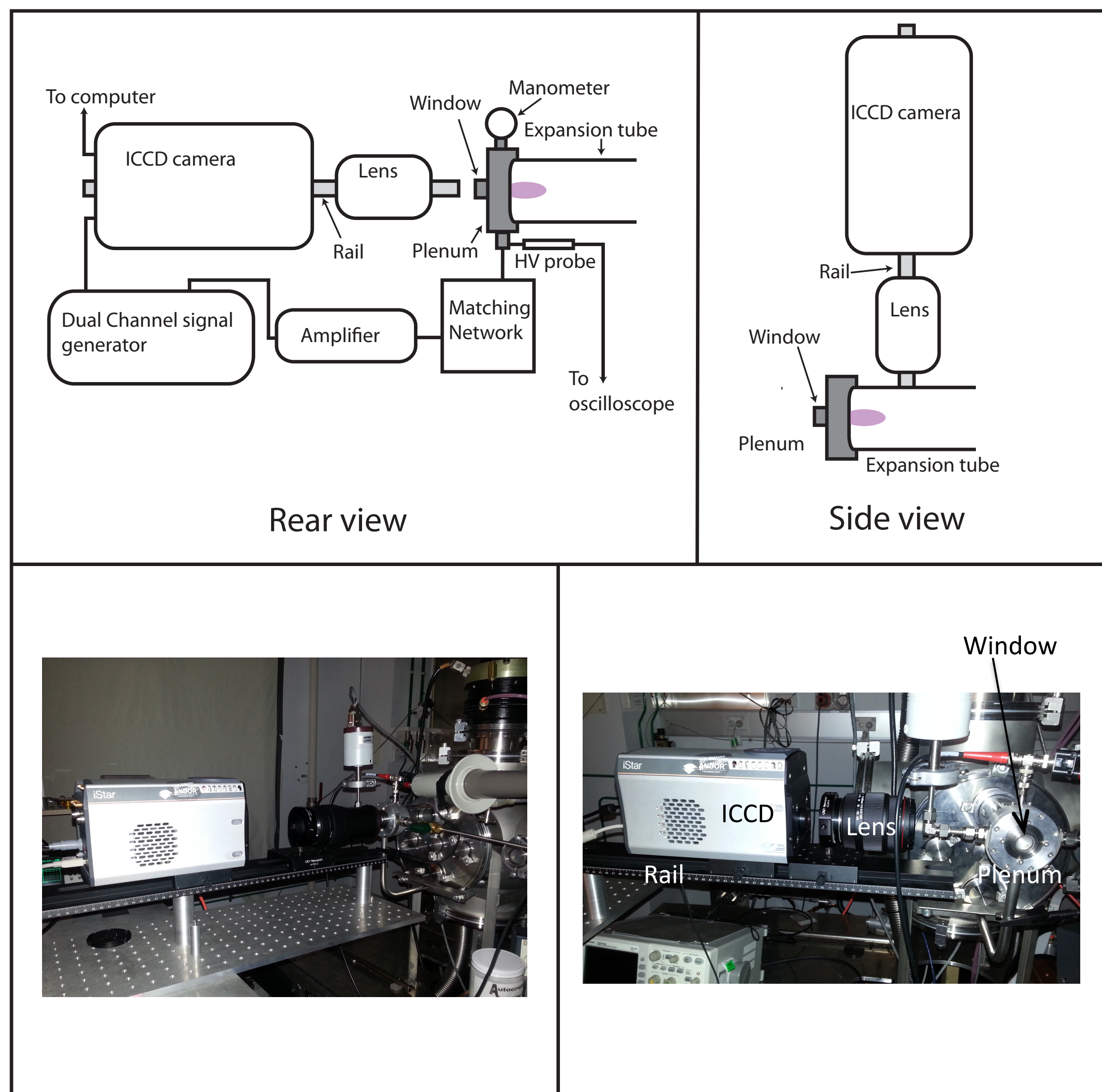

Figure 7.2: Schematics and photographs showing camera and lens orientation relative to the Pocket Rocket source for both rear and side viewing.

The ICCD camera outputs a voltage pulse indicating when it is acquiring data. By comparing the temporal location of this pulse with the HV probe signal measured at the powered electrode, temporal calibration of the HV signal is achieved. It is important to compensate for the internal delay of the HV probe signal when making performing this calibration (measured to be 17.4 ns). The lens serves two purposes: focussing an image of the plasma onto the CCD, and resizing the image to fit completely onto the CCD without redundant pixels to optimise spatial resolution.

To focus the optical system, a light emitting diode (LED) is mounted to the rail at a fixed distance from the camera. Since the edge of the LED is easy to resolve on the CCD, it allows the relative positions and settings of all the optical components to be determined. Subsequently the the optical system is configured such that the plasma is in the focal plane previously occupied by the LED. When viewing from the rear, the camera is centred and focussed on the back of the hollow cathode. When viewing from the side the camera is centred on the expansion tube, in front of the source to ensure that the entire glass expansion tube is in the image. The interface between the hollow cathode chamber is in the focal plane.

Once focussed, the entire diagnostic system is tested to ensure that it is capable of producing repeatable results. Scanning over two full rf cycles shows both the plasma source and the measurement system behave consistently. Figure 7.3 (a) shows an integrated pixel count taken over three regions of interest (ROIs) covering the centre of the hollow cathode, the edge of the hollow cathode and the entirety of the hollow cathode from the rear view. The acquisition settings for the test are those referenced in table 7.1, except the kinetic length was extended to 80 to observe two full rf cycles. The plasma is operated at 350 mTorr in the chamber with a power of 30 W. There is a slight drift in the overall emission with increasing time attributed to the increasing temperature of the source as it is continuously operated. Despite this, all of the critical structures of the emission are well preserved. As such the kinetic length during regular data acquisition can be reduced to span a single rf cycle. This has two benefits: increased operational efficiency during data acquisition, and reducing strain on the Pocket Rocket system. Typical acquisition times are slightly more than five minutes per run. Having a much longer kinetic length significantly increases the

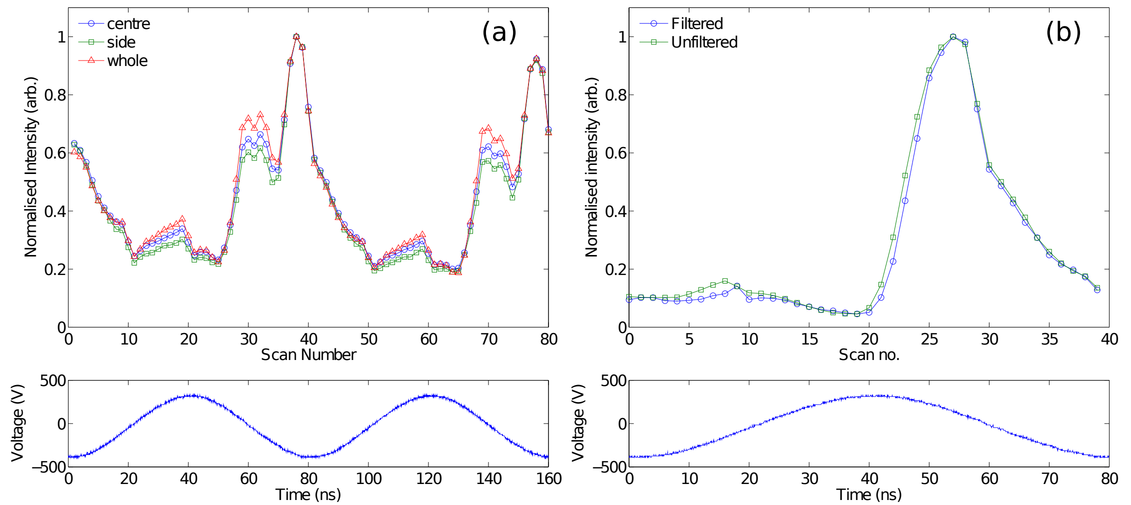

Figure 7.3: (a) Emission for a central ROI, an edge ROI, and total emission from the rear view taken over two rf cycles at a chamber pressure of 350 mTorr and power of 30 W. Each data set is normalised to allow for clarification of their structure. (b) Unfiltered emission and Balmer α emission for the side view, operated at 830 mTorr and 30 W.

risk of catastrophic failure of the system due to heat stress while operating at higher powers.

The Balmer α line (656.28 nm) dominates the emission from the plasma. In similar experiments by others, bandpass filters have been used to investigate the emission of particular species by isolating a line from a single transition [138]. Because the Pocket Rocket plasma emits so strongly at 656.28 nm, using a filter is found to be unnecessary. To validate this claim, the plasma is observed unfiltered and with a 10 nm wide bandpass filter centred at 660 nm to isolate the Balmer α line. The bandpass filter attenuates all signal by an order of magnitude. Figure 7.3 (b) shows the normalised emission for an ROI covering the plume of the plasma in the side view at a chamber pressure of 830 mTorr and 30 W of power. Since the qualitative behaviour is preserved between the two cases, the camera is operated without a filter during experiments to increase the signal to noise ratio. The images are still expected to accurately show emission of atomic hydrogen at the Balmer α wavelength. Figure 7.4 shows a spectrum of the plasma produced by Pocket Rocket acquired with an Ocean Optics spectrometer and fibre optic cable. The spectrum highlights the dominance of the Balmer α line. The fibre is pointed at the interface

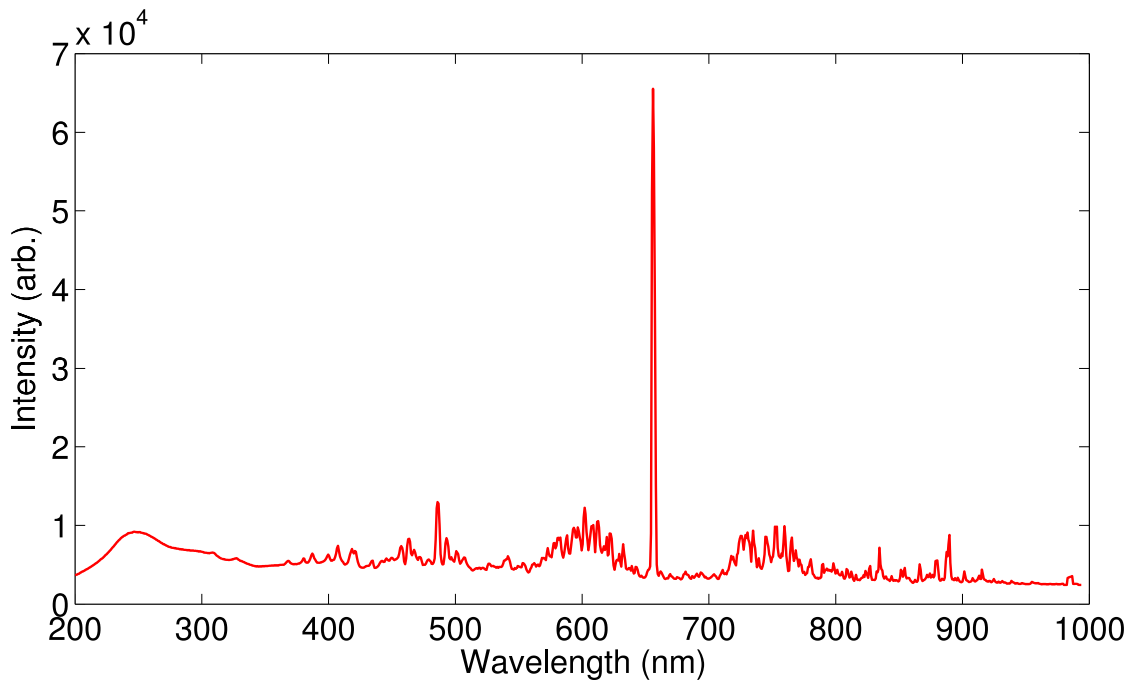

Figure 7.4: Spectrum of the plasma emission taken with an optical fibre pointed at the interface between expansion chamber and hollow cathode in the Pocket Rocket system. The Balmer α line dominates the spectrum.

between the chamber and the hollow cathode.

7.2 Operational Modes

As observed in chapter 6, two distinct operational modes are observed to occur within the Pocket Rocket system. The first is the diffuse mode, which is observed at lower pressures and powers. It is characterised visually by a diffuse and isotropic plume of plasma expanding from the hollow cathode. The second is named the bright mode, and is activated above the power and pressure threshold of around 11 Torr.W, referenced to the expansion tube pressure.

7.2.1 Diffuse Mode

Figure 7.5 shows a series of stills taken from the rear view, looking into the hollow cathode, while operating in the diffuse mode at an expansion tube pressure of 350 mTorr and power of 25 W. The images show the evolution of the plasma over the course of a single rf cycle. The colour scheme in figure 7.5 and all subsequent

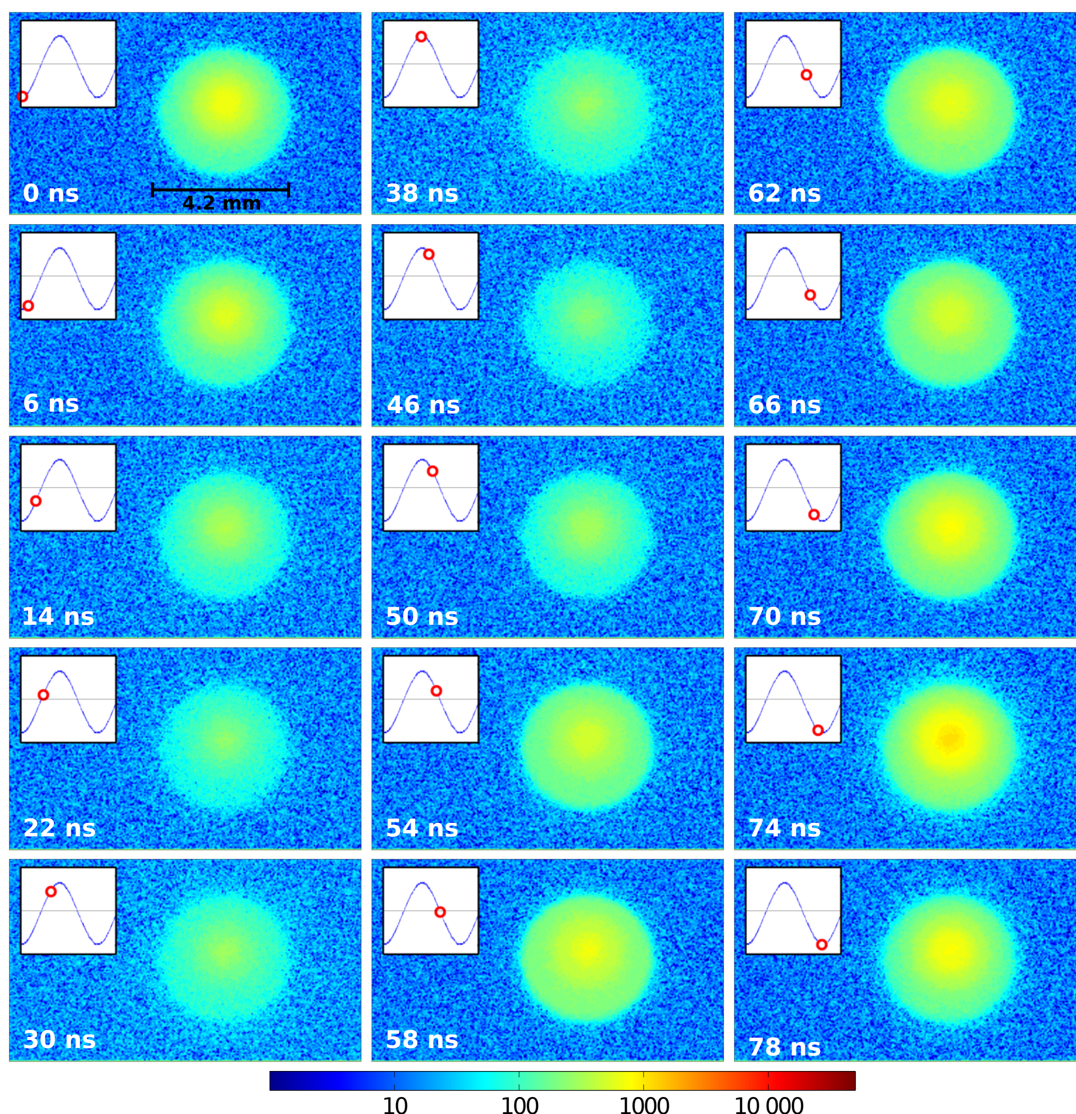

Figure 7.5: Photographs of the evolution of the emission of the interior of the hollow cathode over the course of an rf cycle for 350 mTorr chamber pressure and 25 W of power.

rear view plots are on the same logarithmic scale, allowing for easy comparison. The discharge appears to be azimuthally symmetric and have a peak in intensity in the centre of the hollow cathode throughout the rf cycle. By comparison, an annular structure was observed in the Pocket Rocket system at higher pressure and with a discharge of argon or nitrogen [92]. The primary implication of the consistent central peak in emission is that plasma density is also peaked in the centre of the hollow cathode.

In the diffuse mode, with a plenum pressure of 1 Torr and a chamber pressure of 350 mTorr, the pressure in the axial centre of the hollow cathode is expected to

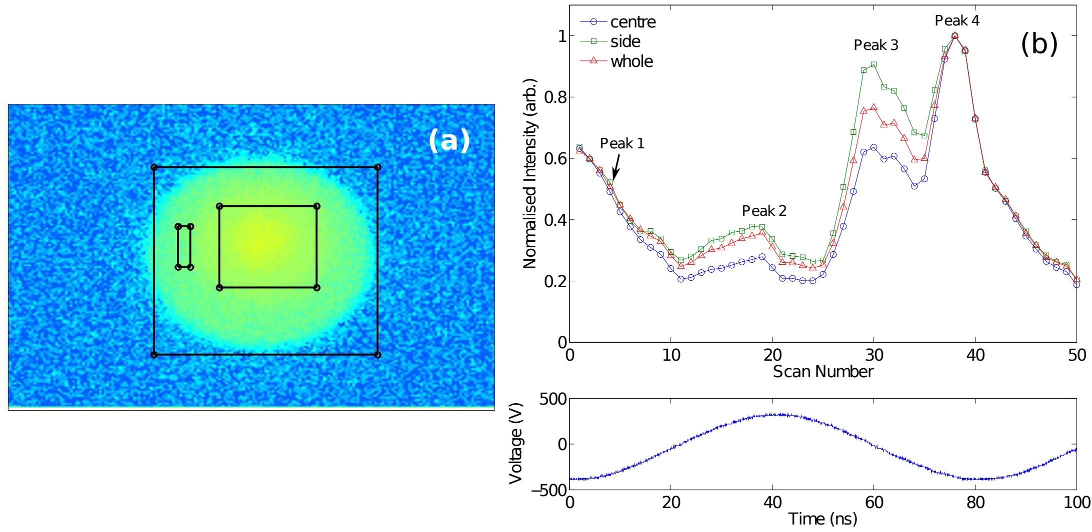

Figure 7.6: (a) Example frame from 350 mTorr and 35 W rear view data showing the locations for the three regions of interest (ROIs) over which the pixel count is integrated. (b) Integrated emission over each ROI, normalised and highlighting the four peaks present over the course of an rf cycle.

be approximately 700 mTorr. At this pressure the mean free path for an electron impact ionisation is considerably longer than the hollow cathode's 4.2 mm diamater for electrons with energies of less than 35 eV. Since these electrons will be trapped in the bulk of the plasma for more than half the rf cycle by the sheath voltage, a bright peak in the centre is in accordance with expectations.

The boundary of the ROIs investigated are detailed in figure 7.6 (a). Over the course of one rf cycle there are four peaks present in the emission profile, named 1 through 4 and highlighted in figure 7.6 (b). The presence of four peaks is similar to those observed by Charles *et al.* in [138], although the shapes and relative heights of the peaks have changed. Peak 1 is small relative to the other peaks and has its maximum just before the point where the voltage on the powered electrode becomes positive. The mechanism driving this peak is unclear. Peaks 2 and 3 occur around the maximum rate of change in applied voltage on the driven electrode. As such they are likely caused by field-electron interactions. Two possible explanations of these peaks are proposed. The first is the field reversal phenomenon, mentioned earlier in this chapter whereby electrons are drawn in a beam to the wall by a short-lived positive field and then ejected back to the bulk plasma as the sheath reforms. The

second is the possibility of some level of inductive coupling between the powered electrode and the plasma.

There is an asymmetry in emission with regards to the rising edge and falling edge of the voltage on the hollow cathode. It can be seen in figure 7.5 between 74 and 0 ns that there is a peak in emission near the most negative excursion of the voltage, labelled peak 4. By contrast, emission is weaker in the positive part of the cycle, between 20 and 40 ns. The structure of the discharge can be investigated in detail by integrating the intensity counts over a region of interest (ROI) covering both the centre and edge of the hollow cathode.

Emission in all three ROIs is dominated by peak 4, which occurs when the applied voltage is at its most negative value. The sustainment mechanism for an rf hollow cathode discharge in this geometry and parameter range is thought to depend on secondary electron emission. This is supported by both fluid based simulation of the Pocket Rocket system [106], as well as a particle in cell (PIC) model of another hollow cathode system [112]. Secondary electron yield from ion bombardment becomes much more efficient with increasing ion energy [139]. When the applied voltage is negative, the sheath voltage at the driven electrode can reach several hundred volts, enhancing secondary electron yield from incident ions. Furthermore, since the sheath voltage is large, secondary electrons will enter the plasma with energies of more than 100 eV, allowing them to participate in multiple ionising collisions. This mechanism forms the basis for both the hollow cathode effect (in this geometry), and the sustainment of a γ discharge. As such it appears that the diffuse mode of operation operates as a typical γ discharge.

Finally, it is worth noting that the ceramic tube forming the inner wall of the Pocket Rocket system introduces a complicating factor when considering the applied voltage. Since the HV probe is connected to the driven electrode, the measured voltages will not completely illustrate the voltages felt by the plasma. Fluid simulations of the Pocket Rocket system performed by Greig [106] show the voltage on the inside of the ceramic tube and the plasma potential change lead the applied voltage by a few nanoseconds. It is also seen that the self bias will mostly be carried on the ceramic sleeve, meaning the HV probe will give an imperfect reading of the

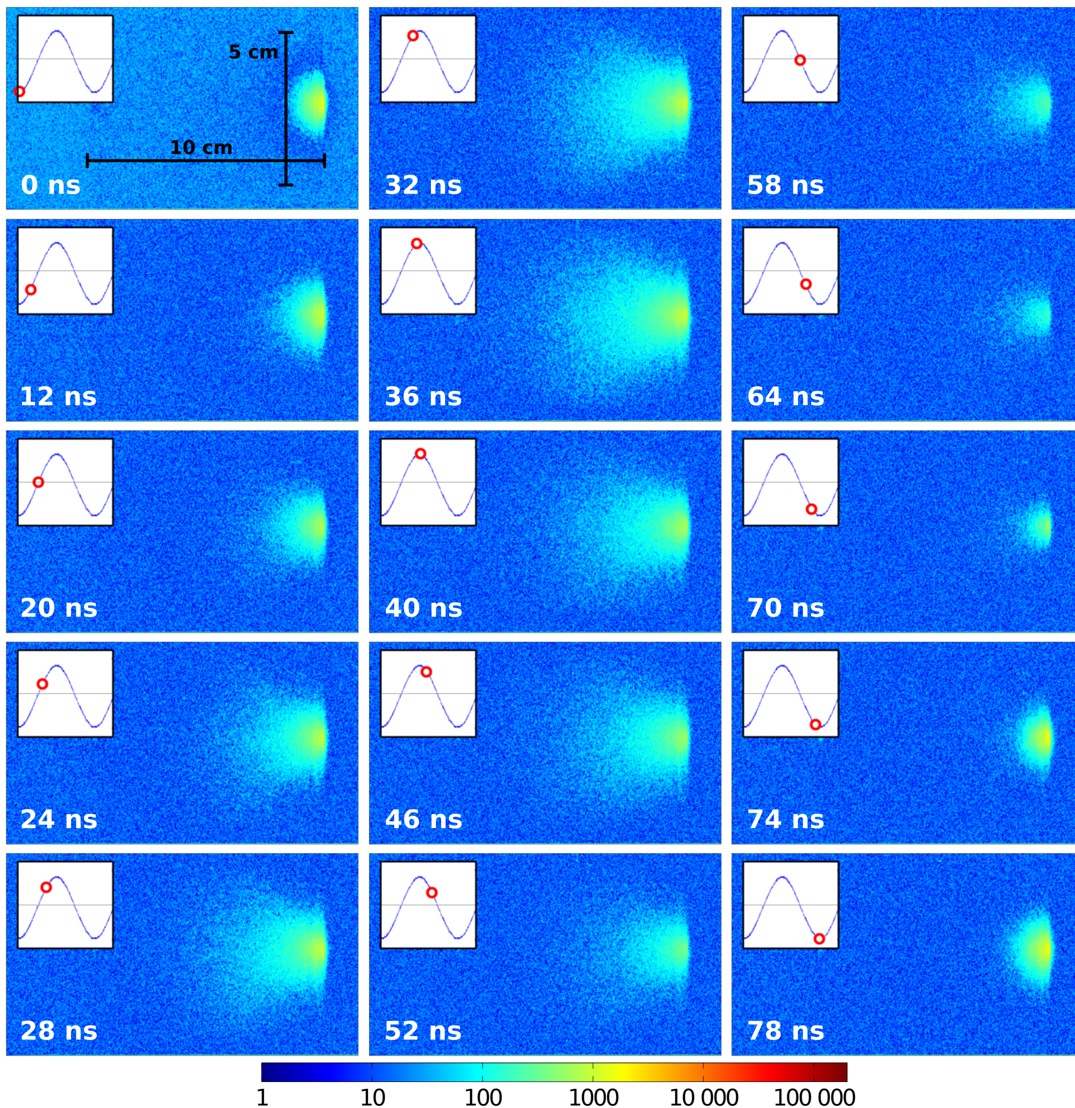

Figure 7.7: Photographs of the evolution of the emission of the expansion of plasma into the glass tube over the course of an rf cycle for 350 mTorr chamber pressure and 25 W of power.

voltage on the inside of the sleeve. It is likely that there will be a slightly stronger negative DC offset to the rf signal displayed in figure 7.6, and to subsequent plots of the same nature.

Figure 7.7 shows the same data set in the diffuse mode from the side and clearly displays the expansion of the plume into the glass tube, it should be noted that all side-on data is not Abel inverted. The plasma diffuses into the expansion chamber with an isotropic profile. The protrusion begins when the applied voltage becomes positive at around 20 ns, and continues to grow until the voltage peaks. From 40 ns onwards the size of the plume decreases steadily until it almost disappears entirely

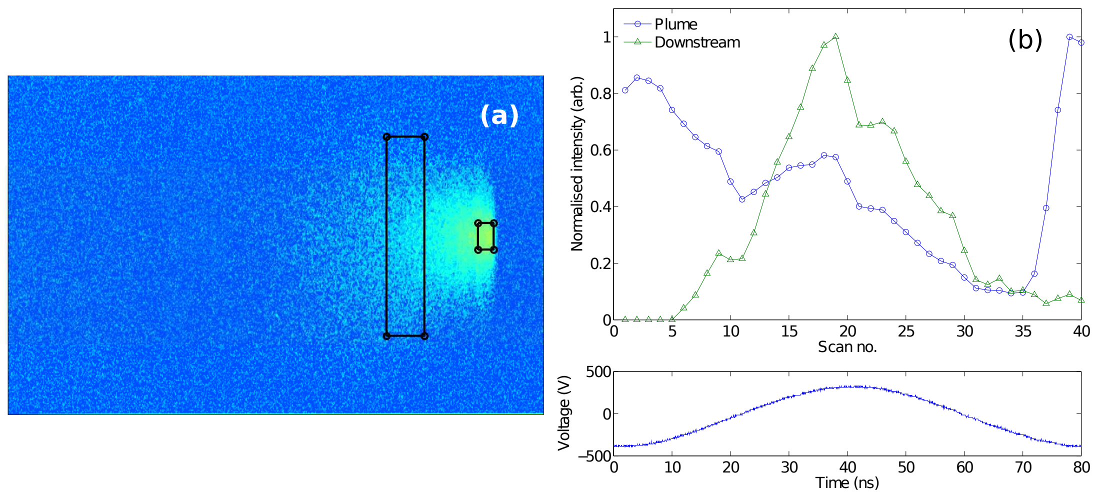

Figure 7.8: (a) Photo at $t = 38$ ns highlighting the two ROIs used in panel (b). Panel (b) shows the integrated pixel counts for these two ROIs, normalised to allow for easy comparison.

around 70 ns. When the voltage is at its most negative, the centre of the plume at the exit of the hollow cathode is at its peak brightness. However, there is no diffusion further into the expansion chamber.

Figure 7.8 (a) shows the ROIs from the side view for the 38 ns image, and panel (b) shows the normalised integrated intensity for each ROI over a single rf cycle. These allow for a quantitative interpretation of the behaviour shown in the series of stills in figure 7.7. The emission from the plume ROI is strongest during the peak 4 phase, while downstream there is a minimum. The maximum emission in the downstream region is π out of phase with the maximum emission inside the hollow cathode. This indicates that the propagation of plasma into the expansion tube is not driven by the internal operation of the hollow cathode, but is more likely controlled by the chamber facing earth plate.

Simulation of the Pocket Rocket system has shown that during the positive phase of the applied voltage there is a burst of secondary electrons released from the earth plate facing the expansion tube [106]. This can be understood by considering that the plasma potential in the discharge will be at its greatest value when the voltage applied to the driven electrode is maximised. The plasma potential must peak during this period so that it will always remain higher than the hollow cathode potential.

The potential on the earth plates is always 0 V and the sheath voltage at an earthed surface is equivalent to the local plasma potential. Therefore, the voltage of the sheath that forms at the earth plates is maximised when the voltage on the driven electrode is positive. This increase in sheath voltage will enhance bombarding ion energy, increasing secondary electron yield. The secondary electrons emitted from the earth plate are accelerated into the expansion tube, driving the propagation of plasma in the diffuse mode. During the positive part of the rf cycle the sheath at the driven electrode is minimised and secondary electron emission is suppressed.

By contrast, when the applied voltage is most negative, secondary electrons will only be emitted from the surface of the driven electrode. During this part of the rf cycle, there is very little electric field in the sheath in front of the earthed electrode as the plasma potential is minimised. However, a strong negative field is present in front of the powered electrode. As has already been discussed, this will drive ions into the hollow cathode wall with an energy equivalent to the sheath voltage, yielding secondary electrons that are accelerated back into the bulk plasma with very high energies to cause ionising collisions. The mean free path for an electron of 200 eV to ionise a hydrogen molecules is approximately $\lambda = 5$ mm, which approximately agrees with the distance between the edge of the powered electrode and the edge of the plume in the chamber. It is for this reason that peak 4 still dominates emission in the side view near the interface between hollow cathode and chamber.

In summary, while operating in the diffuse mode, there are four discernable peaks per rf cycle inside the hollow cathode. The first is the weakest in terms of emission and remains an area for future investigation. The second and third peaks correspond to the points in time when the applied voltage is at its maximum rate of change. Two possible explanations are proposed. The first is that the system has some element of inductive coupling due to the annular geometry of the powered electrode. The second is that there is a small field reversal effect occurring as described for a hydrogen discharge by Czarnetzki *et al.* in [135]. Finally, peak 4 occurs when the voltage reaches its negative maximum, driving the production of secondary electrons via ion bombardment at the surface of the powered electrode. Peak 4 produces the greatest Balmer α emission intensity. From the side view it has been deduced that

the propagation of plasma into the expansion tube is not linked to the emission of secondary electrons within the hollow cathode. It is for this reason that the peak emission from the plume near the interface occurs simultaneously with peak 4. The propagation of plasma into the expansion tube is triggered by a burst of secondary electrons from the chamber facing earth plate. This occurs when the applied voltage is most positive and is due to the increased sheath voltage at the earthed surface during the portion of the rf cycle when plasma potential is highest.

7.2.2 Bright Mode

Increasing the gas flow to raise the chamber pressure to 830 mTorr while retaining a power of 25 W causes the pressure power product to exceed 11 Torr.W, which activates the bright mode. Figure 7.9 shows photographs of the bright mode from the rear view over the course of a single rf cycle. The total emission has increased significantly with respect to the diffuse mode, with the peak emission during the cycle being an order of magnitude more intense. The spatial profile of the discharge's emission within the hollow cathode is similar for both modes with the brightest region of the plasma always being at the centre.

In figure 7.9 there appears to be part of an annulus of relatively strong emission beneath the central discharge. This is especially clear in some of the brighter frames. To investigate whether this is real emission or reflection of the bulk plasma from the wall, the relative intensities of the central ROI and the fringe are compared in figure 7.10. Panel (a) shows the two ROIs compared for this test overlaid on the image from 54 ns. Panel (b) shows that the signal of the bright crescent closely follows that of the main plasma in the centre of the hollow cathode. Because there appears to be no independent behaviour of the crescent, its presence is likely the result of a slight misalignment between the camera and the axis of the hollow cathode. The misalignment allows the reflection of light emitted from the bulk plasma to reach the camera.

The same ROIs for the rear view shown in figure 7.6 (a) are analysed for the diffuse mode and are shown in figure 7.11, and they clearly illustrate the difference between the two modes. Where the maximum emission in the diffuse mode was at

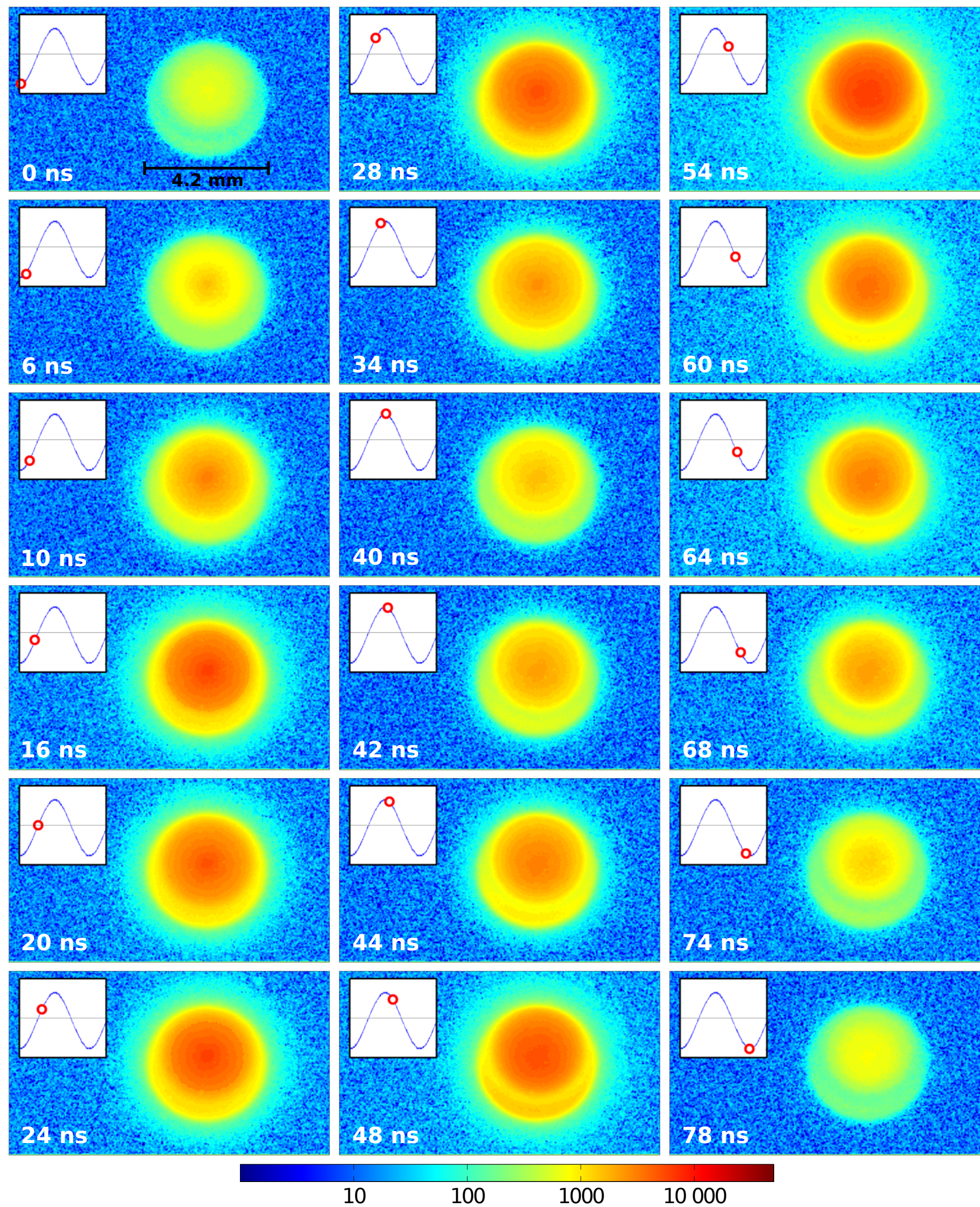

Figure 7.9: Photographs of the evolution of the emission of the interior of the hollow cathode in the bright mode over the course of an rf cycle for 830 mTorr chamber pressure and 25 W of power.

the most negative value of the voltage on the powered electrode, there is now an emission minimum. However, there are still four clear peaks during the rf cycle, labelled in figure 7.11 (a). Peaks 2 and 3 are in approximately the same positions as in the diffuse mode and are therefore likely caused by the same mechanisms. This suggests that the degree to which the electric field-electron coupling is influencing the plasma is greatly increased in the bright mode.

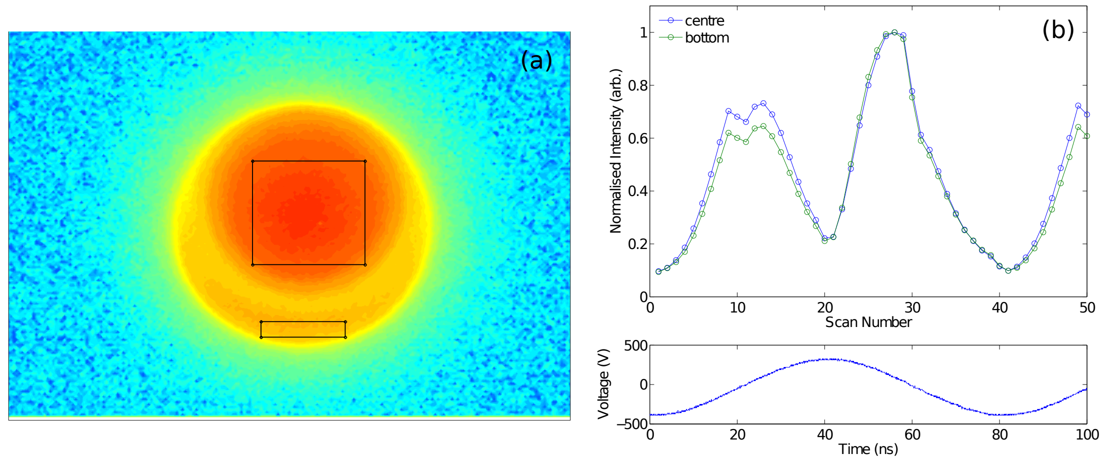

Figure 7.10: Panel (a) shows the photo from 54 ns, and highlights the two ROIs used for testing for independent behaviour between the central and edge regions. Panel (b) shows that the edge ROI closely follows the central one, indicating the signal there is a reflection rather than an annulus of plasma.

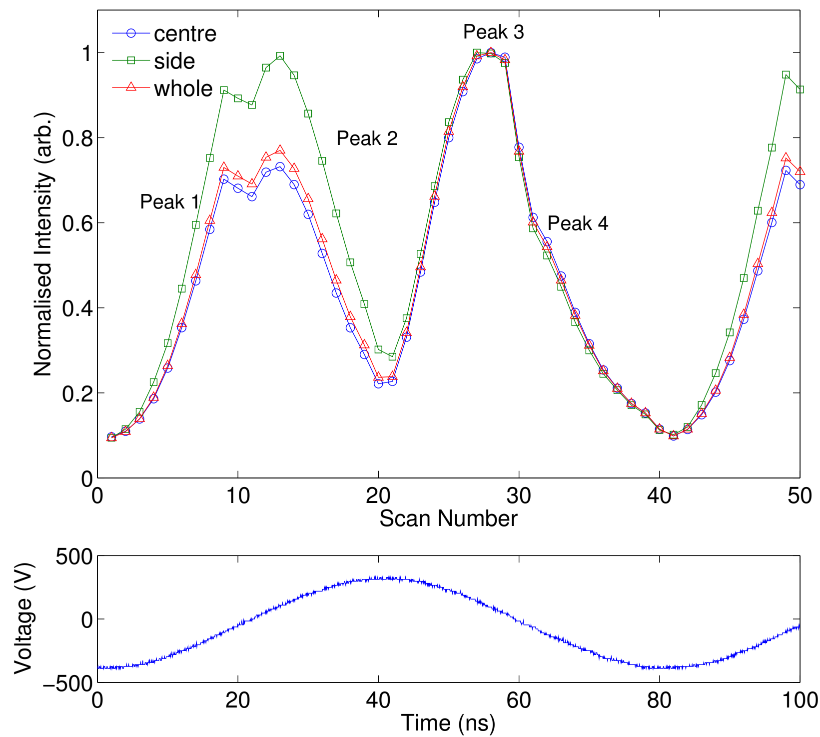

Figure 7.11: Normalised integrated pixel counts for the three ROIs outlined in figure 7.6 (a), highlighting the four peaks present in the bright mode

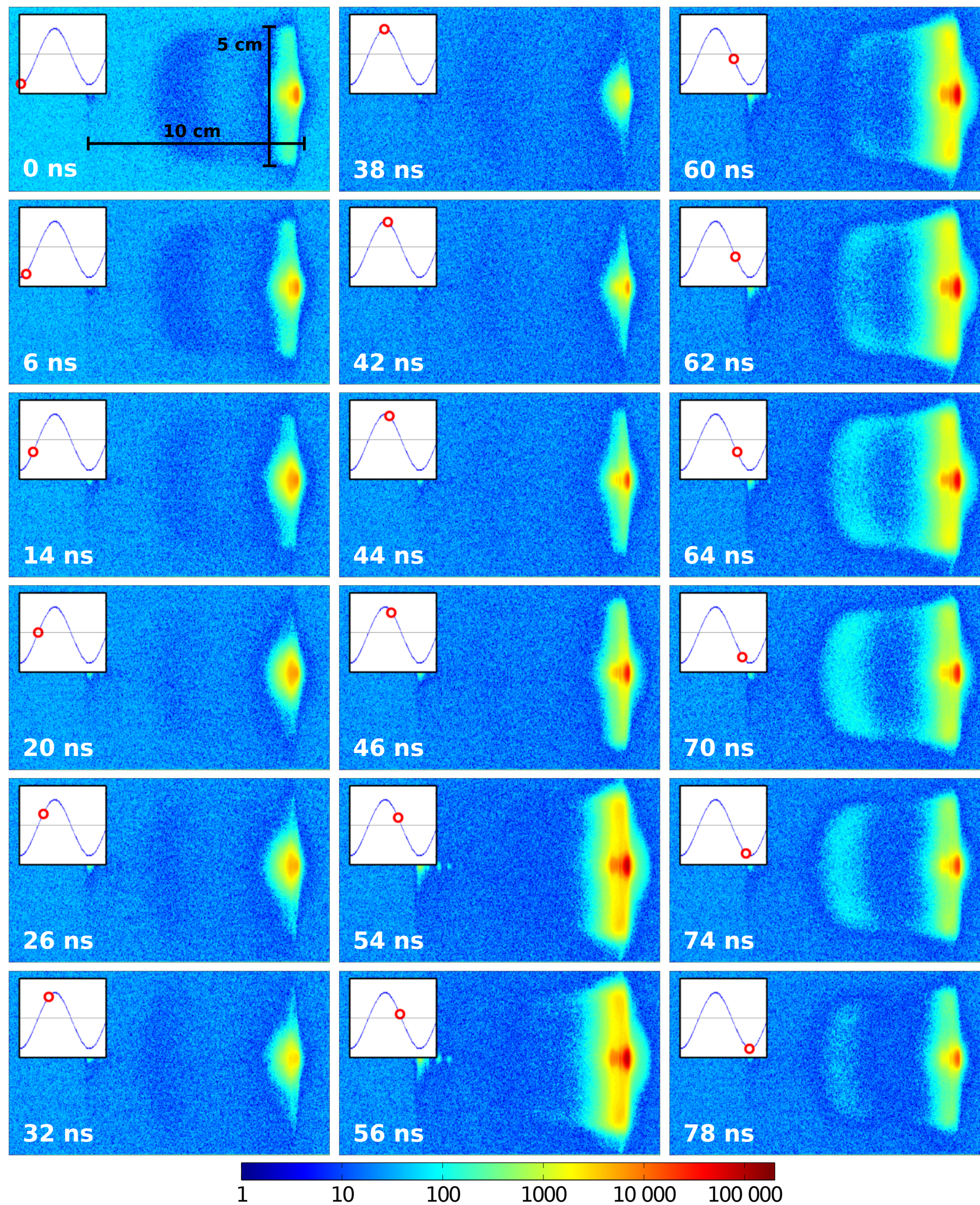

Figure 7.12: Photographs of the evolution of the emission of the expansion of plasma into the glass tube over the course of an rf cycle for 350 mTorr chamber pressure and 25 W of power.

When the bright mode is viewed from the side, as shown in figure 7.12, it can be seen that there is a significant difference between the shape of the plasma in the expansion chamber compared with the diffuse mode. It is convenient to describe the behaviour of the plasma starting at 42 ns. The panels between at 42 and 54 ns show the plasma expanding from the hollow cathode and spreading along the entirety of the aluminium face of the source. In the next panel, 2 ns later, the ionisation

front begins to propagate down the inside of the glass tube, while the centre of the expansion tube stays relatively dark. Following this, at 62 ns, the plasma collapses away from the wall forming a secondary plasma downstream of the source. The next two panels show the plasma emission intensifying and the ionisation front of the expanding plasma continuing to propagate downstream. Finally, at 74 ns, the plasma in the tube detaches completely from the chamber plasma and dissipates. From 0 ns onwards the plasma on the face of the earth plate recedes over the 40 ns period until the applied voltage reaches its positive peak.

This behaviour is similar to that observed by Jansky *et al.* in an atmospheric pressure plasma jet, and is suggestive of a surface wave being launched along the inside of the glass tube [140]. However, in the case of launching these plasma 'bullets', the time scale for the phenomenon is at least an order of magnitude longer [141, 142]. Because the ionisation front propagates and recedes over the course of a single rf period, and the ions are too massive to move at these speeds, the process must be driven by electrons. This constitutes a fundamental difference in operation that exists between these atmospheric experiments and Pocket Rocket.

The vertical dark region approximately 3 cm to the left of the hollow cathode exit is visible once per rf cycle, between 56 and 80 ns. It can be observed as electrons propagate down the expansion tube, causing ionisation and excitation of the neutral gas. The dark region is thought to be associated with the formation of a static supersonic shock in the expanding plasma. It is proposed that emission is suppressed in this region because of the depletion of plasma and neutral species density in the so called 'zone of silence' [143]. This depletion increases the mean free path for excitation and ionisation events in the supersonic region. For the shock to form, the neutral gas in the expansion must exceed the sound speed. This can reasonably be attributed to the increase in translational temperature measured by the Fulcher α spectroscopy in the bright mode. The increase in temperature is primarily caused by the increased power deposition efficiency, leading to higher plasma density.

To further contrast the two operational modes, it is worth noting that the plasma expansion in the bright mode is approximately half an rf cycle out of phase with

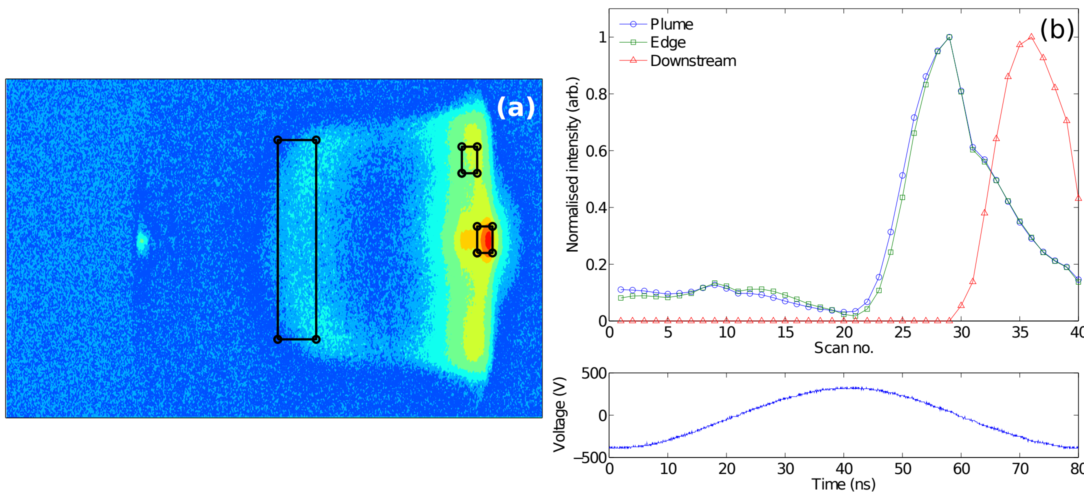

Figure 7.13: (a) Side view of the bright mode at 66 ns, as the plasma is propagating into the expansion tube. The three black boxes show the ROIs displayed in panel (b). (b) Shows the evolution of the integrated emission for each ROI, normalised to its own maximum value.

the diffuse mode. At 40 ns, the voltage on the powered electrode has peaked and the plasma is beginning to spread over the earth plate. This turnover of the applied voltage signals the start of peak 3 when looking at the discharge inside the hollow cathode. The luminosity and position of the ionisation front continue to increase as the voltage on the electrode becomes more negative, and the propagating plasma detaches as the voltage reaches its negative peak. To investigate the downstream emission structure of the discharge in the bright mode, different ROIs are used than those in the diffuse mode. This can be seen in figure 7.13 (a). It is interesting to note that although the plasma within the hollow cathode has four distinct peaks with similar intensity, the emission into the chamber is dominated by peak 3 as can be seen in panel (b) of figure 7.13.

It can be seen in panel (b) that the normalised emission profiles for the plume and edge ROIs are in excellent agreement. As there is no discernible delay between the emission peak for the plume and the plasma at the edge of the earth plate, it is probable that rather than diffusing from the hollow cathode, significant ionisation is occurring within the chamber. This is further evidenced by the fact that there is a small amount of emission for both the centre and edge ROIs at the time when peaks 1 and 2 are present in the hollow cathode.

In summary, the behaviour of the bright mode is dominated by emission when the rate of change of the applied voltage is highest. Two possible explanations are proposed to explain the emission structure within the hollow cathode. The first is that there is inductive coupling between the driven electrode and the plasma. The second is that there is a field reversal driving ionisation through the collapse and reforming of the sheath during the positive part of the rf cycle. In the bright mode there is no evidence of excitation caused by secondary electrons emitted at the most negative part of the rf cycle, contrary to observations made during operation in the diffuse mode. The ionisation front in the expansion tube must be driven by electrons, and its timing is synchronous with peak 3.

7.3 Power Sweep

To observe the effect of varying the power deposited in the discharge, the applied power is varied from 22.5 to 40 W. This represents the full range of available powers from ignition to the highest power accessible without risking system damage. The power sweep is performed at a chamber pressure of 830 mTorr. These operational parameters cause all five of the powers tested to operate in the bright mode.

7.3.1 Rear View

Figure 7.14 shows how the central and edge ROIs, whose boundaries are shown in figure 7.6 (a), vary with power in the rear view. Panels (a) and (b) show the central ROI, while (c) and (d) show the edge. It should be noted that as the applied power is changing, the voltage on the powered electrode will also vary. The voltage signal for 25 W of applied power is shown in the panels as a guide for phase. Panels (a) and (c) show that emission intensity within the hollow cathode is proportional to power. A simple power balance equation says that generally for a plasma, electron density will increase with power [2]. The rotational temperature measurements made in chapter 6 showed that the gas temperature increases with applied power. The combination of increased electron density and gas temperature will lead to an increase in absolute atomic hydrogen density. Furthermore, by considering the work

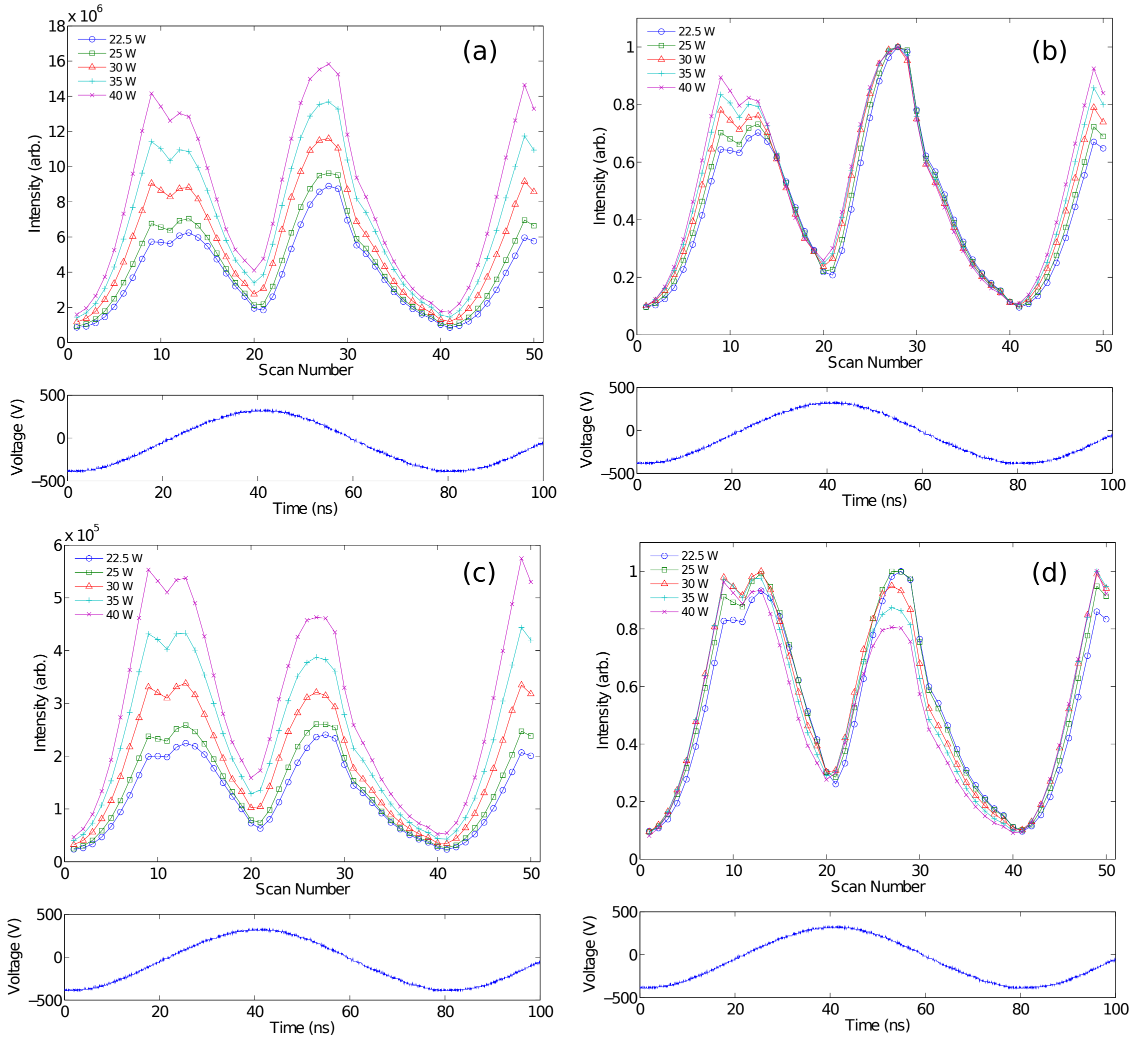

Figure 7.14: Variation in emission structure for the central and edge ROIs with varying power. (a) Shows the raw intensity counts for the central ROI (b) Shows the same data but each sweep is normalised to its own maximum value (c) Raw intensity counts for the edge ROI. (d) The edge ROI, where each sweep is normalised to its own maximum value.

presented in chapter 4 showing static electron temperature with changing power for argon, it is unlikely that variation in the power will affect the EEPF in hydrogen. An unchanged EEPF and increased electron and atomic hydrogen densities will in turn lead to an increase in emission of the Balmer α line, as is seen in figure 7.14.

Panel (b) shows the same set of data as panel (a), but each line is normalised to its own maximum value, allowing easy evaluation of qualitative structural changes within the emission over the course of an rf cycle for each power. Peak 3 is always the most prominent in terms of emission intensity in the central region. But as the power is increased the relative strength of peaks 1 and 2 increases, and above 30 W

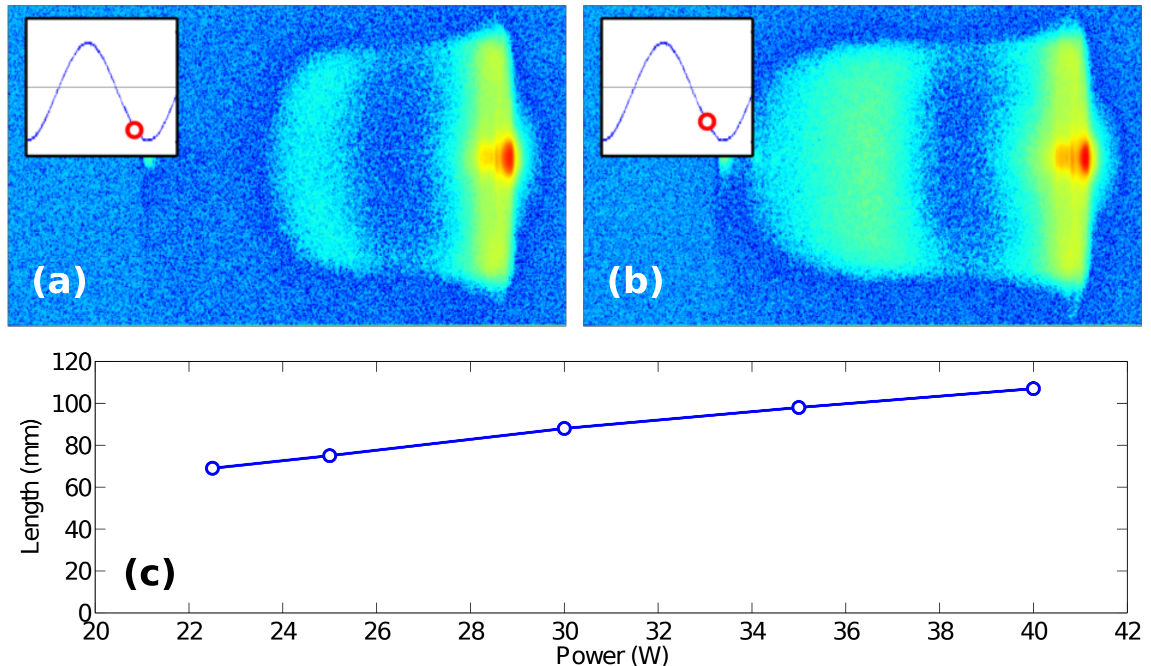

Figure 7.15: (a) Maximum distance of propagation for 25 W of applied power. (b) Maximum distance of propagation for 40 W of applied power. (c) Plot showing variation in the length of the propagating plasma with applied power.

there is a reversal in dominance between peaks 1 and 2, with peak 1 becoming the stronger at higher powers. Panels (c) and (d) show that near the wall of the hollow cathode, peaks 1 and 2 play a much more important role in total emission. For a power of 22.5 W peak 3 is still dominant, but peak 2 is approaching the same emission intensity. As power is increased both peaks 1 and 2 surpass peak 3 in terms of relative intensity. An increase in intensity near the wall for peak 2 is in accordance with the suggestion that the peak is caused by a field reversal at the wall drawing electron current.

7.3.2 Side View

Figure 7.15 shows how the propagation of the ionisation front of the expanding plasma varies as power increases. Panels (a) and (b) display the two extreme examples of 25 and 40 W, showing how the distance that plasma propagates into the expansion tube increases with power. For a power of 25 W the ionisation front propagates 75 mm into the chamber before dissipating. At 40 W the front reaches 107 mm, beyond the end of the glass tube and just into the metal chamber it is

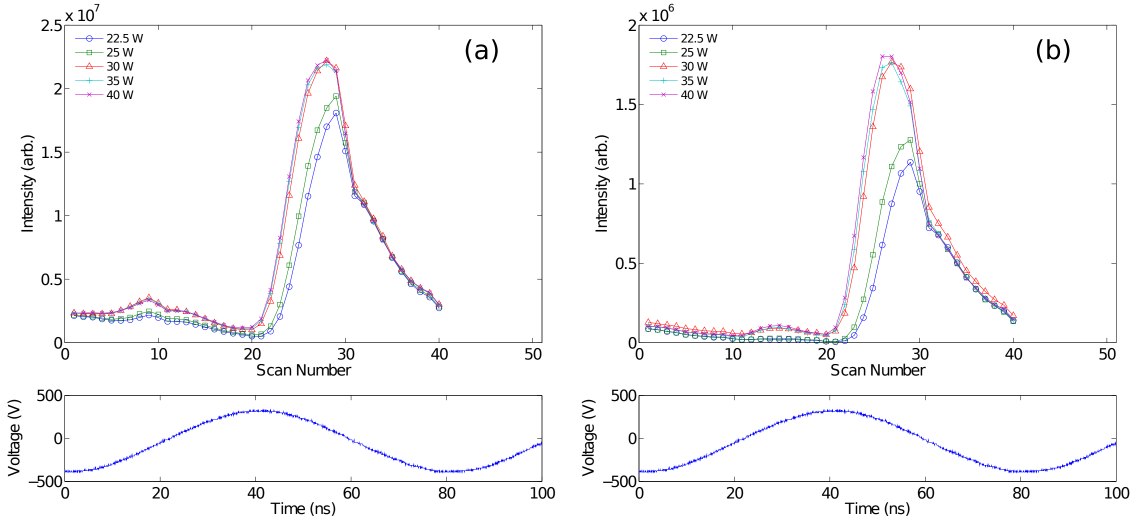

Figure 7.16: Integrated intensity counts over the (a) plume and (b) edge ROIs from the side view for powers between 22.5 and 40 W.

attached to. Panel (c) details the maximum distance of propagation for each of the powers tested. The increasing length of propagation for the ionisation front with power can be linked to an increase in density of the discharge. If as suggested, the density of the discharge within the hollow cathode is increasing with power, then a greater number of electrons will propagate down the expansion tube. If the mean free path for an exciting or ionising collision is unchanged, and the absolute number of electrons propagating increases, then the length of the visible discharge will also increase.

To understand the mechanics of the expansion of plasma into the chamber, the speed of propagation can be measured. By comparing the position of the plasma front between 56 ns and 68 ns for the 40 W case, the speed of the propagation is found to be 2×10^6 ms^{-1}. The calculated speed of propagation of the ionisation front can be compared with that of an ionising or Balmer α exciting electron. To ionise atomic hydrogen 13.56 eV is required and for a hydrogen molecule 15.60 eV. To excite from the ground state of hydrogen to the $n = 3$ state requires approximately 12.1 eV. The energy of an electron propagating at 2×10^6 ms^{-1} is calculated to be 11.4 eV. Considering the agreement between the energy of an electron moving at this speed and the ionisation and excitation energy for atomic hydrogen, it seems likely that the propagation of the plasma down the tube is driven by electrons launched once per rf cycle.

Figure 7.16 uses the plume and edge ROIs defined for the bright mode in section 7.2.2. Panel (a) shows the plume and panel (b) shows the edge region. The emission structure in both is dominated by peak 3, and emission increases with power between 22.5 and 30 W. Above 30 W the emission intensity plateaus, an effect not observed within the hollow cathode. Since the number of electrons propagating through the chamber must increase with power due to the increasing length of propagation, it is possible that the density of atomic hydrogen is limiting emission. This possibly indicates that the density of atomic hydrogen in the region near the chamber facing earth plate is being suppressed.

7.4 Pressure Sweep

Chapter 4 shows that changing the operational pressure in the system has a strong effect on the EEPF in the DASH system, driving up the electron temperature in accordance with a particle balance equation. To quantify how pressure affects the emission of the discharge, pressures in the expansion chamber ranging from 350 to 830 mTorr are observed. This pressure range spans the minimum reliable ignition pressure to the maximum flow the system is capable of delivering. The power used is 30 W and these parameters precipitate a mode change between 350 and 450 mTorr.

7.4.1 Rear View

For pressures of 450 mTorr and above the discharge is in the bright mode and shows a very consistent emission structure as can be seen in figure 7.17. Panels (a) and (b) show the central ROI with raw intensity counts and normalised counts respectively, while panels (c) and (d) show the edge ROI. Panels (a) and (c) provide an indication of the change in total emission intensity between the diffuse (350 mTorr, blue circles) and the bright mode, while panels (b) and (d) allow for easy comparison of their respective emission structures.

It can be seen that at both the centre and at the edge of the interior of the hollow cathode emission intensity increases with decreasing pressure. The most intense emission is seen at 450 mTorr as this is the lowest pressure at which the bright mode

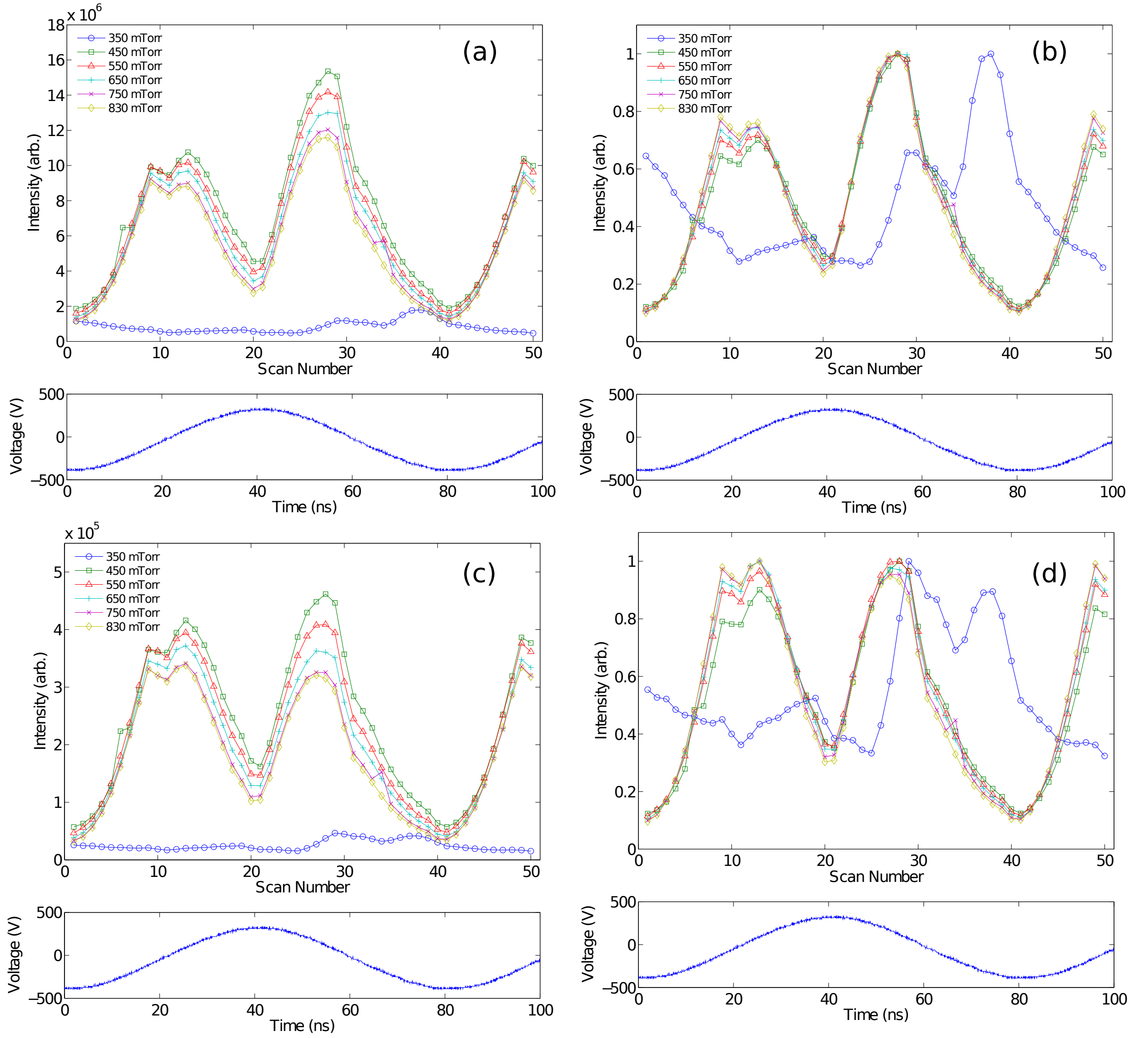

Figure 7.17: ROI analysis from the rear view, looking into the hollow cathode. (a) Integrated intensity count for the central ROI. Panel (b) shows the same data set as (a), but each line is normalised to its own maximum value. (c) Integrated intensity count for the edge ROI. (d) Normalised data from the edge ROIs.

is activated. This inverse relationship is a consequence of the effect of discharge pressure on the electron energy distribution. At a lower pressure, electron temperature increases while the density remains relatively constant. The main atomic hydrogen production channels require either an electron or ion - neutral collision, or an ion striking the wall [134]. Since power is static in this experiment, a simple power balance equation implies density should also be static. As such, atomic hydrogen production is expected to vary only weakly with pressure whereas electron temperature varies strongly. Considering equation 7.1, emission is expected to go up with decreasing temperature, as is observed.

Panels (a) and (c) show that the emission of peak 3 varies strongly with pressure, while panels (b) and (d) again highlight the relative decrease in strength of peak 3 near the wall of the hollow cathode. Peak 3 has already been identified as likely being caused by the interaction between electric fields in the sheath region and electrons, either via a capacitive to inductive (E-H) transition or from a field reversal. This is further supported by the fact that emission at the edge is weakest for peak 3 when pressure is highest, and the electric fields in the sheath region will be weakest. It is also interesting to note in panels (b) and (d) that the location of maximum emission of peak 3 for both diffuse and bright mode closely align. This agreement suggests that the two peaks are caused by the same phenomena, even though they produce different emission intensities.

7.4.2 Side View

Figure 7.18 shows the emission from the plume and side ROIs for the pressures scanned. Panels (a) and (c) show the raw emission intensity for the plume and edge of the expansion tube respectively. It is interesting to note that in contrast to the rear view data, the emission intensity is proportional to the pressure, rather than inversely proportional as is observed with emission from inside the hollow cathode.

To possibly explain this phenomenon three pieces of information are necessary:

1. That there is possibly some mechanism limiting the density of atomic hydrogen in the expansion chamber plume.

2. The largest cross sections for electron impact ionisation and excitation of both H and H_2, occur at approximately 50 eV [144, 145].

3. Emission from the expansion tube in the bright mode occurs simultaneously with peak 3 from inside the hollow cathode. This means that it is probable that the electrons ionising plasma in the expansion tube are heated from field interactions near the hollow cathode. This also means that these electrons are likely mono-energetic if they have been accelerated by a moving sheath. Since the sheath voltages are measured to be hundreds of volts, a smaller sheath will

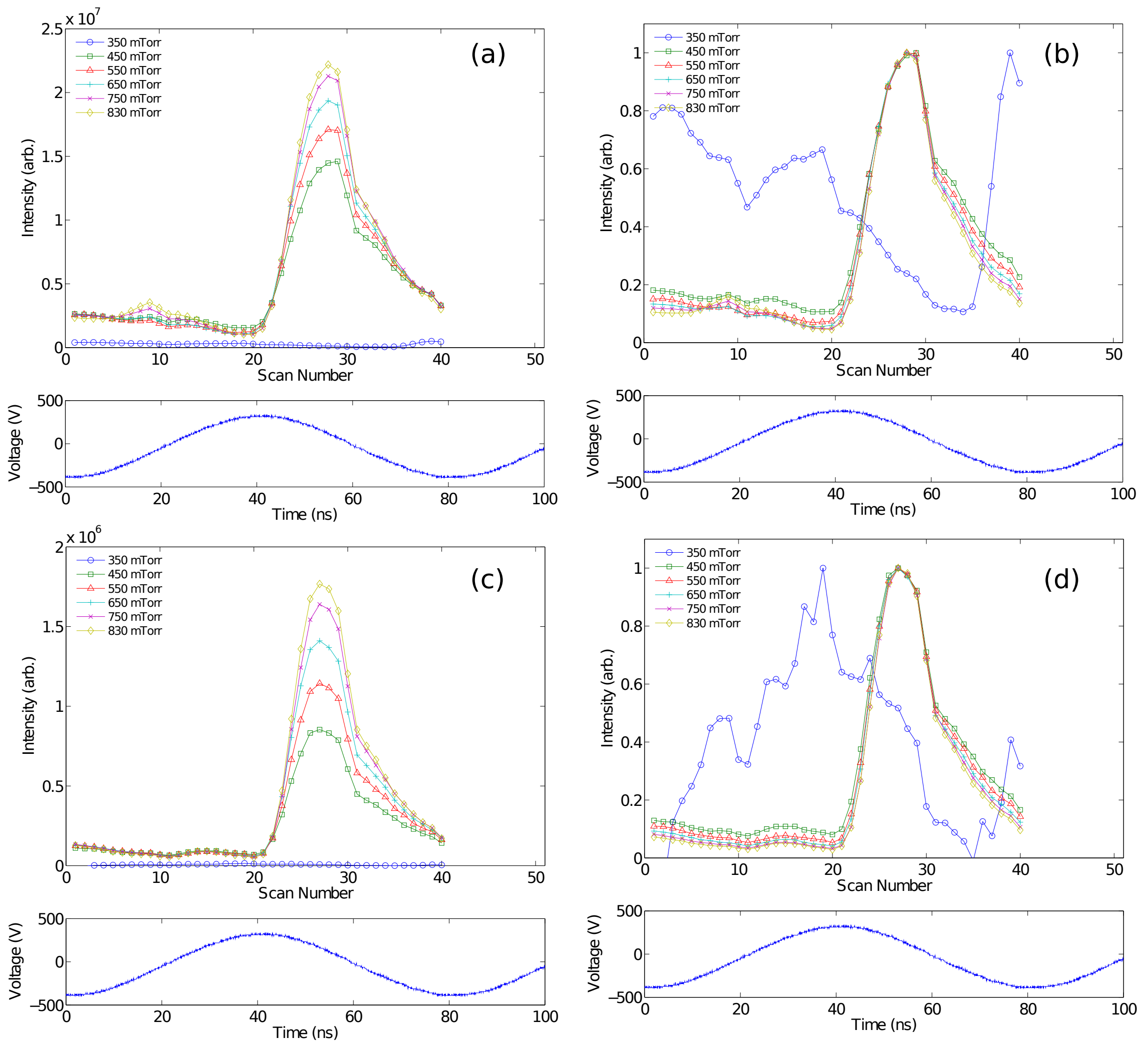

Figure 7.18: ROI analysis from the side view, looking into the expansion tube. (a) Integrated intensity count for the plume ROI. (b) Shows the same data set as (a), but each line is normalised to its own maximum value. (c) Integrated intensity count for the edge ROI. (d) Normalised data from the edge ROIs.

mean lower beam energies. As the beam energy approaches approximately 50 eV, the cross section for inelastic collisions as energies will increase.

To summarise, if the density of hydrogen is the same, and the electrons ejected from the hollow cathode have the same density and are mono-energetic, then the electron beam whose energy is closest to the maximum cross section for emission will produce the strongest emission.

This data set also provides an opportunity to further investigate the suggestion that the vertical dark region seen in the bright mode is caused by a supersonic shock. Figure 7.19 shows examples of zoomed in images of the dark space of the discharge

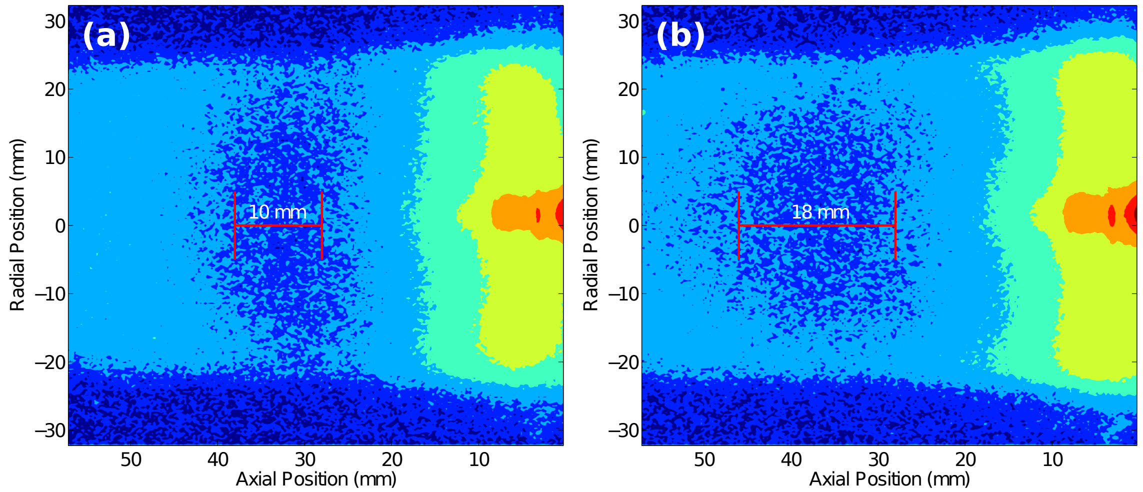

Figure 7.19: Zoomed shots of the dark space present in the expansion chamber downstream of the hollow cathode at two different pressures. Panel (a) is at 550 mTorr and has an approximate darkspace length of 10 mm, while (b) is at 830 mTorr with an approximate dark space length of 18 mm.

at (a) 550 and (b) 830 mTorr in the expansion tube. It can easily be seen that the dark space in the higher pressure discharge is wider, increasing from 10 mm, to 18 mm. Equation 7.2 describes a relationship between the flow rate of gas, the background pressure of the system, and the position at which the supersonic region of gas flow terminates, adapted from the work of Vankan *et al.* [143].

$$z_{end} = \sqrt{\frac{\Phi}{p_b}} \tag{7.2}$$

Where Φ is the flow rate of gas through the system, and p_b is the background pressure. By comparing the flow rate through the hollow cathode with the pressure in the expansion tube, it is found that the ratio between flow and expansion tube pressure increases with increasing flow. As such the increase in length of the dark region with increasing flow is expected if the gas flow is supersonic.

The data in figure 7.19 provides a useful insight into the speed at which gas expands into the tube, indicating the presence of supersonic flow. Directly calculating whether or not the expanding gas exceeds the sound speed is an involved and complex process that depends on the pressure profile, temperature profile and geometry of the Pocket Rocket source. Currently work is being performed by Greig *et al.* to investigate these questions further using computational fluid dynamics

techniques [106].

Finally, to check for the consistency of the argument that the atomic hydrogen present in the chamber is being excited by electrons ejected from the interior of the hollow cathode, the transit time for electrons to the end of the dark space in the expansion chamber is calculated. To do this the electron mobility, μ, is required. The electron mobility for a hydrogen plasma at 1 Torr is given as $\mu = 3.5 \times 10^5$ cm^2 (V.cm)$^{-1}$ [146]. This gives a drift velocity of 1.17×10^7 cm s^{-1} and a transit time of the dark space of the order of around 25 ns, which corresponds to what is measured with the ICCD device.

7.5 Electrical Study of the Mode Transition

To investigate the mode transition further, its electrical properties are characterised. To do this, an Impedans OctIV IV probe is placed between the matching network and the hollow cathode. Because these experiments are performed after the ICCD experiments, the discharge is operating in a much longer expansion tube, and at an rf frequency of 13.56 MHz. It is seen, however, that the same mode transition can be achieved, although the power pressure threshold is lower. The IV data provides insight into the electrical changes occurring within the discharge during the mode transition. The bright mode has lower voltages and currents than the diffuse mode, but a much higher power factor (defined as the cosine of the phase between voltage and current). The product of voltage, current, and cosine of phase gives the actual deposited power in the system. Figure 7.20 shows the change in deposited power for an applied power of 15 W and varying pressure in the system. It is also seen in figure 7.20 that the resistance of the system increases by a factor of four between the two modes. This is usually associated with an increase in the plasma density [95], and agrees with the inference that the order of magnitude increase in total optical emission, and increase in deposited power between the two modes is associated with a large increase in plasma density.

Two sustainment mechanisms of the bright mode have been suggested. The first is that the system undergoes an E-H transition and the bright mode contains some

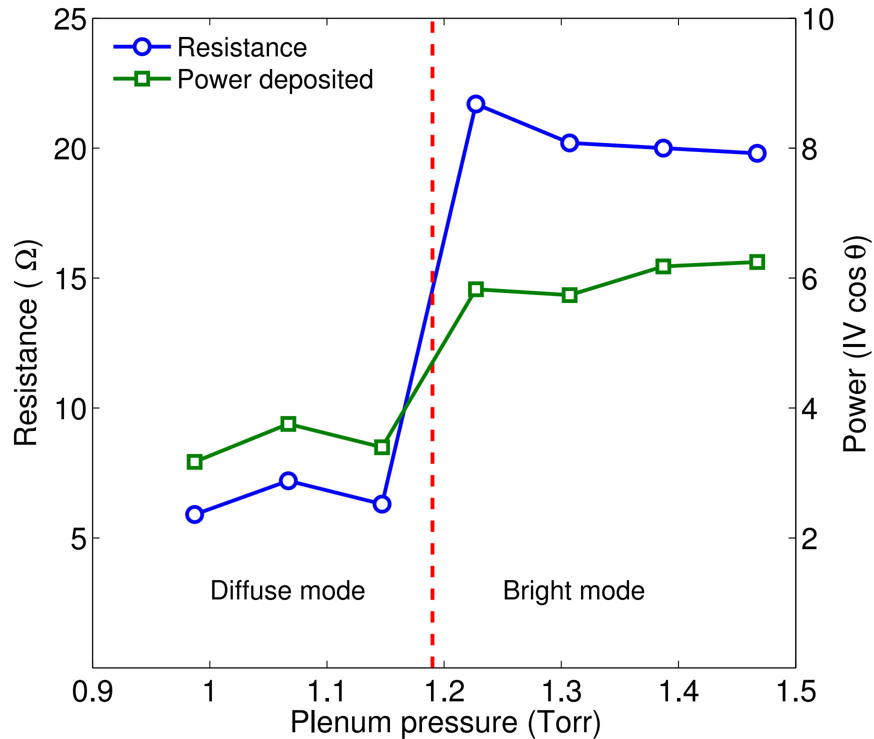

Figure 7.20: Variation in resistance and deposited power as the plasma transitions from the diffuse mode to the bright mode as a function of pressure.

element of inductive coupling between the powered ring electrode and the plasma. The second is that field reversal effects become dominant in the system, driving up the density of the discharge by forming a positive field near the wall once per rf cycle. It can be seen from figure 7.20 that the efficiency of the discharge increases noticeably between the two modes. Futhermore, for this set of data the diffuse mode had an RMS voltage of between 275 and 280 V depending on pressure, and an RMS current of 0.72 A, with a phase of 89.0°. The bright mode had a voltage between 185 and 200 V and a current of 0.53 A, with a phase of 86.4°. All of these parameters suggest some degree of inductive coupling. In light of the electrical data relevant to the mode transition, it seems more likely that the discharge is exhibiting some inductive coupling in the bright mode. However without further experimentation, such as time and spatially resolved measurements of the electric fields within the discharge, eliminating one or other of the proposed sustainment mechanisms is difficult.

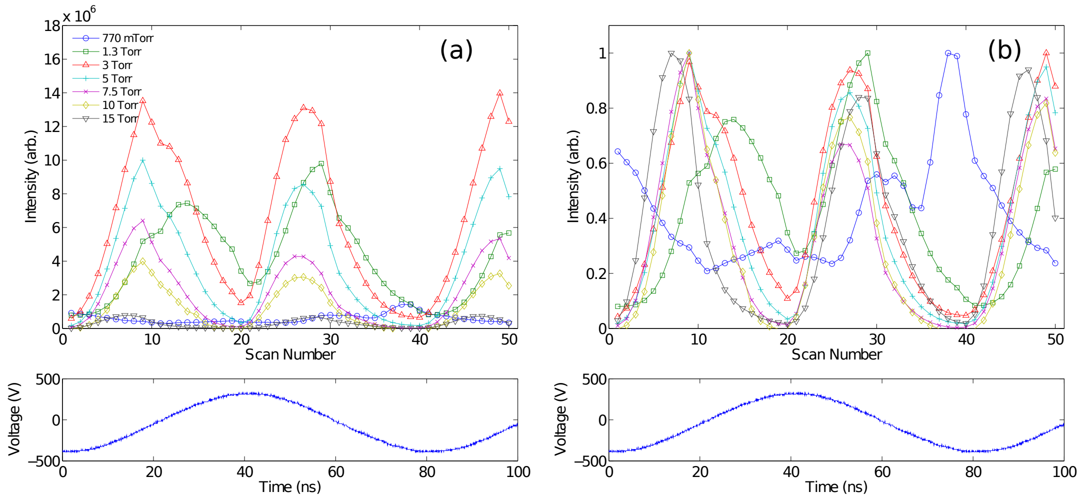

Figure 7.21: (a) Integrated intensity counts for the central ROI in a static flow regime. (b) Shows the data from panel (a), with each line normalised to its own maximum value.

7.6 Static Pressures

As has been discussed in chapter 6, to increase the pressure in the system beyond what is possible with active pumping, the chamber is isolated from the vacuum system. As a direct result of this, the pressure gradient between the plenum and expansion tube is absent, and there is a uniform pressure throughout the system. To investigate this operational regime, the pressure in Pocket Rocket is varied between 770 mTorr and 15 Torr. Figure 7.21 (a) shows the central ROI emission from the rear view for this regime as pressure increases. With a system pressure of 770 mTorr, the discharge operates in the diffuse mode, but at 1.3 Torr, it switches to the bright mode.

It must be noted that for pressures of 770 and 1300 mTorr, the power is at 25 W, but at higher pressures the emission from the discharge becomes too weak to acquire useful data. To combat this, the applied power is increased to 40 W for pressures of 3 Torr and above. It can be seen in panel (a) that the emission intensity increases noticeably from 1300 mTorr to 3 Torr, which is most likely because of the increase in applied power, as emission intensity has previously been seen to decrease with increasing pressure inside the hollow cathode. As the pressure continues to rise in the system, the emission intensity decreases until by 15 Torr the emission is

approximately equal in intensity to the diffuse mode at 770 mTorr.

Panel (b) shows a normalised version of the data displayed in panel (a). Normalising the data provides confirmation that the basic structure of the discharges' emission in the bright mode is not changing significantly as pressure increases and emission goes down, especially for the 15 Torr case. The most striking variation is the suppression of peak 2 and rise of peak 1 in terms of relative emission intensity. At 1300 mTorr Peak 2 is significantly stronger than peak 1. As pressure increases, peak 2 decreases in intensity and by the time the pressure has reached 15 Torr it has disappeared altogether from the discharge.

Figure 7.22 shows the unnormalised side view of the discharge at three pressures: 770 and 1300 mTorr, and 10 Torr. There is little change in this regime from the flowing gas set up. The most noticeable change is that emission decreases between 1300 mTorr and 10 Torr, even with the increased power at 10 Torr. This is in contrast to what is observed at lower pressures where the emission intensity increased as chamber pressure increased. It is possible that for these much higher pressures, the plasma is no longer optically thin and Balmer α emission is being reabsorbed before it can escape the discharge.

7.7 Conclusion

Over the course of the past two chapters the Pocket Rocket system is investigated as an analogue to a single hollow cathode in the DASH source. The optical techniques described are well suited to investigating the hydrogen plasma in this operating regime. This chapter focusses on using an ICCD camera to observe the emission behaviour of the Balmer α line of the course of an rf cycle. The discharge is observed both end on, to observe the interior of the hollow cathode, and side on, to observe the diffusion of the plasma into the expansion tube.

Two distinct operational modes exist depending on the pressure power product of the system. Using the pressure in the expansion chamber as a reference, when the system is operated below 11 Torr.W it is in the diffuse mode, whereas above this threshold it operates in the bright mode. The low brightness, diffuse mode is

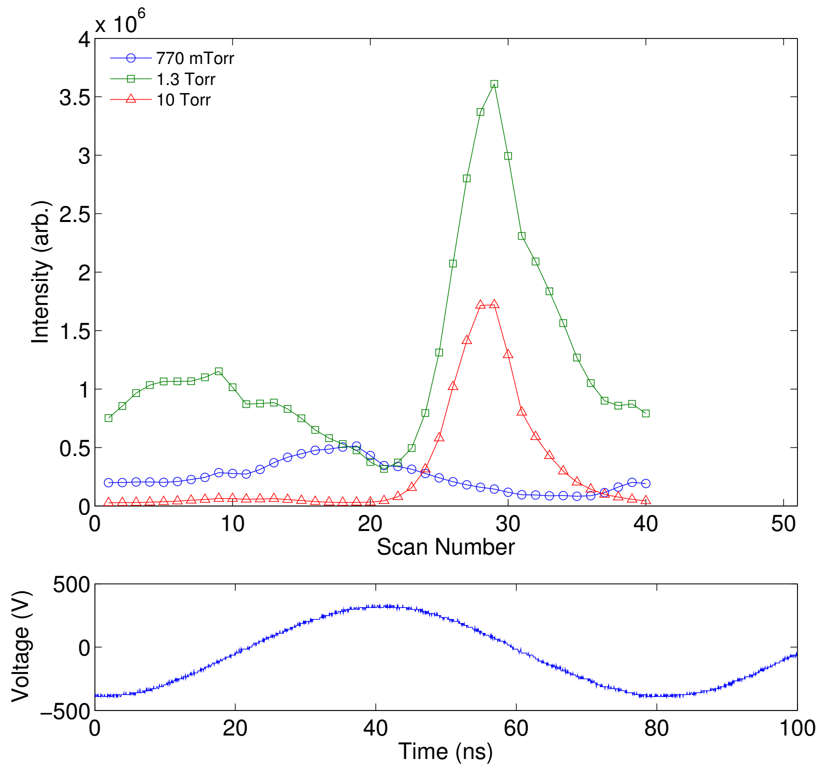

Figure 7.22: Integrated pixel counts for the plume ROI in the side view. To achieve higher pressures during operation the vacuum system is disabled in these measurements.

dominated by ion induced secondary electron emission. The bright mode appears to be dominated by field-electron interactions. The diffuse mode is most likely a capacitive discharge operating in the γ mode, but the main operating mechanism of the bright mode is less certain. It could be the result of an E-H mode transition, but displays very little hysteresis. It is also possible that the discharge is still operating in a capacitive mode, but is now dominated by the field reversal that occurs when the voltage on the powered electrode becomes positive. Measurements of the electric fields within the discharge using a technique such as laser spectroscopy would require modifications to the apparatus, but might provide further insight.

In both modes the plasma is observed to expand significantly into the glass tube once per rf cycle. In the diffuse mode the plasma extends furthest when voltage on the powered electrode is at its maximum value. It is suggested that this is because of the emission of secondary electrons from the earth plate facing the expansion tube, when the sheath at these surfaces is at its highest voltage. In the bright

mode the plasma extends into the expansion tube after the voltage on the driven electrode turns over at its positive maximum. This is also when emission from within the hollow cathode is brightest and is thought to be driven by the interaction of electrons and electric fields in sheath region.

To push the pressure in the system higher than 2 Torr, the pumping is removed and the system allowed to reach a static equilibrium pressure. It is seen in the static case that at higher pressures the structure of emission doesn't deviate from the bright mode with pumping active, although emission is seen to strongly decrease. As pressure increases far past what is achievable with the flowing gas regime the relative emission of peak 1 becomes much stronger, with peak 2 disappearing entirely.

In summary, the plasma is seen to vary between the two modes reliably and with no observable hysteresis. The Pocket Rocket source is shown to be capable of producing a very bright plasma within the hollow cathode in the bright mode at temperatures 100 to 200 K above room temperature. In the bright mode it seems likely that there is a high dissociation fraction, making the source potentially useful for surface processing applications requiring atomic hydrogen. Due to the similar design between Pocket Rocket and DASH, these results provide insight into the fundamental operation of a hydrogen hollow cathode in an array such as DASH, that might be used in deposition processes.

8

Conclusions

This chapter summarises key design features of the Distributed Array Shower Head (DASH) source, as well as the results presented in chapters 3 through 7. The DASH source is a stack of five electrodes. The outer two are earthed and the central one is the powered electrode. Between the powered electrode and the earth plates there are alumina insulators. An array of holes is bored through the stack and gas flows through these and is ignited into a plasma. The source is designed to facilitate the activation of the hollow cathode effect, and the high plasma densities measured suggest that this is achieved. The plasma formed in the hollow cathodes then diffuses into the expansion chamber. The behaviour of the source was investigated with argon due to its simple gas chemistry. Electrostatic probes were used to make measurements of the plasma density, potential, floating potential, and EEPF. The DASH's ability to chemically etch silicon using SF_6 was demonstrated on unbiased wafers. Finally, the suitability of the source for use in a deposition tool is investigated using optical techniques in a hydrogen plasma in the Pocket Rocket source, which is analogous to a single hollow cathode in the DASH. This was achieved through measurements of the neutral gas temperature and time resolved imaging of the discharge's Balmer α emission.

8.1 Summary of Results

During breakdown in the DASH system the plasma ignites between the powered and earthed electrodes, before the density peak moves into the centre of the hollow cathode. For stable operation, the source was found to require a minimum power and flow for every active hollow cathode. In argon these values are 10 sccm of flow

and 2 W of applied power. Using an uncompensated Langmuir probe, measurements of the ion density were made in the expansion chamber. For a flow of 33 sccm and a power of 33 W per hole, the peak density measured at the interface between the active hollow cathode and the expansion chamber is 10^{18} m^{-3}. Through comparison with results presented by Charles *et al.* in [92], it is estimated that the density inside the hollow cathode is approximately 10^{19} m^{-3}. The plasma expands from the hollow cathode as though from a point source, with a $1/z^2$ dependence until it reaches a density of approximately 10^{14} m^{-3}. At this point, the rate of decrease of the density with increasing distance from the source slows. This behaviour is due to the presence of an ambient plasma sustained within the expansion chamber itself rather than diffusing from the source.

Two hollow cathodes were then operated in tandem to produce a more complex discharge maintaining the operational parameters of 33 sccm and 33 W per hole. It was found that the peak densities measured did not vary. Furthermore, there was interaction between the two active hollow cathodes, evidenced by elevated plasma densities in the region between the two active hollow cathodes. It is thought that this behaviour is linked to the increased neutral gas pressure in this region facilitating ionising collisions within the expansion chamber.

To confirm this conclusion, the density map for a single active hollow cathode was used as a building block to see if the measured density maps for two and three hollow cathode arrangements could be reproduced via linear superposition. It was found that this was not the case, due to local pressure effects. An empirical model was developed to account for the ambient plasma present in the expansion chamber, relating density to local pressure. It was found that this model could accurately reproduce density in both two and three active hollow cathode configurations.

In general, the EEPFs measured in the expansion plume of the DASH system displayed bi-Maxwellian behaviour. Below the break energy temperatures of $2-3$ eV were typical, while above the break energy tail temperatures were measured between 7 and 12 eV. The EEPFs measured in the expansion chamber were unaffected by varying the power applied to the discharge, while variations in the flow caused strong changes. The temperature below the break energy was found to be relatively

independent of the flow through the system compared with the tail energy, which was strongly dependent on flow. It varyied from 9 eV at a flow of 20 sccm to 2 eV at 85 sccm per hole. This behaviour was explained by considering particle balances for the inside of the hollow cathode and the expansion chamber. Because the hollow cathode operates at a relatively high pressure of around 1 Torr, it is not sensitive to changes in pressure. Meanwhile the expansion chamber pressure is around 1 to 10 mTorr, and changes in pressure have a much stronger effect on the electron temperature.

Emissive probe measurements of the axial variation of the plasma and floating potentials were made. It was found that plasma potential was inversely proportional to flow, and that decreases with increasing distance from the hollow cathode. Making use of the density measurements made in chapter 3, Boltzmann's equation was used to deduce an electron temperature for the plasma inside the hollow cathode. It was found that an electron temperature of 2.1 eV provided the best fit to the measured potentials. This value agrees with both the particle balance and compensated Langmuir probe measurements of T_e made inside the hollow cathode.

Axial and lateral measurements of the EEPF showed that the plasma emerged from the hollow cathode with an approximately Maxwellian structure and and temperature of slightly above 2 eV. The distribution changes to a bi-Maxwellian for axial positions of $z \geq 2$ mm, before eventually returning to single Maxwellian at the temperature of the hot tail far from the hole. This behaviour was explained by attributing the hot tail to the ambient plasma in chamber. This suggestion was supported by the correlation between the point at which the EEPF returned to a single Maxwellian at the tail temperature and the point at which density maps showed the ambient plasma becoming the dominant density mechanism.

The DASH source was found to successfully dissociate SF_6 to form atomic fluorine. The fluorine diffused from the hollow cathodes and etched unbiased silicon wafers in the expansion chamber. The maximum etch rate measured was 3.2 μm per minute for a power of 500 W, the limit of the rf generator. The etch rate was found to have no dependence on flow through the system. This was attributed to the fact that the level of dissociation of the SF_6 was low, around 1/1000. Using a SEM,

the etch profile measured on wafers masked with positive photoresist was found to be isotropic. In accordance with expectations of the design, damage caused by ion bombardment at the surface was found to be insignificant.

The diffusion of atomic fluorine from the active hollow cathodes was also found to follow a $1/z^2$ dependence, similar to the behaviour observed in argon, before plateauing at $z = 10$ cm. The ambient etch rate in the expansion chamber was measured by placing coupons of silicon at a range of axial positions, without facing them directly towards the source. The point at which the etch rate no longer varied with a $1/z^2$ dependence coincided with the point at which the ambient etch rate became higher than would be expected by follow the $1/z^2$ trend. This behaviour provided further confirmation of the conclusion that the expansion chamber plasma is composed of diffusing plasma and ambient plasma. The uniformity of the etch rate was examined and revealed that the etch rate for complex arrangements of active hollow cathodes could be predicted with a linear superposition of double gaussian functions. It is expected that in a larger system a DASH type plasma source could etch a 300 mm wafer with a uniformity of $\pm 5\%$.

The hollow cathodes were found to produce aluminium fluoride as a byproduct during operation, which was deposited on the wafers being processed. This is problematic to the design, as aluminium fluoride is inert and blocks the etching process. Using X-ray spectroscopy in the SEM, the growth of the film was found to be slow for the first five minutes of operation before becoming approximately linear with time. It was deduced that the exposed alumina in the source was responsible for the production of the film, and that it could be prevented using a quartz insert. However, the quartz was vulnerable to being etched, and a more durable insert is required to pursue these experiments further.

Experiments were also conducted to investigate the suitability of the DASH source for use in deposition processes. To this end, optical experiments were performed in a hydrogen plasma. This was performed in the Pocket Rocket system, which is analogous to a single hollow cathode from the DASH source, due to its superior optical access. Optical emission spectroscopy of the Fulcher α system was performed to calculate gas temperature in hydrogen plasma. It was found that in hydrogen two

operational modes are achievable in Pocket Rocket, named the diffuse and bright modes after their appearances. The discharge operated in the diffuse mode below power pressure products of 11 Torr.W, and above this threshold the bright mode was activated. The diffuse mode was found to have temperatures around 350 K, while the bright mode had temperatures of approximately 500 K. These measurements were used in preliminary Lyman α absorption spectroscopy measurements in the DASH source, and will be essential for the continuation of this work.

Finally, the hydrogen hollow cathode discharge was investigated using time resolved imaging of the Balmer α line, performed with an ICCD camera. The camera was configured to observe down the axis of the hollow cathode as well as at the expansion plume. It was found that the diffuse mode is operating primarily as a capacitive γ discharge. This is evidenced by the strong emission from inside the hollow cathode when the voltage on the powered electrode is at its most negative. By contrast, the bright mode appeared to have some element of coupling between electric fields and the electrons in the discharge. The strongest emission from within the hollow cathode appeared when the rate of change of voltage on the powered electrode was maximised.

Observing the two modes in the expansion tube of the Pocket Rocket system showed that in both cases, plasma propagated down the expansion tube once per rf cycle. The diffuse mode propagation is driven by the emission of secondary electrons from the expansion tube facing earth plate during the positive part of the rf cycle. By contrast, the bright mode launches plasma down the expansion tube at the same time as the most intense emission is observed from inside the hollow cathode, implying that the electrons driving the process are ejected from inside the hollow cathode. The speed of propagation was measured to be approximately 2×10^6 ms^{-1}, slightly below the speed of an ionising electron. There is a dark region observed in front of the earth plate in the bright mode. This has been attributed to the formation of a barrel shock in the system. The decrease of neutral and charged species in the zone of silence causes an increase in the mean free path for an excitation event. Investigations of the electrical characteristics of the system during the mode transition showed that the resistance increased from 5 Ω to 20 Ω and the power factor also increased by a

factor of two. Both of these are strong indicators of an E-H mode transition.

8.2 Future Work

There are three fundamental directions in which the work presented in this thesis might be meaningfully extended. In brief they are: pursuit of a suitable material for sleeves for use in SF_6 dissociation, Lyman α absorption spectroscopy, and fluid simulation of the system.

It was seen that the DASH source is capable of producing enough atomic fluorine to chemically etch silicon at a reasonable rate and without exposing it to high energy bombarding ions. However, for the source to progress any further in this direction the problem of aluminium fluoride deposition needs to be solved. Ideally the material for a new sleeve will be machinable, resistant to etching by fluorine, resistant to sputtering by ions, and resistant to high temperatures. Boron nitride is one candidate for such a role, but is very expensive. An alternative to this would be to redesign the insulating electrodes to be made of a different dielectric material, not containing aluminium.

Pursuing Lyman α absorption spectroscopy may be a productive area for future investigation into both the DASH source and hydrogen hollow cathode plasmas in general. The preliminary data presented in chapter 6 provides a good framework for estimating temperatures of the atomic hydrogen in the expansion plume given the high pressure in these experiments. The first part of this task is to modify the VUV diode to allow it to sample quickly enough to observe the afterglow of a pulsed hydrogen plasma in the DASH source.

Finally to corroborate the conclusions drawn concerning the fundamental operational mechanics of the DASH system, simulation would be appropriate. Some work, yet unpublished, has been performed by Greig *et al.* on modelling the Pocket Rocket system using the CFD-ACE+ package. Their findings appear to closely resemble the operational mechanics of the diffuse mode observed with the ICCD in hydrogen. Adaptation of the model to simulate the DASH system would be a valuable addition to the work presented in this thesis.

Bibliography

[1] F. F. Chen. *Introduction to Plasma Physics and Controlled Fusion*, volume 1. Springer, 2nd edition, 2006.

[2] M.A. Lieberman and A.J. Lichtenberg. *Principles Of Plasma Discharges and Materials Processing*. Wiley-Interscience, 2005.

[3] P. Chabert and N. Braithwaite. *Physics of Radio-Frequency Plasmas*. Cambridge University Press, 2011.

[4] Á. Yanguas-Gil, J. Cotrino, and L. L. Alves. An update of argon inelastic cross sections for plasma discharges. *Journal of Physics D: Applied Physics*, 38(10):1588, 2005.

[5] S. Ashida, C. Lee, and M. A. Lieberman. Spatially averaged (global) model of time modulated high density argon plasmas. *Journal of Vacuum Science & Technology A*, 13(5):2498–2507, 1995.

[6] C. Lee and M. A. Lieberman. Global model of Ar, O_2, Cl_2, and Ar/O_2 high density plasma discharges. *Journal of Vacuum Science & Technology A*, 13(2):368–380, 1995.

[7] W. Lotz. Electron-impact ionization cross-sections and ionization rate coefficients for atoms and ions from hydrogen to calcium. *Zeitschrift für Physik*, 216(3):241–247, 1968.

[8] H. B. Smith, C. Charles, and R. W. Boswell. Breakdown behavior in radio-frequency argon discharges. *Physics of Plasmas*, 10(3):875–881, 2003.

[9] K. U. Riemann. The bohm criterion and sheath formation. *Journal of Physics D: Applied Physics*, 24(4):493, 1991.

[10] V. Vahedi, C. K. Birdsall, M. A. Lieberman, G. DiPeso, and T. D. Ronhlien. Capacitive rf discharges modelled by particle-in-cell monte carlo simulation. ii. comparisons with laboratory measurements of electron energy distribution functions. *Plasma Sources Science and Technology*, 2(4):273, 1993.

[11] H. Singh and D. B. Graves. Measurements of the electron energy distribution function in molecular gases in an inductively coupled plasma. *Journal of Applied Physics*, 87(9):4098–4106, 2000.

[12] J. T. Gudmundsson, J. Alami, and U. Helmersson. Evolution of the electron energy distribution and plasma parameters in a pulsed magnetron discharge. *Applied Physics Letters*, 78(22):3427–3429, 2001.

[13] G. D. Conway, A. J. Perry, and R. W. Boswell. Evolution of ion and electron energy distributions in pulsed helicon plasma discharges. *Plasma Sources Science and Technology*, 7(3):337, 1998.

[14] V. A. Godyak, R. B. Piejak, and B. M. Alexandrovich. Measurement of electron energy distribution in low-pressure rf discharges. *Plasma Sources Science and Technology*, 1(1):36, 1992.

[15] R. L. F. Boyd and N. D. Twiddy. Electron energy distributions in plasmas. i. *Proceedings of the Royal Society of London. Series A. Mathematical and Physical Sciences*, 250(1260):53–69, 1959.

[16] A. P. Paranjpe, J. P. McVittie, and S. A. Self. A tuned langmuir probe for measurements in rf glow discharges. *Journal of Applied Physics*, 67(11):6718–6727, 1990.

[17] V. A. Godyak and V. I. Demidov. Probe measurements of electron-energy distributions in plasmas: what can we measure and how can we achieve reliable results? *Journal of Physics D: Applied Physics*, 44(23):233001, 2011.

[18] T. I. Cox, V. G. I. Deshmukh, D. A. O. Hope, A. J. Hydes, N. S. J. Braithwaite, and N. M. P. Benjamin. The use of langmuir probes and optical emission

spectroscopy to measure electron energy distribution functions in rf-generated argon plasmas. *Journal of Physics D: Applied Physics*, 20(7):820, 1987.

[19] T. Hori, M. Kogano, M. D. Bowden, K. Uchino, and K. Muraoka. A study of electron energy distributions in an inductively coupled plasma by laser thomson scattering. *Journal of Applied Physics*, 83(4):1909–1916, 1998.

[20] P. L. G. Ventzek, R. J. Hoekstra, and M. J. Kushner. Two dimensional modeling of high plasma density inductively coupled sources for materials processing. *Journal of Vacuum Science & Technology B*, 12(1):461–477, 1994.

[21] J. Dawson. On Landau Damping. *Physics of Fluids*, 4(7):869–874, 1961.

[22] F.F. Chen and R.W. Boswell. Helicons-the past decade. *Plasma Science, IEEE Transactions on*, 25(6):1245–1257, 1997.

[23] A. W. Degeling, C. O. Jung, R. W. Boswell, and A. R. Ellingboe. Plasma production from helicon waves. *Physics of Plasmas*, 3(7):2788–2796, 1996.

[24] V. A. Godyak and R. B. Piejak. Abnormally low electron energy and heating-mode transition in a low-pressure argon rf discharge at 13.56 MHz. *Phys. Rev. Lett.*, 65:996–999, 1990.

[25] G. Gozadinos, M. M. Turner, and D. Vender. Collisionless electron heating by capacitive rf sheaths. *Phys. Rev. Lett.*, 87:135004, Sep 2001.

[26] S. Y. Moon, J. K. Rhee, D. B. Kim, and W. Choe. α, γ, and normal, abnormal glow discharge modes in radio-frequency capacitively coupled discharges at atmospheric pressure. *Physics of Plasmas*, 13(3), 2006.

[27] F. Paschen. Bohrs heliumlinien. *Annalen der Physik*, 355(16):901–940, 1916.

[28] P. F. Little and A. von Engel. The hollow-cathode effect and the theory of glow discharges. *Proceedings of the Royal Society of London. Series A. Mathematical and Physical Sciences*, 224(1157):209–227, 1954.

[29] J.W. Gewartowski and H.A. Watson. *Principles of electron tubes: including grid-controlled tubes, microwave tubes, and gas tubes.* Van Nostrand, 1965.

[30] G. Stockhausen and M. Kock. Proof and analysis of the pendulum motion of beam electrons in a hollow cathode discharge. *Journal of Physics D: Applied Physics*, 34(11):1683, 2001.

[31] H. Eichhorn, K. H. Schoenbach, and T. Tessnow. Paschen's law for a hollow cathode discharge. *Applied Physics Letters*, 63(18):2481–2483, 1993.

[32] K. H. Schoenbach, A. El-Habachi., W. Shi, and M. Ciocca. High-pressure hollow cathode discharges. *Plasma Sources Science and Technology*, 6(4):468, 1997.

[33] G. J. Kim, F. Iza, and J. K. Lee. Electron and ion kinetics in a micro hollow cathode discharge. *Journal of Physics D: Applied Physics*, 39(20):4386, 2006.

[34] C. M. Horwitz. Hollow cathode reactive sputter etching—a new highrate process. *Applied Physics Letters*, 43(10):977–979, 1983.

[35] L. Bardoš. Radio frequency hollow cathodes for the plasma processing technology. *Surface and Coatings Technology*, 86:648–656, 1996.

[36] D. Vender and R.W. Boswell. Numerical modeling of low-pressure rf plasmas. *Plasma Science, IEEE Transactions on*, 18(4):725–732, 1990.

[37] L. Bardoš, S. Berg, and H-O. Blom. Superhigh rate plasma jet etching of silicon. *Applied Physics Letters*, 55(16):1615–1617, 1989.

[38] R Mohan Sankaran and K P Giapis. High-pressure micro-discharges in etching and deposition applications. *Journal of Physics D: Applied Physics*, 36(23):2914, 2003.

[39] John A. Thornton. Influence of apparatus geometry and deposition conditions on the structure and topography of thick sputtered coatings. *Journal of Vacuum Science & Technology*, 11(4):666–670, 1974.

[40] J. J. Cuomo and S. M. Rossnagel. Hollow cathode enhanced magnetron sputtering. *Journal of Vacuum Science & Technology A*, 4(3):393–396, 1986.

[41] Z. Hubička, G. Pribil, R.J. Soukup, and N.J. Ianno. Investigation of the rf and dc hollow cathode plasma-jet sputtering systems for the deposition of silicon thin films. *Surface and Coatings Technology*, 160(2–3):114 – 123, 2002.

[42] C. M. Horwitz and D. R. McKenzie. High-rate hollow-cathode amorphous silicon deposition. *Applications of Surface Science*, 22–23, Part 2(0):925 – 929, 1985.

[43] L. Bardoš and V. Dušek. High rate jet plasma-assisted chemical vapour deposition. *Thin Solid Films*, 158(2):265 – 270, 1988.

[44] R. M. Sankaran and K. P. Giapis. Hollow cathode sustained plasma microjets: Characterization and application to diamond deposition. *Journal of Applied Physics*, 92(5):2406–2411, 2002.

[45] S. Saloum and M. Naddaf. Optical constants of silicone-like (Si:Ox:Cy:Hz) thin films deposited on quartz using hexamethyldisiloxane in a remote RF hollow cathode discharge plasma. *Vacuum*, 82(1):50 – 55, 2007.

[46] B. Zimmermann, F. Fietzke, H. Klostermann, J. Lehmann, F. Munnik, and W. Möller. High rate deposition of amorphous hydrogenated carbon films by hollow cathode arc PECVD. *Surface and Coatings Technology*, 212(0):67 – 71, 2012.

[47] K. H. Becker, K. H. Schoenbach, and J. G. Eden. Microplasmas and applications. *Journal of Physics D: Applied Physics*, 39(3):R55, 2006.

[48] K. H. Schoenbach, R. Verhappen, T. Tessnow, F. E. Peterkin, and W. W. Byszewski. Microhollow cathode discharges. *Applied physics letters*, 68:13, 1996.

[49] J. W. Frame and J. G. Eden. Planar microdischarge arrays. *Electronics Letters*, 34(15):1529–1531, 1998.

[50] D. D. Hsu and D. B. Graves. Microhollow cathode discharge stability with flow and reaction. *Journal of Physics D: Applied Physics*, 36(23):2898, 2003.

[51] P. Kurunczi, H. Shah, and K. Becker. Hydrogen Lyman alpha and Lyman beta emissions from high-pressure microhollow cathode discharges in Ne-H2 mixtures. *Journal of Physics B: Atomic, Molecular and Optical Physics*, 32(22):L651, 1999.

[52] R. M. Sankaran and K. P. Giapis. Maskless etching of silicon using patterned microdischarges. *Applied Physics Letters*, 79(5):593–595, 2001.

[53] D. M. Manos and D. L. Flamm. *Plasma etching: an introduction*. Elsevier, 1989.

[54] L. Martinu and D. Poitras. Plasma deposition of optical films and coatings: A review. *Journal of Vacuum Science & Technology A*, 18(6):2619–2645, 2000.

[55] D. Rosso. Global semiconductor industry posts highest-ever first quarter sales, 2014.

[56] W. R. Grove. On the electro-chemical polarity of gases. *Philosophical transactions of the Royal Society of London*, 142:87–101, 1852.

[57] M.P. Lepselter, H.A. Waggener, R.W. MacDonald, and R.E. Davis. Beam-lead devices and integrated circuits. *Proceedings of the IEEE*, 53(4):405–405, 1965.

[58] P. D. Davidse. Rf sputter etching—a universal etch. *Journal of The Electrochemical Society*, 116(1):100–103, 1969.

[59] S. M. Irving. Plasma oxidation process for removing photoresist films. *Solid State Technology*, 14(6):47, 1971.

[60] R. A. H. Heinecke. Control of relative etch rates of SiO2 and Si in plasma etching. *Solid-State Electronics*, 18(12):1146 – 1147, 1975.

[61] D. L. Flamm, V. M. Donnelly, and J. A. Mucha. The reaction of fluorine atoms with silicon. *Journal of Applied Physics*, 52(5):3633–3639, 1981.

[62] R. W. Boswell and D. Henry. Pulsed high rate plasma etching with variable Si/SiO2 selectivity and variable Si etch profiles. *Applied Physics Letters*, 47(10):1095–1097, 1985.

[63] T.C. Penn. Forecast of VLSI processing; A historical review of the first dry-processed IC. *Electron Devices, IEEE Transactions on*, 26(4):640–643, Apr 1979.

[64] J. A. Bondur. Dry process technology (reactive ion etching). *Journal of Vacuum Science & Technology*, 13(5):1023–1029, 1976.

[65] J. W. Coburn and H. F. Winters. Plasma etching-a discussion of mechanisms. *Journal of Vacuum Science & Technology*, 16(2):391–403, 1979.

[66] H. W. Lehmann and R. Widmer. Profile control by reactive sputter etching. *Journal of Vacuum Science & Technology*, 15(2):319–326, 1978.

[67] Y. Horiike and H. Okano. RIE apparatus utilizing a shielded magnetron to enhance etching, 1984. US Patent 4,431,473.

[68] V. J. Minkiewicz and B. N. Chapman. Triode plasma etching. *Applied Physics Letters*, 34(3):192–193, 1979.

[69] A. R. Reinberg, G. N. Steinberg, and C. B. Zarowin. Inductively coupled discharge for plasma etching and resist stripping, 1984. US Patent 4,431,898.

[70] A. J. Perry, D. Vender, and R. W. Boswell. The application of the helicon source to plasma processing. *Journal of Vacuum Science & Technology B*, 9(2):310–317, 1991.

[71] T. Ono, M. Oda, C. Takahashi, and S. Matsuo. Reactive ion stream etching utilizing electron cyclotron resonance plasma. *Journal of Vacuum Science & Technology B*, 4(3):696–700, 1986.

[72] J. J. Chen, R. G. Veltrop, and T. E. Wicker. Multiple coil antenna for inductively-coupled plasma generation systems, 2000. US Patent 6,164,241.

[73] N. M. P. Benjamin, B. N. Chapman, and Rod W Boswell. Progress of an advanced diffusion source plasma reactor. In *Santa Cl-DL tentative*, pages 95–105. International Society for Optics and Photonics, 1991.

[74] T. Yamamoto, N. T. Chien, M. Ando, N. Goto, M. Hirayama, and T. Ohmi. Design of radial line slot antennas at 8.3 ghz for large area uniform plasma generation. *Japanese Journal of Applied Physics*, 38(4R):2082, 1999.

[75] Y. Yang and M. J. Kushner. 450 mm dual frequency capacitively coupled plasma sources: Conventional, graded, and segmented electrodes. *Journal of Applied Physics*, 108(11), 2010.

[76] D. L. Flamm, D. N. K. Wang, and D. Maydan. Multiple-etchant loading effect and silicon etching in ClF_3 and related mixtures. *Journal of The Electrochemical Society*, 129(12):2755–2760, 1982.

[77] S. Samukawa. Highly selective and highly anisotropic SiO_2 etching in pulse-time modulated electron cyclotron resonance plasma. *Japanese Journal of Applied Physics*, 33(4S):2133, 1994.

[78] Takayuki Fukasawa, Akihiro Nakamura, Haruo Shindo, and Yasuhiro Horiike. High rate and highly selective s i o 2 etching employing inductively coupled plasma. *Japanese Journal of Applied Physics*, 33(4S):2139, 1994.

[79] B. E. E. Kastenmeier, P. J. Matsuo, J. J. Beulens, and G. S. Oehrlein. Chemical dry etching of silicon nitride and silicon dioxide using $CF_4/O_2/N_2$ gas mixtures. *Journal of Vacuum Science & Technology A*, 14(5):2802–2813, 1996.

[80] J. Y. Jeong, S. E. Babayan, A. Schütze, V. J. Tu, J. Park, I. Henins, G. S. Selwyn, and R. F. Hicks. Etching polyimide with a nonequilibrium atmospheric-pressure plasma jet. *Journal of Vacuum Science & Technology A*, 17(5):2581–2585, 1999.

[81] G. J. H. Brussaard, K. G. Y. Letourneur, M. Schaepkens, M. C. M. van de Sanden, and D. C. Schram. Stripping of photoresist using a remote thermal

Ar/O_2 and Ar/N_2/O_2 plasma. *Journal of Vacuum Science & Technology B*, 21(1):61–66, 2003.

[82] G. J. Stueber, G. S. Oehrlein, P. Lazzeri, M. Bersani, M. Anderle, E. Busch, and R. McGowan. On the photoresist stripping and damage of ultralow k dielectric materials using remote H_2 and D_2 based discharges. *Journal of Vacuum Science & Technology B*, 25(5):1593–1602, 2007.

[83] J. J. Beulens, B. E. E. Kastenmeier, P. J. Matsuo, and G. S. Oehrlein. Chemical downstream etching of silicon–nitride and polycrystalline silicon using CF_4/O_2/N_2: Surface chemical effects of O_2 and N_2 additives. *Applied Physics Letters*, 66(20):2634–2636, 1995.

[84] B. Wu, A. Kumar, and S. Pamarthy. High aspect ratio silicon etch: A review. *Journal of Applied Physics*, 108(5):–, 2010.

[85] S. Somekh, H. C. Casey Jr, et al. Dry processing of high resolution and high aspect ratio structures in GaAs-$Al_xGa_{1-x}As$ for integrated optics. *Applied optics*, 16(1):126–136, 1977.

[86] P. G. Glöersen. Ionbeam etching. *Journal of Vacuum Science & Technology*, 12(1):28–35, 1975.

[87] A. Herrick, A. J. Perry, and R. W. Boswell. Etching silicon by SF_6 in a continuous and pulsed power helicon reactor. *Journal of Vacuum Science & Technology A*, 21(4):955–966, 2003.

[88] V. M. Donnelly and A. Kornblit. Plasma etching: Yesterday, today, and tomorrow. *Journal of Vacuum Science & Technology A*, 31(5), 2013.

[89] M. E. Barone and D. B. Graves. Molecular-dynamics simulations of direct reactive ion etching of silicon by fluorine and chlorine. *Journal of Applied Physics*, 78(11):6604–6615, 1995.

[90] F. Laermer and A. Schilp. Method of anisotropically etching silicon, 1996. US Patent 5,501,893.

[91] F. Laermer, A. Schilp, K. Funk, and M. A. O. M. Offenberg. Bosch deep silicon etching: improving uniformity and etch rate for advanced mems applications. In *Micro Electro Mechanical Systems, 1999. MEMS'99. Twelfth IEEE International Conference on*, pages 211–216. IEEE, 1999.

[92] C. Charles and R. W. Boswell. Measurement and modelling of a radiofrequency micro-thruster. *Plasma Sources Science and Technology*, 21(2):022002, 2012.

[93] W. Cox, C. Charles, R. W. Boswell, and R. Hawkins. Spatial retarding field energy analyzer measurements downstream of a helicon double layer plasma. *Applied Physics Letters*, 93(7), 2008.

[94] S. A. Smith, C. A. Wolden, M. D. Bremser, A. D. Hanser, R. F. Davis, and W. V. Lampert. High rate and selective etching of GaN, AlGaN, and AlN using an inductively coupled plasma. *Applied Physics Letters*, 71(25):3631–3633, 1997.

[95] R. B. Piejak, V. A. Godyak, and B. M. Alexandrovich. A simple analysis of an inductive rf discharge. *Plasma Sources Science and Technology*, 1(3):179, 1992.

[96] G. Grammer. *A Course In Radio Fundamentals*. The American Radio Relay League, 1972.

[97] H. B. Smith, C. Charles, R. W. Boswell, and H. Kuwahara. Bias formation in a pulsed radiofrequency argon discharge. *Journal of Applied Physics*, 82(2):561–565, 1997.

[98] J. E. Allen, R. L. F. Boyd, and P. Reynolds. The collection of positive ions by a probe immersed in a plasma. *Proceedings of the Physical Society. Section B*, 70(3):297, 1957.

[99] T. E. Sheridan. How big is a small langmuir probe? *Physics of Plasmas*, 7:3084, 2000.

[100] K. Takahashi, C. Charles, R. W. Boswell, T. Kaneko, and R. Hatakeyama. Measurement of the energy distribution of trapped and free electrons in a current-free double layer. *Physics of Plasmas*, 14(11):114503, 2007.

[101] N. S. J. Braithwaite, N. M. P. Benjamin, and J. E. Allen. An electrostatic probe technique for rf plasma. *Journal of Physics E: Scientific Instruments*, 20(8):1046, 1987.

[102] M. J. Druyvesteyn. Der niedervoltbogen. *Zeitschrift für Physik*, 64(11-12):781–798, 1930.

[103] I. D. Sudit and R. C. Woods. A workstation based langmuir probe system for lowpressure dc plasmas. *Review of Scientific Instruments*, 64(9):2440–2448, 1993.

[104] J. R. Smith, N. Hershkowitz, and P. Coakley. Inflectionpoint method of interpreting emissive probe characteristics. *Review of Scientific Instruments*, 50(2):210–218, 1979.

[105] R. F. Kemp and Jr. J. M. Sellen. Plasma potential measurements by electron emissive probes. *Review of Scientific Instruments*, 37(4):455–461, 1966.

[106] A. Greig, C. Charles, and R. W. Boswell. private communication. 2014.

[107] C. Charles and R. W. Boswell. private communication. 2014.

[108] C. Charles, R. W. Boswell, A. Bouchoule, C. Laure, and P. Ranson. Plasma diffusion from a low pressure radio frequency source. *Journal of Vacuum Science & Technology A: Vacuum, Surfaces, and Films*, 9(3):661–663, 1991.

[109] M. F. A. M. van Hest, J. R. Haartsen, M. H. M. van Weert, D. C. Schram, and M. C. M. van de Sanden. Analysis of the expanding thermal argon–oxygen plasma gas phase. *Plasma Sources Science and Technology*, 12(4):539, 2003.

[110] T. Lafleur, C. Charles, and R. W. Boswell. Detailed plasma potential measurements in a radio-frequency expanding plasma obtained from various electrostatic probes. *Physics of Plasmas*, 16(4):044510, 2009.

[111] S. Dixon, C. Charles, R. W. Boswell, W. Cox, J. Holland, and R. Gottscho. Interactions between arrayed hollow cathodes. *Journal of Physics D: Applied Physics*, 46(14):145204, 2013.

[112] T. Lafleur and R. W. Boswell. Particle-in-cell simulations of hollow cathode enhanced capacitively coupled radio frequency discharges. *Physics of Plasmas*, 19(2):023508–023508, 2012.

[113] A. Greig, C. Charles, R. W. Boswell, R. Hawkins, M. Bowden, and Y. Sutton. Neutral gas temperature measurements of a radio frequency micro-thruster. In *20th International Workshop on Electron Cyclotron Resonance Ion Sources*, 2012.

[114] C. Charles and R. W. Boswell. Current-free double-layer formation in a high-density helicon discharge. *Applied Physics Letters*, 82(9):1356 –1358, mar 2003.

[115] X. Sun, A. M. Keesee, C. Biloiu, E. E. Scime, A. Meige, C. Charles, and R. W. Boswell. Observations of ion–beam formation in a current–free double layer. *Phys. Rev. Lett.*, 95:025004, Jul 2005.

[116] G. Hairapetian and R. L. Stenzel. Observation of a stationary, current-free double layer in a plasma. *Phys. Rev. Lett.*, 65:175–178, Jul 1990.

[117] C. Charles, R. Boswell, and K. Takahashi. Boltzmann expansion in a radiofrequency conical helicon thruster operating in xenon and argon. *Applied Physics Letters*, 102(22):223510, 2013.

[118] V. Godyak, R. Lagushenko, and J. Maya. Spatial evolution of the electron-energy distribution in the vicinity of a discharge-tube constriction. *Phys. Rev. A*, 38:2044–2055, Aug 1988.

[119] S. Yoshida, A. V. Phelps, and L. C. Pitchford. Effect of electrons produced by ionization on calculated electron-energy distributions. *Phys. Rev. A*, 27:2858–2867, Jun 1983.

[120] A. Greig, C. Charles, R. Hawkins, and R. Boswell. Direct measurement of neutral gas heating in a radio-frequency electrothermal plasma micro-thruster. *Applied Physics Letters*, 103(7), 2013.

[121] R. W. Boswell and R. K. Porteous. Etching in a pulsed plasma. *Journal of applied physics*, 62(8):3123–3129, 1987.

[122] M. J. de Graaf. *A new hydrogen particle source*. PhD thesis, Boek-en Offsetdrukkerij Letru, 1994.

[123] H. G. Gale, G. S. Monk, and K. O. Lee. Measurements of waveengths in the secondary spectrum of hydrogen. *The Astrophysical Journal*, 67:89, 1928.

[124] G. Herzberg. *Molecular Spectra and Molecular Structure, Volume 1 - Spectra of Diatomic Molecules*, volume 1. Van Nostrand, 1950.

[125] T. Gans, Chun C. Lin, V. Schulz-von der Gathen, and H. F. Döbele. Phase-resolved emission spectroscopy of a hydrogen rf discharge for the determination of quenching coefficients. *Phys. Rev. A*, 67:012707, 2003.

[126] T. Gans, V. Schulz von der Gathen, and H. F. Döbele. Time dependence of rotational state populations of excited hydrogen molecules in an rf excited plasma reactor. *Plasma Sources Science and Technology*, 10(1):17, 2001.

[127] S. A. Astashkevich, M. Käning, E. Käning, N. V. Kokina, B. P. Lavrov, A. Ohl, and J. Röpcke. Radiative characteristics of 3p Σ, Π; 3d Π^-, Δ^- states of H_2 and determination of gas temperature of low pressure hydrogen containing plasmas. *Journal of Quantitative Spectroscopy and Radiative Transfer*, 56(5):725 – 751, 1996.

[128] E. Surrey and B. Crowley. Spectroscopic measurement of gas temperature in the neutralizer of the jet neutral beam injection system. *Plasma Physics and Controlled Fusion*, 45(7):1209, 2003.

[129] J. A. M. van der Mullen. Excitation equilibria in plasmas; a classification. *Physics Reports*, 191(2–3):109 – 220, 1990.

[130] T. Shikama, S. Kado, Y. Kuwahara, K. Kurihara, F. Scotti, and S. Tanaka. Fulcher α band spectra in mixed hydrogen isotope plasmas. *Plasma and Fusion Research*, 2:S1045–S1045, 2007.

[131] B. Xiao, S. Kado, S. Kajita, and D. Yamasaki. Rovibrational distribution determination of H_2 in low temperature plasmas by Fulcher α band spectroscopy. *Plasma Physics and Controlled Fusion*, 46(4):653, 2004.

[132] J. Laimer, R. Posch, G. Misslinger, C. G. Schwarzler, and H. Stori. Determination of absolute hydrogen atom densities by Lyman α absorption. *Measurement Science and Technology*, 6(9):1413, 1995.

[133] J. Dedrick, D. Connell, T. Gans, R. W. Boswell, and C. Charles. Formation of spatially periodic fronts of high-energy electrons in a radio-frequency driven surface microdischarge. *Applied Physics Letters*, 102(3), 2013.

[134] R. Zorat, J. Goss, D. Boilson, and D. Vender. Global model of a radiofrequency H_2 plasma in DENISE. *Plasma Sources Science and Technology*, 9(2):161, 2000.

[135] U. Czarnetzki, D. Luggenhölscher, and H. F. Döbele. Space and time resolved electric field measurements in helium and hydrogen rf-discharges. *Plasma Sources Science and Technology*, 8(2):230, 1999.

[136] U. Czarnetzki, D. Luggenhölscher, and H. F. Döbele. Investigations on ionic processes and dynamics in the sheath region of helium and hydrogen discharges by laser spectroscopic electric field measurements. *Applied Physics A*, 72(5):509–521, 2001.

[137] *iStar Manual*. Andor Technology, 2012.

[138] C. Charles, J. Dedrick, R. W. Boswell, D. Connell, and T. Gans. Nanosecond optical imaging spectroscopy of an electrothermal radiofrequency plasma thruster plume. *Applied Physics Letters*, 103(12), 2013.

[139] C. Böhm and J. Perrin. Retarding field analyzer for measurements of ion energy distributions and secondary electron emission coefficients in low pres-

sure radio frequency discharges. *Review of Scientific Instruments*, 64(1):31–44, 1993.

[140] J. Jansky, Q. T. Algwari, D. O'Connell, and A. Bourdon. Experimental-modeling study of an atmospheric-pressure helium discharge propagating in a thin dielectric tube. *Plasma Science, IEEE Transactions on*, 40(11):2912–2919, 2012.

[141] M. Teschke, J. Kedzierski, E.G. Finantu-Dinu, D. Korzec, and J. Engemann. High-speed photographs of a dielectric barrier atmospheric pressure plasma jet. *Plasma Science, IEEE Transactions on*, 33(2):310–311, Apr 2005.

[142] N. Mericam-Bourdet, M. Laroussi, A. Begum, and E. Karakas. Experimental investigations of plasma bullets. *Journal of Physics D: Applied Physics*, 42(5):055207, 2009.

[143] P. Vankan, S. Mazouffre, R. Engeln, and D. C. Schram. Inflow and shock formation in supersonic, rarefied plasma expansions. *Physics of Plasmas*, 12(10), 2005.

[144] M. B. Shah, D. S. Elliott, and H. B. Gilbody. Pulsed crossed-beam study of the ionisation of atomic hydrogen by electron impact. *Journal of Physics B: Atomic and Molecular Physics*, 20(14):3501, 1987.

[145] H. C. Straub, P. Renault, B. G. Lindsay, K. A. Smith, and R. F. Stebbings. Absolute partial cross sections for electron-impact ionization of H_2, N_2, and O_2 from threshold to 1000 eV. *Phys. Rev. A*, 54:2146–2153, Sep 1996.

[146] A. L. Ward. Calculations of cathode-fall characteristics. *Journal of applied physics*, 33(9):2789–2794, 1962.